Seismic Performance of Glulam Frames with Buckling Restrained Braces (BRBs)

PhD Thesis submitted in partial fulfilment

of the requirements for the degree of

DOCTOR OF PHILOSOPHY

in

CIVIL ENGINEERING

by

Wenchen Dong

Supervised by:

Associate Professor Minghao Li, University of Canterbury

Dr Chin-Long Lee, University of Canterbury

Associate Professor Gregory MacRae, University of Canterbury

Associate Professor Anthony Abu, University of Canterbury

Department of Civil and Natural Resources Engineering

University of Canterbury

Christchurch, New Zealand

http:// www.civil.canterbury.ac.nz

ABSTRACT

This research investigates the in-plane seismic performance of glulam frames with buckling restrained braces (BRBs) through experimental testing, numerical modelling and design approach development.

With the advancement of engineered wood products (EWPs) and digital fabrication technology, there is an increasing interest and implementation of EWPs for mid-rise and high-rise buildings (also called mass timber buildings) around the world. However, the elastic modulus of timber is only around one-third of reinforced concrete and one-twentieth of structural steel. Additionally, limited ductility is assumed during mass timber building design due to the possibility of timber's brittle failure in tension. Seismic considerations usually govern the design of lateral force resisting systems (LFRS) in earthquake-prone countries like New Zealand. The relatively lower elastic modulus and limited ductility of timber may cause uneconomical member sizes and increase the number of LFRS (e.g. shear walls and braces). These limitations motivated this research with the main objective to improve the seismic performance of mass timber building using a timber-steel hybrid system.

Experimental tests were conducted for BRB-braced glulam frames (BRBGFs). Following the capacity design approach, BRBs were designed as ductile elements while timber members and BRB-timber interface connections were designed as non-ductile elements. Two 8 m wide and 3.6 m high full-scale BRBGFs were built and tested under cyclic loading. Dowelled connections with inserted steel plates were used in one specimen to connect the glulam members and BRBs, while screwed connections with steel side plates were used in the other specimen. The test results showed that replacing the traditional timber braces with BRBs significantly increased the energy dissipation capacity and minimized the damage in the connections as well as glulam members. The BRBGF with the dowelled connections (S-D) had more initial slips than the BRBGF with the screwed connections (S-S), but both specimens had comparable performance after the serviceability limit state (SLS) load level.

Component-based numerical models were developed in OpenSees to investigate BRBGFs with general configurations. The test data of S-D and S-S were first used to calibrate the numerical models. Then, parametric studies were conducted to investigate the influence of connection stiffness and initial slips on the cyclic performance of BRBGFs. It was shown that the component-based numerical models represented the force-drift responses, accumulated energy dissipation and BRB deformations of S-D and S-S well. When the connection relative overstrength factor $\gamma_{os,con}$ was over the BRB overstrength factor $\gamma_{os,BRB}$, the connections were sufficiently stiff to engage BRBs. The strength and stiffness of BRBs and initial slips caused by manufacturer tolerances had a negligible effect on the ultimate strength and energy dissipation under cyclic loading.

A direct displacement-based design (DDBD) approach was developed for the BRBGF system to avoid the complicated process of numerical modelling and facilitate the application of the hybrid system. The critical parameters for extending the DDBD approach to the BRBGF

system were first discussed including the displacement profile, yield drift, connection stiffness, hysteresis damping ratio and displacement reduction factor η_{in}. Then, the component-based numerical modelling method was used to build one-bay one-storey BRBGFs and verify the critical parameters by pushover analyses and nonlinear time-history analyses (NLTHA). Moreover, the DDBD approach was used to design a set of BRBGF buildings with three, six, and nine storeys. The multi-storey BRBGF models were built in the OpenSees and analysed under a set of ground motions to verify the DDBD approach. The pushover analyses showed that the stiffness of BRB-timber connections needed to be considered when estimating the yield drift of BRBGFs. The NLTHA of one-bay one-storey BRBGFs showed that the relationship between η_{in} and ductility factor μ for the Takeda fat model was also suitable for BRBGFs on the conservative side. The NLTHA results of the multi-storey BRBGF models confirmed that the DDBD approach effectively controlled the inter-storey drift ratios of the BRBGF system under seismic loads.

Keywords: buckling restrained braces (BRBs); glulam frames; dowelled connections; screwed connections; experimental tests; numerical modelling; direct displacement-based design (DDBD).

DEDICATION

I dedicate this thesis to my wife and my parents for nursing me with affections and love.

ACKNOWLEDGEMENTS

It has been the most fantastic three and half years in my life since I came to New Zealand to conduct my PhD study. I feel so fortunate and proud to reach this milestone. I believe that if I achieve anything important, the credits should all belong to the people who support me.

Firstly, I would like to thank my supervisors, Associate Professor Minghao Li, Dr Chin-Long Lee, Associate Professor Gregory MacRae and Associate Professor Anthony Abu. Especially, I would like to thank Associate Professor Minghao Li for all the opportunities, the trust, the guidance and the support on both study and life.

Secondly, I would like to thank the Natural Hazard Research Platform, Department of Civil and Natural Resources Engineering at the University of Canterbury, QuakeCore, Shanghai Research Institute of Materials, Timber Connect Ltd. and Techlam NZ Ltd. for generously funding this research project and my study.

Thirdly, I would like to thank the technical support from Professor Roger Nokes, Professor Timothy Sullivan, Dr Theodore Zhang and Dr Daniel Moroder during the experimental tests and analytical modelling. In addition, I highly appreciate the technical assistance, physical training and company from lab technicians Russell McConchie, Alan Thirlwell, Alan Poynter, Gavin Keats, Michael Weavers, Peter Coursey and Dave Carney during my one-and-half years' lab journey. The kind offer on manufacturing my specimens from Master Carpenter Michael Gödert from Atamai Structures and Senior Structural Engineer Björn Stankowitz from ENGCO Consulting Engineers is also acknowledged.

Fourthly, I would like to thank my timber research colleagues Professor Minjuan He (also my master supervisor), Associate Professor Zheng Li, Assistant Professor Hyungsuk Lim, Dr Lisa Ottenhaus, Dr Gabriele Granello, Dr Thomas Ehrhart, Justin Brown, Thomas Wright, Ben Moerman and Paul Horne for collaborating on the paper publications and improving my understanding on timber engineering. Specially thank Justin for all the kind advice and accompanying on many nights and weekends in the lab and office.

Last but not least, I would like to thank all my friends. Specially thanks Ana & Justin, Chiara & Giuseppe, Ben & Julia, Mahdi & Mozhgan, Arsalan & Sara, Hossein & Mina, Ben & Tessa, Brandy, Claudio, Giovanni, Lizzy, Cain, Mayank, Darren, Royce, Hayato, and Hanlin for always looking after me and thinking of me.

I cannot make it without any of you. Thank you very much to everyone I met during my PhD journey!

CONTENTS

1 INTRODUCTION

1.1 Research background

The construction sector accounts for more than 40% of the global CO_2 emissions by using concrete, bricks and steel (Ali et al., 2020). As the population is set to increase by two billion people over the next 30 years (Department of Economic and Social Affairs Population Division United Nations, 2019), the demand for infrastructures will expand exponentially, which has become a severe issue for our environment. In response to this issue, New Zealand has declared a climate change emergency and committed to a carbon-neutral government by 2025 (RNZ, 2020). One way to face the challenges and meet the climate mitigation targets is to use low embodied carbon building materials, e.g. timber, because New Zealand has extensive sustainably managed plantation forests. Timber has been widely used as a structural material around the world to build mainly residential houses under three storeys. Its large availability and high structural quality provide excellent living environments and exceptional seismic performance (Buchanan et al., 2008). In the 20th century, the construction industry replaced timber with mineral-based building materials. Although New Zealand has a strong tradition of timber light-frame construction for low-rise residential buildings, timber solutions have not been widely used in taller buildings when compared with their counterparts like steel and concrete. Today, sawn timber pieces can be glued together to produce engineered wood products (EWPs), such as glulam and cross-laminated timber (CLT). With the development of EWPs, the advancement of digital fabrication technology and drivers of sustainability, there are increasing interests in designing and building multi-storey timber buildings for residential and commercial occupancy, such as Arvida House and Nelson Airport in New Zealand. The uptake of timber will benefit the improvement of sustainability for the construction sector and the achievement of climate mitigation goals (Woodard and Milner, 2016).

1.2 Research motivation

a) Light timber frame (ThinkWood, n.d.)

b) Heavy timber frame (StructureCraft, 2016)

Figure 1.1 Timber frames

Timber frames including light timber frames and heavy timber frames as shown in Figure 1.1 are widely used for multi-storey timber buildings. Light timber frames use many small and closely spaced members that can be assembled by nailing. In contrast, heavy timber frames use EWPs like glulam with larger cross-sections as beams and columns that are usually connected by fasteners with larger diameters like bolts and dowels. This research focuses on heavy timber frames, and all timber frames in this thesis will refer to the heavy timber frames. Heavy timber frames are usually designed to carry only shear and axial forces due to the limited moment-resisting strength of timber beam-column joints and brittle failure modes such as the timber-splitting in the perpendicular-to-grain direction (Lam et al., 2008). Additional structural members such as braces and shear walls are usually needed to form lateral force resisting systems (LFRS) for wind and earthquake loads.

The brace system shows a direct force transferring path and high lateral stiffness, so traditional timber-braced frames are often used in multi-storey timber buildings as LFRS, such as those examples in Figure 1.2. In earthquake-prone countries like New Zealand, seismic loads usually govern the design of LFRS. Timber members have the possibility of brittle failure in tension and limited energy dissipation capacity. In addition, the energy dissipation of traditional timber-braced frames primarily relies on the yielding of connections at the end of timber braces as shown in Figure 1.3, which makes it harder to replace or repair the structures after severe earthquake events. In terms of the limited energy dissipation capacity, relatively low ductility is usually assumed for the traditional timber-braced frames. Larger member sizes are often needed to satisfy the lateral stiffness requirements (Kirstein et al., 2018). This engineering practice can cause uneconomical member sizes and increase the number of braces. Excess braces may restrict the flexibility of architectural plans and decrease space efficiency.

a) TREET (Abrahamsen and Malo, 2014), Norway

b) Beatrice Tinsley, New Zealand

c) Mjøstarnet, Norway

d) 25 King Street, Australia (Aurecon, n.d.)

Figure 1.2 Traditional timber-braced buildings

Figure 1.3 Connection detail at the end of braces in Beatrice Tinsley

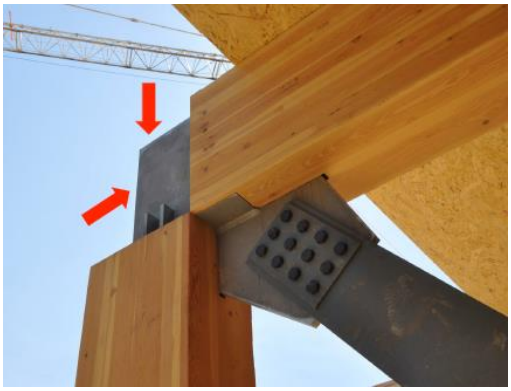

Figure 1.4 Steel braces in ESB building (Will, n.d.)

To improve the energy dissipation capacity, more ductile LFRS systems are required for high seismic hazard countries. Many timber-related LFRS have been proposed for multi-storey timber buildings to resist earthquake loads. One of them is timber-steel hybrid systems. Timber-steel hybrid systems combine the respective strength and benefits of two construction materials and provide robust solutions for various building systems, such as steel frames with timber light-frame shear walls (He et al., 2014; Li et al., 2014, 2015) and steel frames with CLT shear walls (Bezabeh et al., 2016a, 2016b; Dickof et al., 2014). In traditional timber-braced frames, such as the ESB building (Will, n.d.) in Canada as shown in Figure 1.4, the traditional timber braces can be replaced by steel braces to form a timber-steel hybrid system. However, steel braces tend to have buckling problems in compression, which causes either asymmetric performance when the buckling happens or affects the structural efficiency when braces with large cross-sections are used to avoid buckling.

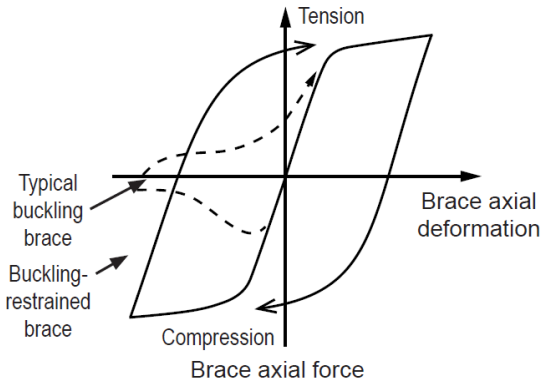

Figure 1.5 BRB behaviour compared with typical steel brace (Kersting et al., 2015)

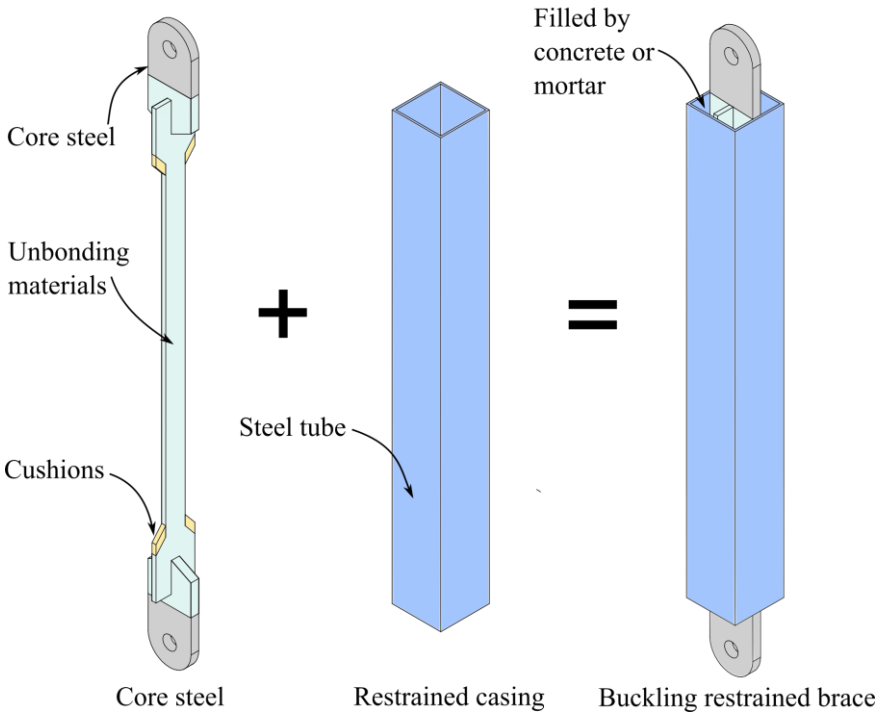

Figure 1.6 BRB configuration

Buckling restrained braces (BRBs) can achieve higher ductility and prevent the global buckling of steel braces in compression as shown in Figure 1.5. A BRB typically consists of the components shown in Figure 1.6: core steel, unbonding materials and buckling restraints. The core steel is designed to carry equal axial tensile and compressive loads without buckling. Unbonding materials are used to avoid adhesion and reduce friction between the core steel and the buckling restraints. The buckling restraints include the restrained casing and fillers between the casing and the core steel. The buckling restraints are applied to prevent buckling of the core steel in compression. BRBs were initially developed at the Architectural Institute of Japan in 1973 (Xie, 2005) and literature reviews on BRB-related research were reported in publications (Della Corte et al., 2011; Jones et al., 2014; Lin et al., 2012). In the past 40 years, BRBs have become an increasingly popular alternative to traditional steel braces for seismic design. Their ability to develop full and balanced hysteresis loops under tension and compression has significant advantages over the typical steel braces with asymmetric behaviour (Jones et al.,

2014). Therefore, there is a possibility to integrate BRBs into heavy timber frames to form a hybrid LFRS and achieve better lateral performance for multi-storey timber buildings.

1.3 Research questions and objectives

1.3.1 Research questions

BRBs are considered as an alternative for timber braces to improve the seismic performance of traditional timber-braced frames. To achieve the effective hybridization of BRBs and heavy timber frames, the following questions need to be answered:

1) How can this hybrid system consisting BRBs and timber frames be designed? Which kinds of timber-steel interface connections are suitable to connect BRBs with timber frames? How will this hybrid system perform under cyclic loading?
2) How can this hybrid system be simulated?
3) How can this hybrid system be designed and used in a building by engineers with a practical design approach?

1.3.2 Research objectives

The purpose of this thesis is to investigate the seismic performance of heavy timber frames with BRBs and prove the feasibility of this system for multi-storey buildings so that a low-damage solution can be provided for multi-storey timber buildings in high seismic hazard zones.

The objectives of this thesis are listed as follows:

1) Design the BRB-timber interface connections that can transfer the loads between timber frames and BRBs efficiently. The connections should also provide high strength and stiffness to engage BRBs early and avoid severe damage when BRBs reach their ultimate strength.
2) Design the hybrid system that has enhanced cyclic performance. The BRBs provide system strength and stiffness before yielding, and dissipate energy with improved system ductility under severe earthquake events. Other parts in the hybrid system are designed as non-ductile elements and should be protected from severe damages.
3) Develop detailed numerical models to simulate the performance of this hybrid system so that parametric studies can investigate the critical design parameters that influence the seismic performance.
4) Develop a design approach for practical design. The design approach should provide rational structural design with predictable building performance.

1.4 Thesis outline

Chapter 2 provides a literature review of this research and summarizes the further study requirement from the literature review. The literature review included relevant research on mass timber technology, BRBs and seismic design.

Chapter 3 presents experimental tests and results of two full-scale BRB-braced glulam frames (BRBGFs) with two different types of connections, two glulam bare frames without BRBs, and BRB component tests. The connection behaviour of two types of connections was measured and analysed by particle tracking technology (PTT).

Chapter 4 presents numerical modelling of BRBGFs based on component-based models. The methods on connection stiffness predictions were provided to improve the accuracy of stiffness predictions. In addition, parametric studies on the connection stiffness and manufacturing tolerances were conducted to investigate their influence on the cyclic performance of BRBGFs.

Chapter 5 shows a direct displacement-based design (DDBD) approach and the extension of the DDBD approach to the BRBGF system. The critical parameters for the DDBD approach such as the connection stiffness and the displacement reduction factor were discussed and verified by pushover analyses and nonlinear time-history analyses (NLTHA).

Chapter 6 outlines the application of the DDBD approach to multi-storey BRBGFs with three, six and nine storeys. The DDBD approach was verified by NLTHA of the multi-storey BRBGFs under the ultimate limit state (ULS).

Chapter 7 summarizes the main conclusions, answers the research questions raised in Chapter 1 and provides recommendations for future research.

2 LITERATURE REVIEW

This chapter provides an overview of relevant research on mass timber technology, BRBs and seismic design approaches. The literature review facilitates this study and helps to identify the research gaps that need to be filled for the research objectives.

2.1 Mass timber technology

2.1.1 Timber-braced frames

The production of EWPs such as CLT is increasing exponentially (Muszynski et al., 2020). The wide application of mass timber in mid-rise and high-rise timber buildings requires efficient structural systems to resist significantly higher lateral loads caused by wind and earthquake loads when compared with residential timber houses made of dimension lumbers. One of the most popular LFRS is the timber-braced frames (Popovski, 2004). Until 2020, ten tall timber structures have been built and another two are under construction (FPInnovations, 2021) using timber-braced frames.

Popovski et al. (2003) conducted shake table tests on single-storey timber-braced frames with five different connections between the timber frames and the braces as shown in Figure 2.1. It was found that the seismic performance of the timber-braced frames was significantly influenced by the connections, and the connections with slender fasteners were recommended because of their good energy dissipation capacity. Xiong and Liu (2016) conducted monotonic and cyclic tests on full-scale one-bay one-storey timber-braced frames with different brace types as shown in Figure 2.2. The results showed that the timber frames with X-type braces and K-type braces provided high elastic stiffness but low ductility (ductility factor μ=1.02-1.18). In addition, the timber frame with knee braces had moderate elastic stiffness and improved ductility (μ=1.85) when compared with timber frames with X-type braces and K-type braces. He et al. (2020) tested timber beam-column connections with knee braces as shown in Figure 2.3 and verified the improved ductility of timber-braced frames with knee braces reported by Xiong and Liu (2016). Chen and Popovski (2020) derived and verified the relationship between system ductility and the connection ductility for timber-braced frames. The results showed that when the desired system ductility was achieved, the connection ductility needed to be at least double than the system ductility. To reduce the ductility requirements for the connections, it was also recommended to ensure the connections on both sides of the braces yielded together.

To improve the resilience of timber-braced frames, Di Cesare et al. (2020) conducted a shake table test for a 2/3-scale three-storey timber-braced frame where post-tensioning was added on the beam-column connections and U-shape flexural plate dissipaters were installed at the intersection of two timber braces as shown in Figure 2.4. The timber-braced frame showed full recentring capability without structural damages. Yousef-beik et al. (2020) tested

a timber brace with resilient slip friction joint (RSFJ) and Hashemi et al. (2021) assessed the seismic performance of timber-braced frames with RSFJ through NLTHA. The NLTHA showed that the timber-braced frames with RSFJ could meet the performance requirement of drifts, accelerations and lateral stability for a low-damage structure.

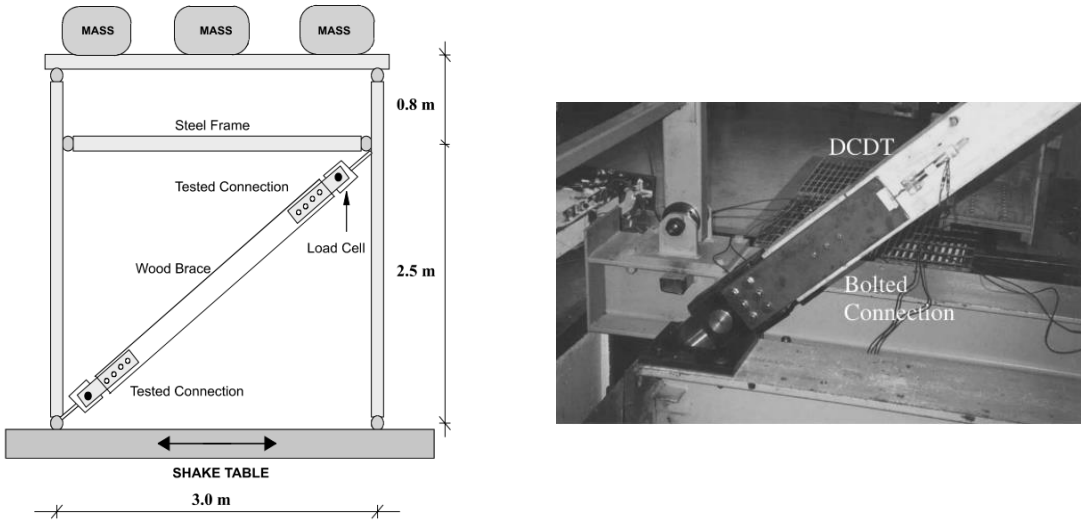

a) Test setup b) Connection detail

Figure 2.1 Shake table tests by Popovski et al. (2003)

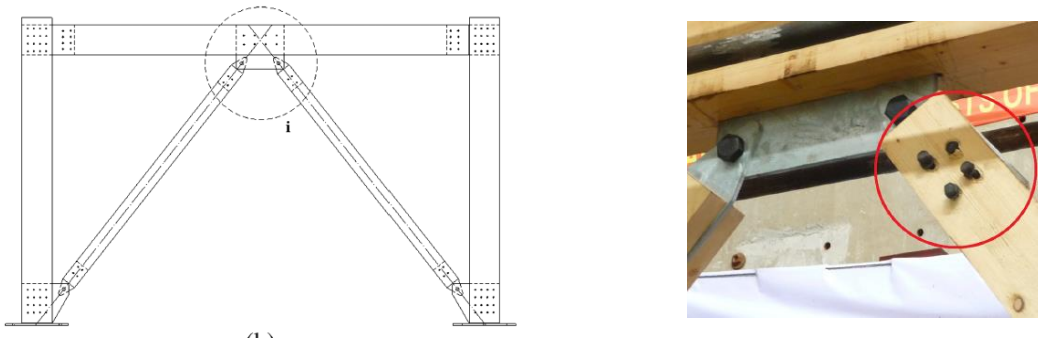

a) Test setup b) Connection detail

Figure 2.2 Full-scale tests by Xiong and Liu (2016)

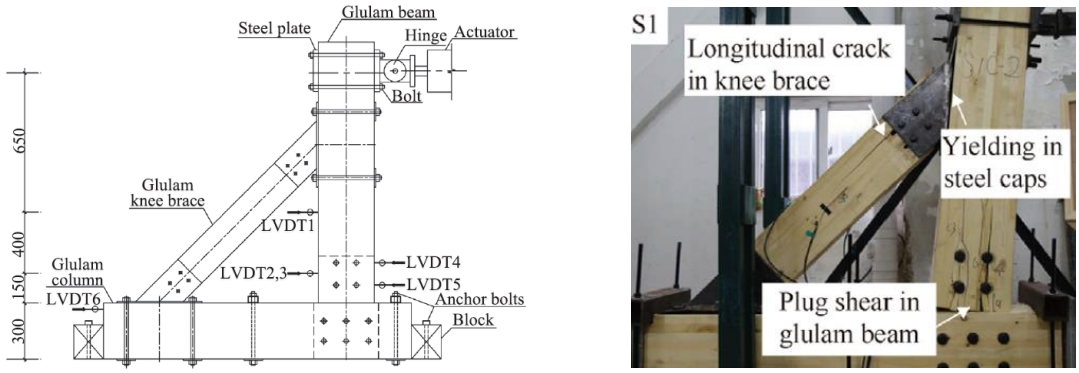

a) Test setup b) Failure mode

Figure 2.3 Connection tests with knee braces (He et al., 2020)

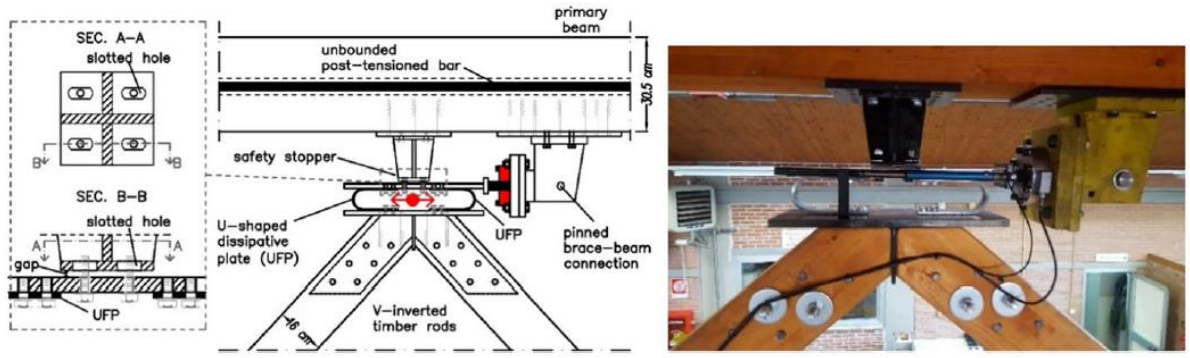

Figure 2.4 Post-tensioned bar and dissipater detail in 2/3 scale shake table test (Di Cesare et al., 2020)

2.1.2 BRB-braced timber frames

The feasibility of timber-steel hybrid structures was proved by Khorasani (2011). State of the art for hybrid timber LFRS was conducted by Gallo et al. (2020) showing the great potential of achieving improved seismic performance by using timber-steel hybrid structures. Blomgren et al. (2016) tested BRBs with timber casings (T-BRBs) as shown in Figure 2.5 and used them in the numerical analyses of a 12-storey timber building. The results showed the feasibility of incorporating BRBs in heavy timber frames but the information on the design method and the connection details was missing. Murphy et al. (2019) tested six full-scale T-BRB components. The results showed that they could meet the requirement of AISC 341-16 (American Institute of Steel Construction (AISC), 2016b) when suitable EWPs were used for the casing. Timmers and Tsay Jacobs (2018) conducted a comparative study by numerical modelling on a high-rise RC building and a high-rise heavy timber building containing BRBs as shown in Figure 2.6. It was demonstrated that EWPs could provide a viable alternative to RC frames in high seismic risk regions. However, further research was required to investigate the behaviour of the critical connections to engage BRBs. F. Zhang et al. (2018) conducted a shake table test on a half-scale five-storey glulam frame structure with glulam braces and T-BRBs as shown in Figure 2.7a. It was found that the BRBs improved the building performance but timber splitting in the braces and buckling of the gusset plates were observed in the tests as shown in Figure 2.7b. Again, this research emphasised the importance of introducing enhanced BRB-timber interface connections to engage BRBs and maximize the BRB efficiency in a timber system. Gilbert and Erochko (2019) performed half-scale cyclic tests of a type of timber-steel hybrid beam-column moment connections made of glued-in rods and steel hubs as shown in Figure 2.8. This connection type can be used to connect BRBs. However, glued-in-rod connections typically require strict quality controls during the manufacturing process and no widely accepted design method is available (Stepinac et al., 2013).

Past research on hybrid timber-steel structures indicated the importance of BRB-timber interface connections to integrate BRBs into timber frames. However, limited research has been done on these critical connections because timber-steel hybrid structures are new to the construction market. Timber materials have lower strength and stiffness in the perpendicular-

to-grain direction and the connections suitable for steel and RC BRB frames cannot be directly applied to timber structures. More research is needed to select suitable timber-steel connections from existing timber connection types and to ensure the structural efficiency of heavy timber frames with BRBs.

Figure 2.5 Testing of BRBs with timber casings (T-BRBs) (Blomgren et al., 2016)

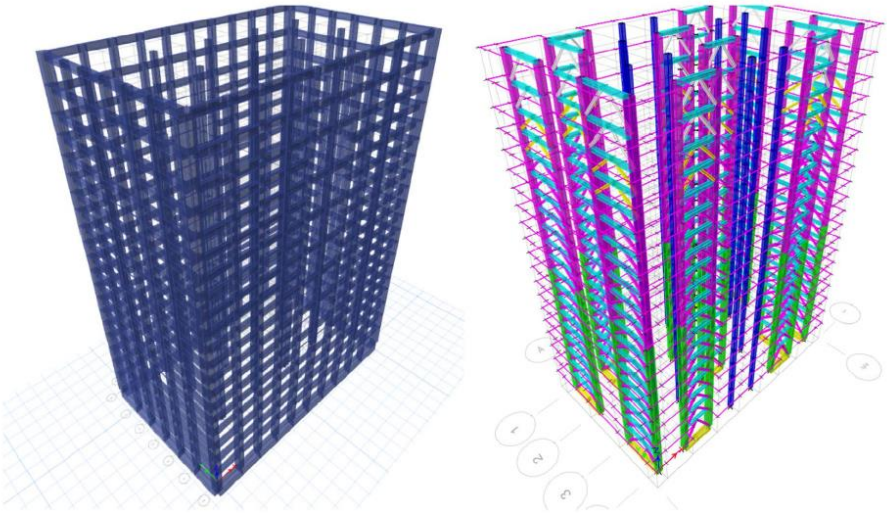

Figure 2.6 Concrete (left) and mass timber (right) ETABS model (Timmers and Tsay Jacobs, 2018)

a) Shake table test specimen b) Failure mode

Figure 2.7 Shake table test of glulam frame structure with glulam braces and T-BRBs (F. Zhang et al., 2018)

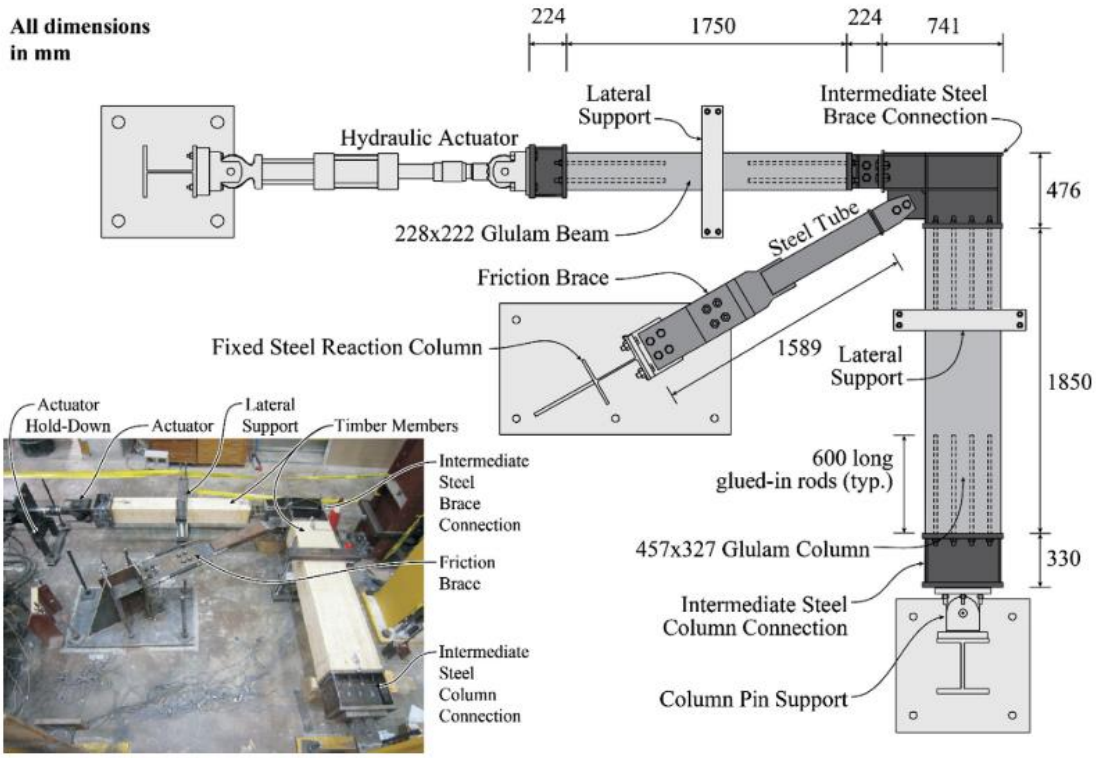

Figure 2.8 Glue-in rod connection subassembly test (Gilbert and Erochko, 2019)

2.1.3 High-performance timber connections

2.1.3.1 Dowel-type connections with inserted steel plates

Dowel-type connections consisting of bolts or dowels and inserted steel plates as shown in Figure 2.9 are commonly used in heavy timber frames (Xiong and Liu, 2016). These connections can achieve high strength by using many fasteners with multiple inserted steel plates, so they are considered to be a good solution for the BRB-timber interface connections.

Design standards such as Eurocode 5 (British Standard Institution (BSI), 2004) provided detailed design formulas for dowel-type connections with one inserted steel plate (Figure 2.9a) based on Johansen's theory (Johansen, 1949). Brittle failures are usually avoided by satisfying the minimum spacing requirements. The rotational stiffness is usually negligible for bolted connections due to the oversized holes for the convenience of installation (Lam et al., 2008). At the same time, the limited moment-carrying capacity may have a positive effect such as avoiding the torsion of gusset plates. To achieve higher strength, multiple inserted steel plates (e.g. two inserted steel plates in Figure 2.9b) are preferred to reduce the total amount of dowels and the area of the connection zone. The lateral load-carrying capacity for dowel-type connections with multiple inserted steel plates has been validated experimentally (Sawata et al., 2006) and design equations have been derived (Bocquet et al., 2018; Fan et al., 2011). Experimental tests of high-strength dowel-type connections with CLT were conducted (Brown and Li, 2021; Ottenhaus et al., 2018a, 2018b). The results showed that dowel-type connections were capable of carrying high loads as hold-downs for multi-storey timber buildings and the overstrength factor was derived to avoid brittle failures of non-ductile members in the system. However, the connections used to integrate BRBs are loaded with an angle to the timber grain, which is more complicated (Dong and Li, 2019). The initial slips of dowel-type connections due to manufacturing tolerances can reduce the efficiency of BRBs as well. Their effects need to be investigated by further experimental tests.

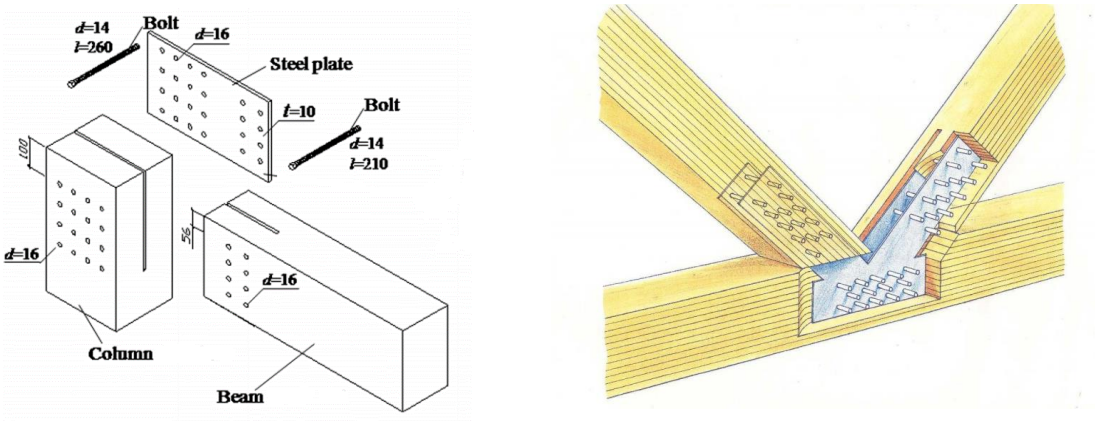

a) Bolted connection (Xiong and Liu, 2016) b) Dowelled connection (Abrahamsen and Malo, 2014)

Figure 2.9 Dowel-type connections

Past research on various types of dowel-type connections (Gattesco and Toffolo, 2004; Sandhaas and van de Kuilen, 2017; Sawata et al., 2006; Sawata and Yasumura, 2003) has shown that Eurocode 5 (2004) tends to predict the strength of dowel-type connections conservatively. However, the stiffness prediction equation in Eurocode 5 (2004), shown in Eq. 2.1, often considerably overestimates the connection stiffness (Jorissen, 1998; Sandhaas and van de Kuilen, 2017; Wang et al., 2020). Jockwer and Jorissen (2018) also found that stiffness equations among current standards are quite different and none of them provides accurate stiffness predictions for dowel-type connections with multiple dowels and inserted steel plates.

In this regard, the beam-on-foundation (BOF) model as shown in Figure 2.10 was developed and recommended to estimate the stiffness for dowel-type connections (Lemaitre et al., 2018), but further investigations were suggested, especially for determining the modulus of foundation by experimental tests (Lemaitre et al., 2019).

$$k_{ser,lat} = \lambda_m \rho_m^{1.5} \frac{d}{23} \qquad \text{Eq. 2.1}$$

where $k_{ser,lat}$ is the lateral stiffness per shear plane per fastener under serviceability limit state (SLS);

λ_m =1 and λ_m =2 are the modification factor for timber-to-timber connection and timber-to-steel connection, respectively;

ρ_m is the mean density of timber; and

d is the diameter of fasteners.

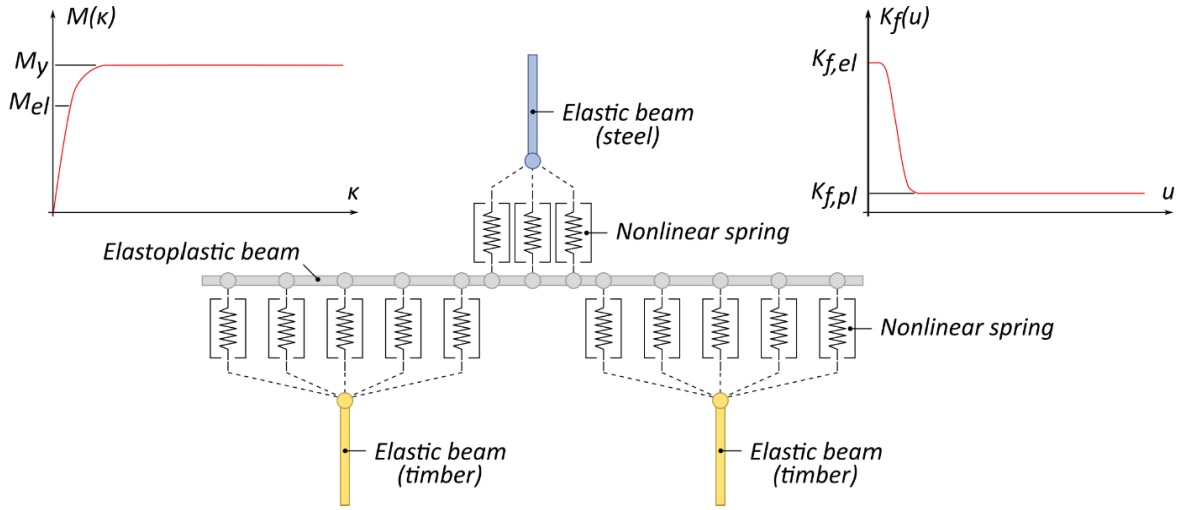

Figure 2.10 Beam-on-foundation (BOF) model for dowel-type connection (Lemaitre et al., 2018)

2.1.3.2 Connections with inclined self-tapping screws (STS)

Connections with inclined self-tapping screws (STS) as shown in Figure 2.11 are another popular option for timber structures due to their cost-effectiveness and easy installation. Bejtka and Blass (2002) exploited the high tensile capacity of STS in glulam by installing inclined STS such that the connection capacity was not just limited by the embedment strength of the timber member and bending capacity of the fastener ($f_{h,1}$ and $f_{h,2}$ in Figure 2.12). Withdrawal capacity of the fastener (N_1 and N_2 in Figure 2.12) and friction between the timber members also contributed to the connection capacity. The inclined STS with proprietary washers called ZD Plates as shown in Figure 2.13 were used as non-ductile connections to construct 2/3-scale moment-resisting connection specimens and showed high load-carrying capacity (Gohlich, 2015). The high strength of connections with inclined STS makes them another good solution for BRB-timber interface connections.

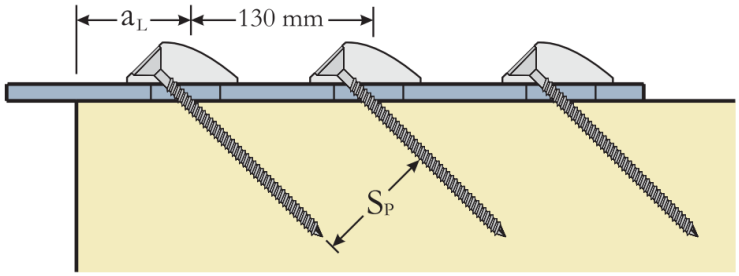

Figure 2.11 Connections with inclined STS (Gohlich, 2015)

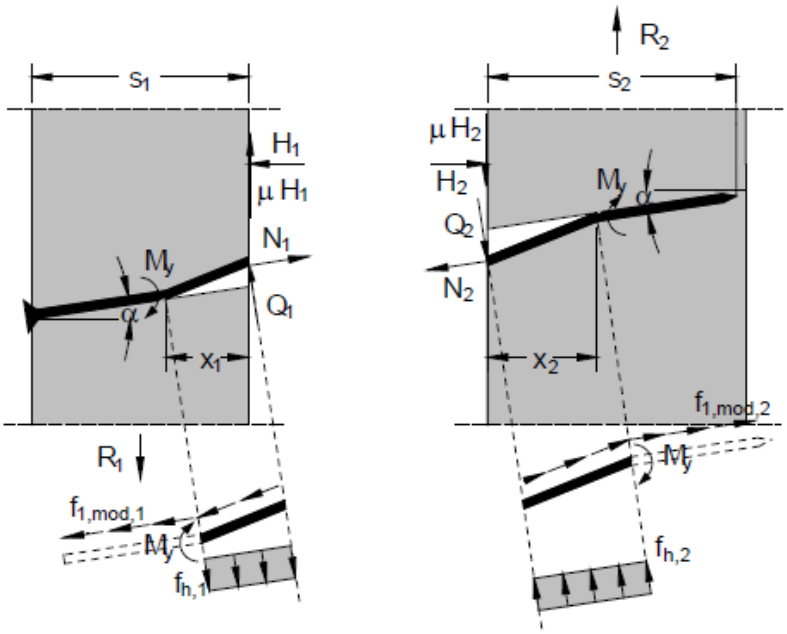

Figure 2.12 Calculation model for timber-to-timber connection with inclined STS (Bejtka and Blass, 2002)

The strength prediction equations for connections with inclined STS were derived by Bejtka and Blass (2002). It was shown that if the inclined angle of the STS was greater than 30°, the ultimate withdrawal capacity of STS and maximum efficiency could be reached. Design equations on the strength of connections with inclined STS were introduced into Eurocode 5 (2004) based on the research by Bejtka and Blass (2002). Experimental tests were also conducted for inclined STS on timber-to-timber connections (Khan et al., 2021; Piazza et al., 2011; Tomasi et al., 2010) and steel-to-timber connections (Closen, 2012; Gohlich et al., 2018; Krenn and Schickhofer, 2009; Mirdad and Chui, 2020) to investigate the influence of inclined angles, the number of STS and STS layouts on connection strength, stiffness and ductility. The test results from Tomasi et al. (2010) showed that their proposed calculation model provided conservative strength prediction for timber-to-timber connections with inclined STS. The test results showed that the increase of inclined angle increased the load-carrying capacity, but the strength prediction model did not consider the influence of the inclined angle. The test results from Piazza et al. (2011) illustrated that the inclined angle of STS had a significant influence on the ductility and it was essential to define a reliable

procedure for identifying elastic displacement. The embedment tests of STS from Khan et al. (2021) as shown in Figure 2.14 indicated that the STS diameter did not have a pronounced influence on the embedment stiffness but the stiffness was very sensitive to the inclined angle of STS. Krenn and Schickhofer (2009) developed a truss model as shown in Figure 2.15 for the strength prediction on timber-to-steel connections with inclined screws and discussed the effective number of STS in the connections. Test results from Closen (2012) indicated that the effective number of STS and the capacity of timber-to-steel connections with inclined STS decreased when subjected to reverse cyclic loading. The decrease might be due to the gaps formed between the main and side members during cyclic testing. It was suggested to conduct further research on the cyclic performance of connection with inclined STS.

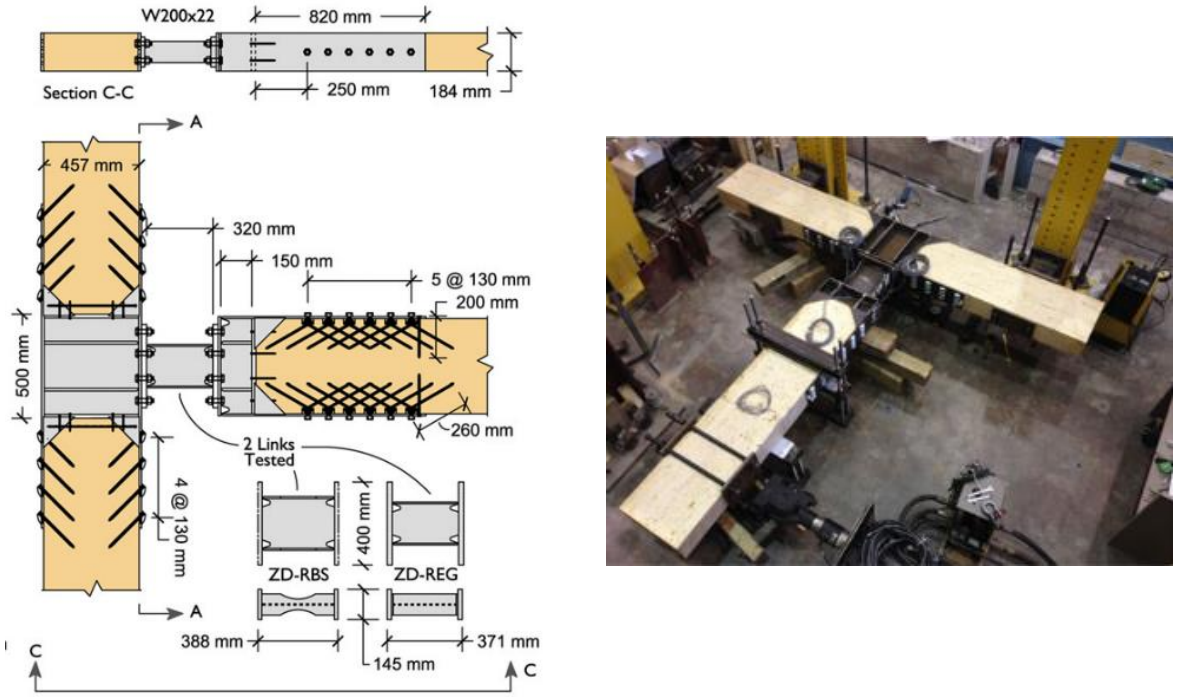

a) ZD-plate connection b) Test setup

Figure 2.13 Moment-resisting connection test with ZD-plate (Gohlich, 2015)

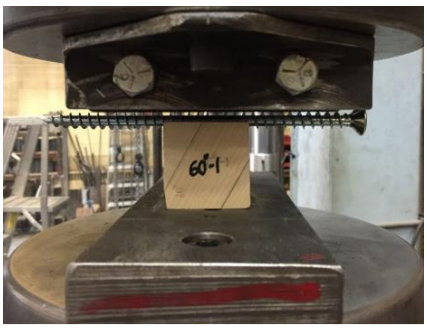

Figure 2.14 Embedment test of STS (Khan et al., 2021)

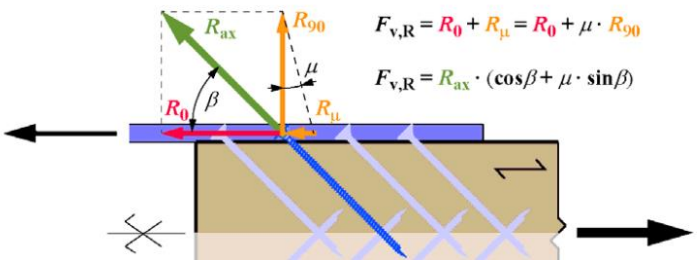

Figure 2.15 Truss model for strength prediction (Krenn and Schickhofer, 2009)

Axial withdrawal stiffness calculations of STS can follow European Technical Approval (ETA) reports provided by screw suppliers. Eq. 2.2 and Eq. 2.3 from ETA 11/0190 (2016) and

ETA 11/0030 (2019) are often used to estimate the STS axial withdrawal stiffness under serviceability $k_{ser,ax,\theta}$ in softwood with an angle θ to the timber grain. However, the prediction errors were found up to 720% (Dietsch and Brandner, 2015; Ringhofer, 2017). Several analytical models were developed for concrete-to-timber connections (Mirdad and Chui, 2020), and timber-to-timber connections (Girhammar et al., 2017; Tomasi et al., 2010). The test results from Tomasi et al. (2010) showed that the stiffness prediction from Eurocode 5 (2004) was not suitable for connections with inclined STS as well. The proposed stiffness prediction by Tomasi et al. (2010) provided a good stiffness approximation. Research from Closen (2012) indicated that the stiffness of connections with inclined STS decreased when subjected to reverse cyclic loading due to the gaps between main and side members. Mirdad and Chui (2020) developed a calculation model to predict the stiffness of concrete-to-timber connections with inclined STS in timber concrete composite (TCC) floor. In their model, the gaps (i.e. insulation layer in Figure 2.16) between concrete and timber were considered. However, the feasibility of these analytical models for timber-to-steel connections still needs to be verified. In addition, the effects of cyclic loading on the stiffness of the timber-to-steel connections with inclined STS are still unknown, especially for the load with an angle to the timber grain.

$$k_{ser,ax,\theta,1} = 780 d^{0.2} l_{ef}^{0.4} \quad \text{Eq. 2.2}$$

$$k_{ser,ax,\theta,2} = 25 d l_{ef} \quad \text{Eq. 2.3}$$

where d is the outer diameter of the STS; and

l_{ef} is the effective penetration length in the timber member.

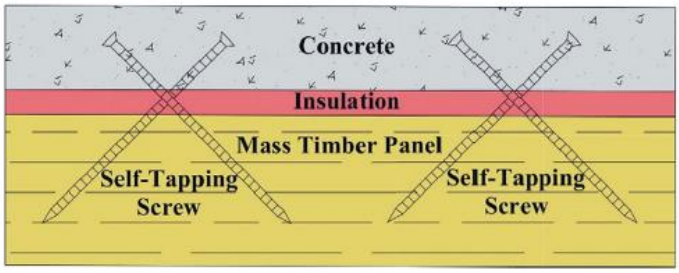

Figure 2.16 Timber-concrete composite floor (Mirdad and Chui, 2019)

2.2 Research on buckling restrained braces (BRBs)

2.2.1 BRBs and BRB frames

BRB is usually considered as proprietary products and each BRB is custom-fabricated for each project (Kersting et al., 2015), so design information of BRBs is usually provided by BRB manufacturers, such as BRB strain hardening adjustment factor (ω) and BRB compression strength adjustment factor (β) as shown in Figure 2.17. During BRB design, BRB manufacturers also play an important part in determining performance parameters such as the geometry of steel core and thickness of unbonding material. Design-aid tools provided by BRB

manufacturers like design tables (Corebrace, 2019) and software (Lin et al., 2020) have been available to facilitate structural engineers' selection of BRBs at the preliminary design stage.

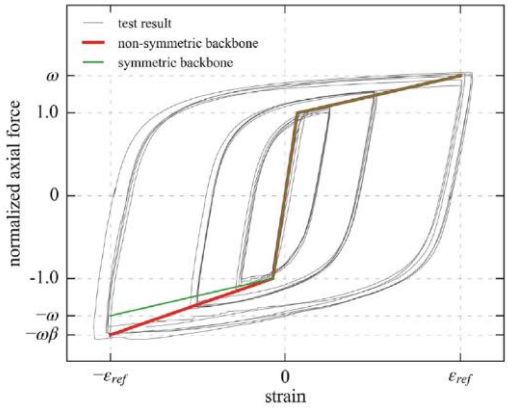

Figure 2.17 BRB overstrength in tension and compression (Vigh et al., 2017)

Extensive experimental studies on BRB component tests, sub-assemblage tests and BRB frame tests have been conducted for steel structures (Black and Aiken, 2002; Chou et al., 2012; Della Corte et al., 2011; Jones, 2020; Palmer et al., 2014; Tsai et al., 2004; Uang et al., 2004; Wang et al., 2018; Xie, 2005). Watanabe et al. (1988) and Takeuchi et al. (2012) tested BRBs and recommended global and local buckling prevention strategies, respectively. Different forms of BRBs were proposed and tested (Avci-Karatas et al., 2018; Guo et al., 2017; G. Li et al., 2019; Pan et al., 2020; Sun et al., 2019). It has also been confirmed that most BRBs can sustain stable cyclic performance in the component tests. However, some BRB frame tests (Aiken et al., 2002; Chou et al., 2012; Tsai et al., 2008) showed buckling or welding fracture of gusset plates, highlighting the importance of conducting BRB frame tests at a system level. Aiken et al. (2002) tested a 0.7-scale one-bay one-storey steel BRB frame with rigid beam-column-brace connections. The results showed gusset plate distortion and crack propagation at the welding between the column and the gusset plate at a 2.0% drift ratio. Tsai et al. (2008) tested a full-scale three-bay three storey dual system consisting BRB frame and moment-resisting frame as shown in Figure 2.18a. During the tests, out-of-plane gusset plate distortion was observed in multiple locations as shown in Figure 2.18b. The gusset plate distortion failure illustrated that rigid beam-column-brace connections negatively impacted the overall performance. Fahnestock et al. (2007) tested a 0.6-scale one-bay four-storey steel BRB frame with improved connection details and pinned-end BRBs as shown in Figure 2.19. The test frame sustained a 4.8% drift ratio with minimal damages and no significant strength degradation was observed. Berman and Bruneau (2009) tested a 1/3-scale three-storey steel BRB frame with unconstrained gusset connections as shown in Figure 2.20. The results showed that the unconstrained gusset connections reduced the negative impact of the frame action and the shear force carried by the frame decreased. The system-level tests highlighted the importance of the proper connection details to ensure the overall performance of BRB frames.

a) Specimen setup b) Gusset plate distortion

Figure 2.18 Test of a full-scale three-storey steel BRB frame (Tsai et al., 2008)

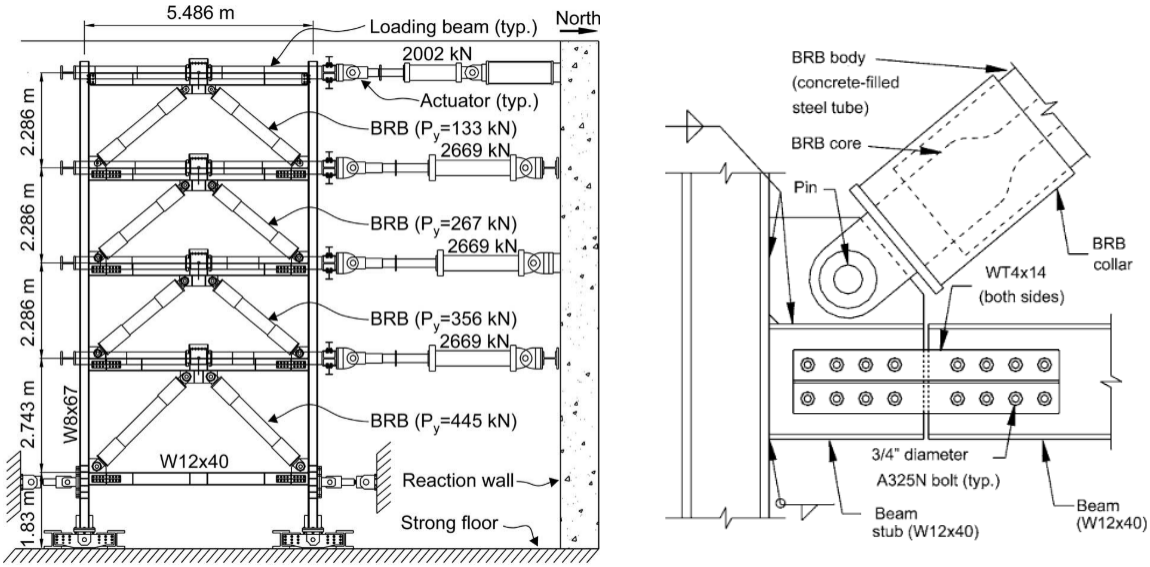

a) Specimen setup b) Connection detail

Figure 2.19 Test of a 0.6-scale four-storey steel BRB frame (Fahnestock et al., 2007)

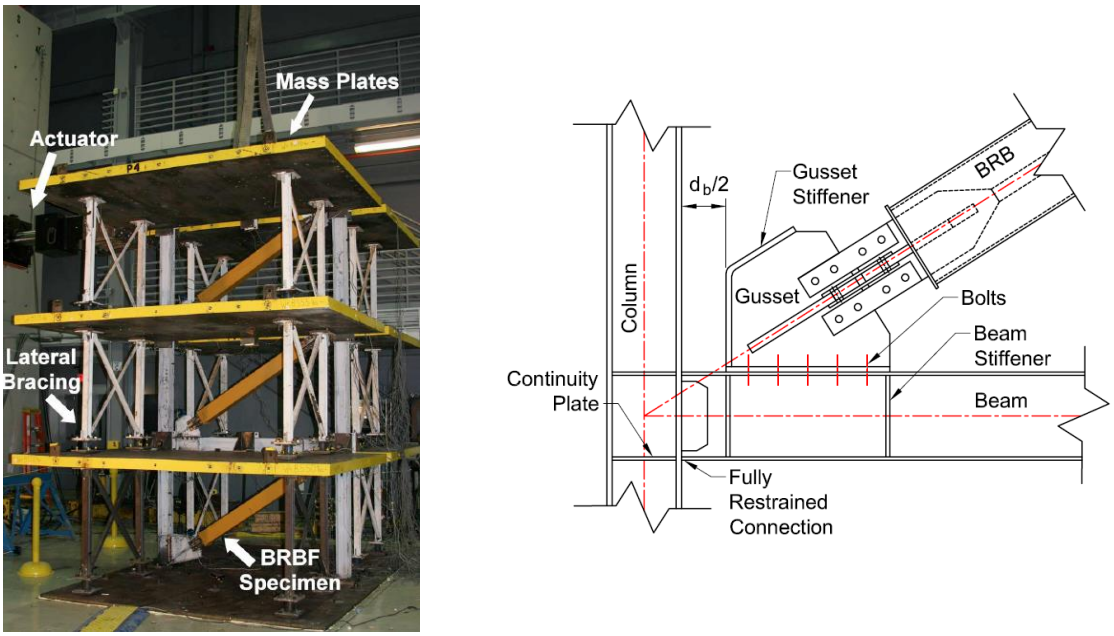

a) Specimen setup b) Connection detail

Figure 2.20 Test of a 1/3-scale three-storey steel BRB frame (Berman and Bruneau, 2009)

BRB frames can also experience out-of-plane (OOP) seismic loading because earthquakes may come from any direction. Khoo et al. (2016) conducted bidirectional pseudo-dynamic tests on a full-scale two-storey BRB frame as shown in Figure 2.21a. The test results showed that the frame action significantly increased the demand of the gusset plates and the BRB frame experienced fractures of gusset weld at an inter-storey drift ratio of 3.0% in both directions as shown in Figure 2.21b. Numerical modelling by Cui et al. (2018) also showed that the capacity and energy dissipation of BRBs and BRB frames might be overestimated. Ozaki et al. (2014) proposed a method to evaluate the OOP stability of BRBs. Takeuchi et al. (2014) derived equations to cover the stability conditions of BRBs with OOP drift and conducted BRB cyclic tests to verify the equations. MacRae et al. (2021) developed a method to assess the stability of BRBs with recommended structural details. Intensive research (Cui, 2021; Jones, 2020) on BRBs and BRB frames by experimental testing and numerical modelling is still ongoing at the University of Canterbury to further study the effects of combined in-plane and OOP loading on BRBs.

Various models were developed to simulate BRB and BRB frame behaviour under cyclic loading (Guerrero et al., 2016; Nakamura et al., 2012; Yu et al., 2011). For example, the bilinear model (Sabelli et al., 2003), the Bouc-Wen smooth law model (Black et al., 2004), Ramberg-Osgood model (Tremblay et al., 2008), Menegotto-Pinto model (Qu et al., 2017; Vigh et al., 2017), elastoplastic model (Zona and Dall'Asta, 2012) and core-spring model (Naghavi et al., 2019) were used to simulate BRBs, while fixed joints (Rahnavard et al., 2018; Sabelli et al., 2003; Tremblay et al., 2008), rigid offset fixed joints (Atlayan and Charney, 2014) and fully-pinned joints (Vigh et al., 2017) were used to simulate beam-column connections. In general, these models were able to predict the experimental behaviour well with examples shown in

Figure 2.22. By comparing different modelling methods, Zsarnoczay (2013) emphasised the importance of including isotropic hardening, kinematic hardening and asymmetric characteristics for BRBs in modelling the overall performance of BRB frames.

a) Specimen setup

b) Fracture of gusset weld

Figure 2.21 Bidirectional tests on a full-scale two-storey BRB frame (Khoo et al., 2016)

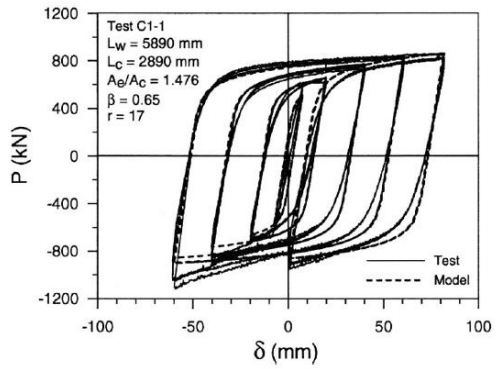

a) Ramberg-Osgood model (Tremblay et al., 2008)

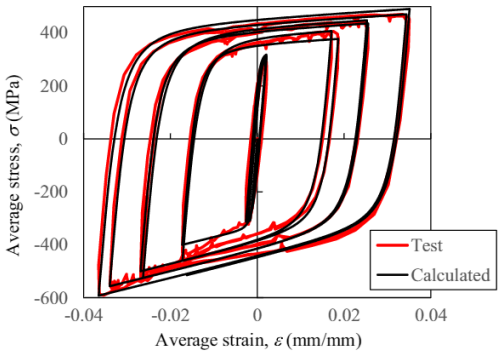

b) Menegotto-Pinto model (Qu et al., 2017)

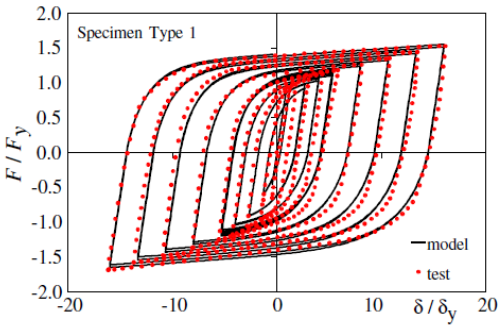

c) Elastoplastic model (Zona and Dall'Asta, 2012)

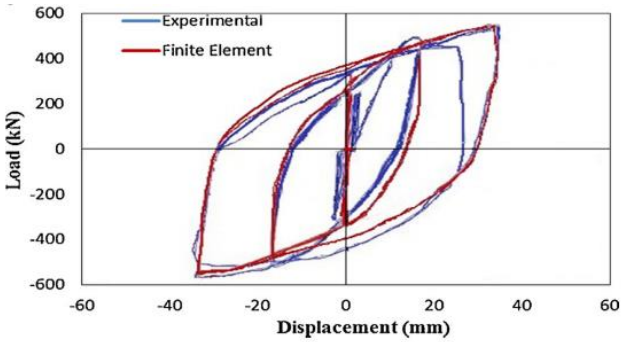

d) core-spring model (Naghavi et al., 2019)

Figure 2.22 Comparison between tests and simulations with different models

Research has also been conducted to integrate BRBs into reinforced concrete (RC) frame structures and retrofit RC frames as an economical retrofit solution (Di Sarno and Manfredi, 2012; Mahrenholtz et al., 2015; Ozcelik and Erdil, 2019; Qu et al., 2013, 2017; Wu et al., 2017;

Zhang et al., 2020). Special connection details between BRBs and RC frames such as bearing block and cast-in steel brackets were proposed for existing and newly constructed RC frames (Tsai et al., 2017). Numerical models were developed to simulate the performance of RC BRB frames (Qu et al., 2015; Tsai et al., 2018). The experimental tests and numerical analyses showed that BRBs improved the strength, stiffness and energy dissipation capacity of the RC frames.

2.2.2 Gusset plate design

Gusset plates are used to connect BRBs with frames as shown in Figure 2.23. One of the most popular design methods proposed by Thornton (1984) was to assume gusset plates as equivalent column elements shown in Figure 2.23. The gusset plate buckling load P_{cr} was obtained using Euler's buckling formula (Eq. 2.4). The width of the equivalent column was defined by the Whitmore width considering the dispersion angle (=30°) (Whitmore, 1952). The length of the equivalent column L_e was the average lengths of $L1$, $L2$ and $L3$ in Figure 2.23. Other effects such as the boundary condition effects of the gusset plates were not considered in this P_{cr}. The method in AISC 360-16 (American Institute of Steel Construction (AISC), 2016a) was also based on the equivalent column concept and included the effects of residual stresses, eccentric loading and inelastic buckling (Vazquez-Colunga et al., 2019). The method suggested K_{gs}=1.2 for gusset plates with free edges and K_{gs}=0.65 for those with edge stiffeners. K_{gs}=2.0 was recommended by Tsai and Hsiao (2008) based on the flexural buckling modes of BRB-to-gusset joints observed on their tests. The buckling mode did not consider the rotational stiffness of BRB-to-gusset joints. The negligible rotational stiffness can be achieved by special details of the joints suggested by MacRae et al. (2021) and K_{gs}=2.0 was generally conservative for gusset plates with a thickness less than 18 mm and a short connection length (Vazquez-Colunga et al., 2019). Bruneau et al. (2011) and Chou et al. (2012) also suggested using K_{gs}=2.0 to account for the OOP buckling of gusset plates. Another design method was to assume gusset plates as equivalent plates using the inelastic plate buckling method as shown in Figure 2.24 (Fang et al., 2015; Sheng et al., 2002). This method had a slightly higher dispersion when compared with the equivalent column method (Fang et al., 2015).

Most gusset plate design methods did not consider the additional actions such as frame actions and OOP displacements. Takeuchi et al. (2016) proposed a design method where the OOP failure mechanisms and the effect of OOP displacements were included to check the global stability of BRB frames. Vazquez-Colunga et al. (2018, 2019) investigated the effects of bidirectional loads on the axial strength of gusset plates by numerical analyses. The analyses showed that the axial strength of gusset plates decreased with the increase of OOP displacement. Intensive research (Vazquez-Colunga, 2021) by experimental testing and numerical modelling is still ongoing at the University of Canterbury to further study the effects of additional actions including frame actions and combined in-plane and OOP loading on BRB gusset plates.

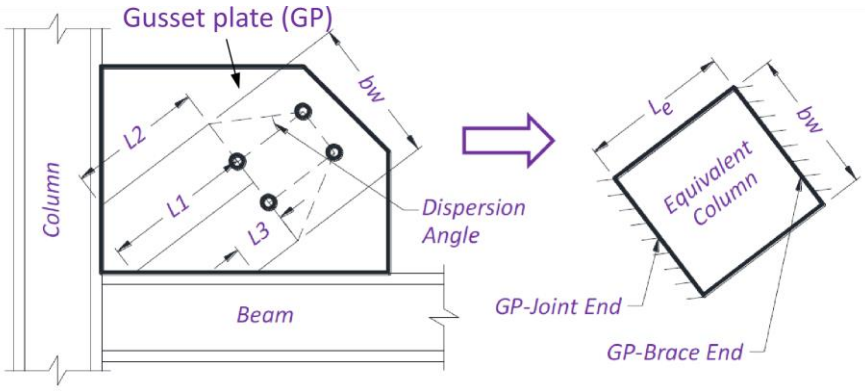

Figure 2.23 Gusset plate design (Vazquez-Colunga, 2021)

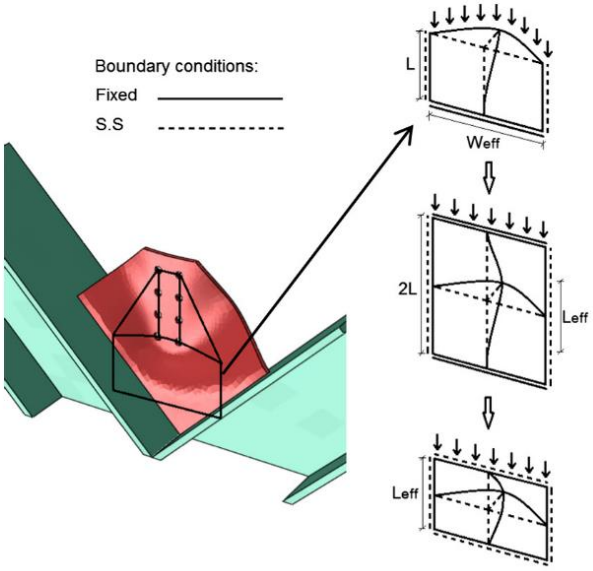

Figure 2.24 Design of gusset plate connections using plate buckling method (Fang et al., 2015)

$$P_{cr} = \frac{\pi^2 E_s I_e}{(K_{gs} L_e)^2} \quad \text{Eq. 2.4}$$

where P_{cr} is the buckling load;

E_s is the elastic modulus of steel;

I_e is the moment of inertia of the equivalent column;

L_e is the length of the equivalent column; and

K_{gs} is the effective length factor.

2.2.3 Effect of slips in lateral force resisting systems (LFRS)

The assembly of BRB frames requires installation tolerances. The installation tolerances may cause some initial slips for the LFRS, especially for those BRB frames with pin-end BRBs (Avci-Karatas et al., 2018; Wijanto and Clifton, 2014) as shown in Figure 2.25. When the initial slips of systems caused by the installation tolerances were overcome, systems would have a

rapid increase in stiffness at a non-zero velocity, which might cause a sudden force increase on the contents moving with the systems (English et al., 2012; Lin et al., 2015). The initial slips may also reduce the system energy dissipation of LFRS under cyclic loading (Wijanto and Clifton, 2014). Xie et al. (2019) numerically investigated the influence of connection stiffness on the structural performance of a structure with viscous fluid dampers. The simulations showed that the effectiveness of viscous fluid dampers might be overestimated and the base shear demand might be underestimated by ignoring the connection stiffness. Ishida and Takewaki (2021) found that a viscous-hysteretic hybrid damper system attained large acceleration when the gaps of the damper were overcome. However, the effects of installation tolerances on LFRS were not well considered for BRB frame systems. Further investigation is required to quantify the effects of installation tolerances on BRB frame systems.

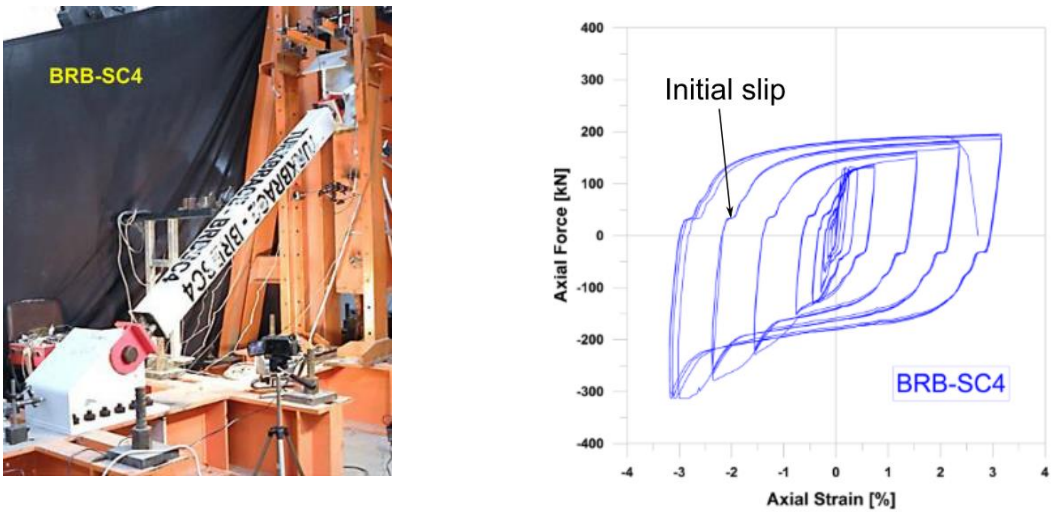

a) Pin-end BRB test setup b) Hysteresis loops

Figure 2.25 Pin-end BRB test (Avci-Karatas et al., 2018)

2.3 Seismic design

2.3.1 NZS1170.5 design approach

The equivalent static method in NZS1170.5 (Australia and New Zealand Standards, 2004) is a simplified technique to calculate the horizontal seismic design action for low-rise and mid-rise buildings where the structural configurations are relatively symmetric and the fundamental mode governs the building responses (Bourahla, 2013). The equivalent static method is widely used by modern design standards. For example, the equivalent static method is also called the lateral force method of analysis in Eurocode 8 (British Standard Institution (BSI), 2005b) and the equivalent lateral force procedure in ASCE 7-16 (ASCE/SEI(ASCE/Structural Engineering Institute), 2016).

The equivalent static method substitutes the seismic loads by static laterally distributed forces on a structure. The total base shear force $V_{base,F}$ is evaluated in two horizontal directions, respectively and calculated by Eq. 2.5. The seismic weight of the structure W_t includes the total

dead load and partial live load according to the earthquake load combination. The acceleration spectrum $S_a(T_1, Z, R, N)$ is a spectral pseudo-acceleration of a single-degree-of-freedom (SDOF) elastic system depending on the fundamental period of the structure, seismic zone, design earthquake return period, and soil condition. The force reduction factor $f(\mu)$ is a function of ductility factor μ that depends on the practical experience of different structural types and is a measure of a structure's ability to accommodate earthquake loads and absorb energy without collapse. The force reduction factor $f(\mu)$ is used to reduce the load demand due to the structure's inelastic response. After obtaining $V_{base,F}$ on both directions, $V_{base,F}$ is distributed along with the building height by assuming a uniform triangular force distribution. The lateral force at *i*-th level F_i is calculated by Eq. 2.6 and F_i is used to design the structure's LFRS. The top additional force F_t is used to account for the higher mode participation that does not conform to the uniform triangular force distribution assumption. Because the equivalent static method usually starts from the force calculation and considers the force demand as the fundamental design quantity with initial stiffness (i.e. elastic stiffness) and initial period, it is categorized as a force-based design (FBD) approach by Priestley et al. (Priestley et al., 2007a).

$$V_{base,F} = C_d(T_1)W_t \quad \text{Eq. 2.5a}$$

$$C_d(T_1) = C(T_1, Z, R, N)f(\mu) = \frac{S_a(T_1, Z, R, N)}{g} f(\mu) \quad \text{Eq. 2.5b}$$

where W_t is the seismic weight of the structure;

$S_a(T_1, Z, R, N)$ is the pseudo-acceleration spectrum;

g is gravitational acceleration;

T_1 is the fundamental period of the structure; and

Z, R, N are related to the return period and site seismicity in NZS 1170.5 (2004).

$$F_i = F_t + 0.92V_{base}\frac{W_i h_i}{\sum_{i=1}^{n} W_i h_i} \quad \text{Eq. 2.6a}$$

$$F_t = \begin{cases} 0 & i < n \\ 0.08V_{base} & i = n \end{cases} \quad \text{Eq. 2.6b}$$

2.3.2 Direct displacement-based design (DDBD) approach

Displacement responses of buildings due to seismic excitations are directly correlated to building damage levels (Erduran and Yakut, 2004; Ghobarah et al., 1999; Kim and Chun, 2004; Krawinkler et al., 2003; Medina and Krawinkler, 2005). The direct displacement-based design (DDBD) approach, as one of the performance-based seismic design approaches, is to consider structural deformations as the primary input for the design process (Priestley et al., 2007b). The DDBD approach was first proposed by Priestley et al. (1994; 1995, 2003) to provide an alternative design solution for the FBD approach.

The DDBD approach also substitutes the seismic loads by static laterally distributed forces on a structure. Different from the FBD approach, the DDBD approach starts from setting a displacement target Δ_d such as the inter-storey drift target and considers displacement as the fundamental design quantity with secant stiffness and equivalent period. The structure's ductility factor μ is obtained as the ratio of Δ_d and the yield displacement of the structure Δ_y. The total base shear force $V_{base,D}$ is evaluated by Eq. 2.7. $V_{base,D}$ is distributed along with the building height by using Eq. 2.6 as well. The detailed process of the DDBD approach will be further discussed in Chapter 5.1.

It is found that $V_{base,F}$ can be expressed as Eq. 2.8 by combining Eq. 2.5 with Eq. 2.7b. The M_e in Eq. 2.7a is usually very close to M_t because both of them are based on the seismic weight under earthquake load combination. The comparison between Eq. 2.7a and Eq. 2.8 shows that the base shear force calculation of the FBD approach is quite similar to the DDBD approach. One difference is that the FBD approach is based on initial stiffness K_1 while the DDBD approach is based on the secant stiffness K_e as shown in Figure 2.26. The other difference is that the FBD approach uses the force reduction factor $f(\mu)$, while the DDBD approach uses displacement reduction factor $\eta_{in}(\mu)$ to consider the effects of inelastic response on the structure.

$$V_{base,D} = K_e \Delta_d = \frac{4\pi^2}{T_e^2} M_e S_d(T_e) \eta_{in}(\mu) \qquad \text{Eq. 2.7a}$$

$$S_d(T_e) = \frac{T_e^2}{4\pi^2} S_a(T_e, Z, R, N) \qquad \text{Eq. 2.7b}$$

where K_e is the secant stiffness of the structure at Δ_d as shown in Figure 2.26;

M_e is the effective mass calculated by the earthquake load combination;

$S_d(T)$ is the pseudo-displacement spectrum; and

$\eta_{in}(\mu)$ is the displacement reduction factor.

$$V_{base,F} = S_a(T_1, Z, R, N) f(\mu) \frac{W_t}{g} = \frac{4\pi^2}{T_e^2} S_d(T_1) M_t f(\mu) \qquad \text{Eq. 2.8}$$

where M_t is the seismic mass of the structure.

Past research (Maley et al., 2010; Priestley et al., 2007a; Sullivan, 2013) has shown that the FBD approach may have its limitations for seismic design in some conditions. One limitation is that the elastic analysis is used to estimate inelastic force distributions and the displacement limit states are given only secondary importance and checked as a final design step. More discussions on the limitations of the FBD approach can be found in Priestley et al. (2007a). Additionally, past research has shown the benefits of the DDBD approach in some conditions when compared with the FBD approach for the nonlinear seismic design (Salawdeh and Goggins, 2016; Terán-Gilmore and Ruiz-García, 2011). Because of that, the DDBD approach has been used in a variety of structural systems as an alternative to the FBD approach including RC structures (Belleri, 2017; Pennucci et al., 2009; Priestley and Kowalsky, 2000;

Sullivan et al., 2006; Yang and Lu, 2018), steel structures (Nievas and Sullivan, 2015; Roldan et al., 2016; Sahoo and Prakash, 2019; Sullivan, 2013; Wijesundara, 2012) and timber structures (Filiatrault and Folz, 2002; Hashemi et al., 2020; Z. Li et al., 2019; Pang and Rosowsky, 2009; Zonta et al., 2011). A model code for the DDBD approach was further developed as a guideline for practical design (Sullivan et al., 2012).

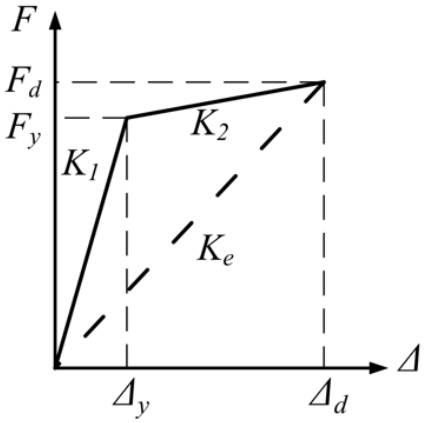

Figure 2.26 Force-displacement relationship of a structure

Although the DDBD approach has been developed for applications to a wide range of structures, with intensive research on emerging systems including some timber-steel hybrid systems (Brown et al., 2021; Dickof et al., 2014; He et al., 2014; Li et al., 2017; Quintana Gallo et al., 2020), further developments and verifications are still required to facilitate its widespread adoption. Some research was conducted about the application of DDBD to brace systems. Medhekar and Kennedy (2000b, 2000a) designed steel concentrically braced frame (CBF) structures by the DDBD approach without considering the axial deformation of columns. Della Corte and Mazzolani (2008) derived the yield displacement profile of steel CBF structures using the buckling state of braces. Wijesundara and Rajeev (2012) derived the yield displacement profile of steel CBF structures on the basis of tensile yielding of the braces. Al-mashaykhi et al. (2019) improved the yield displacement profile of steel CBF structures from Wijesundara and Rajeev (2012) by including the effects of higher mode amplifications. Moghaddam and Hajirasouliha (2006) proved the feasibility of pushover analyses on estimating the displacement profile for steel CBF structures. Sullivan et al. (2012) summarized research outcomes of steel CBF structures and introduced a DDBD approach for steel BRB frames. Maley et al. (2010) used the DDBD approach from Sullivan et al. (2012) to design a dual steel system with BRBs and moment-resisting frames. The results showed good control of displacements and inter-storey drifts. Teran-Gilmore and Virto-Cambray (2009) introduced a DDBD approach to design a 5-storey RC frame structure with BRBs. Teran-Gilmore and Coeto (2011) used the DDBD approach to design a 24-storey steel frame structure with BRBs. Their research has shown that DDBD provided adequate strength and stiffness to satisfy the predefined deterministic performance levels. Teran-Gilmore and Ruiz-Garcia (2011) designed and retrofitted steel BRB frames through FBD and DDBD approaches and compared the seismic performance of the two approaches. The results showed that the DDBD approach

provided advantages over the traditional FBD approach because the DDBD approach was able to limit the building damage through the control of the inter-storey drift responses. So far, several attempts have been made to design steel and RC frame systems with BRBs, but the research on BRB-braced system is still limited and timber frames have not been applied before. The feasibility of the DDBD approach for BRBGF system requires further investigation.

Another challenge for the DDBD approach is the determination of the displacement reduction factor $\eta_{in}(\mu)$. The $\eta_{in}(\mu)$ is usually expressed as a function of the equivalent viscous damping ξ_{eq} as suggested by Priestley et al. (2007a). Many research has reported ξ_{eq} for different structural types by either the area-based method proposed by Jacobsen (1960) or NLTHA (Blandon and Priestley, 2005; He and Liu, 2015; Khan et al., 2016; Landi et al., 2007; Liu et al., 2015; Mazza and Vulcano, 2014; Sullivan and O'Reilly, 2014; Wijesundara et al., 2011; Yahyai and Rezayibana, 2015; Yan et al., 2018). However, the area-based method might overestimate the ξ_{eq} (Dwairi et al., 2007; Grant et al., 2005). In addition, the ξ_{eq} is not an intrinsic parameter of a building or the soil type (Millen, 2015; Pennucci et al., 2011), so the derived ξ_{eq} by NLTHA might not generally be suitable for different structures and soil types. All these limitations may cause the determination of ξ_{eq} and the process of the DDBD approach more complicated. A detailed discussion will be provided in Subsection 5.2.3.

2.3.3 Capacity design

The capacity design approach for seismic loads was proposed by Park and Paulay (1975). The approach relies on the strength hierarchy of structural components to ensure that inelastic response is localized in well detailed ductile structural components. These structural fuses have well-established yielding behaviour with high energy dissipation capacity to ensure structural integrity under strong ground motions. This hierarchy stretches along the load path where the load demand for protected brittle components is amplified to the maximum inelastic strength of the ductile elements. This hierarchy is also used to counteract the uncertainties of the design ground motions and the amplification effects associated with soil conditions. Moreover, the capacity design approach ensures seismic performance requirements to be met through strength progression and limiting localized inelastic deformations (Gilbert, 2016).

Following the capacity design approach, ductile elements or primary structural fuses (e.g. the BRBs in the proposed hybrid system) are designed to satisfy the inelastic demands with respect to the specific seismic hazard level. The intended localized plastic deformations and material properties must provide adequate energy dissipation and prevent the collapse of the whole buildings under severe seismic loads. Additionally, the cyclic behaviour of the structural fuses must be detailed to satisfy their strength degradation limits. The probabilistic inelastic resistances of the ductile elements are then determined based on the sections selected through the seismic design. After that, these anticipated seismic forces are factored by an overstrength factor γ_{Rd} that is defined as the difference between the design strength of the ductile elements and the 95^{th} percentile of the actual strength distribution of the ductile elements (possibly achieved high-bound strength) as shown in Figure 2.27. The overstrength factor γ_{Rd} was used

to design the remaining structural elements of the LFRS (e.g. timber frame members and connections in the proposed hybrid system), so the non-ductile elements remain essentially elastic and minimize the damage. The capacity design approach ensures that the building reaches its maximum performance by fulfilling inelastic demands when the structural integrity is maintained.

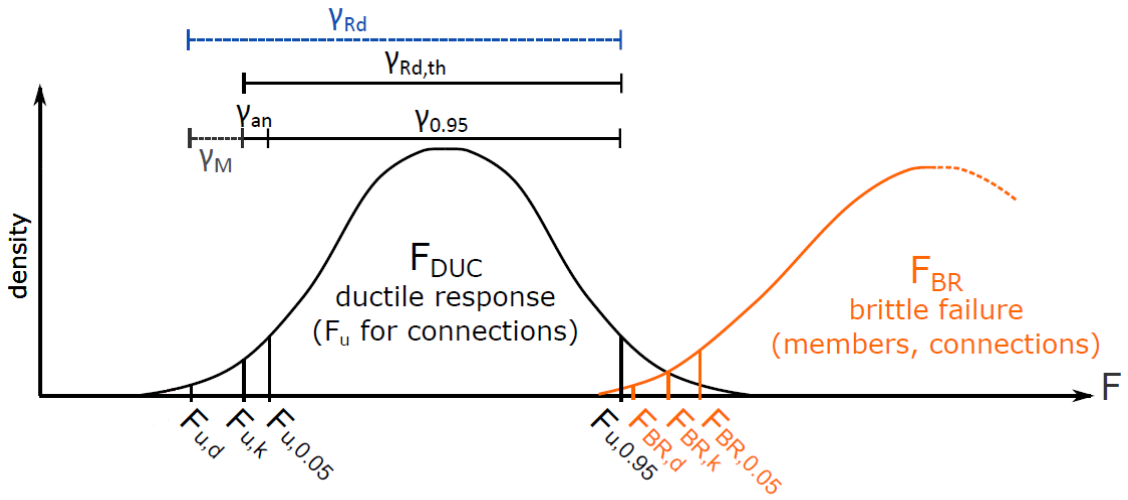

Figure 2.27 Definition of the overstrength factor (Ottenhaus, 2019)

2.4 Summary

The literature review on relevant mass timber technology showed that timber-braced frames generally had limited ductility and the energy dissipation mainly relied on the timber connections. Only one glulam frame with BRBs and BRB-timber interface bolted connections was tested on a shake table in the attempts to integrate BRBs into heavy timber frames, and the structural failure was partially caused by critical connection failure. Additionally, the premature connection failure restricted the full development of system ductility, reduced the structural efficiency, and thus highlighted the importance of enhanced connection design in this hybrid system. Only a few studies are available for the connections between BRBs and heavy timber frames. Two potential connection types for BRBs and heavy timber frames were reviewed. However, the timber-to-steel connections need to be carefully designed and information about their performances in a system is required.

Previous studies on BRBs and BRB frames showed that pin-end BRBs allow the structure to reach a higher drift ratio without imposing obvious damages and are less demanding for the gusset plates. The moment resisting capacity of the two potential BRB-timber connections needs to be quantified and the effects of their rotational stiffness on the overall performance are still unknown. The design methods for BRBs and gusset plates generally predicted their structural performance reasonably. However, the OOP performance of BRBs and gusset plates under bi-direction loads still requires further investigation and is currently ongoing at the University of Canterbury. The BRB component behaviour could be generally well represented

by the numerical models primarily developed for steel structures and it is more important to conduct research on BRB frames at a system level. In the BRB-braced timber frame system, connection stiffness becomes a more critical design criterion because additional deformations will be introduced into the system if too flexible connections are used and the initial slips might have some negative effects on the overall performance. In this regard, the effects of initial slips need to be investigated.

For the seismic design of BRBGF system, the FBD and DDBD approach were reviewed. The DDBD approach might be a good alternative for the FBD approach and provide a more economical seismic design in some conditions. However, the DDBD approach required further investigation on the determination of the equivalent viscous damping and the displacement reduction factor. In addition, due to the brittle characteristics of failure modes of timber members, it is recommended to apply the capacity design approach to ensure the ductile behaviour of the hybrid system. Knowledge of the overstrength factor is crucial, but research and design information of a suitable overstrength factor for the timber connections in BRBGFs is limited.

The research gaps above restrain the transfer of knowledge developed for steel and RC structures to timber structures. Therefore, experimental tests are required to understand the overall performance of this hybrid system comprehensively. Furthermore, to thoroughly investigate the performance of this hybrid system, parametric studies are needed to study the influence of critical design parameters. Reliable numerical models of this hybrid system also need to be developed based on the experimental tests of this hybrid system and existing models for steel and RC structures. At last, a practical design approach is preferred to facilitate the seismic design of BRBGFs.

3 EXPERIMENTAL TESTS

The research gaps mentioned in Chapter 2 highlighted the importance of experimental tests to understand the system behaviour of the BRB-braced timber frame systems. This chapter describes the experimental tests of two full-scale BRB-braced glulam frames (BRBGFs) as well as requisite tests for the performance verification of connections and numerical modelling. This chapter is based on a journal paper (Dong et al., 2020) published on *Engineering Structures*.

3.1 Design of test specimens

3.1.1 Prototype building

A six-storey glulam frame office building located in Christchurch, New Zealand was used as a prototype building as shown in Figure 3.1. BRBGFs were used as the LFRS. According to the literature review, the beam-column connections were assumed as pinned connections to reduce the frame action. The building had CLT floors and roofs that transferred lateral loads to the BRBGFs. The CLT floors and roofs were assumed as a rigid diaphragm according to the research by Moroder (2016). The seismic demand calculation followed the equivalent static method in New Zealand standard NZS 1170.5 (2004) with an assumed ductility factor μ=3.0. The loading information is listed in Table 3.1.

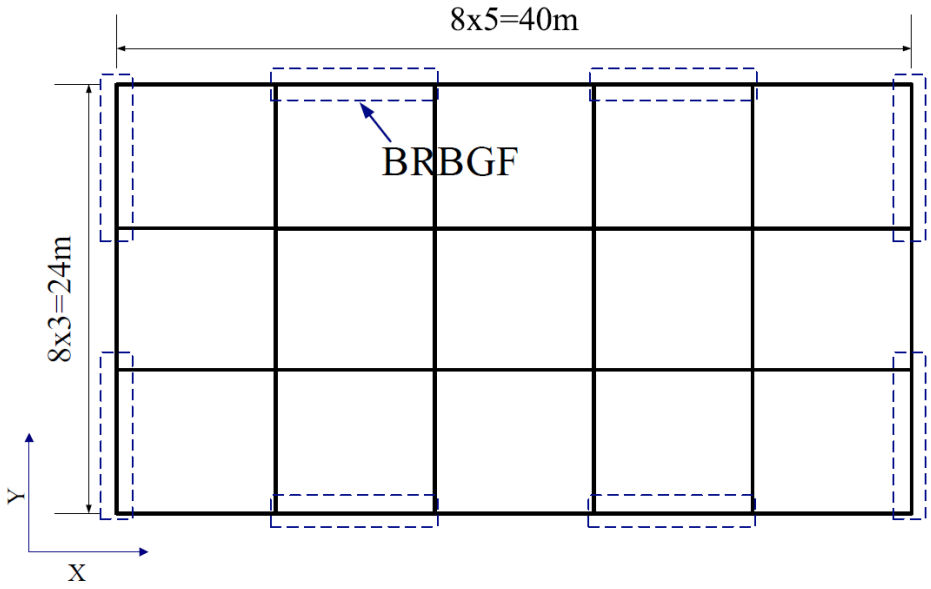

a) Plan view

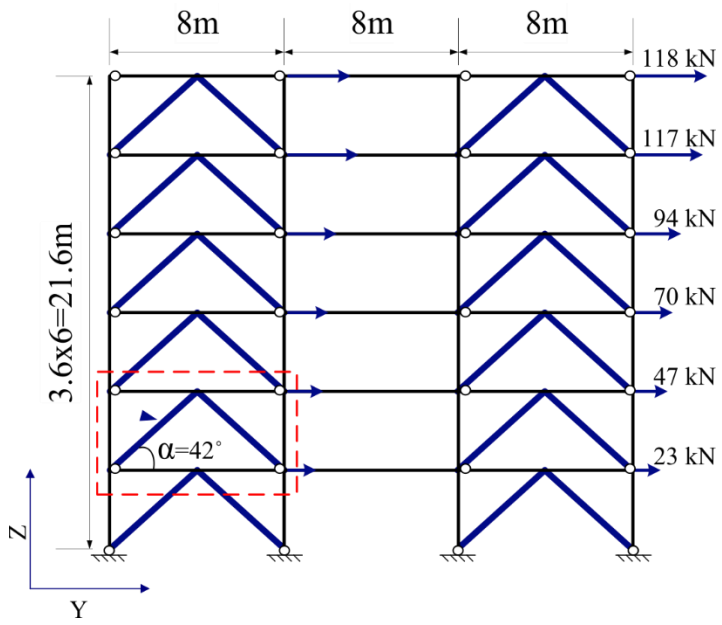

b) Side view

Figure 3.1 Plan and side view of the prototype building

Table 3.1 Loading information of the prototype building

Item	Value	Item	Value
Importance level	2	Return period factor *R*	1.0
Design working life	50 years	Near-fault factor *N*	1.0
Annual probability of exceedance	1/500	Dead load on the floor	1.8 kPa
Site subsoil class	C	Dead load on the roof	1.6 kPa
Hazard factor *Z*	0.3	Live load	3.0 kPa

The seismic load in the Y direction of the prototype building as shown in Figure 3.1 was resisted by four BRBGFs. The specimens represented one of the BRBGFs on the second storey highlighted in Figure 3.1b. The BRBGF on the second storey was chosen instead of the first storey because the BRBGF on the second storey contained all critical BRB-timber interface connections, i.e. the mid-span connection linking inverted-V BRBs and the top beam (referred as the top connection) and the corner connection linking one BRB with the bottom beam and one side column (referred as the bottom connection). The BRBs at the first storey can be directly connected to the concrete foundation via embedded steel gusset plates, so the bottom connections might not be represented well. The other reason was that the peak inter-storey drift was also likely to occur on the second storey of a multi-storey building, as indicated in previous experimental tests (Fahnestock et al., 2007) and numerical analysis (Chou et al., 2012; Sahoo and Chao, 2010).

Two BRBGF specimens were designed and tested as shown in Figure 3.2. Both specimens were 8 m wide and 3.6 m high. The two specimens were identical except for the use of different connection details. One specimen used dowels and inserted steel plates to construct its top and bottom connections. The connections are referred as the dowelled connections and the

specimen is denoted as S-D. The other specimen used inclined STS and steel side plates to construct its connections. The connections are referred as the screwed connections and the specimen is denoted as S-S. All material properties used for specimens are listed in Table 3.2. P-Δ effects were not considered in the specimen design because the column base connections were assumed as pinned connections. Sahoo and Chao (2010) indicated that P-Δ effects might not significantly influence the overall behaviour of steel BRB frames as long as the lateral drift was well controlled. The timber frames usually have less deformation capacity compared with steel frames due to timber splitting in the perpendicular-to-grain direction, so the allowable lateral drift of BRBGFs would be smaller than steel BRB frames and the influence of P-Δ effects should be smaller than steel BRB frames as well.

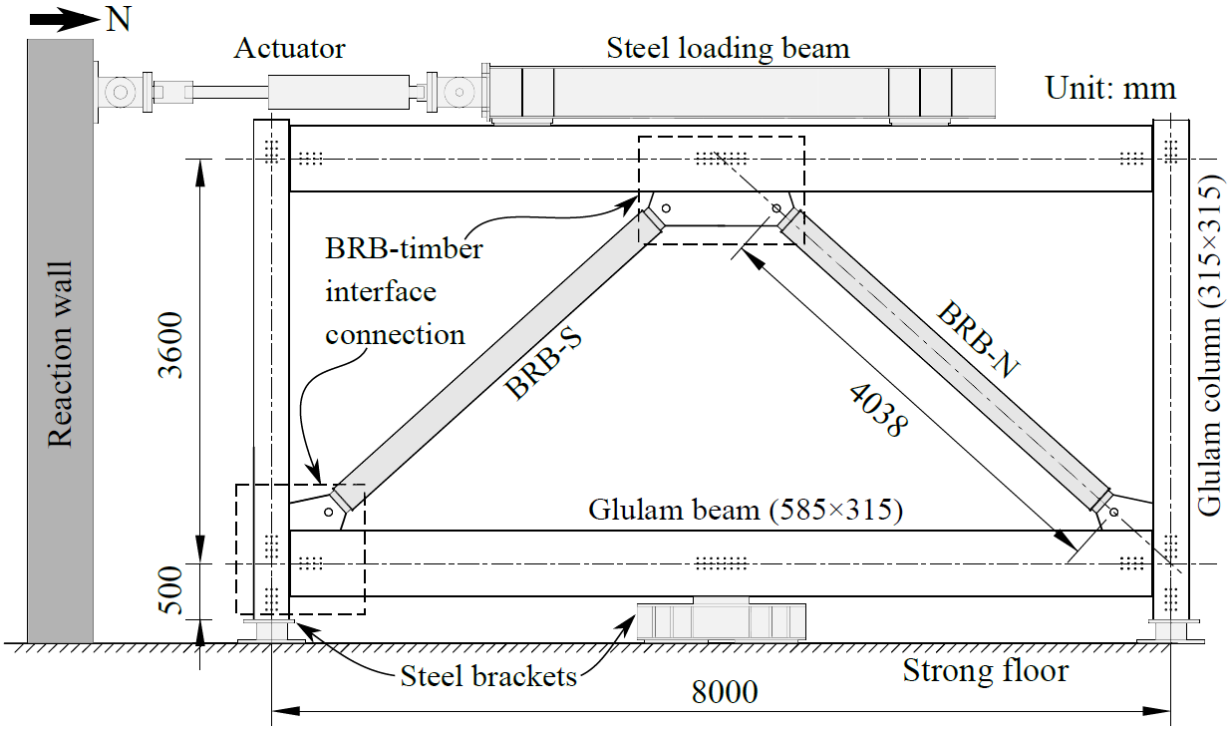

Figure 3.2 Elevation view of the BRBGF specimen test setup

Table 3.2 Material properties

Members	Materials	Properties
BRBs	16×70 mm Grade 235 flat plate (Chinese Global Standards, 2017)	Nominal yield strength $f_{ys,BRB}$ = 235 MPa; Elastic modulus $E_{s,BRB}$ = 206 GPa; Yield zone length l_c = 3056 mm; Yield zone area A_c = 1120 mm^2; Transition length l_{tr} = 120 mm; Transition area A_{tr} = 2320 mm^2; Elastic length l_e = 860 mm; Elastic area A_e = 8800 mm^2.

Beams and columns	GL10 New Zealand *Radiata Pine* (New Zealand Standards, 1993)	Bending strength f_b = 22 MPa; Compression strength parallel to grain f_c = 26 MPa; Tension strength parallel to grain f_t = 11 MPa; Compression strength perpendicular to timber grain $f_{cp,0}$ = 8.9 MPa; Shear strength f_s = 3.7 MPa; Elastic modulus E_{GL} = 10 GPa; Modulus of rigidity G_{GL} = 670 MPa; Characteristic density ρ_k = 434 kg/m^3; Mean density ρ_m = 466 kg/m^3; Average moisture contents = 12%.
Gusset plate in S-D	20 mm-thick Grade 300 flat plate (NZS 3404 (1997))	Nominal yield strength f_{ys} = 300 MPa; E_s = 210 GPa; minimum tensile strength f_{us} = 430 MPa.
Dowels in S-D	Ø12 Grade 300 round bar	f_{ys} = 300 MPa; E_s = 210 GPa; Tensile strength $f_{u,k}$ = 345 MPa.
Gusset plate in S-S	12 mm-thick Grade 350 flat plate (NZS 3404 (1997))	f_{ys} = 350 MPa; E_s = 210 GPa; f_{us} = 450 MPa.
Screws in S-S	Ø11×300 VGS self-tapping screws (ETA 11/0030 (2019))	Tensile strength $f_{ten,k}$ = 38 kN; Withdrawal parameter $f_{ax,k}$ = 11.7 N/mm^2; Effective diameter d_{ef} = 7.3 mm; Elastic modulus E_{STS} =210 GPa.
Washers for STS	VGU 45° washers (Rothoblaas, 2017)	f_{ys} = 235 MPa; E_s = 210 GPa.

3.1.2 Capacity design

Following the capacity design approach, the BRBs in this hybrid system were assumed as ductile elements while all glulam members and connections were assumed as non-ductile elements and designed to remain elastic. Therefore, the glulam members and connections were designed considering the overstrength of BRBs. For steel BRB frames, the American steel code AISC 341-16 (2016b) requires:

$$R_{d,brittle} \geq \phi_m \omega \beta R_{k,BRB} \qquad \text{Eq. 3.1}$$

where $R_{d,\ brittle}$ is the capacity of brittle and non-ductile elements;

ϕ_m (=1.15) is the material overstrength factor suggested by AISC 341-16 (2016b);

ω is the BRB strain hardening adjustment factor;

β is the BRB compression strength adjustment factor;

$R_{k,BRB}$ (=$f_{ys,BRB}A_c$) is the nominal characteristic yield capacity of BRB; and

A_c is the cross-section area of the yield zone in the BRB.

In Eq. 3.1, ω and β consider the BRB overstrength caused by the steel strain hardening effect after yielding and the transfer of stress to the casing under compression, respectively (López and Sabelli, 2004). The BRB overstrength factor $\gamma_{os,BRB}$ for capacity design was taken as the product of ω and β, and the product was assumed to be 1.5 suggested by the BRB supplier.

3.1.3 BRB member and gusset plate design

The ULS seismic load demand for each BRBGF at each storey is shown in Figure 3.1b. The load demand for the BRBGF specimens on the second storey was 446 kN and the load demand for each BRB component was 301 kN considering the inclined angle α (=42°). Commercial BRB products were used in this test with nominal characteristic yield capacity $R_{k,BRB}$=263 kN. The yield zone was a flat steel plate with Grade Q235 according to GB50017 (Chinese Global Standards, 2017) and a cross-section of 16×70 mm. The geometry of the steel core is listed in Table 3.2. The steel core was covered by 4 mm bituminous felt unbonding layers and then put into a 250×250×6 mm Grade Q235 steel casing. C30 concrete according to GB 50010 (Chinese Global Standards, 2010) was used to fill the space between the steel core and the steel casing. The BRBs were connected with the steel gusset plates by Ø70 mm pins. The pins were made of AISI 4140 high-strength steel (Woolman and Mottram, 2013). All the steel gusset plates were designed according to NZS 3404 (New Zealand Standards, 1997) for tensile strength $F_{d,gs,ten}$ (Eq. 3.2) and Section E of AISC 360-16 (2016a) for stability $F_{d,gs,st}$ (Eq. 3.3). The effective length factor K_{gs} was chosen as 2.0 instead of 0.65 because the research by Tsai and Hsiao (2008) illustrated that K_{gs}=0.65 was unconservative to predict the test results and K_{gs}=2.0 was a more suitable value as discussed in Subsection 2.2.2. Table 3.3 lists the design strength of gusset plates according to Eq. 3.2-Eq. 3.3 and their corresponding gusset plate relative overstrength factor $\gamma_{os,gs}$ defined by Eq. 3.4 as the ratio between gusset plate design strength $F_{d,gs}$ and the load $F_{k,BRB}$ transferred from BRBs to the connections when the BRBs yield. Higher $\gamma_{os,gs}$ means higher over-design of the gusset plates. The steel plate thickness of the screwed connections was limited to 12 mm by the geometry of washers for STS, which caused the gusset plates were not strong enough as non-ductile members (i.e. $\gamma_{os,gs} < \gamma_{os,BRB}$ as shown in Table 3.3). Stiffeners were welded on the gusset plates by fillet weld to reinforce them, which was similar to those in research by Ozcelik and Erdil (2019). The fillet weld was designed according to clause 9.7.3.10 in NZS 3404 (1997) to limit the possibility of brittle failures of the weld.

$$F_{d,gs,ten} = \phi_s t_{gs} a_e f_{us} n_{gs} \quad \text{Eq. 3.2}$$

$$F_{d,gs,st} = \phi_s F_{cr} A_{gs} \quad \text{Eq. 3.3a}$$

with

$$F_{cr} = \begin{cases} Q\left(0.658^{\frac{Qf_{ys}}{F_e}}\right)f_{ys} & if\ \frac{K_{gs}L_{gs}}{r_{gs}} \le 4.71\sqrt{\frac{E_S}{Qf_{ys}}} \\ 0.877F_e & if\ \frac{K_{gs}L_{gs}}{r_{gs}} \le 4.71\sqrt{\frac{E_S}{Qf_{ys}}} \end{cases} \quad \text{Eq. 3.3b}$$

$$A_{gs} = b_{gs}t_{gs} \quad \text{Eq. 3.3c}$$

$$F_e = \frac{\pi^2 E_s}{\left(\frac{K_{gs}L_{gs}}{r_{gs}}\right)^2} \quad \text{Eq. 3.3d}$$

$$\gamma_{os,gs} = \frac{F_{d,gs}}{\phi_m F_{k,BRB}} \quad \text{Eq. 3.4}$$

where ϕ_s (=0.9) is the strength reduction factor;

t_{gs} is the gusset plate thickness;

a_e is the minimum distance from the edge of a hole to the edge of the gusset plate, and is measured by the gusset plate geometry as shown in Figure 3.3;

f_{us} is the tensile strength of gusset plate in Table 3.2;

n_{gs} (= 2) is the number of gusset plates in each connection;

F_{cr} is the buckling stress for the section;

A_{gs} is the effective area of the gusset plate;

Q is the net reduction factor accounting for all slender compression elements according to Section B4.1 in AISC 360-16 (2016a);

f_{ys} is the nominal yield strength of gusset plate;

F_e is the elastic buckling stress;

b_{gs} is the width of the gusset plate, i.e. the distance from the free edge to the centre of the pin as shown in Figure 3.3;

L_{gs} is the laterally unbraced length of the gusset plate as shown in Figure 3.3;

r_{gs} is the radius of gyration of the gusset plate; and

$F_{k,BRB}$ is the load transferred from BRBs to the connections when the BRBs yield.

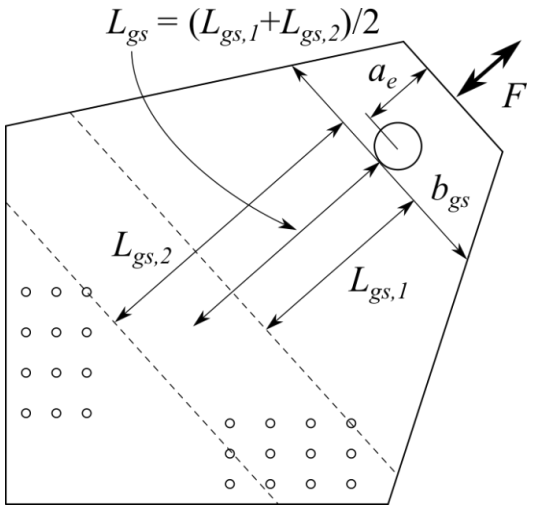

Figure 3.3 Gusset plate calculation parameters

Table 3.3 Gusset plate design strength (kN) and the corresponding relative overstrength factor $\gamma_{os,gs}$

Specimen	Gusset plate position	Compression	Tension	$\gamma_{os,gs}$
S-D	Top	569.4	1188.0	2.16
	Bottom	859.5	1188.0	3.27
S-S	Top	265.2	712.8	1.01
	Bottom	426.6	712.8	1.62

3.1.4 Glulam member and connection design

Grade GL10 glulam members according to NZS 3603 (New Zealand Standards, 1993) were used as the beams and columns. Because BRBs do not carry gravity loads after yielding, the glulam beams were designed with a full span of 8 m and the strength was checked according to Eq. 3.5 extracted from NZS 3603 (1993). The beam and column cross-sections were 585×315 mm and 315×315 mm, respectively, considering all possible load combinations in the prototype building. There was also a 10 mm gap between the beam and column to allow the rotation of beam-column connections without significantly crushing the column in the perpendicular-to-grain direction.

$$M^* \leq \phi_{GL} M_n = \phi_{GL} k_b f_b Z \quad \text{Eq. 3.5a}$$

$$V^* \leq \phi_{GL} V_n = \phi_{GL} k_s f_s A_s \quad \text{Eq. 3.5b}$$

$$N_c^* \leq \phi_{GL} \min\{N_{ncx}, N_{ncy}\} = \phi_{GL} f_c A_{GL} \min\{k_{cx}, k_{cy}\} \quad \text{Eq. 3.5c}$$

$$N_t^* \leq \phi_{GL} N_{nt} = \phi_{GL} f_t k_t A_{GL} \quad \text{Eq. 3.5d}$$

where M^*, V^*, N_c^* and N_t^* are moment, shear force, compression force and tension force demands, respectively;

ϕ_{GL} (=0.8) is the strength reduction factor for glulam;

M_n, V_n, N_{ncx}, N_{ncy}, and N_{nt} are nominal bending strength, shear strength, compression strength along the strong axis, compression strength along the weak axis, and tension strength for glulam members;

k_b, k_s, k_{cx}, k_{cy}, and k_t are modification factors for bending, shearing, compression along the strong axis, compression along the weak axis and tension, respectively;

A_s is the shear area; and

A_{GL} is the cross-section of glulam members.

In S-D, the dowelled connections consisted of Ø12 mm Grade 300 steel dowels and 20 mm-thick Grade 300 steel plates as shown in Figure 3.4. Each connection had two internal steel plates as the gusset plates that had predrilled holes in a diameter of 13 mm. The glulam members had two 22 mm-wide slots with a spacing of 125 mm and Ø12 mm holes. The tolerance in the dowelled connections can cause slips and reduce the efficiency of the hybrid system. To minimize its impact, all the steel plates and the glulam members were manufactured by computer numerically controlled (CNC) machines and the same diameter holes with the dowels were drilled in the glulam members as recommended by Eurocode 5 (2004). Cracks and checks caused by the fluctuation of moisture contents could reduce the strength and stiffness of dowelled connections significantly (J. Zhang et al., 2018, 2021). Therefore, all dowels were configured within the middle one-third height of glulam members as shown in Figure 3.4c to reduce the risks due to the initiation of cracks and checks. During the installation, some dowels were installed to fix the location of gusset plates and carry the self-weight of specimens and the rest of dowels were installed when the glulam members' moisture contents became constant after several weeks' resting in the lab. When the dowelled connections were installed, the tip of each dowel was chamfered to fit the hole and prevent damaging the glulam surface. All these practical measurements similar to the construction sites were taken to ensure that our test specimens represented the building scenario. Other measurements such as screw reinforcements (Elbashir et al., 2020) could be an efficient solution to preventing premature splitting and visible cracks caused by the moisture content fluctuation, however, this is out of the scope of this project.

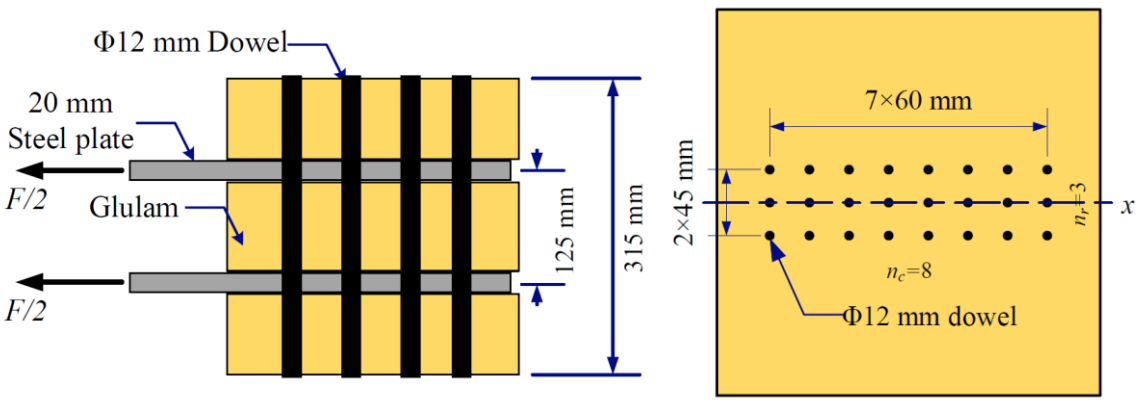

a) Connection details b) Top connection layout

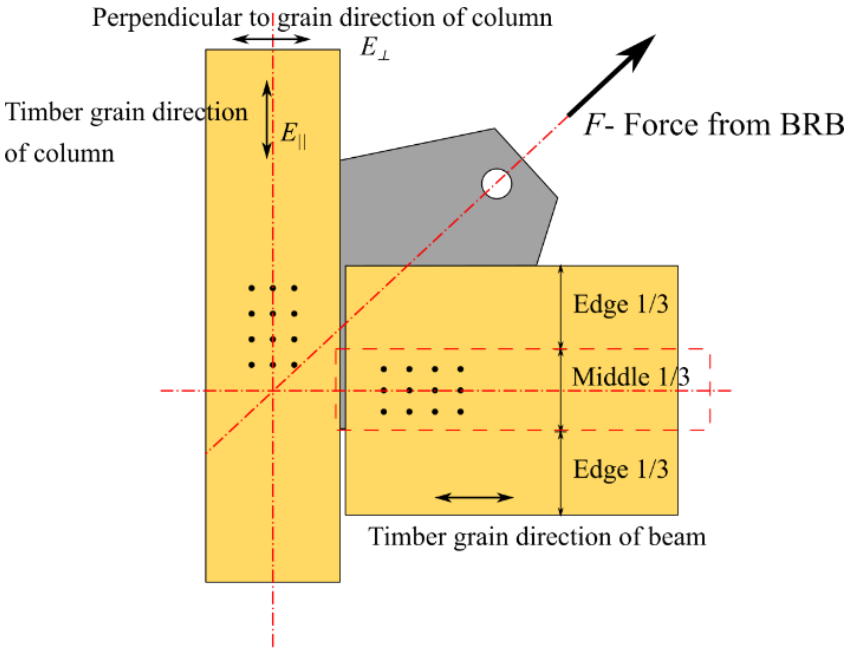

c) Dowel configuration

Figure 3.4 The dowelled connection

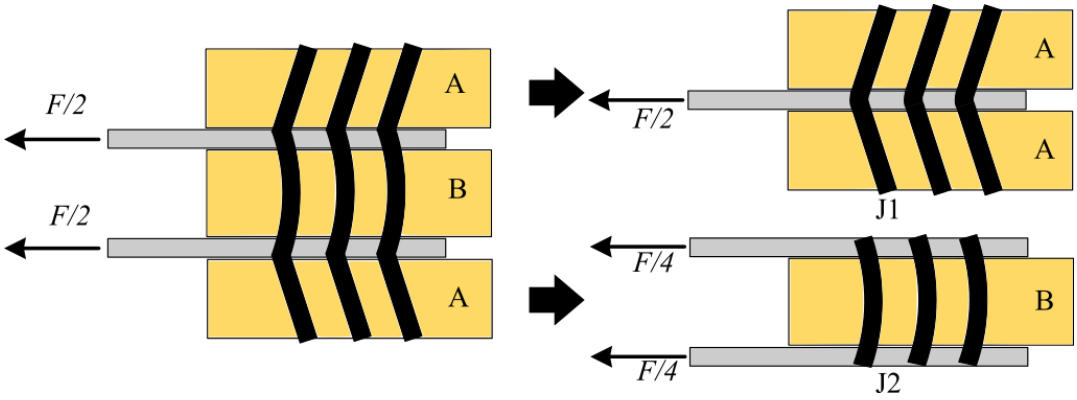

Figure 3.5 Calculation model from Fan et al. (Fan et al., 2011)

The characteristic strength $F_{V,Rk}$ of the dowelled connections was calculated by Eq. 3.6a using the model proposed by Fan et al. (2011) as shown in Figure 3.5. The joints J1 and J2 could be calculated by Eq. 3.6b and Eq. 3.6c, respectively, according to Eurocode 5 (2004) considering the effective number n_{ef} of dowels in each row. The top connection and bottom connections were at the same design strength hierarchy, so Figure 3.4b shows the top connection layout as an example in which n_r and n_c are the row and column number of the dowel groups. The spacing follows the spacing requirements for dowels in Eurocode 5 (2004). The spacing notations are shown in Figure 3.6 and the actual spacing of the dowelled connections was compared with the minimum spacing requirements in Eurocode 5 (2004) as listed in Table 3.4. The dowel groups in all connections were aligned with the glulam member axes to reduce the moment caused by eccentricity and avoid timber splitting perpendicular to timber grain. The design strength of the connections $F_{d,con}$ was calculated by Eq. 3.7 and listed in Table 3.5. Table 3.5 also lists the connection relative overstrength factor $\gamma_{os,con}$ that was

defined by Eq. 3.8 as the ratio between connection design strength $F_{d,con}$ and the load $F_{k,BRB}$ transferred from BRBs to the connections when the BRBs yield. Higher $\gamma_{os,con}$ means higher over-design of the connections.

$$F_{V,Rk} = n_{ef} n_r (n_{J1} F_{V,Rk,J1} + n_{J2} F_{V,Rk,J2}) \quad \text{Eq. 3.6a}$$

with

$$F_{V,Rk,J1} = \min \begin{cases} f_{h,0,k} t_A d \\ f_{h,0,k} t_A d \left[\sqrt{2 + \frac{4 M_{y,Rk}}{f_{h,0,k} d t_A^2}} - 1 \right] \\ 2.3 \sqrt{M_{y,Rk} f_{h,0,k} d} \end{cases} \quad \text{Eq. 3.6b}$$

$$F_{V,Rk,J2} = \min \begin{cases} 0.5 f_{h,0,k} t_B d \\ 2.3 \sqrt{M_{y,Rk} f_{h,0,k} d} \end{cases} \quad \text{Eq. 3.6c}$$

$$f_{h,0,k} = 0.082(1 - 0.01d)\rho_k \quad \text{Eq. 3.6d}$$

$$M_{y,Rk} = 0.3 f_{u,k} d^{2.6} \quad \text{Eq. 3.6e}$$

$$n_{ef} = \min \left\{ n_c \, , n_c^{0.9} \sqrt{\frac{a_1}{13d}} \right\} \quad \text{Eq. 3.6f}$$

where $F_{V,Rk,J1}$ and $F_{V,Rk,J2}$ are the load-carrying capacity per shear plane for steel plate as the central member and the outer member, respectively;

n_{J1} (=2) and n_{J2} (=2) are the shear plane number of joint J1 and J2, respectively;

$f_{h,0,k}$ is the characteristic embedment strength parallel to timber grain;

$M_{y,Rk}$ is the characteristic yield moment of a dowel;

t_A (=83 mm) and t_B (=105 mm) are the side glulam member and central glulam member thickness, respectively as shown in Figure 3.5;

d is the diameter of fasteners; and

a_1 is the spacing of dowel parallel to timber grain as listed in Table 3.4.

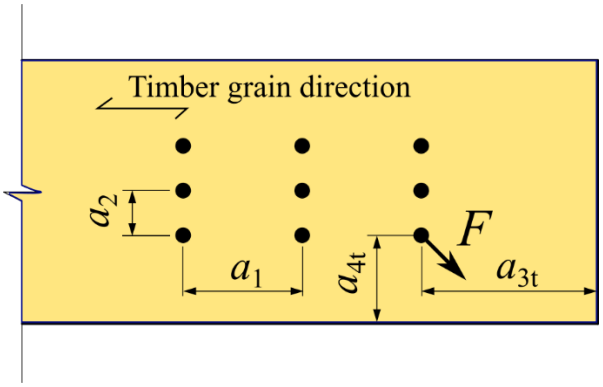

Figure 3.6 Spacings and end and edge distance notation in Eurocode 5 (2004)

Table 3.4 The spacing information of the dowelled connections (mm)

Spacing	The dowelled connection spacing	Eurocode 5 specification
a_1 (parallel to grain)	60 (5d)	60 (5d)
a_2 (perpendicular to grain)	45 (3.75d)	36 (3d)
a_{3t} (loaded end)	90 (7.5d)	max{80, 7d}
a_{4t} (loaded edge)	112.5 (9.4d)	48 (4d)

Table 3.5 Connection design strength (kN) and the corresponding relative overstrength factor $\gamma_{os,con}$

Connection position	S-D (n_r×n_c)	$\gamma_{os,con}$	S-S (n_r×n_c)	$\gamma_{os,con}$
Top connection	619.9 (3×8)	1.59	619.0 (4×4)	1.59
Bottom connection on the beam side (BC-B)	332.2 (3×4)	1.70	309.5 (2×4)	1.58
Bottom connection on the column side (BC-C)	332.2 (3×4)	1.89	309.5 (2×4)	1.76

$$F_{d,con} = F_{V,Rk}\frac{k_{mod}}{\gamma_M} \quad \text{Eq. 3.7}$$

$$\gamma_{os,con} = \frac{F_{d,con}}{\phi_m F_{k,BRB}} \quad \text{Eq. 3.8}$$

where k_{mod} (=1.1) is the modification factor; and

γ_M (=1.25) is the partial factor as per Eurocode 5 (2004).

In S-S, the screwed connections consisted of Ø11×300 fully threaded STS, washers and 12 mm-thick Grade 350 steel plates according to NZS 3404 (1997) as shown in Figure 3.7a. Each connection had two steel side plates as gusset plates. The washers were used to accommodate the 45° inclined STS installation. Slotted holes for the washers were laser cut on the gusset plates following the washer product manual (Rothoblaas, 2017). The geometry of the washers limited the gusset plate thickness to 12 mm, so stiffeners were welded on the gusset plates to increase the strength in compression as mentioned in Subsection 3.1.3. All STS were considered as tension-only STS. For example, the screws in the dark colour as shown in Figure

3.7a are engaged in tension and transfer the load *F* because slotted holes on the steel side plates were oversized and 4 mm longer than the washers as shown in Figure 3.8. The geometry of washers and slotted holes were specified by the washer product manual (Rothoblaas, 2017).

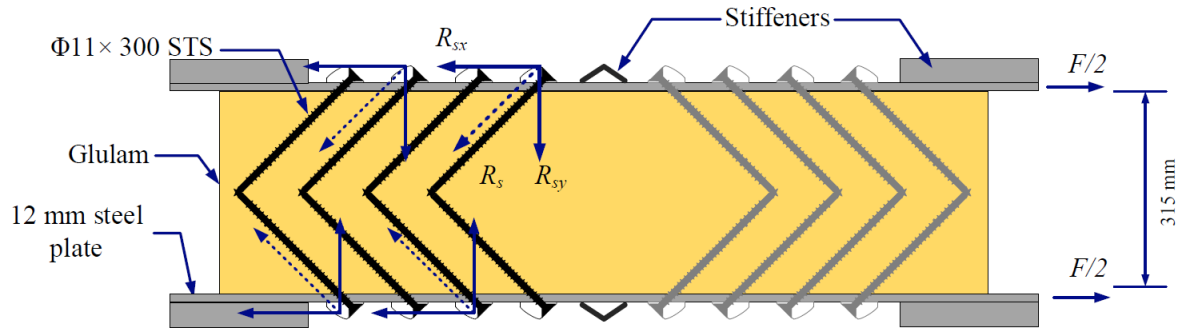

a) Connection details

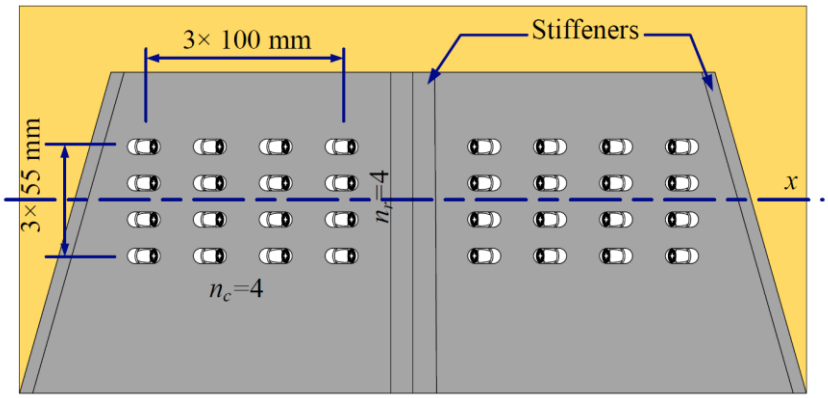

b) Top connection layout

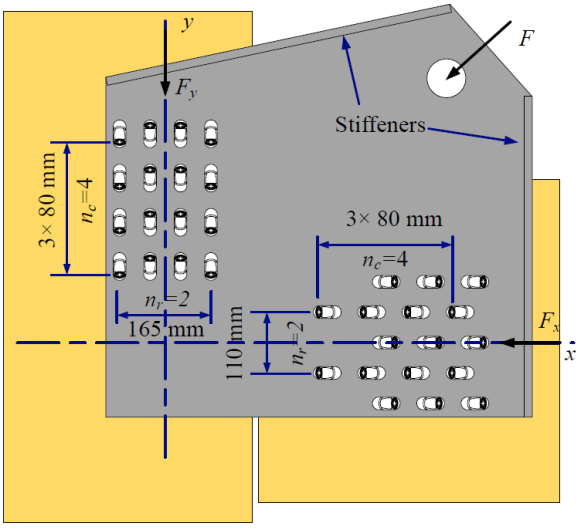

c) Bottom connection layout

Figure 3.7 The screwed connection

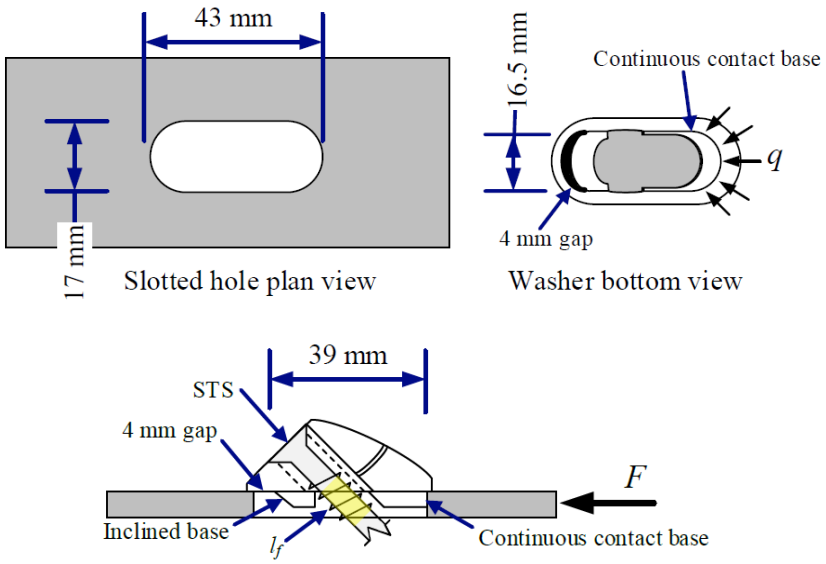

Figure 3.8 Geometry of slotted holes and washers

The characteristic strength $F_{V,Rk}$ of the screwed connections was calculated by Eq. 3.9 as per Eurocode 5 (2004). These screws were designed as axially loaded screws and R_{sx} represents the lateral capacity of individual STS. The connection strength was governed by the smaller value between the STS withdrawal strength $F_{ax,45,Rk}$ and STS tensile strength $f_{ten,k}$. The top and bottom connections in S-S were also designed at the same strength hierarchy. Tests by Krenn and Schickhofer (2009) showed that friction between the steel side plate and timber could also contribute to the connection strength due to the high vertical component R_{sy}. However, the ETA report from the screw supplier, ETA 11/0030 (2019), does not allow to consider the benefits from friction. As the screwed connections in this hybrid system were considered as non-ductile elements and should remain elastic, the friction contribution that could provide additional connection strength was not considered. The effective number of STS, n_{ef} was chosen to be 0.9 times the total STS number based on the tests by Krenn and Schickhofer (2009). The top connection and bottom connection layouts are shown in Figure 3.7b and Figure 3.7c, respectively. In the top connection, the STS that carried the loads in different directions were installed symmetrically along the centre of the top glulam beam, while in the bottom connections, the STS in different directions were installed staggeringly due to the limited space of the connection area. Table 3.5 lists the design strength of the screwed connections $F_{d,con}$ and connection relative overstrength factor $\gamma_{os,con}$. The n_r and n_c are the number of rows and columns of the STS group in tension under the load shown in Figure 3.7a.

$$F_{V,Rk} = n_{ef} n_r R_{sx} \quad \text{Eq. 3.9a}$$

with

$$R_{sx} = \min\{F_{ax,45,Rk}, f_{ten,k}\} cos45° \quad \text{Eq. 3.9b}$$

$$F_{ax,45,Rk} = \frac{f_{ax,k} d l_{ef}}{1.2cos^2 45° + sin^2 45°} \left(\frac{\rho_k}{\rho_a}\right)^{0.8} \quad \text{Eq. 3.9c}$$

$$n_{ef} = 0.9n_c \quad \text{Eq. 3.9d}$$

where $F_{ax,45,Rk}$ is the characteristic withdrawal capacity of STS;

$f_{ten,k}$ is the tensile strength of STS as listed in Table 3.2;

$f_{ax,k}$ is the characteristic withdrawal parameter as listed in Table 3.2;

l_{ef} (=239 mm) is the effective penetration length of the threaded part of STS;

ρ_k is the characteristic timber density; and

ρ_a (=350 kg/m^3) is the relative density.

3.2 Test programme

3.2.1 Test matrix and loading protocol

The experimental tests were conducted in the Structural Engineering Laboratory, University of Canterbury. Table 3.6 lists the test matrix including the frame tests and the BRB component tests. The drift ratios in Table 3.6 were the maximum drift ratios achieved in each test.

Table 3.6 Test matrix

Test phase	Specimen	Test No.	Objective	Drift ratio
I: frame tests	S-D	T1:BRBGF cyclic test	Evaluate ULS	1.5%
		T2: bare frame test	Evaluate the bare frame's deformation capacity	2.0%
	S-S	T3: BRBGF cyclic test	Evaluate ULS	1.5%
		T4: bare frame test	Evaluate the bare frame's deformation capacity	2.0%
II: BRB component tests	BRB-D	T5: cyclic test	Evaluate the BRB residual performance	2.0%*
	BRB-S	T6: cyclic test	Evaluate the BRB residual performance	
	BRB-U	T7: cyclic test	Evaluate the BRB residual performance	

*Note: BRBs were loaded to the displacement they would achieve when the BRBGF was loaded to this drift ratio.

In the frame tests, glulam column bases and the mid-span shear connection of the bottom glulam beam were anchored to the strong floor by steel brackets and the dowelled connections, so the specimens were fixed horizontally and vertically at the bases in the frame plane as shown in Figure 3.9. The top glulam beam was connected to a steel loading beam and the steel loading beam was connected to an 800 kN actuator mounted on the reaction wall. The out-of-plane movement was restrained by two actuators at the positions of the columns, so the specimens were restrained from the out-of-plane movement.

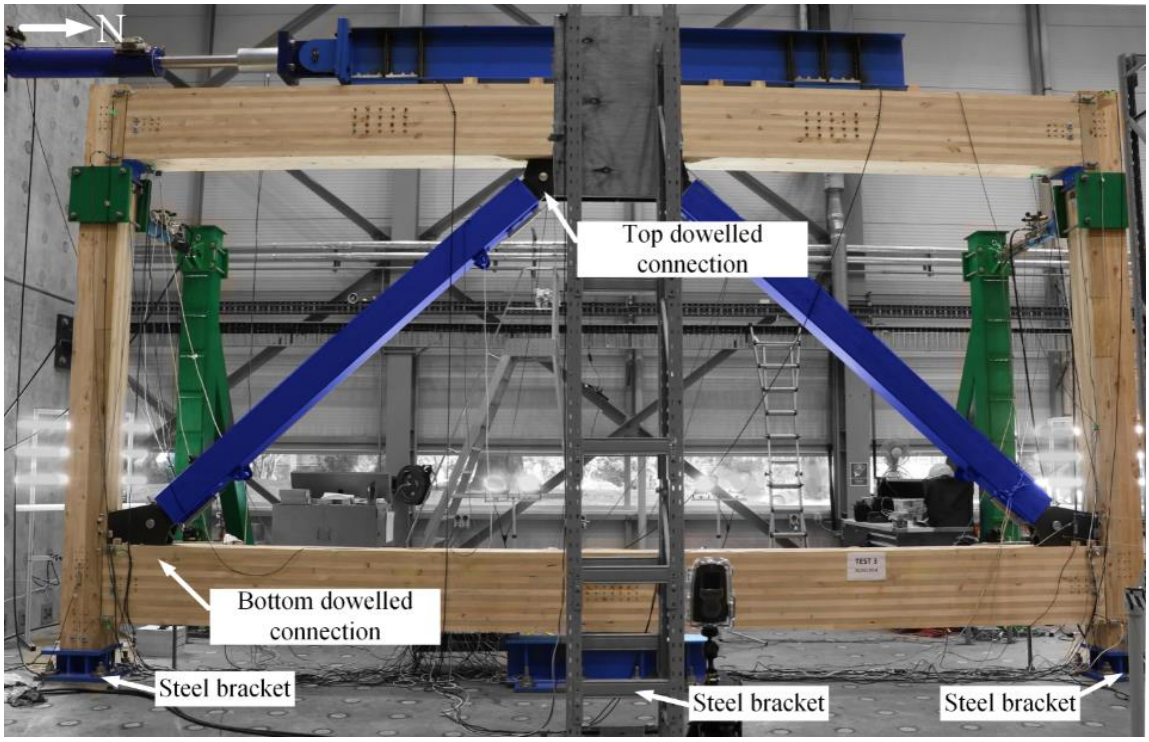

a) S-D with the dowelled connections

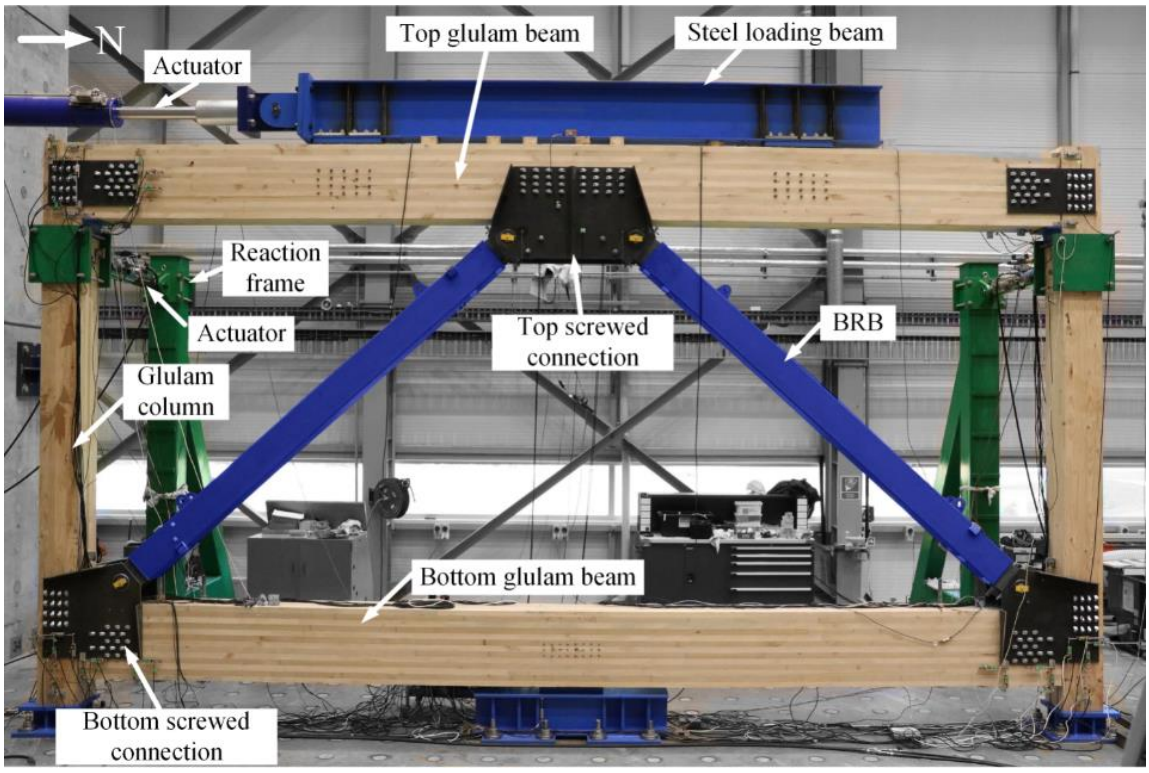

b) S-S with the screwed connections

Figure 3.9 Test specimens

The frame tests followed loading protocol in ISO 16670 (International Organization for Standardization (ISO), 2003) as shown in Figure 3.10 and the positive direction was the north (N) direction in Figure 3.9. The specimens were loaded with incremental drift ratios of 0.03%, 0.06%, 0.13%, 0.19%, 0.25%, 0.5%, 1.0%, 1.5% and 2.0%, and the loading rate was between

8 mm/min and 12 mm/min. The tests T1 and T3 were finished at the 1.5% drift ratio when the maximum capacity of the actuator was reached, but the tests T2 and T4 were finished at the 2.0% drift ratio.

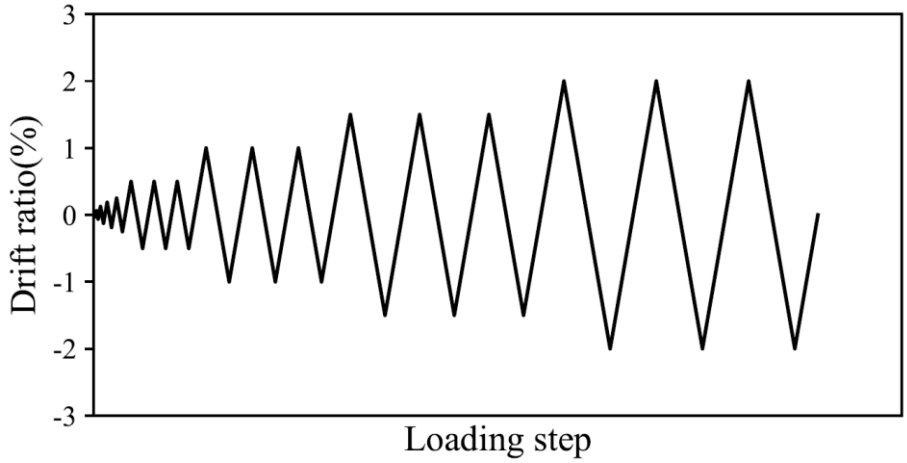

Figure 3.10 ISO 16670 loading protocol (2003)

Because the BRBs were designed to govern the hybrid system performance, it is crucial to ensure the BRB design parameters such as $f_{ys,BRB}$, ω and β were consistent with the design specifications. In the BRBGF tests, two BRBs carried the lateral load together and the force distribution between two BRBs could not be measured accurately. In this regard, three BRB component tests were also conducted under uniaxial cyclic loading as shown in Figure 3.11. Two BRBs were taken from the specimens S-D and S-S, respectively, after the frame tests. They were denoted as BRB-D and BRB-S, respectively. In addition, one BRB was unused but manufactured in the same batch as the BRBs installed in the glulam frames. This BRB was denoted as BRB-U. The loading protocol followed AISC 341-16 (2016b) as shown in Figure 3.12. The predicted design storey drift was 23 mm that was the product of the assumed ductility μ (=3) and assumed yield drift (=Δ_{by}/cos α=7.6 mm where Δ_{by} is the yield displacement of the BRB). The yield drift was calculated by acting the lateral load as shown in Figure 3.1b and neglecting the deformations of the connections (i.e. considering them as translationally rigid connections). Because 23 mm was smaller than the minimum design storey drift ratio for BRB frames (1%, i.e. 36 mm) as per AISC 341-16 (2016b), the design storey drift ratio was set as 1% for the BRB component tests and the corresponding displacement Δ_{bm} was 27 mm. All BRBs were loaded to the displacement corresponding to two times the design storey drift ratio, which was 54 mm ($2\Delta_{bm}$) considering the inclined angle α=42° in the glulam frame as shown in Figure 3.1a. The results of three BRB components were compared to check the consistency of BRB performance.

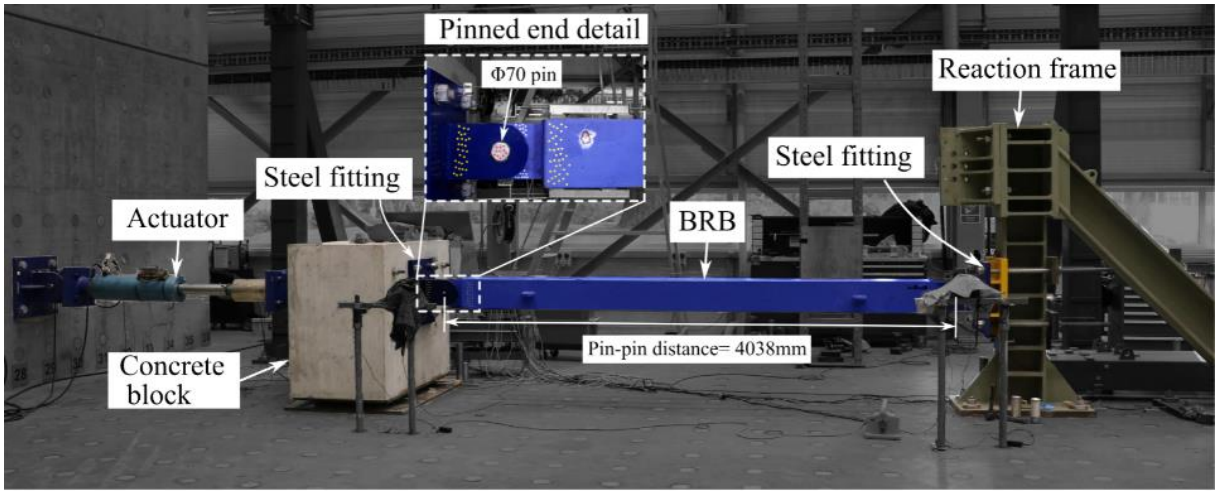

Figure 3.11 BRB component test setup

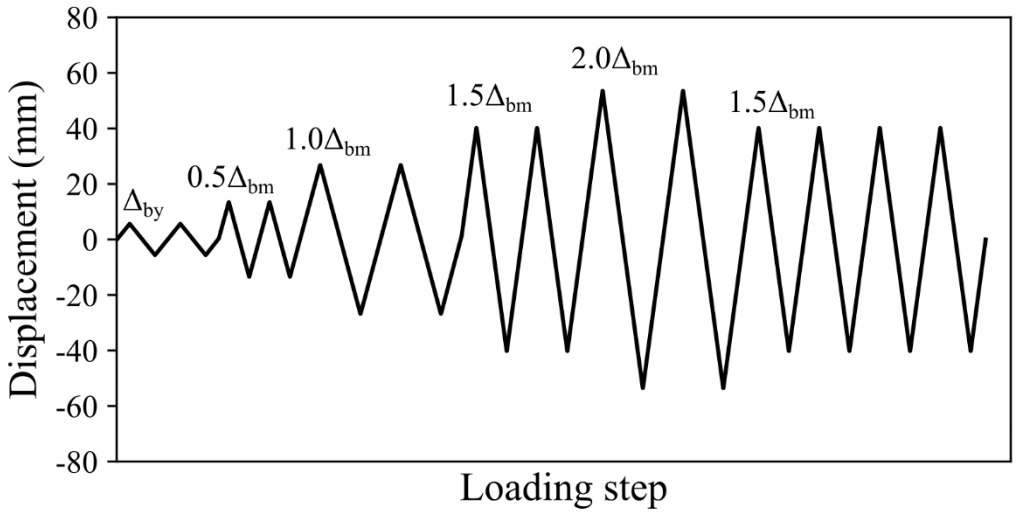

Figure 3.12 Loading protocol of the BRB component tests

3.2.2 Measurements

The locations of measuring devices for BRBGF specimens are shown in Figure 3.13a. A load cell was used to measure the load in the actuator; inclinometers (Is) were installed at beam-column connections to measure the connection rotation (Figure 3.13b); string potentiometers (SPs) were installed at the top glulam beam and bottom glulam beam to measure the frames' inter-storey drift (Figure 3.13c); and linear-motion potentiometers (LPs) were installed on both ends of BRBs' steel casing to measure the BRBs' elongating and shortening (Figure 3.13d). BRBs' tension and compression deformations were the sums of the deformations on both ends.

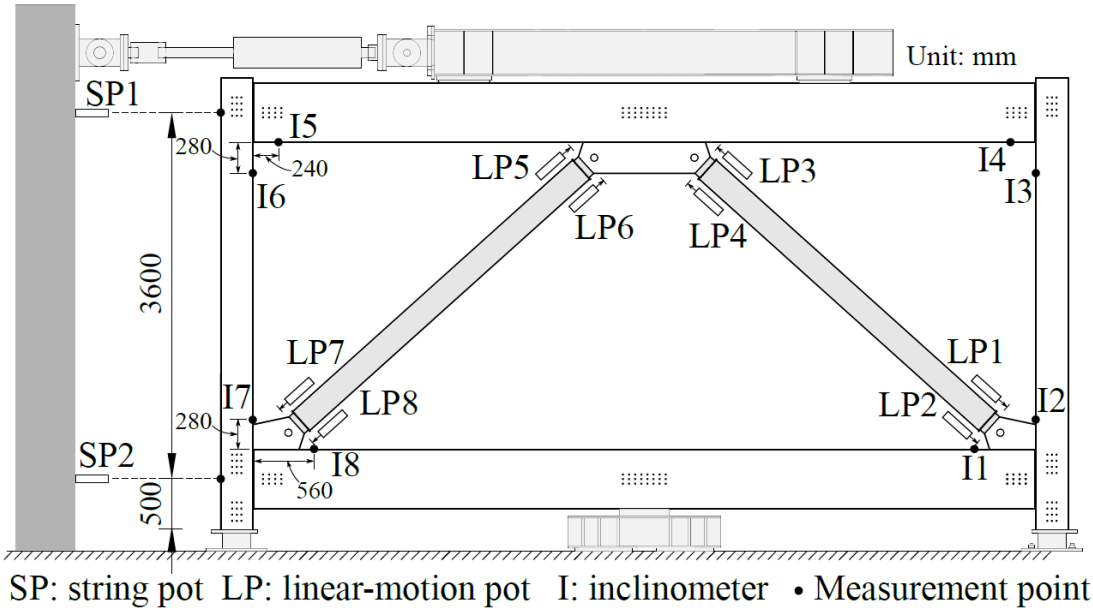

a) Instrument layout

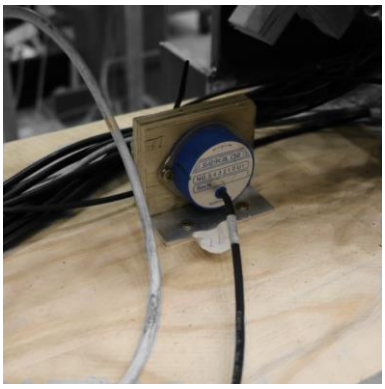

b) Inclinometer

c) Spring potentiometer

d) Linear-motion potentiometer

Figure 3.13 Instruments of BRBGF tests

In S-D, gusset plates were inserted into glulam; in S-S, glulam surfaces were covered by the gusset plates as the side plates in the connection areas. It is challenging to measure the connection movement with traditional instrumentation accurately. Therefore, a contact-free measurement technique called Particle Tracking Technology (PTT) (Nokes, 2017) was adopted in this study. The PTT usually uses cameras to continuously take photos of moving particles that are dyed in different colours from the photo background. Two sequential photos are shown in Figure 3.14a and Figure 3.14b, and they are denoted as Frame 1 and Frame 2, respectively. All particles in Frame 1 are compared to match their corresponding locations in Frame 2 using decision-making algorithms such as the auction algorithm. For example, particle 1 in Frame 1 and particle 1' in Frame 2 are a match. In this way, the trajectories of particles can be calculated as shown in Figure 3.14c. With many particles in a small area, the displacement field and strain can be derived based on the trajectories of particles. PTT was recently used in structural timber tests to capture crack growth of exposed timber surfaces in dowelled connections and also compute the resulting displacement field (Brown et al., 2020; Ottenhaus et al., 2019).

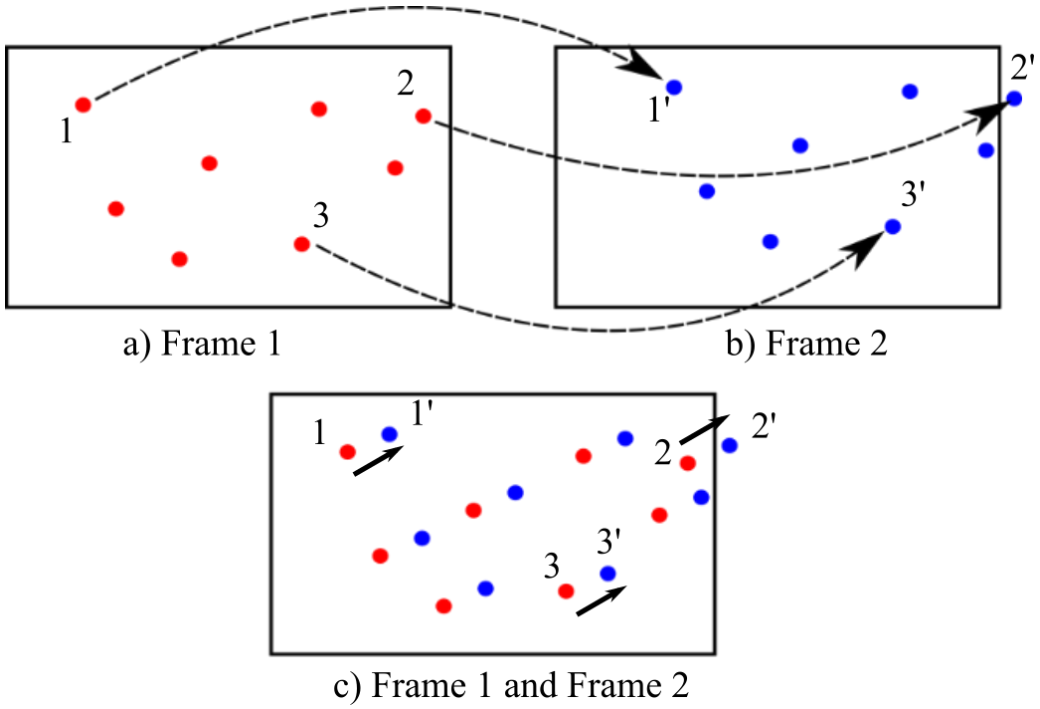

Figure 3.14 PTT process

The PTT measurements for S-D specimen are shown in Figure 3.15 by taking the southern bottom connection as an example. Small particles were attached to the surface of glulam members and gusset plates, as shown in Figure 3.15a. Digital cameras were used to take photos at each load step and track the movement of the particles. To avoid the glare of dowels, the cross-sections of dowels and their surrounding areas were painted black. All photos were processed by computer software Streams (Nokes, 2017) developed at University of Canterbury by Prof. Nokes to obtain the displacement of particles and their corresponding displacement field. In this manner, the movement of each visible point in the photos was exported from the displacement field. Because all gusset plates and glulam members' elastic deformations were negligible when compared with the connection deformations, the gusset plates and glulam members in the connection zones could be assumed to have rigid body motions. As shown in Figure 3.15a, the movement of points *A* and *B* on the gusset plate and point *C'* at the centroid of a dowel on the glulam surface was directly tracked by PTT. The movement of point *C* at the centroid of the dowel on the gusset plate plane was derived by the movement of points *A* and *B* in the triangle ΔABC because point *C* was covered by the glulam and was not visible. The relative movement of point *C'* and point *C* defined the dowel deformations as shown in Figure 3.15b. In this manner, each connection's movement could be evaluated. For S-S, a similar process was conducted by PTT to track the movement of washers and glulam members. The relative movement between washers and glulam members was used to estimate the STS deformations.

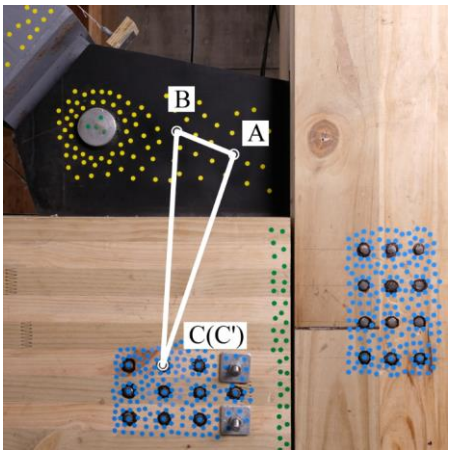

a) Particles on the connection

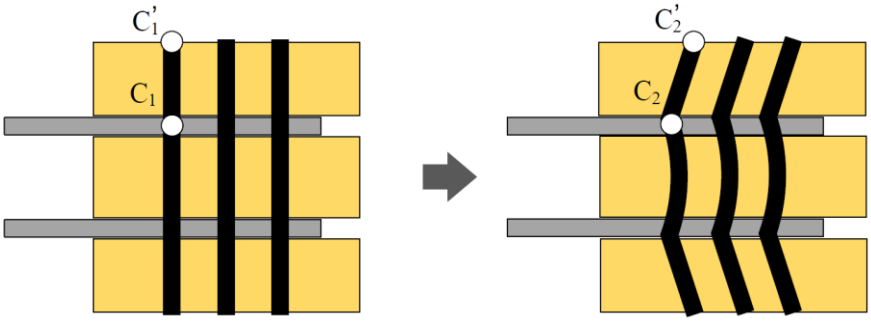

b) Connection movement calculation process

Figure 3.15 PTT measurements of S-D specimen

For the BRB component tests, the locations of measuring devices are shown in Figure 3.16. LPs were fixed on the steel casing of BRBs to measure the relative moment between the steel casing and the steel core, $\Delta_{BRB,s}$. BRBs' tension and compression deformations were the sums of the deformations on both ends.

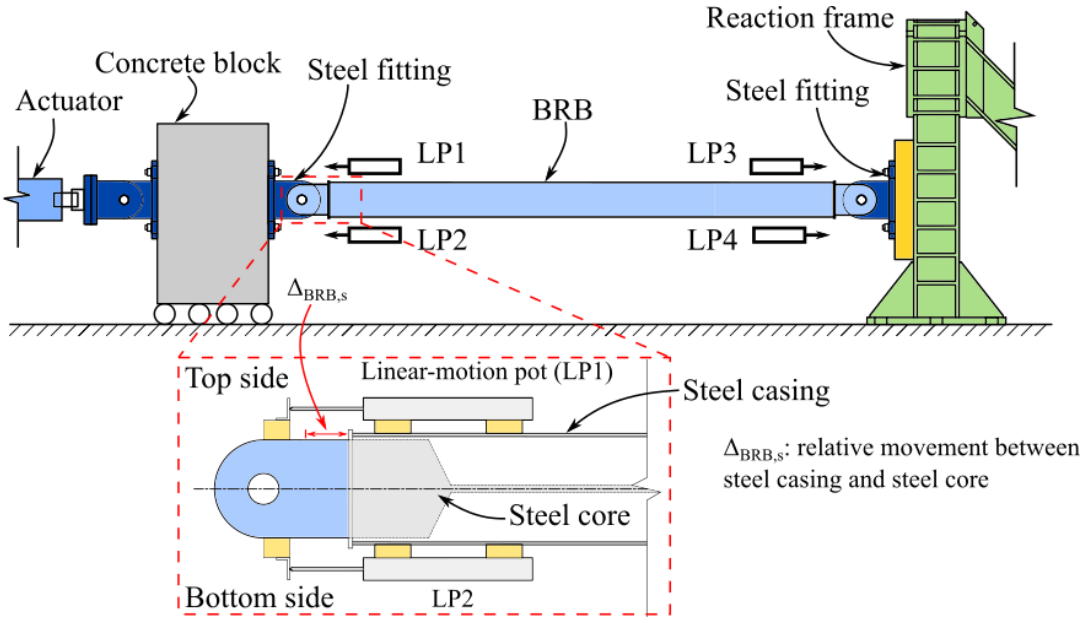

Figure 3.16 Instrument layout of BRB component tests

3.3 Experimental results

3.3.1 Component responses in S-D and S-S specimens

In S-D, a small number of dowels experienced minor bending deformations as shown in Figure 3.17a. In both the top and bottom connections, some holes in the gusset plates had minor crushing under the dowel bearing loads, as shown in Figure 3.17b. In S-S, slight bending deformations at the edge of the gusset plates were observed in the top connection as shown in Figure 3.18 when the load exceeded the design load. After the tests, STS were removed from the screwed connections and no visible damage was observed. Both specimens had residual drifts due to the residual deformations of the BRBs as shown in Figure 3.19. All the glulam members were well protected and no damage was observed in the glulam beams and columns.

a) Dowel bending

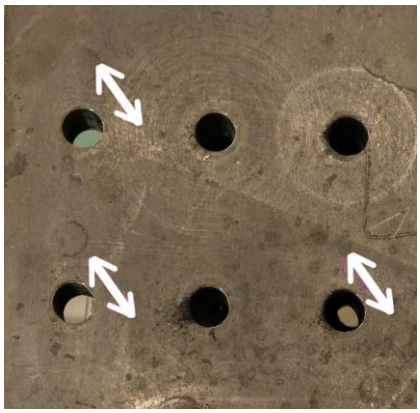

b) Oval holes in the gusset plate

Figure 3.17 Damage of connection for S-D

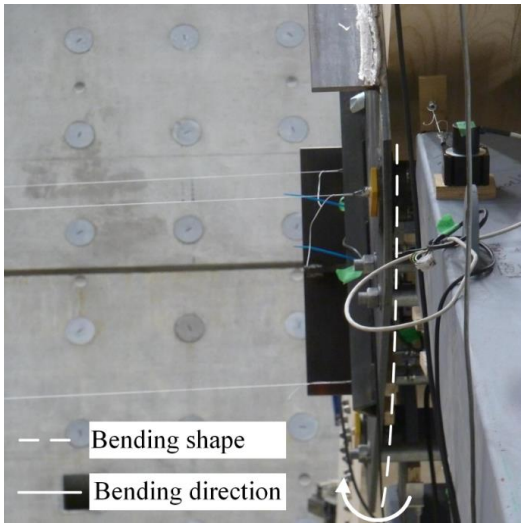

Figure 3.18 Gusset plate bending deformation in S-S

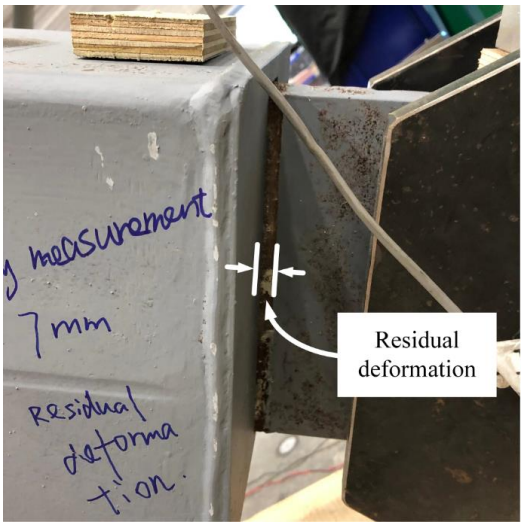

Figure 3.19 BRB's residual deformation

3.3.2 Load-drift hysteresis curves of BRBGF specimens

In tests T1 and T3, both specimens were loaded to a 1.5% drift ratio. The hysteresis curves and their backbone curves are shown in Figure 3.20. The drift was the inter-storey drift by removing the displacement of SP2 from that of SP1 shown in Figure 3.13a.

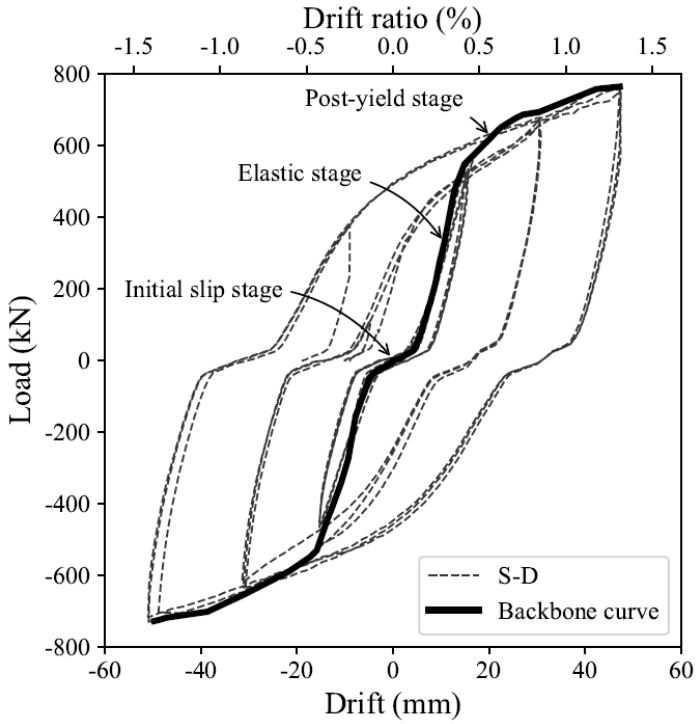

a) S-D (test T1) hysteresis curve and backbone curve

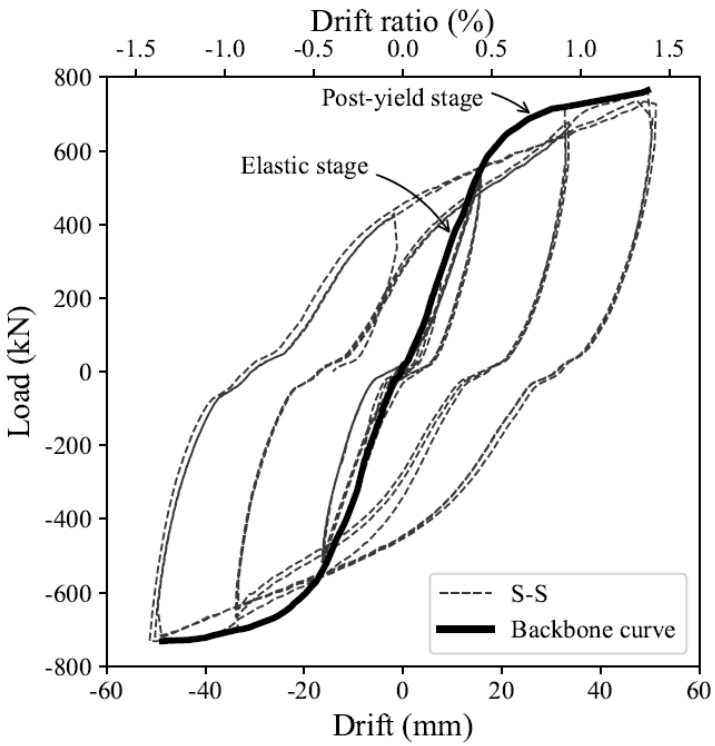

b) S-S (test T3) hysteresis curve and backbone curve

Figure 3.20 Hysteresis curves and backbone curves

Figure 3.20a shows that S-D experienced three stages: initial slip stage, elastic stage and post-yield stage. At first, the initial stiffness was low when the drift was within ±4.5 mm. The initial slips were primarily attributable to three factors: 1) the holes in the BRBs for the pinned connections were manufactured by plasma cutting and were up to 2 mm oversized. 2) the holes in the gusset plates for the dowels were 1 mm oversized for convenience of installation. 3) the stiffness of the wood embedment around the dowel holes was lower than that of the rest wood (Dorn, 2012). After the initial slip stage, BRBs were fully engaged in carrying the loads and the system became very stiff until BRBs' yielding. The stiffness of S-D decreased gradually when the BRBs started to yield. The maximum residual drift ratio was 0.9% (32.1 mm drift).

Figure 3.20b shows that S-S had similar performance with S-D. The main difference was that S-S had fewer initial slips, which were within ±2.0 mm. This difference was because the inclined STS engaged in the axial direction were tight-fit and stiffer than laterally loaded dowels with similar diameters (Krenn and Schickhofer, 2009). However, the unloading process showed that the slips gradually increased at around zero loads. The increasing slips might be because the slotted holes were oversized (Figure 3.8) and the rotation of beam-column connection caused the slips of washers in the slotted holes. Some washers became loose and gaps were observed between the washers and the screw heads during the testing (Figure 3.21). These STS were not in tension until the washers contacted the gusset plates tightly again. The maximum residual drift ratio was also about 0.9% (31.5 mm drift).

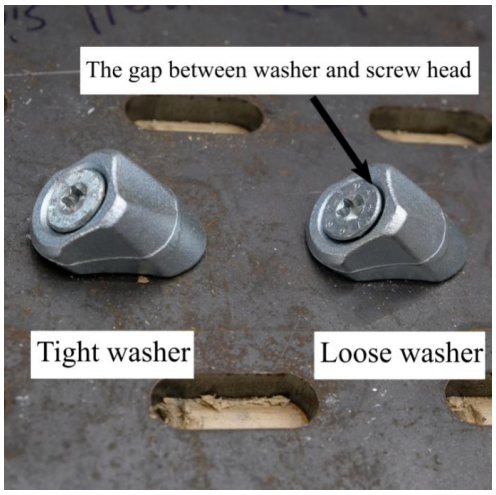

Figure 3.21 Tight washer and loose washer

The maximum strength of both specimens is listed in Table 3.7. Popovski et al. (2003) conducted shake table tests on glulam frames braced by diagonal braces (cross-section 130×152 mm) and bolted connections. The maximum lateral strength was 79.8 kN only. Xiong and Liu (2016) tested two 4110 mm wide and 2740 mm high glulam frames with inverted-V glulam braces (cross-section 135×105 mm) and bolted connections under cyclic loading. The maximum strength was only 129.5 kN and 128.1 kN, respectively. In this study, the tested two BRBGF specimens had much higher capacity by integrating BRBs. Thus this hybrid system

has the potential to be applied in mid-rise or high-rise buildings as the LFRS to provide much higher lateral resistance.

Table 3.7 Strength, stiffness and ductility properties of two BRBGF specimens

Property	S-D			S-S		
	Positive	Negative	Mean	Positive	Negative	Mean
Maximum strength F_{max} (kN)	763.5	729.9	*746.7*	764.4	731.8	*748.1*
Maximum drift δ_{max} (mm)	47.4	51.0	*49.2*	51.3	51.3	*51.3*
Yield strength F_y (kN) (CEN)	595.6	539.6	*567.6*	626.5	593.1	*609.8*
Yield drift $\delta_{y,s}$ (mm) (CEN)	15.5	14.7	*15.1*	16.9	16.2	*16.6*
SLS stiffness k_{SLS} (kN/mm)	32.0	35.4	*33.7*	34.7	35.2	*35.0*
Elastic stiffness k_{el} (kN/mm)	55.2	53.2	*54.2*	38.7	40.4	*39.5*
Plastic stiffness k_{pl} (kN/mm)	6.0	5.6	*5.8*	4.5	5.1	*4.8*
Initial slip δ_s (mm)	4.7	4.5	*4.6*	0.7	1.6	*1.2*
Ductility factor μ (CEN)	3.1	3.5	*3.3*	3.0	3.1	*3.1*

The SLS stiffness k_{SLS} is defined as the secant stiffness at 1/300 drift ratio according to New Zealand engineering practice (Hashemi et al., 2020) and past research on non-structural elements (Galambos and Ellingwood, 1986; Griffis, 1993). The backbone curves had two well-defined linear parts, and their tangent stiffness values were defined as elastic stiffness k_{el} and plastic stiffness k_{pl} to calculate the yield strength F_y and yield drift $\delta_{y,s}$ as per EN 12512 (British Standard Institution (BSI), 2002). It is noted that $\delta_{y,s}$ included the initial slip δ_s. The three stiffness values are listed in Table 3.7. Although S-D had larger initial slips than S-S, it achieved higher k_{el} than S-S when the dowels were fully engaged. Because of this, k_{SLS} of S-S was only slightly higher than that of S-D. It illustrated that when the lateral load was lower than the SLS load, S-S would be stiffer and had less drift when compared with S-D, while S-D and S-S would have similar drift responses when the lateral load was higher than the SLS load.

Furthermore, the tangent stiffness of the backbone curves is shown in Figure 3.22. The stiffness decreased significantly after BRB yielding, which was quite different from the BRB frames with moment-resisting connections. For example, the test results from Jia et al. (2014) showed BRB composite frame's tangent stiffness decreased gradually but still kept more than 20% of initial stiffness until failure. The stiffness results illustrated that the beam-column connections were closer to pinned connections, which could help to reduce the frame action and avoid early failure of the frames (Palmer et al., 2014).

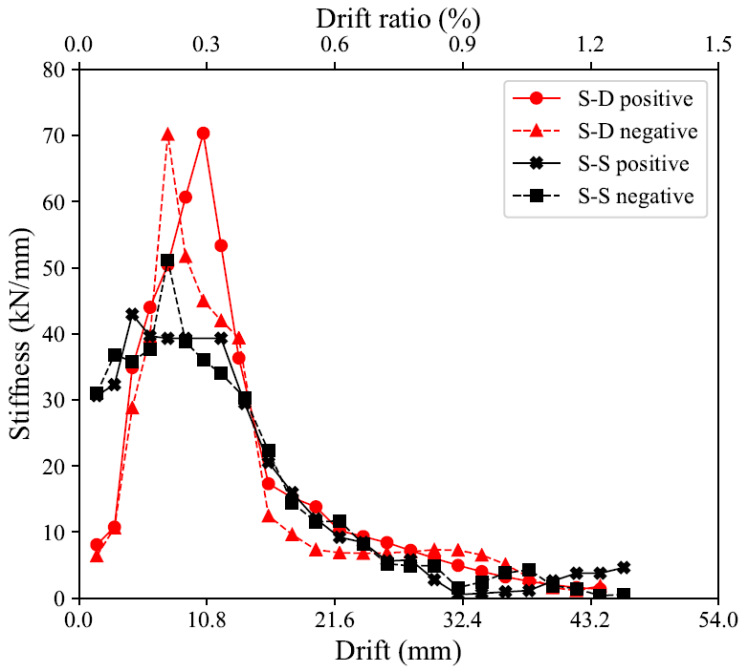

Figure 3.22 Stiffness degradation of backbone curves

3.3.3 Energy dissipation and ductility

The ductility factor μ is usually defined by Eq. 3.10, which is the ratio between the ultimate displacement δ_u and the yield displacement $\delta_{y,s}$. δ_u is typically defined as the displacement at which the load drops to 80% of the peak load. In the BRBGF testing, because no apparent failure or load decrease was observed, $\delta_u=\delta_{max}$ was used to calculate μ and δ_{max} is the maximum drift at the peak load. There are different methods to define $\delta_{y,s}$. The CEN method in EN 12512 (2002) obtains reasonable $\delta_{y,s}$ for systems with an elevated initial stiffness (Munoz et al., 2008), so it was used in this study to calculate $\delta_{y,s}$ and μ as listed in Table 3.7. The EEEP method in ASTM E2126 (American Society for Testing and Materials, 2011) tends to overestimate yield strength and may lead to a misclassification of systems (Munoz et al., 2008). Nevertheless, EEEP-based μ was still calculated to compare with test results of traditional timber-braced frames from Xiong and Liu (2016). Based on the EEEP method, the ductility factors of the BRBGFs were 2.3-2.8, which was more than double that of the traditional timber-braced frames (1.0-1.2). It should also be noted that the derived ductility from this study was the minimum ductility the hybrid system could achieve because the post-peak ultimate displacement was not reached.

$$\mu = \frac{\delta_u}{\delta_{y,s}} \qquad \text{Eq. 3.10}$$

Figure 3.23 shows the accumulated energy dissipation of two BRBGF specimens. The energy dissipation started to increase significantly after BRBs' yielding at cycle 9. In total, S-D and S-S dissipated 289 kJ and 304 kJ in 14 cycles, respectively. The full hysteresis curves and accumulated energy dissipation showed high energy dissipation capacity.

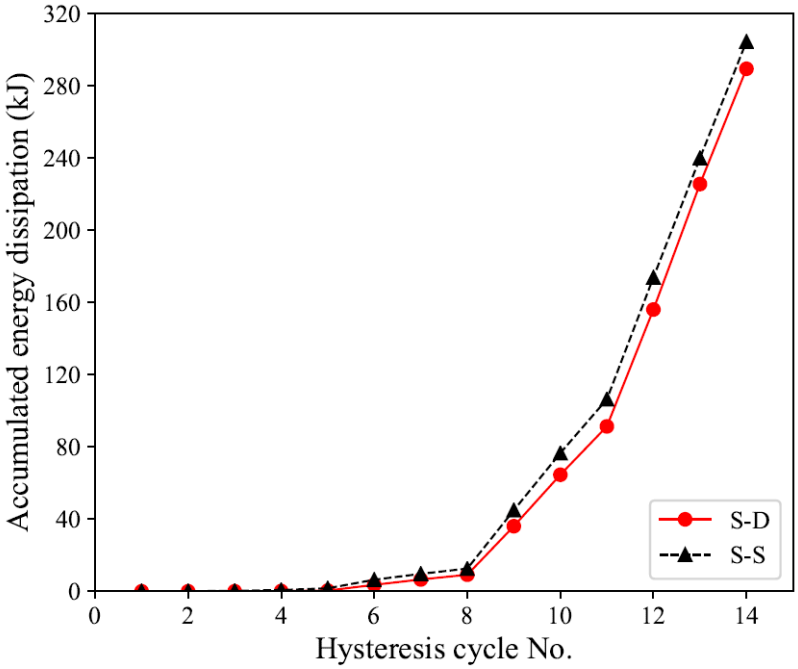

Figure 3.23 Energy dissipation capacity of two specimens

3.3.4 BRB component tests

Figure 3.24 shows the hysteresis curves of the three BRBs and the maximum displacement was slightly smaller than the loading protocol value (54 mm) shown in Figure 3.12 after the slips at pin holes on both ends of BRBs were removed. Their strength at similar displacements was compared and listed in Table 3.8. The BRB strength properties were consistent with a coefficient of variation (COV) of less than 5%.

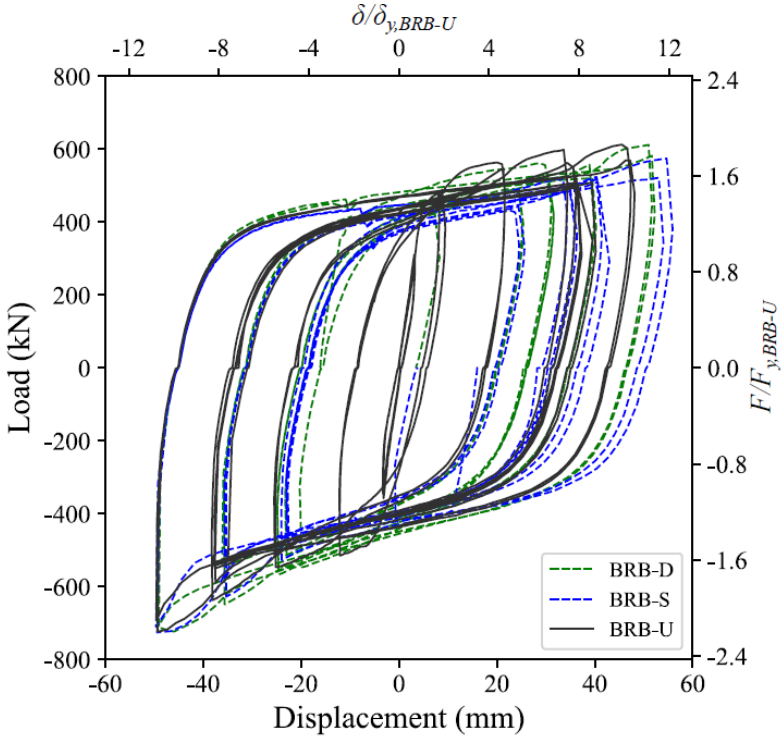

Figure 3.24 BRB hysteresis curves

Table 3.8 BRB strength comparison

Specimen	Displacement (mm)		Strength (kN)	
	Tension	Compression	Tension	Compression
BRB-D	49.3	49.3	568.3	709.0
BRB-S	49.6	49.6	563.1	710.0
BRB-U	48.1	49.6	612.7	723.1
Maximum of COV			4.7%	1.1%

The BRBs were stronger than the specification ($\phi_m R_{k,BRB}$=302 kN) as shown in Figure 3.24. To investigate the reasons, coupon tests were first conducted as shown in Figure 3.25 by using the offcut from the steel core of BRBs after the BRB component tests. The actual yield strength $f_{ys,act}$ from the coupon tests was 294 MPa with ϕ_m =1.25, which was slightly higher than the specified ϕ_m (=1.15) in AISC 341-16 (2016b). The actual yield strength of BRB-U $F_{y,BRB-U}$ and yield displacement of BRB-U $\delta_{y,BRB-U}$ were 329.3 kN and 4.6 mm calculated by Eq. 3.11 and Eq. 3.12, respectively, based on the research by Tsai and Hsiao (2008) and the geometry listed in Table 3.2. The accumulated ductility of BRB-U was 321, which met the minimum accumulated ductility requirement (=200) in AISC 341-16 (2016b). However, ω and β were 1.86 and 1.18, respectively. The BRB overstrength factor $\gamma_{os,BRB}$ (=ωβ) was 46% higher than the specification (1.5). The significantly higher $\gamma_{os,BRB}$ caused that the actuator reached its loading capacity before two BRBGF specimens were loaded to the planned 2.0% drift ratio in the frame tests.

$$F_{y,BRB-U} = f_{ys.act} A_c \qquad \text{Eq. 3.11}$$

$$\delta_{y,BRB-U} = \frac{F_{y,BRB-U}}{K_{eff,BRB}} \qquad \text{Eq. 3.12a}$$

with

$$K_{eff,BRB} = E_{s,BRB} \frac{A_c A_{tr} A_e}{A_c A_{tr} l_e + A_c A_e l_{tr} + A_{tr} A_e l_c} \qquad \text{Eq. 3.12b}$$

To further understand the reasons that caused the significantly higher $\gamma_{os,BRB}$, one BRB specimen was cut open, as shown in Figure 3.26. It was found that the unbonding materials were stuck on the steel core tightly with narrow gaps. The higher $\gamma_{os,BRB}$ in compression could be caused by the inappropriate size of the gaps surrounding the steel core. The steel core did not have sufficient space to expand under compression and the steel core was stuck in the concrete casing (Sitler and Takeuchi, 2021; Zsarnoczay, 2013), which caused high friction as shown in Figure 3.27. The tests from Zsarnoczay (2013) also showed that BRBs with low capacity were more sensitive to the size of the gaps. This issue can be avoided by proper detailing and quality control of BRBs.

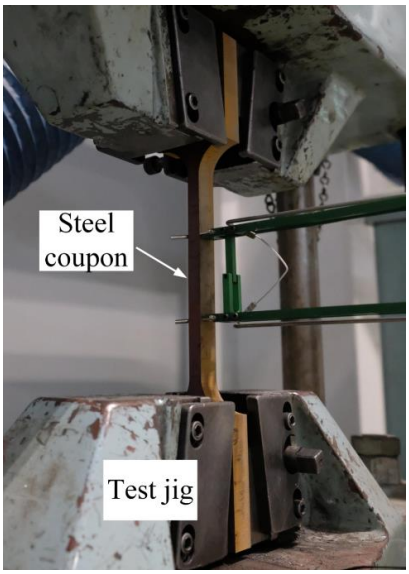

Figure 3.25 Steel coupon test

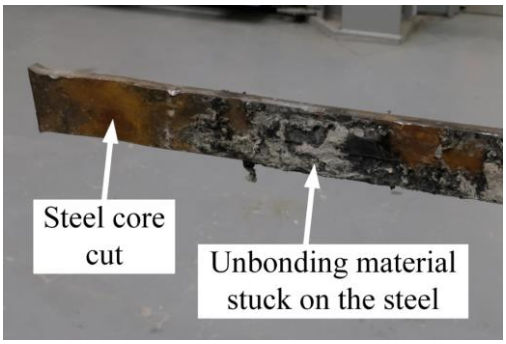

Figure 3.26 Steel core cut open

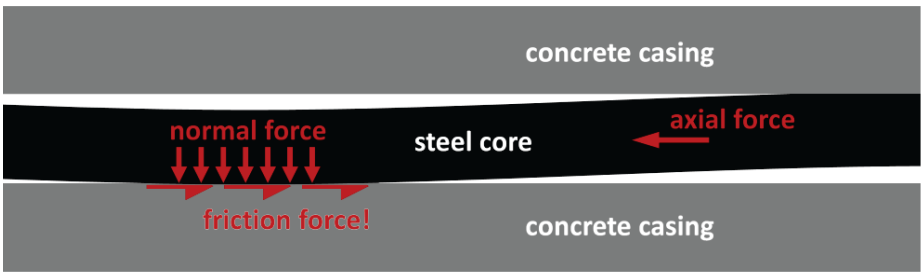

Figure 3.27 Friction induced by flexural buckling of the steel core (Zsarnoczay, 2013)

The theoretical value of the initial stiffness of the BRB $K_{eff,BRB}$ was 71 kN/mm according to Eq. 3.12b and the post-yield stiffness was expected to be below 2% of the initial stiffness (Hosford, 2005). However, test results of BRB-U in Figure 3.24 showed that the initial stiffness and post-yield stiffness were 98 kN/mm and 3 kN/mm, respectively. There were several potential reasons for the higher stiffness, and they might also be the reasons for the higher $\gamma_{os,BRB}$ in tension: 1) unbonding materials were stuck on the steel core tightly and transferred some loads to the concrete so the concrete worked as a spring parallel to the steel core; 2) due to inappropriate casting of concrete grout, the spaces on both ends of the BRBs were not sufficient, so the outward movement of steel core pushed concrete against the end cap plate as shown in Figure 3.28; 3) there was out of straightness of the steel core during manufacturing, which required extra forces to straighten the steel core; and 4) there might be a viscoelastic (or load duration) effect as shown in Figure 3.29 even in quasi-static tests. Displacement-controlled ramp loading (e.g. the loading protocol in Figure 3.10 and Figure 3.12) introduced very high acceleration in a short period, so the test might unintentionally introduce a short duration of high-velocity loading at the beginning of the loading step before yielding and caused an additional viscoelastic force. This viscoelastic force was proportional to the core surface area, so it would be more pronounced for BRBs with a relatively lower capacity (Kasai and Nishizawa, 2010). After yielding of the BRBs, the relative movement was primarily

concentrated on a local area close to the transition zone as shown in Figure 3.30, so the restraints from concrete were reduced. In terms of these potential issues, BRB quality control is essential to ensure that the actual BRB performance is consistent with the design specifications (Macrae and Clifton, 2015). In addition, at least one brace test and one subassemblage test for each batch of BRB products are recommended as per AISC 341-16 (2016b) to ensure that the quality of BRBs meets their performance requirements.

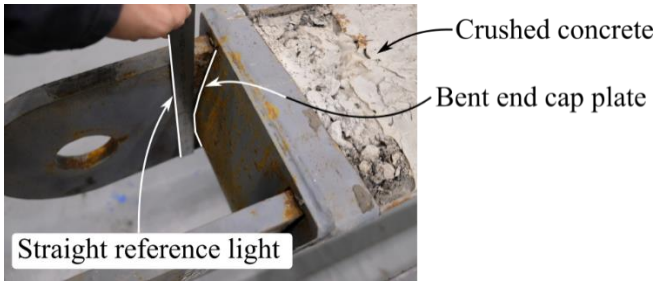

Figure 3.28 End cap plate bending

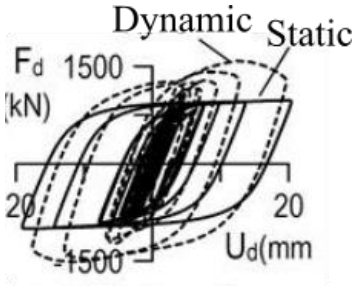

Figure 3.29 Debonding material viscoelastic effect (Kasai and Nishizawa, 2010)

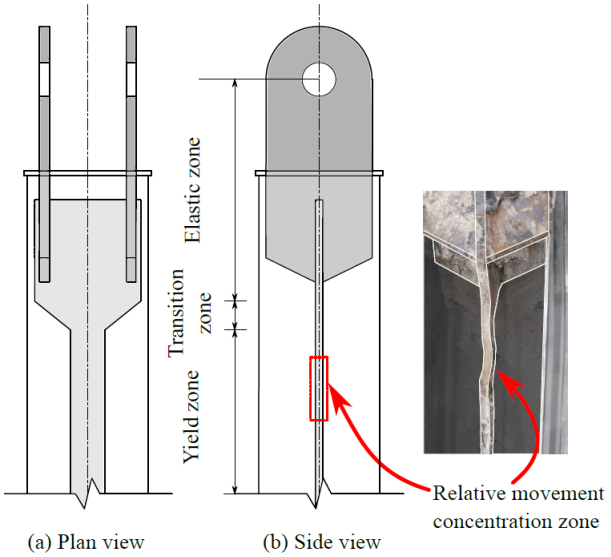

Figure 3.30 BRB movement concentration

3.3.5 Connection behaviour analysis

3.3.5.1 Connection rotational stiffness

In test T1 and T3, the rotation of columns was measured by inclinometers. Two columns in each specimen had similar rotation responses, so the results of the southern column in each specimen are shown in Figure 3.31 as an example. The results illustrated that the top and bottom of columns had co-directional rotation, so the columns carried minimum moments. The top of the column had a slightly larger rotation than the bottom of the column because the column bottom was compacted on the steel brackets and carried a small moment action caused by the force couple (F and F_R) shown in Figure 3.32. According to the rotation-drift relationship

shown in Figure 3.31, the beam-column connections can be approximately considered as pinned connections.

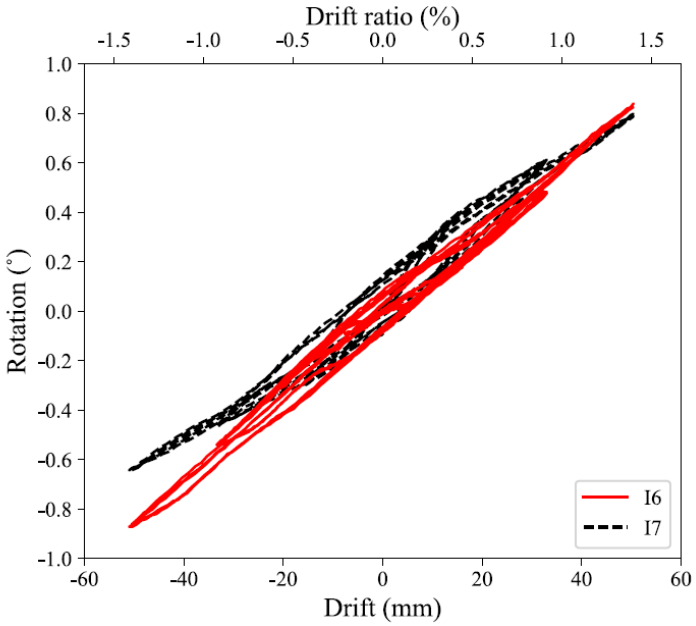

a) S-D

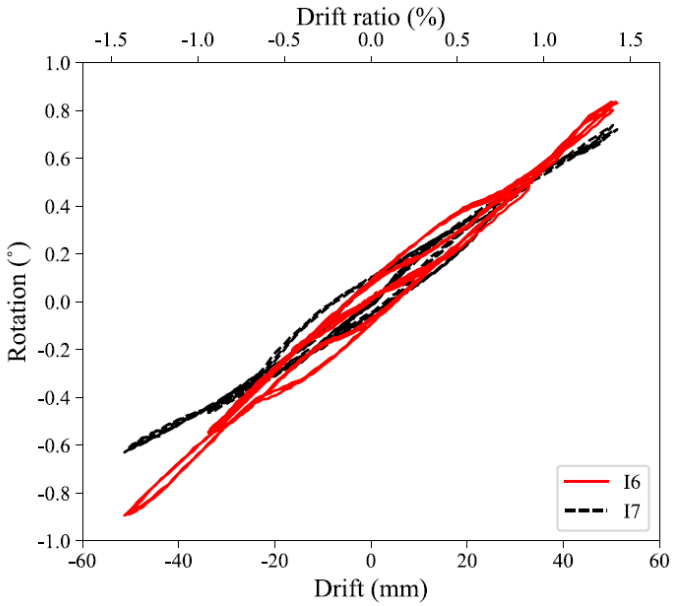

b) S-S

Figure 3.31 The column rotation measured by inclinometers

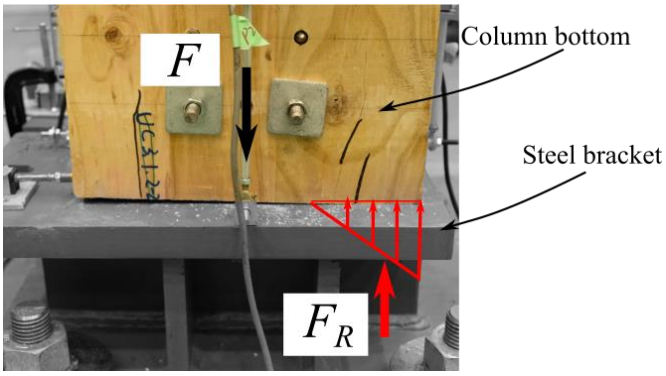

Figure 3.32 Column bottom bearing

In test T2 and T4, two bare frames (S-D and S-S without BRBs) were tested to a 2.0% drift ratio. The hysteresis curves are shown in Figure 3.33. The bare frames carried less than 35 kN lateral load at the 1.5% drift ratio, so the bare frames' contribution to the total capacity of the hybrid system was less than 5% at this drift ratio. Tests of the moment-resisting frames (MRF) with BRBs showed that the MRF could carry 30% to 50% of the total lateral load (Chou et al., 2012). Therefore, the beam-column connections in the BRBGF behaved as pinned connections approximately, which also matched with the BRBGF behaviour discussed above.

The bare frame tests also showed that the beam-column connections had enough flexibility to accommodate a 2.0% drift ratio and the BRB component tests showed that the deformations of the BRBs could also accommodate a 2.0% drift ratio without significant loss of the capacity. Consequently, it would be possible for the BRBGF specimens to achieve a minimum ductility of 4.2 according to the CEN method at the 2.0% drift ratio if $\gamma_{os.BRB}$ could be well controlled.

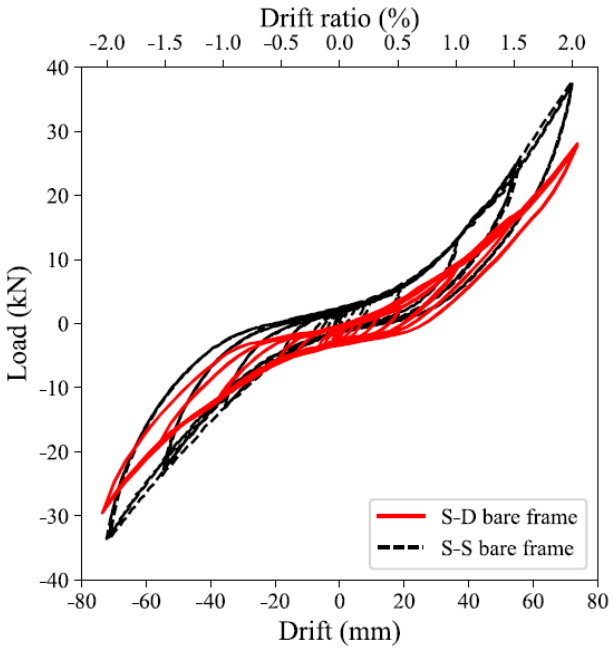

Figure 3.33 Bare frame hysteresis curves

3.3.5.2 Top connection behaviour

PTT well captured the top connections' relative movement between the gusset plate and the glulam members. Figure 3.34a shows the layout of the top connection in S-D. The movement of a group of 24 dowels was tracked by PTT. All the dowels (A1-C8) had similar movement. Figure 3.35a illustrates the load-displacement relationship of the top connection in S-D. Table 3.9 lists its movement in the *x* and *y* direction shown in Figure 3.34a. The horizontal movement was the connection movement in the *x* direction and the load was estimated as 95% of the actuator's load in terms of that the load carried by the bare frame was less than 5%. Figure 3.35a shows that the dowelled connection had low initial stiffness but the stiffness increased significantly after a small displacement. The low initial stiffness could be caused by 1) the holes in the gusset plates for the dowels were 1 mm oversized for convenience of installation; and 2) the wood embedment stiffness around the dowel holes was lower than that of the rest part (Dorn, 2012). The design strength listed in Table 3.5 is plotted in Figure 3.35a as well. At the design strength, the stiffness of the top connection started to round off. Because the stiffness of the connection is essential to engage BRBs efficiently, the connection limit state was considered to be reached at this design strength. Therefore, Eurocode 5 (2004) provided a reasonable prediction for the strength of the dowelled connections.

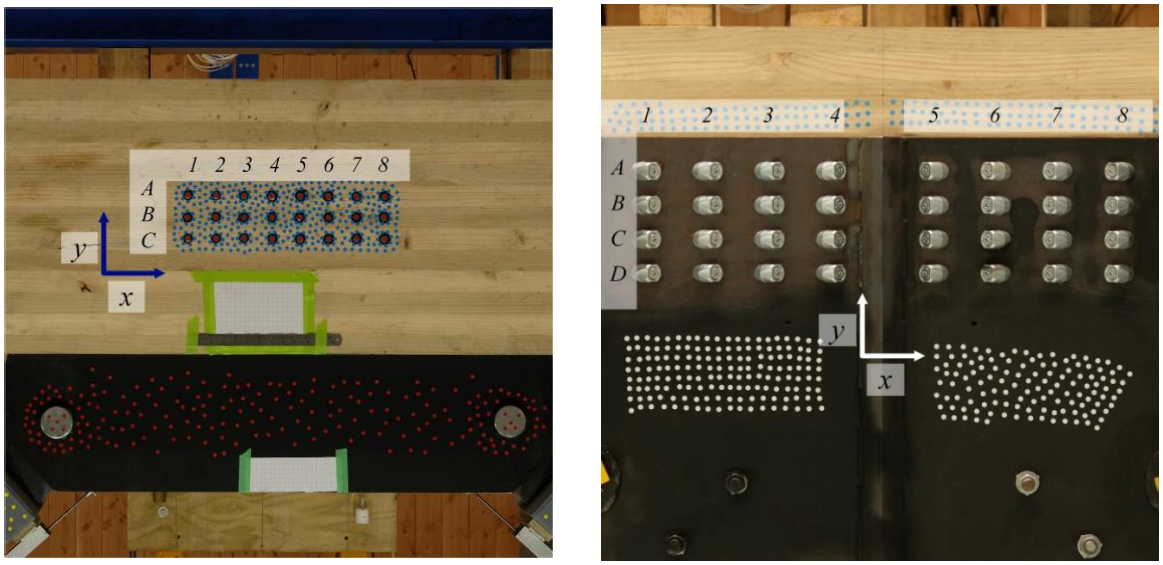

a) The dowelled connection b) The screwed connection

Figure 3.34 Top connection details in S-D and S-S

Table 3.9 Top connection movement (mm)

Connection	Magnitude in the *x* direction	Magnitude in the *y* direction
The dowelled connection	+2.2/-2.6	+0.7/-1.1
The screwed connection	+2.5/-2.2	+1.1/-2.9

The predicted stiffness at SLS k_{ser} and ULS k_u for the dowelled connections were calculated by Eq. 3.13 and Eq. 3.14 as per Eurocode 5 (2004). The actual stiffness at SLS from the tests was defined as the slope of the load-slip curve between $0.1F_{max}$ and $0.4F_{max}$ according

to EN12512 (2002), where F_{max} is the maximum load reached in the tests. The actual stiffness at ULS was defined as the secant stiffness at 70% of F_{max} (Ehlbeck and Larsen, 1993). The stiffness results are listed in Table 3.10 and plotted in Figure 3.35a. The actual stiffness values listed in Table 3.10 were the average value of positive and negative backbone curves. It was found that the actual stiffness did not decrease significantly at ULS when compared to that of SLS (502 kN/mm versus 473 kN/mm with a 6% difference). In addition, the connection movement was small (within ±3mm) as listed in Table 3.9. Therefore, the dowelled connections were stiff enough to engage BRBs. However, the predicted stiffness was significantly higher than the test values. Similar observations were reported by Sandhaas and van de Kuilen (2017), Rahim (2019) and Brown and Li (2021). The stiffness prediction requires further investigation and will be further discussed in Chapter 4.

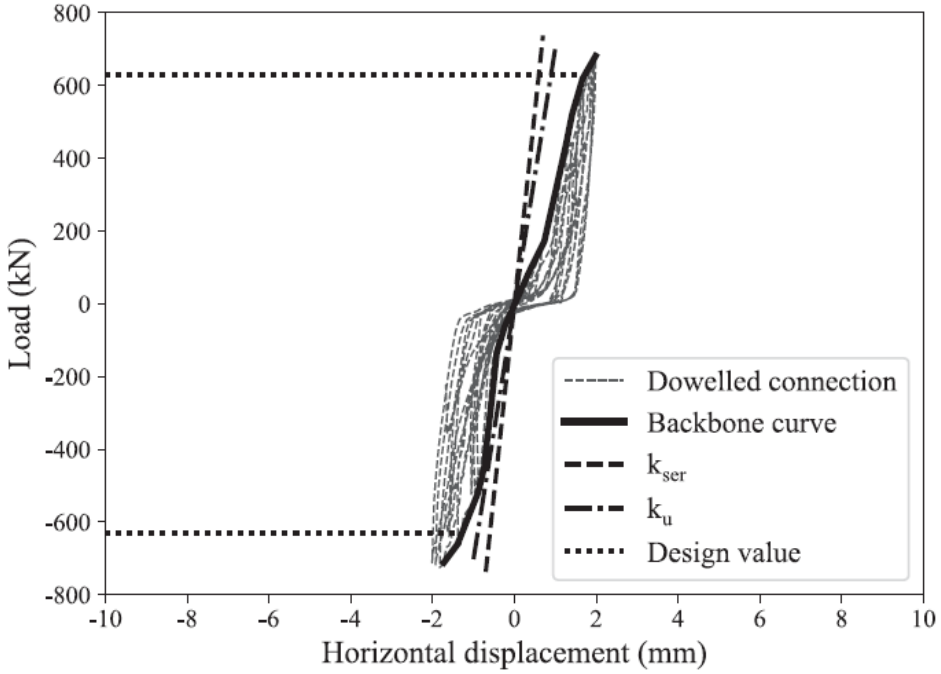

a) S-D

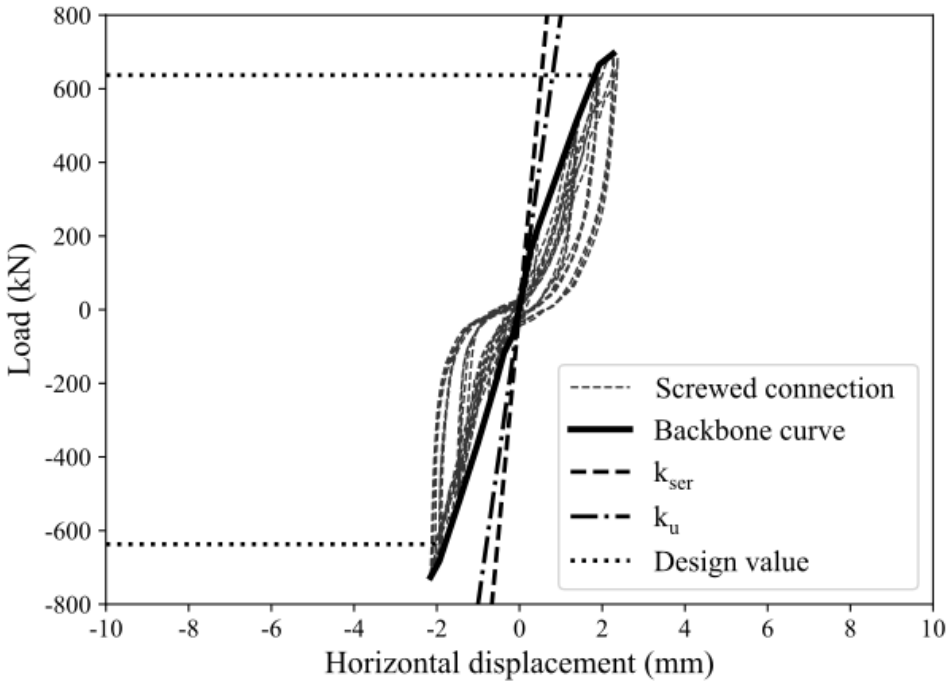

b) S-S

Figure 3.35 Load–displacement relationships in the top connections of S-D and S-S

$$k_{ser} = \lambda_m n_{sp} n_f \rho_m^{1.5} \frac{d}{23} \quad \text{Eq. 3.13}$$

$$k_u = \frac{2}{3} k_{ser} \quad \text{Eq. 3.14}$$

where, $\lambda_m = 2$ is the modification factor for timber-to-steel connection;

n_{sp} is the number of shear planes;

n_f is the number of fasteners;

ρ_m (= 466 kg/m^3) is the mean timber density; and

d is the diameter of fasteners.

Table 3.10 Top connection stiffness (kN/mm)

Stiffness	S-D		S-S	
	k_{ser}	k_u	k_{ser}	k_u
Predicted value	1007	672	1198	798
Actual value	502	473	371	366

Similarly, Figure 3.34b shows the layout of the top connection in S-S. The 16 STS on the left (A1-D4 in Figure 3.34b) all had similar movement, and the 16 STS on the right (A5-D8) had symmetric movement with the 16 STS on the left. The load-displacement relationship of the left group is shown in Figure 3.35b. The screwed connections did not have the low initial stiffness observed in the dowelled connections due to the tight fit of STS installation. The

backbone curve was almost linear without stiffness degradation. Moreover, the strength prediction in Eurocode 5 (2004) was conservative. The conservative prediction might be partially due to the factor that the additional contribution from friction was not considered. Previous research, however, showed that the friction contribution could increase the strength by at least 25% (Krenn and Schickhofer, 2009).

The predicted stiffness k_{ser} for the screwed connections was calculated by Eq. 3.15 based on past research by Tomasi et al. (2010). The predicted stiffness and the actual stiffness from tests are listed in Table 3.10 and plotted in Figure 3.35b. It was found that the actual stiffness almost kept the same during the tests (371 kN/mm at SLS versus 366 kN/mm at ULS with a 1% difference). Although the stiffness of the screwed connections was lower than that of the dowelled connections, the movement of the screwed connections was also within ±3mm as shown in Table 3.9. Therefore, the screwed connections had similar stiffness performance with the dowelled connections at the design load level. It was also noticed from Table 3.10 and Figure 3.35b that the predicted stiffness of the screwed connections was significantly higher than the test values. The stiffness prediction for the screwed connections requires further investigation and will be further discussed in Chapter 4.

$$k_{ser} = n_{sp} n_f \left[k_{\perp} \sin\theta \left(\sin\theta - \mu_f \cos\theta \right) + k_{\parallel} \cos\theta \left(\cos\theta + \mu_f \sin\theta \right) \right] \quad \text{Eq. 3.15a}$$

with

$$k_{\perp} = k_{ser,lat} = 2\rho_m^{1.5} \frac{d_{ef}}{23} \quad \text{Eq. 3.15b}$$

$$k_{\parallel} = k_{ser,ax,\theta,2} = 25 d l_{ef} \quad \text{Eq. 3.15c}$$

where $k_{\perp}$ is the SLS stiffness perpendicular to STS axis as per Eurocode 5 (2004);

$k_{\parallel}$ is the SLS stiffness parallel to STS as per ETA 11/0030 (2019);

θ is the angle between STS axis and timber grain;

μ_f is the frictional coefficient at the timber-steel interface, assumed to be zero according to ETA 11/0030 (2019);

d_{ef} (=7.3 mm) is the effective diameter of STS; and

d (=11 mm) is the outer diameter of STS.

3.3.5.3 Bottom connection behaviour

The bottom connections' relative movement between the gusset plates and glulam members was also well captured by PTT. Figure 3.36 shows the layout of one bottom connection in S-D and S-S, respectively. The load transferred from the BRBs into the bottom connections could not be estimated accurately. It was because the two BRBs carried the lateral load together and loaded in compression and tension, respectively. BRB performance under compressive and tensile loads was different due to the incomplete unbonding and friction (Saxey and Daniels, 2014; Sitler and Takeuchi, 2021), so the load distribution between the two

BRBs was hard to estimate accurately. Therefore, only the connection movement in the bottom connections is listed in Table 3.11 where BC-B represents the bottom connection on the beam side and BC-C represents the bottom connection on the column side. Table 3.11 shows similar displacement magnitudes for the bottom connections compared with the top connections. Thus, the bottom connections should have comparable strength and stiffness to the top connections. However, it was noticed that BC-C in both S-D and S-S had larger movement in the direction perpendicular to timber grain when compared with the top connections. This difference illustrated that the horizontal loads were partially transferred to the columns. For the dowelled connections, the horizontal loads to the columns did not have a significant influence because the connection load capacity perpendicular to timber grain was much higher than the potential horizontal load transferred to the column (Dong and Li, 2019). For the screwed connections, the horizontal loads could cause extra slips of washers in the screwed connections because the STS had a very low capacity to resist the horizontal loads. The horizontal loads could loosen the STS and washers, and thus increase the slips at the unloading stage. Some lateral STS installed 90° to the timber surface and gusset plate surface are recommended to resist the horizontal loads in BC-C, or the washers should be fixed on the steel plate by welding to minimize the slips.

a) The dowelled connection b) The screwed connection

Figure 3.36 Bottom connection details in S-D and S-S

Table 3.11 Bottom connection movement (unit: mm)

Connection	Position	Magnitude in the *x* direction	Magnitude in the *y* direction
The dowelled connection	BC-B	+1.4/-2.0	+0.9/-0.6
	BC-C	+1.8/-1.5	+1.8/-2.5
The screwed connection	BC-B	+1.5/-1.7	+1.1/-1.2
	BC-C	+3.2/-3.0	+2.3/-1.8

Although the stiffness predicted by design standards such as Eurocode 5 (2004) overestimated the stiffness significantly, the connections protected by the capacity design were strong and stiff enough to allow BRBs to yield and dissipate energy with small connection deformations. The experimental results showed that the capacity design approach was not only able to protect the non-ductile members but also to ensure enough stiffness of the connections under high load demands. Moreover, the connection behaviour analysis will help the calibration of numerical models in Chapter 4.

3.4 Summary

This chapter presented experimental test results to assess the cyclic performance of two full-scale 8 m wide and 3.6 m high BRBGFs with two different connection options (the dowelled connections and the screwed connections). The capacity design approach was used to design the hybrid system. BRBs were specified as ductile elements, while glulam members and connections were specified as non-ductile elements. The dowelled and screwed connections were used to connect glulam frames with BRBs. A summary of the test results is listed as follows:

1) The BRBGFs had much higher load-carrying capacity when compared with traditional timber-braced frames in literature. The capacity design approach proved to work well for this hybrid frame system. The BRBs performed as ductile elements and provided enhanced ductility and energy dissipation for the glulam frames. The ductility was double when compared with that of traditional timber-braced frames. Non-ductile glulam members and connections were well protected with minor damage after the load exceeded the design values.
2) The dowelled connections and the screwed connections proved to have high strength and stiffness. They were efficient in engaging the BRBs and resisting lateral loads. The BRBGF specimen with the screwed connections (S-S) had smaller initial slips than the BRBGF specimen with the dowelled connections (S-D) when the load was below the SLS load level. However, both BRBGF specimens had comparable performance when the load exceeded the SLS load level because the BRBs governed the system behaviour. Eurocode 5 provided a reasonably accurate strength prediction for the dowelled connections but a conservative prediction for the screwed connections because the frictional contribution to the connection strength was not considered. The stiffness predictions from Eurocode 5 and the ETA reports significantly overestimated the actual stiffness for the dowelled and screwed connections. Further research is required to address these issues.
3) The stiffness of the dowelled connections decreased after reaching their design strength. Therefore, the quality control of BRBs is essential to avoid a higher overstrength factor than the specification. The screwed connections at the bottom had larger slips perpendicular to the timber grain than the dowelled connections due to the rotation of beam-column connections and the inclined loading to the timber grain. To

minimize the slips, Some lateral STS installed 90° to the timber surface and gusset plate surface are recommended to resist the perpendicular-to-grain load or the washers should be fixed on the steel plates by welding.

4) The connection analysis illustrated that Eurocode 5 could not provide a conservative stiffness prediction on the timber connections with multiple fasteners. The influence of connection stiffness on the BRBGF system behaviour should be further studied using numerical modelling or analytical methods.

4 NUMERICAL MODELLING

Large-scale structural testing is expensive and time-consuming and can only study a minimal number of design configurations. Detailed numerical models can provide a more comprehensive understanding of structural behaviour. This chapter presents component-based numerical models to simulate the cyclic behaviour of BRBGFs. The numerical models of the BRBGFs consist of three main components: glulam members, BRBs and BRB-timber interface connections. Their modelling methods will be discussed first. The model will then be validated by the experimental data obtained from Chapter 3. After that, parametric studies will be conducted to investigate the influence of key design variables. This chapter is based on a journal paper (Dong et al., 2021a) published on *Engineering Structures*.

4.1 Modelling of BRB components

In the literature review presented in Chapter 2, various models for BRBs have been developed and the performance of BRBs can be represented well by the proposed models. *Steel4* material model in OpenSees (Mazzoni et al., 2006) is a phenomenon-based model developed from Menegotto-Pinto model (Carreno et al., 2020; Menegotto, 1973). This model has been successfully used to simulate BRB behaviour including asymmetric hardening and its advancement was discussed by Zsarnoczay (2013) when compared with other BRB models. Thus, in this study, the BRB component was represented by *Steel4* in OpenSees with a truss element and a cross-section area of the yield zone (A_c). To consider the extra stiffness outside the yield zone of BRBs, i.e. transition zone and elastic zone, the BRB effective stiffness $K_{eff,BRB}$ defined by Eq. 4.1a was used and a stiffness modification factor (f_{sm} =1.22) as shown in Eq. 4.1b was introduced by Zsarnoczay (2013) to amplify the steel core elastic modulus to effective elastic modulus $E_{eff,BRB}$. Eq. 4.1 also illustrates that f_{sm} is only dependent on the BRB geometry. Because *Steel4* is highly customizable, overfitting becomes a potential issue (Zsarnoczay, 2013) if limited BRB test data are used for parameter calibrations. Only three BRBs were tested uniaxially in our tests according to Subsection 3.2.1, so calibrating parameters of *Steel4* by hysteresis curves of the three BRBs was not enough and might cause the overfitting issue. To avoid this issue, the BRB test calibrations from Zsarnoczay and Vigh (2017) were used except for the yield strength $f_{ys,BRB}$ and the isotropic hardening ratio b_{iso}, because these two parameters should be determined by the properties of the core steel material (Zsarnóczay, 2013). An average $f_{ys,BRB}$ =294MPa and b_{iso} =0.08% were verified by the steel coupon tests and the BRB component tests conducted in Subsection 3.3.4, respectively. The parameters about *Steel4* used in this model are listed in Table 4.1 and more details about *Steel4* calibrations and parameter meanings can be found in the research by Zsarnoczay and Vigh (2017).

$$K_{eff,BRB} = E_{s,BRB}\frac{A_c A_{tr} A_e}{A_c A_{tr} l_e + A_c A_e l_{tr} + A_{tr} A_e l_c} = E_{eff,BRB}\frac{A_c}{l_{wp}} \qquad \text{Eq. 4.1a}$$

with

$$E_{eff,BRB} = f_{sm} E_{s,BRB} \quad \text{Eq. 4.1b}$$

$$l_{wp} = l_e + l_{tr} + l_c \quad \text{Eq. 4.1c}$$

where l_{wp} is the BRB length between work points.

Table 4.1 Parameters for *Steel4*

Parameters	Tension	Compression
Steel properties	A_c = 1120 mm^2 $E_{s,BRB}$ = 206000 MPa	
f_{sm}	1.22	
$E_{eff,BRB}$ (MPa)	$E_{s,BRB}f_{sm}$ = 256200	
$f_{ys,BRB}$ (MPa)	294	
Ultimate strength $f_{u,BRB}$ (MPa)	1.65$f_{ys,BRB}$ = 485	2.4$f_{ys,BRB}$ = 706
Hardening ratio b_k	0.5%	(3-0.5f_A)%
r_1	0.91	0.89
r_2	0.10	0.02
R_0	25.0	
R_u	2.0	
b_i	0.08%	
b_l	0.01%	(0.04-0.007f_A)%
ρ_i	0.25+0.05f_A	
R_i	3.0	
l_{yp}	1.0	
f_A	(A_c/5000)$^{0.5}$	

The BRB component tests in Subsection 3.3.4 showed higher strength, initial stiffness and post-yield stiffness than the theoretical values. The discrepancy was likely to be due to the quality control issues of the BRB manufacturing, which has been discussed in detail in Subsection 3.3.4. All the possible reasons including steel core binding, out-of-straightness of the steel core, restraints from the end cap plates and the viscoelastic effect caused by the quasi-static cyclic loading worked together as a restraint spring parallel to the steel core. After yielding of the BRBs, the relative movement was primarily concentrated on a local zone close to the transition zone as shown in Figure 3.30, so the restraints to the steel core were reduced. Capturing all these effects require 3D detailed BRB models with a large amount of test data. In addition, research on some effects such as the core binding (Sitler and Takeuchi, 2021) has attracted intensive interest and is still ongoing. Because only a limited number of BRBs were tested in this study and the BRBs were supplied by a commercial manufacturer, modelling the

BRBs with detailed models and considering all those effects were not possible and out of scope of the research objectives of this thesis.

To consider the additional restraints for the steel core and to match the experimental behaviour, an elastoplastic spring was added parallel to the BRB with calibrated initial stiffness of 27 kN/mm and post-yield stiffness of 2.7 kN/mm as shown in Figure 4.1. The spring was modelled by *Steel01* material model in OpenSees and its yield displacement was the same as the BRB yielding displacement (4.6 mm) derived from the testing in Figure 3.24. Figure 4.1 shows that the BRB component modelling results matched the experimental results well. The BRB specimen still showed slightly higher unloading stiffness in compression than the model. This was likely because the limited gaps between the steel core and concrete grout restrained the steel core's transverse expansion in compression and the steel core was out of straightness in tension. They caused extra friction and engaged the concrete in both loading directions, as shown in Figure 3.27.

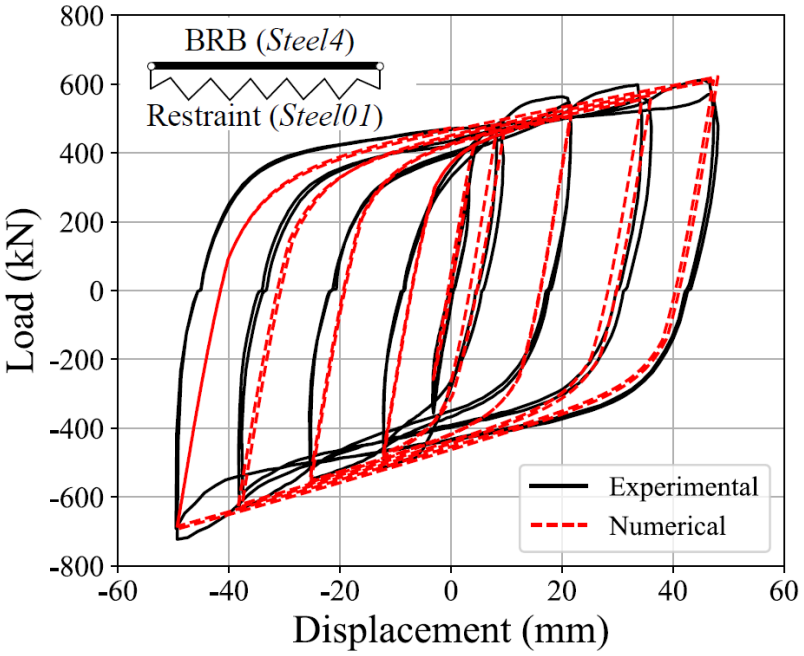

Figure 4.1 Comparison of BRB

4.2 Modelling of BRB-timber interface connections

4.2.1 Modelling of the dowelled connections

Subsection 3.3.5 illustrated that the connection stiffness from the tests was only 50% of the predicted value by Eurocode 5 (2004). One reason was that Eq. 3.13 was highly simplified and only considered the influence of density and dowel diameters. More design parameters such as the number of dowels (Jockwer and Jorissen, 2018) and the slenderness of dowels (Lemaitre et al., 2018) could affect the connection stiffness as well. Another reason could be that using λ_m =2 in Eq. 3.13 for timber-to-steel connections was not appropriate (Izzi et al., 2016). The hole deformations were observed during the tests as shown in Figure 3.17b, which

illustrated that the steel interface was not fully rigid. For the connections with the test layouts, it is suggested to take λ_m as 1 instead of 2 to consider those factors that are not considered in Eurocode 5 (2004), which was also recommended by Wang et al. (2020) and Dong et al. (2021).

The research by Jockwer and Jorissen (2018) showed that stiffness prediction equations from different standards and studies are quite different and most of them are based on the regression of test data. None of them provided a reasonable prediction for the dowelled connections. To estimate the connection stiffness for general dowel layouts more accurately, numerical modelling or analytical methods are needed. One of these methods is the beam-on-foundation (BOF) model based on simple dowel embedment tests. The BOF model was proposed and used to predict the stiffness of timber-to-timber dowel-type connections (Lemaitre et al., 2019; Lemaitre et al., 2018). It was shown that the BOF model improved the prediction accuracy of stiffness. However, for steel-to-timber dowel-type connections, the accuracy of the BOF model requires further verification (Lemaitre et al., 2019).

In this study, the BOF model proposed by Lemaitre et al. (2019) was used to build the dowelled connection model in OpenSees. Figure 4.2 shows the model of dowelled connections and the parameters used in the BOF model are listed in Table 4.2. The timber members and steel plates were assumed to be elastic. Steel plates that transferred the load to the dowels by steel bearing were assumed to be rigid. All non-linearity was from dowel yielding and the timber embedment deformation. The dowels were modelled as elastoplastic beams and the timber embedment behaviour was modelled by a series of non-linear springs. The distance between springs was 4 mm ($<0.4d$, where d is the diameter of fasteners) as suggested by Lemaitre et al. (2019). As shown in Figure 4.3, six glulam embedment tests were conducted in accordance with ASTM D5764 (ASTM standard, 2002) to obtain the compressive load-displacement relationship at the dowel-timber interface. The average curve was used to calibrate the non-linear springs as shown in Figure 4.3b where the vertical coordinate is presented as the equivalent distributed load (N/mm) at unit length along the dowel. The force of each foundation in Figure 4.2 will be the product of the equivalent distributed load and the distance between foundations (i.e. 4 mm). The BOF model results were used as the backbone curves to model the cyclic response of the dowelled connections by *Pinching4* material model in OpenSees. The *Pinching4* model parameters are listed in Table 4.3 and their definitions are shown in Figure 4.4. More details about *Pinching4* can be found in OpenSees documentations (Mazzoni et al., 2006).

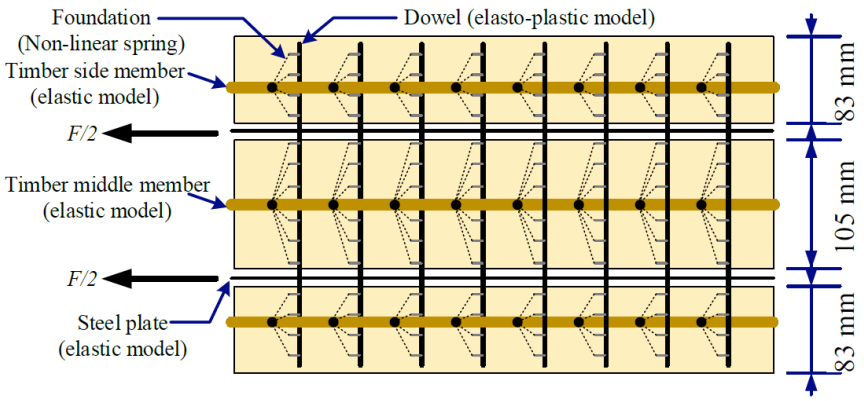

Figure 4.2 Schematics of the BOF model for the dowelled connection

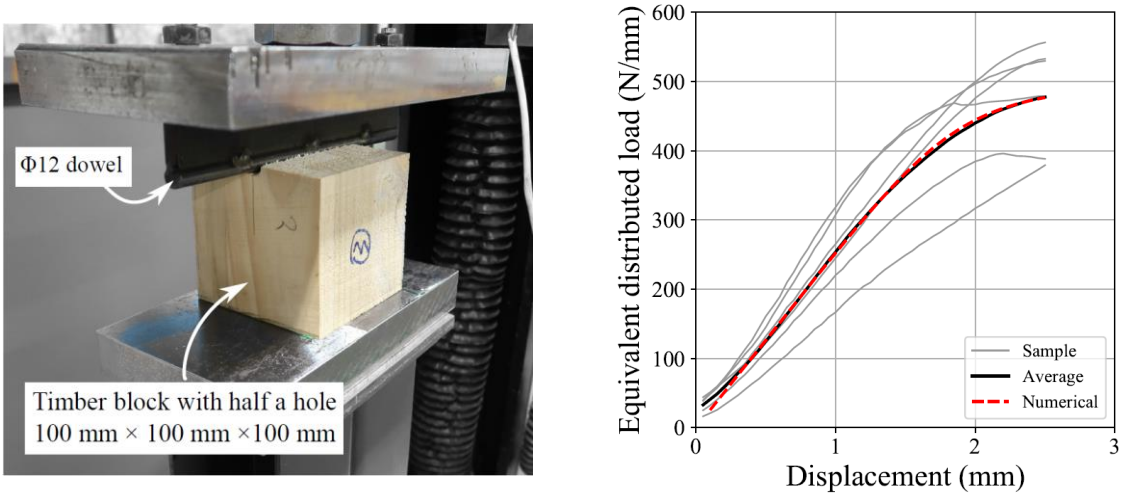

a) Embedment test setup b) Experimental and numerical results

Figure 4.3 Embedment tests and model calibration

Table 4.2 The BOF model parameters for the dowelled connection

Members	Element and materials	Parameters
Timber members	*elasticBeamColumn*	Side member: A_s =585×83 mm^2 E_{GL} =10000 MPa; Middle member: A_m =585×105 mm^2 E_{GL} =10000 MPa;
Steel plates	*elasticBeamColumn*	A_s =120×20 mm$^{2;}$ E_s =210000 MPa;
Steel-steel interface	*EqualDOF*	N/A
Dowels	*dispBeamColumn* with fibre cross-section	f_{ys} =300 MPa; E_s =210000 MPa; d =12 mm;
Timber-steel interface	*ZeroLength* with *Steel02*	Element size =4 mm Yield strength f_{ts} =1964 N; Elastic modulus E_{ts} =1012 N/mm; B =0.01; R =6.0; r_1 =0.925; r_2 =0.15.

Note: the parameter definition follows OpenSees documentations (Mazzoni et al., 2006)

Table 4.3 The cyclic model parameters for the dowelled connection

Material	Parameters
Pinching4	ePd1 =0.01 m, ePf1 =12028 N; ePd2 =0.7 mm, ePf2 =421008 N; ePd3 =2.0 mm; ePf3 =774948 N; ePd4 =3.4 mm. ePf4 =962000 N; rDsipP =0.0, rDispP =0.0, uForceP =-0.05; gKlim = gDlim = gFlim = gE =0.0;
ElasticMultiLinear	-strain: [-2.0 -0.5 0.0 0.5 2.0] (mm) -stress: [-50000000 -6000 0 6000 5000000] (N)

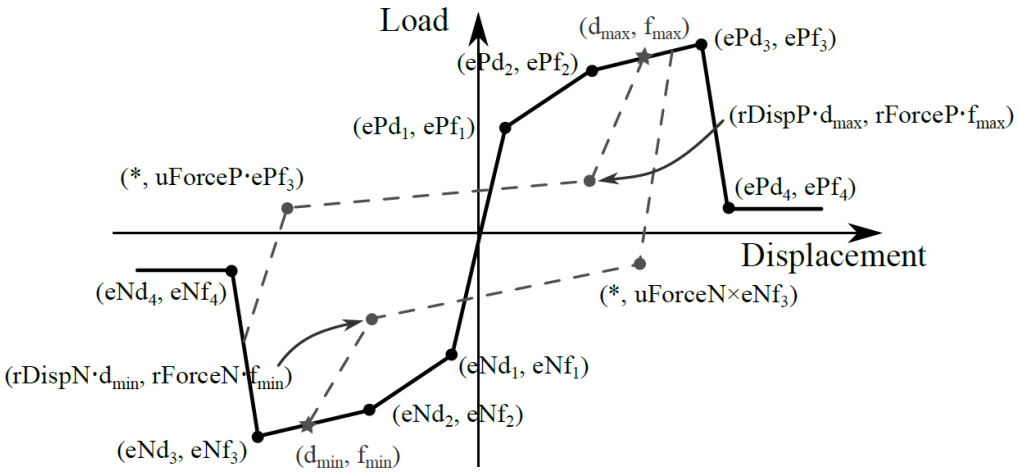

Figure 4.4 *Pinching4* model parameters (Mazzoni et al., 2006)

Because the holes in steel plates are slightly larger than the dowel diameter and the predrilling in timber causes the surrounding area of the holes in timber members softer than the rest part of the timber (Dorn, 2012), initial slips are typically observed on load-displacement curves of dowelled connections. An additional spring with low initial stiffness within ±0.5 mm and very high stiffness beyond ±0.5 mm was implemented by *ElasticMultiLinear* model in OpenSees and placed in series with the *Pinching4* model to capture the actual connection response as shown in Figure 4.5. The range of ±0.5 mm was chosen because the diameter of the holes in the steel plate was 1 mm bigger than the dowels. It was also observed that even in small displacements, there were some permanent bearing deformations and the unloading stiffness was higher than the initial stiffness (Popovski, 2000). The unloading stiffness was considered to be twice the initial stiffness based on the experimental observation. No strength degradation was considered in the model because these connections were protected as non-ductile elements and were not expected to be damaged severely. Figure 4.5 shows that the model predicted the test results conservatively. The asymmetry force response could be due to the asymmetry distribution of the gaps for each dowel. Some dowels might be engaged earlier on one side than the other. In addition, timber defects such as knots could also contribute to the asymmetric performance.

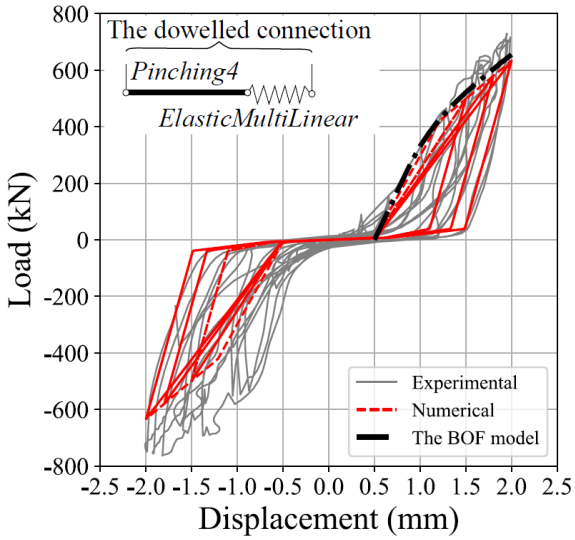

Figure 4.5 Comparison of the dowelled connection

4.2.2 Modelling of the screwed connections

Table 3.10 showed that Eq. 3.15 from Tomasi et al. (2010) and ETA 11/0030 (2019) considerably overestimated the actual stiffness of STS connections by 223% even without considering the frictional effects. Monotonic tests of timber-to-timber connections with inclined STS by Krenn and Schickhofer (2009) showed that the predicted stiffness k_{ser} of 45° inclined STS could be roughly 12 times that of laterally loaded STS installed with 90° angles. Although the Eurocode 5 (2004) tends to over predict $k_{\perp}$ for screwed connections under lateral loads, which is similar to the dowelled connections (Eq. 3.13), $k_{\perp}$ for the screwed connections should be much smaller than $k_{\parallel}$ that is along the screw axial direction (Girhammar et al., 2017). The main reasons for the over-predictions of k_{ser} should come from $k_{\parallel}$ (Eq. 3.15c). The over prediction of $k_{\parallel}$ was because that Eq. 3.15c was highly simplified and $k_{\parallel}$ did not consider the flexibility of STS (Closen, 2012; Mirdad and Chui, 2020) and timber density. The STS flexibility was caused by the free length l_f highlighted in Figure 4.6. The free length l_f was from the oversized slotted holes in the steel plates and the lack of bearing (shank or thread) of STS. The screw shank along the free length l_f had elastic bending deformation under the lateral load. Because STS are slender fasteners, the bending deformations can be comparable to the STS embedment and withdrawal movement. The flexibility of STS was also why the stiffness of the screwed connections was lower than that of the dowelled connections after dowels were fully engaged. In addition, the cyclic loading could increase the bending deformations of STS and gradually reduce the stiffness (Closen, 2012). Furthermore, the over-prediction of stiffness could result from the assumption in Eq. 3.15c that $k_{\parallel}$ is proportional to the effective penetration length l_{ef}. This assumption might be inappropriate, especially for long STS (Blass et al., 2006).

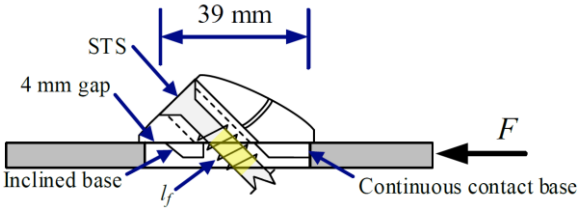

Figure 4.6 STS free length

To overcome the limitation of Eq. 3.15, Girhammar et al. (2017) presented an analytical model for timber-to-timber STS connections that considers the effects of flexibility and extensibility of screws. Mirdad and Chui (2020) proposed another analytical model for TCC floors with inclined STS connections as shear keys and gaps between the timber layer and the concrete topping. These two analytical models were combined in this study to estimate k_{ser} as Eq. 4.2a, where the effective axial withdrawal stiffness per unit area K_{ax} (N/mm^3) and embedment stiffness per unit area K_h (N/mm^3) were based on the STS axial stiffness $k_{ser,ax,\theta}$ and the STS lateral stiffness $k_{ser,lat,\theta}$ as shown in Eq. 4.2f-Eq. 4.2g, respectively. $k_{ser,ax,\theta}$ and $k_{ser,lat,\theta}$ were determined by STS withdrawal tests and embedment tests, respectively.

Compared to the STS embedment tests conducted by Mirdad and Chui (2020), the BRBGF tests used the same type of STS and similar density of timber (466 kg/m^3 versus 419 kg/m^3 from Mirdad and Chui (2020)). Past research also showed that the density of timber members had a minor impact on stiffness (Jockwer and Jorissen, 2018). Thus, K_h =6.52 N/mm^3 from the STS embedment tests by Mirdad and Chui (2020) was used in this study directly. However, K_{ax} from the STS withdrawal tests by Mirdad and Chui (2020) was only for 80 mm and 100 mm long STS. Past research on screwed-in threaded rods indicated that the axial stiffness of the rods was disproportional to the penetration length (Blass and Kruger, 2010). Because of this, K_{ax} from Mirdad and Chui (2020) might not be suitable for 300 mm long STS used in the BRBGF tests. In this regard, monotonic STS withdrawal tests with different embedment lengths were conducted to quantify K_{ax}.

$$k_{ser} = \frac{3E_{STS}I_{STS}d[2(3l_f + 2l_{ef})K_{ax,eq}\pi l_{ef}(cos^2\theta + 0.5\mu_f sin2\theta) + K_{h,eq}l_{ef}^2(sin^2\theta - 0.5\mu_f sin2\theta)]}{6E_{STS}I_{STS}(3l_f + 2l_{ef}) + K_{h,eq}dl_{ef}^2 l_f^3 sin^2\theta} \quad \text{Eq. 4.2a}$$

with

$$K_{ax,eq} = K_{ax}\frac{\tanh(\omega_{ax}l_{ef})}{\omega_{ax}l_{ef}} \quad \text{Eq. 4.2b}$$

$$K_{h,eq} = 2K_h\frac{sinh^2(\lambda_h l_{ef}) - sin^2(\lambda_h l_{ef})}{\omega l[\sinh(\lambda_h l_{ef})\cosh(\lambda_h l_{ef}) - \sin(\lambda_h l_{ef})\cos(\lambda_h l_{ef})]} \quad \text{Eq. 4.2c}$$

$$\omega_{ax} = 2\sqrt{\frac{K_{ax,eq}}{E_{STS}d}} \quad \text{Eq. 4.2d}$$

$$\lambda_h = \sqrt[4]{\frac{K_h d}{E_{STS} I_{STS}}} \quad \text{Eq. 4.2e}$$

$$K_{ax} = \frac{k_{ser,ax,\theta}}{\pi l_{ef} d} \quad \text{Eq. 4.2f}$$

$$K_h = \frac{k_{ser,lat,\theta}}{l_{ef} d} \quad \text{Eq. 4.2g}$$

where d is the diameter of fasteners;

E_{STS} is STS elastic modulus;

$I_{STS} = \pi d^4/64$;

l_f (=12 mm) is the free length of STS;

l_{ef} (=l_{em} -10 mm) is the effective penetration length of STS;

l_{em} (=249 mm) is the penetration length including the screw tip; and

$k_{ser,ax,\theta}$ and $k_{ser,lat,\theta}$ are determined by STS withdrawal tests, respectively.

Figure 4.8 shows the test setup of the withdrawal tests as per EN 1382 (British Standard Institution (BSI), 2016a). Four different penetration lengths were selected and three replicates of the withdrawal tests were conducted for each penetration length (l_{ef}=100 mm, 145 mm, 195 mm and 245 mm). The three replicates are similar to each other, so Figure 4.8a shows one of the load-withdrawal displacement curves for each penetration length as an example. The axial stiffness was determined by the curve fitting of the linear part of load-withdrawal displacement curves. Figure 4.8b shows the axial stiffness test results with the prediction curves of $k_{ser,ax,\theta,1}$ (Eq. 2.2) and $k_{ser,ax,\theta,2}$ (Eq. 2.3 or Eq. 3.15c) because they are two widely used equations for axial stiffness prediction of STS recommended by ETAs. It is illustrated that $k_{ser,ax,\theta,1}$ provided a conservative prediction while $k_{ser,ax,\theta,2}$ overestimated the axial stiffness considerably. This overprediction also proved that $k_{ser,ax,\theta,2}$ from ETA 11/0030 (2019) was not suitable for long STS. Figure 4.8b also shows two power series models $k_{ser,ax,\theta,3}$ and $k_{ser,ax,\theta,4}$ based on the mean value (Eq. 4.3) and 5th-percentile value (Eq. 4.4) of test results calculated by EN 14358 (2016b), respectively. $k_{ser,ax,\theta,3}$ and $k_{ser,ax,\theta,4}$ can be used to estimate K_{ax} in modelling and design of the screwed connections, respectively. It should be noted that although $k_{ser,ax,\theta,1}$ from ETA 11/0190 (2016) provided conservative prediction, Blass et al. (2006) stated that $k_{ser,ax,\theta,1}$ was not applicable outside of their test series and should not be transferred to screws from other manufacturers directly. Therefore, it is recommended that screw manufacturers conduct STS withdrawal tests and provide conservative stiffness equations in the form of $k_{ser,ax,\theta,4}$ for their products in their ETAs. It is also worth mentioning that although the STS products are proprietary products, the analytical model is for a general setup of timber-to-steel connections, so it has the possibility to be extended to estimate the stiffness of STS products from other manufacturers with embedment and withdrawal test data. More tests are required to further investigate how accurate the analytical model will be for different types of STS.

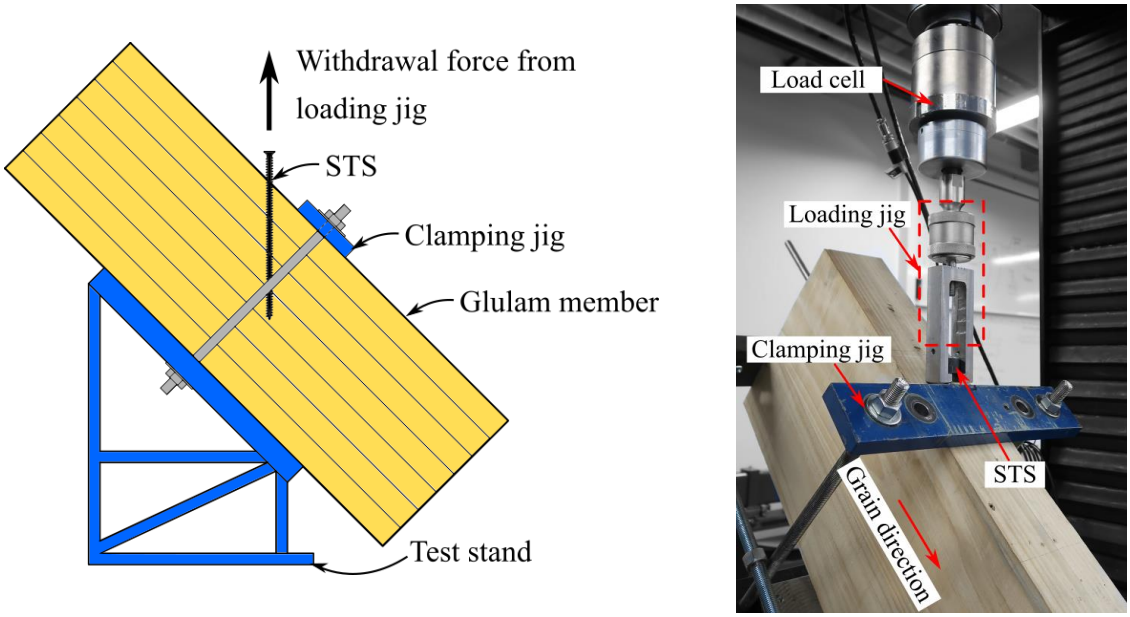

a) Test side view b) Test setup

Figure 4.7 STS withdrawal test setup

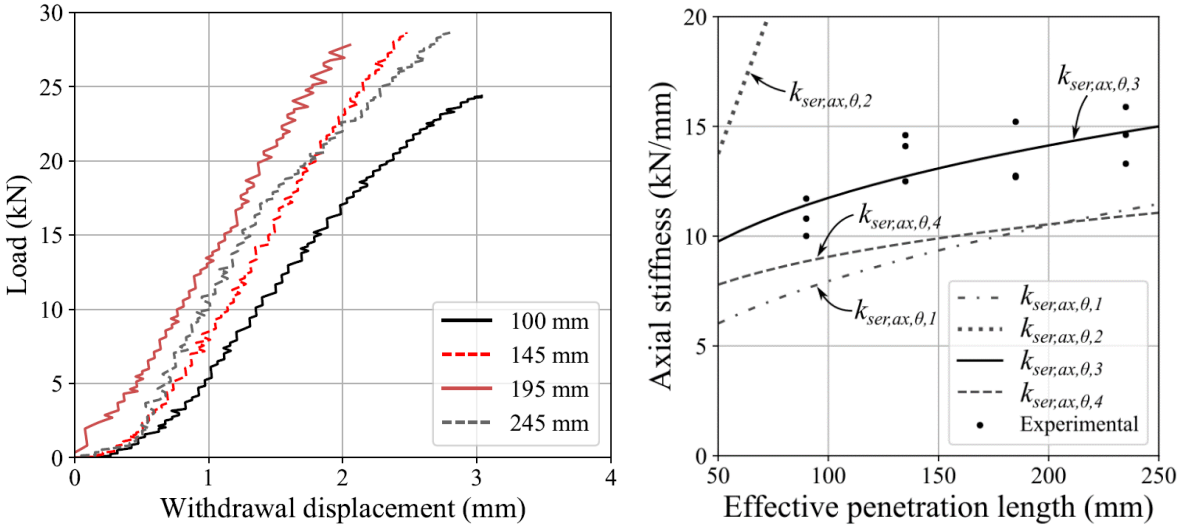

a) Test setup b) Test results and curve fitting

Figure 4.8 STS withdrawal test results

$$k_{ser,ax,\theta,3} = 3433 l_{ef}^{\ 0.267} \text{ for mean value (N/mm)} \quad \text{Eq. 4.3}$$

$$k_{ser,ax,\theta,4} = 3321 l_{ef}^{\ 0.218} \text{ for 5th-percentile value (N/mm)} \quad \text{Eq. 4.4}$$

Based on the withdrawal tests, K_{ax} =1.81 N/mm^3 calculated by Eq. 4.2f and Eq. 4.3 was used to calculate the $k_{ser,SLS}$ in Eq. 4.2a. It should be noted that the K_{ax} obtained from our tests was only 48% of the value (3.82 N/mm^3) reported by Mirdad and Chui (2020). This difference proved that the axial stiffness of STS was disproportional to l_{ef}. Table 4.4 shows that the analytical results underestimated the test results by 18% with a frictional coefficient μ_f=0.25, which was recommended by Krenn and Schickhofer (2009) based on the European practice. The reasons could be: 1) the actual μ_f was higher than 0.25 (Girhammar et al., 2017) (for

example, μ_f =0.45 was reported by Mirdad and Chui (2020)); and 2) the assumption that withdrawal stresses along the length of the STS are evenly distributed was not appropriate. The part of STS deeply embedded into timber might engage less, so the uniform distribution assumption underestimated the K_{ax} close to the timber surface. Because the analytical model provided a reasonably conservative prediction of the stiffness, it was used to model the screwed connection performance in the BRBGFs.

Table 4.4 Stiffness prediction comparison (kN/mm)

μ_f	Analytical model	Experimental*(Dong et al., 2020)	Difference (%)
0.25	303	371	-18
0.45	340	371	-8

*Note: this is for the screwed connection with 32 STS in the top connections in S-S

Because no damage to the screwed connections was observed in the BRBGF tests in Chapter 3 the screwed connection loading stiffness was assumed to be constant. The stiffness prediction with μ_f=0.25 from the analytical model above was input as the loading stiffness for the cyclic model for the screwed connections simulated by *Pinching4* model in OpenSees. The reason for choosing μ_f as 0.25 was that it provided conservative predictions and was recommended by the European practice (Krenn and Schickhofer, 2009). The parameters of *Pinching4* are listed in Table 4.5. The unloading stiffness of the screwed connections was assumed to be three times their loading stiffness based on the test observations to consider the loosening of STS and stiffness degradation under cyclic loading (Closen, 2012). Figure 4.9 shows the comparison between the experimental results and the numerical results for the screwed connection, which presented that the model could represent the performance of the screwed connections.

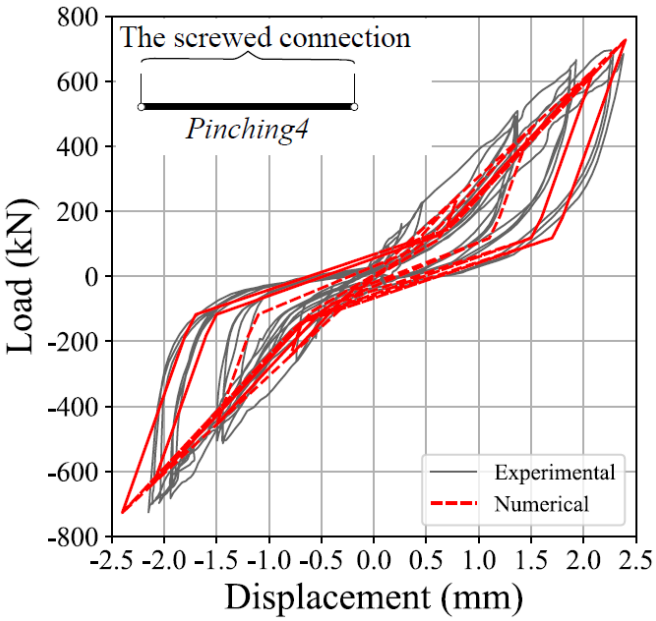

Figure 4.9 Comparison of the screwed connection

Table 4.5 *Pinching4* parameters for the screwed connection

Material	Parameters
Pinching4	ePd1 =0.05 mm, ePf1 =9090 N; ePd2 =2.0 mm, ePf2 =606000 N; ePd3 =4.0 mm; ePf3 =1212000 N; ePd4 =10.0 mm. ePf4 =1333200 N; rDsipP =0.3, rDispP =0.2, uForceP =-0.1; gKlim = gDlim = gFlim = gE =0.0;

4.3 BRBGF model validation

The models of BRBGF specimens with the dowelled connections (S-D) and screwed connections (S-S) were established in OpenSees using the component models as shown in Figure 4.10. The BRBGF tests in Chapter 3 showed that the dowelled connections and the screwed connections had limited moment-resisting capacity, so the beam-column connections were modelled as pinned connections. The BRB-timber interface connections were modelled by elements 1-4 with two overlapped nodes. For each element, the translational stiffness, i.e. the horizontal and vertical connection stiffness, was modelled by the connection models introduced in Subsection 4.2.1 and 4.2.2. The rotational stiffness was neglected due to the limited moment-resisting capacity of the connections. The initial slips in the top connection (element 1) and the bottom connections (elements 2 and 3) were superposed together in the top connection and simulated by the *ElasticMultiLinear* model in OpenSees to simplify the models and improve the model convergence. Figure 4.11 shows the hysteresis curves of the component-based models in comparison with the experimental results. Overall, a good agreement was achieved. The differences between the experimental and the numerical results were primarily from the BRB fit error shown in Figure 4.1 and the maximum force error of experimental tests between the positive and negative loading directions. The accumulated energy dissipated by models was comparable to the test results as shown in Figure 4.12. The models dissipated slightly less energy in cycles No.8-No.11, which might be due to the higher unloading stiffness of the BRBs in the tests as mentioned before.

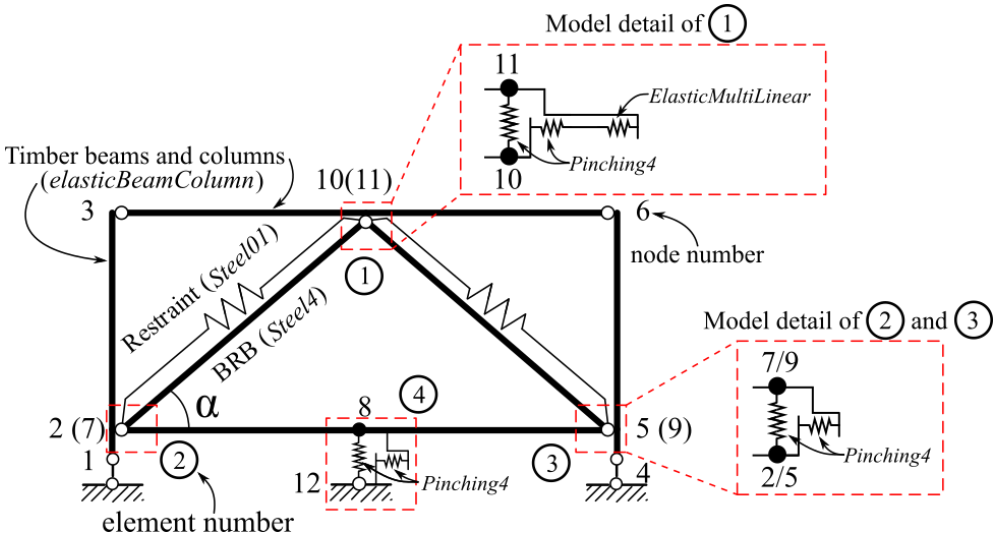

Figure 4.10 BRBGF model

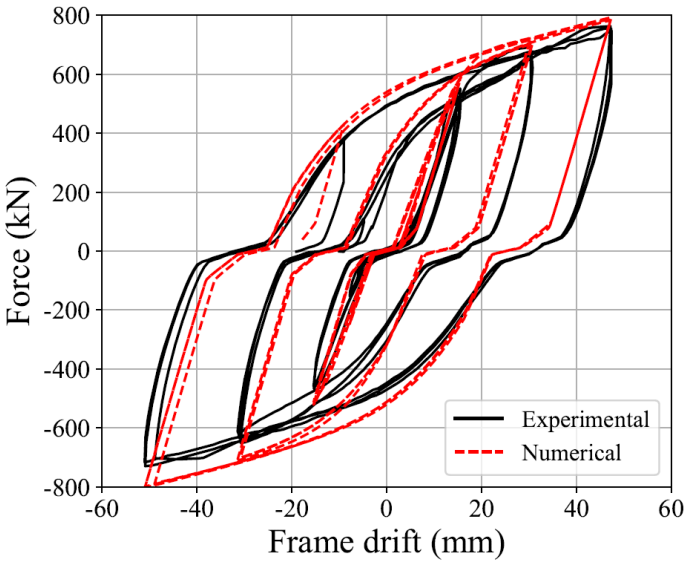

a) S-D (Dowelled connections)

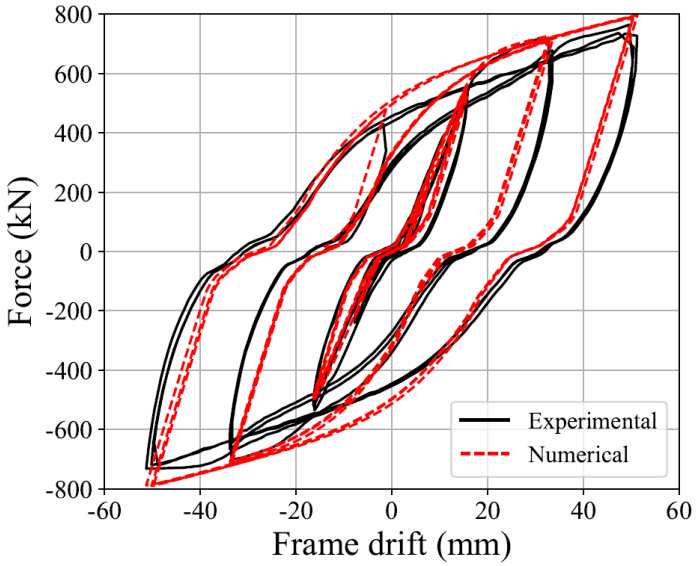

b) S-S (Screwed connections)

Figure 4.11 Comparison of BRBGF hysteresis curves

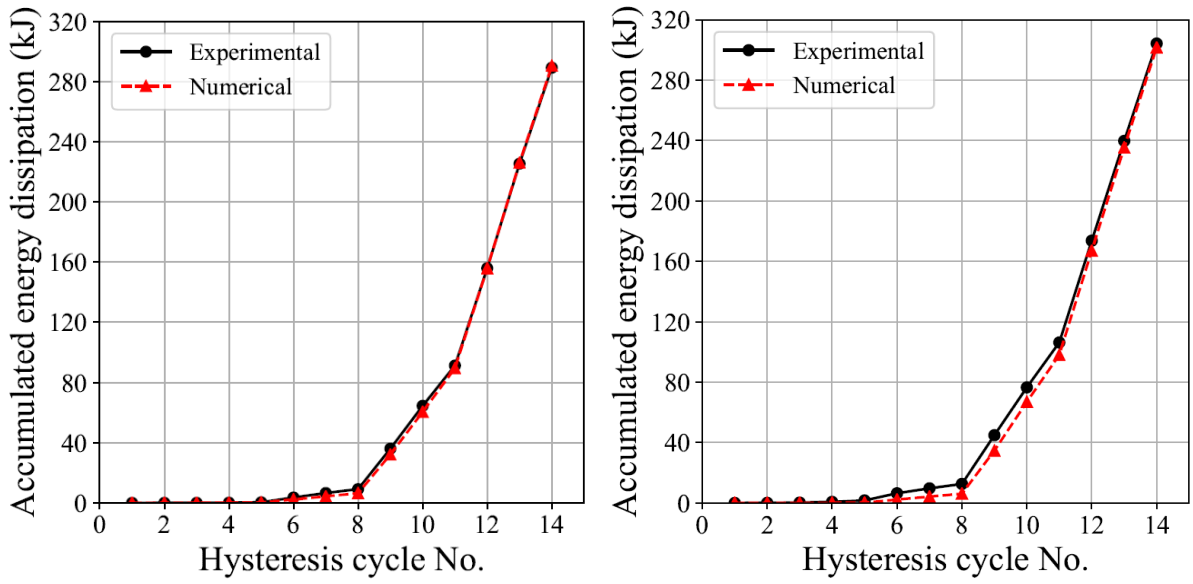

a) S-D (Dowelled connections) b) S-S (Screwed connections)

Figure 4.12 Comparison of BRBGF accumulated energy dissipations

Figure 4.13 and Figure 4.14 show the BRB deformations versus the BRBGF drift for S-D and S-S, respectively. BRB-S and BRB-N represent the southern BRB and northern BRB in Figure 3.2, respectively. The positive drift (toward the north in Figure 3.2) caused elongation in the BRB-S and shortening in the BRB-N. At small drift levels, the BRB deformations in the tests matched the simulation results very well. At large drift levels, the BRB had greater elongation than the shortening, which was not well captured by the model. The errors were likely because the BRB in compression had slightly higher stiffness than the BRB in tension due to the core bonding and more deformations were concentrated on the BRB in tension. The difference in the BRB deformations between S-D and S-S might be partially caused by the variation of the yield location in tension. The yielding location could concentrate on any location along the yield zone and the restraints around the location could be different. The strength differences of BRBGFs were also partially caused by the variation of restraints. Better quality control of BRB manufacturing will reduce the variabilities of BRBs and help achieve more consistent performance.

To investigate the influence of the BRB-timber interface connections on the overall performance of the BRBGFs, the *Pinching4* models of the S-S model in Figure 4.11 were removed to establish a new model. In this way, the new model only included the initial slips caused by the pin-end BRBs, but the screwed connections were simulated to be translationally rigid. The hysteresis loops of the S-S model were compared with the new model with the rigid connections as shown in Figure 4.15. Figure 4.15 shows that the stiffness of the S-S model before BRBs' yielding was overestimated by 67% (65 kN/mm for the new model with translationally rigid connections versus 39 kN/mm for the S-S model). In addition, neglecting the increased slips during cyclic loading caused by the high unloading stiffness of the screwed

connections will overestimate the energy dissipation. Therefore, it is important to include the connection models in the BRBGFs.

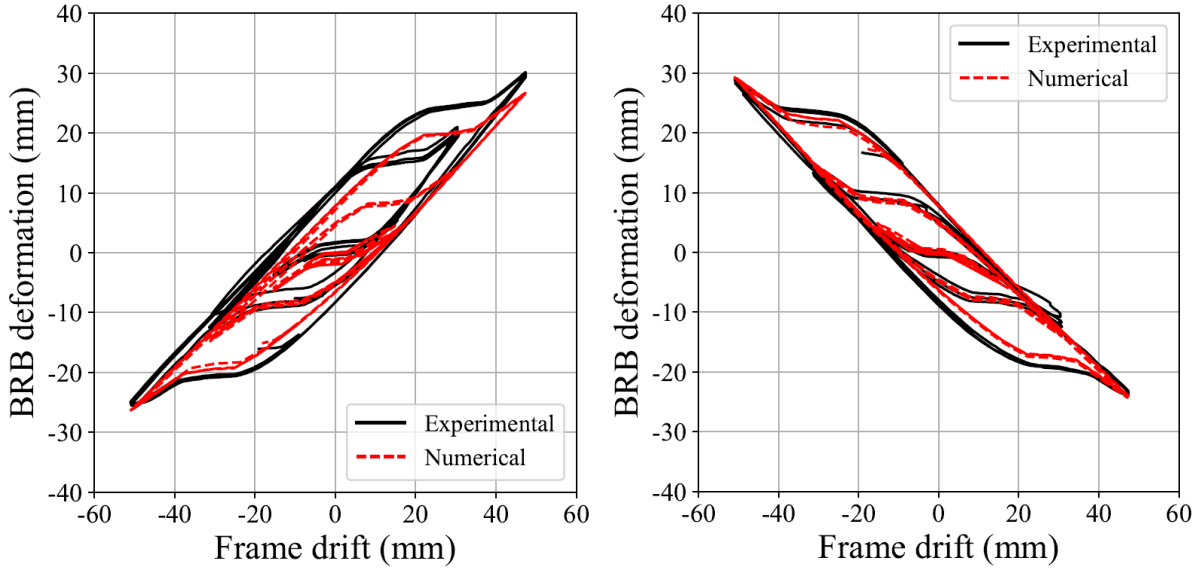

a) BRB-S b) BRB-N

Figure 4.13 Comparison of BRB deformation in S-D (Dowelled connections)

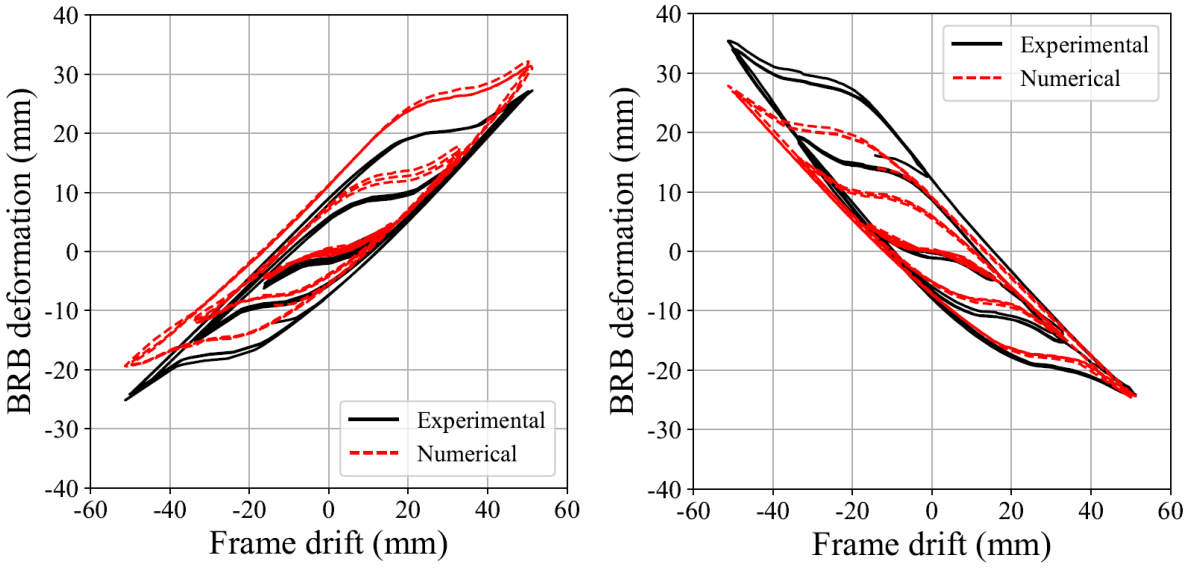

a) BRB-S b) BRB-N

Figure 4.14 Comparison of BRB deformation in S-S (Screwed connections)

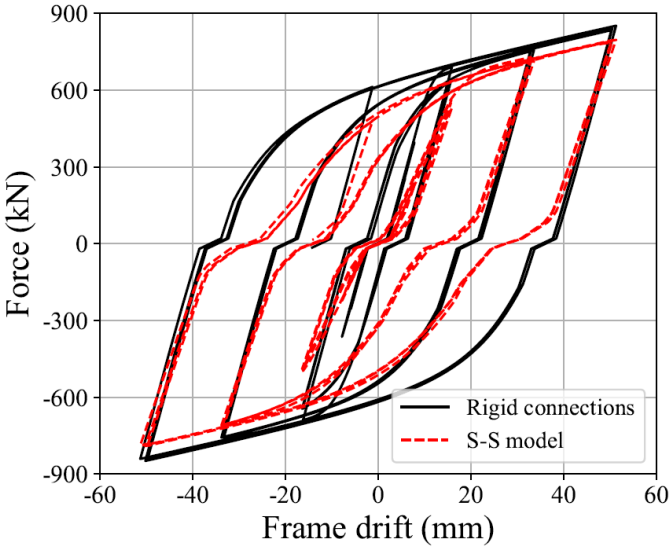

Figure 4.15 Comparison of the hysteresis curves with different connection modelling methods

4.4 Parametric studies

The validated one-bay one-storey BRBGF model in Figure 4.10 was used as a benchmark model for parametric studies to investigate the influence of the critical BRB-timber interface connection details on the cyclic behaviour. The additional BRB restraint elements shown in Figure 4.10 were removed in the parametric studies assuming that good quality controls of the BRBs can prevent the additional restraints. According to the BRB model analyses, the design overstrength factor of BRBs ($\gamma_{os,BRB}=\omega\beta$) was set as 1.5 at the 2.0% drift ratio. This $\gamma_{os,BRB}$ is also typically used in practical applications (Zsarnoczay, 2013).

4.4.1 Influence of interface connection stiffness

The stiffness of the BRB-timber interface connections impacts the efficiency of the BRBs in the hybrid system. Compared with welded or bolted connections in steel BRB frames, timber connections are more flexible. Eq. 4.5 defines the lateral system stiffness ratio η_{con} between the BRBGFs considering the stiffness ($K_{lat,\gamma}$) of the dowelled connections or screwed connections and the BRBGFs with translationally rigid connections ($K_{lat,\infty}$). Following the capacity design approach, the connection relative overstrength factor $\gamma_{os,con}$ as shown in Eq. 4.6 defines the ratio between connection design strength $F_{d,con}$ and the load $F_{k,BRB}$ transferred from BRBs to the connections when the BRBs yield. $\gamma_{os,con}$ was used to establish the strength hierarchy between the structural components. Higher $\gamma_{os,con}$ means higher over-design of connections.

$$\eta_{con} = \frac{K_{lat,\gamma}}{K_{lat,\infty}} \qquad \text{Eq. 4.5}$$

$$\gamma_{os,con} = \frac{F_{d,con}}{F_{k,BRB}} \qquad \text{Eq. 4.6}$$

$$F_{k,BRB} = 2\phi_m f_{ys,BRB} A_c \cos\ \alpha \qquad \text{Eq. 4.7}$$

where ϕ_m (=1.25) is the material overstrength factor obtained from the coupon tests in Chapter 3; and

α is the inclined angle of BRBs as shown in Figure 4.10.

The same BRBs were used in all BRBGF models to investigate the influence of interface connection stiffness, so $F_{k,BRB}$ was assumed to remain constant, but $\gamma_{os,con}$ varied from 1.0 to 2.5 by using more dowels and screws in the connections. This also led to an increased connection stiffness ratio η_{con}. The relationships between η_{con} and $\gamma_{os,con}$ for BRBGF with the dowelled connections (S-D) and BRBGF with the screwed connections (S-S) are shown in Figure 4.16. It was found that η_{con} was increased by 19% (from 0.75 to 0.89) and 38% (from 0.58 to 0.80) for S-D and S-S, respectively, when $\gamma_{os,con}$ was increased from 1.0 to 2.5. However, increasing $\gamma_{os,con}$ did not improve η_{con} proportionally. For example, when $\gamma_{os,con}$ was increased from 1.5 to 2.5 by 67% and the interface connections became significantly stronger, η_{con} was increased by only 9% (from 0.82 to 0.89). For S-S, η_{con} was increased by 18% when $\gamma_{os,con}$ was increased from 1.5 to 2.5.

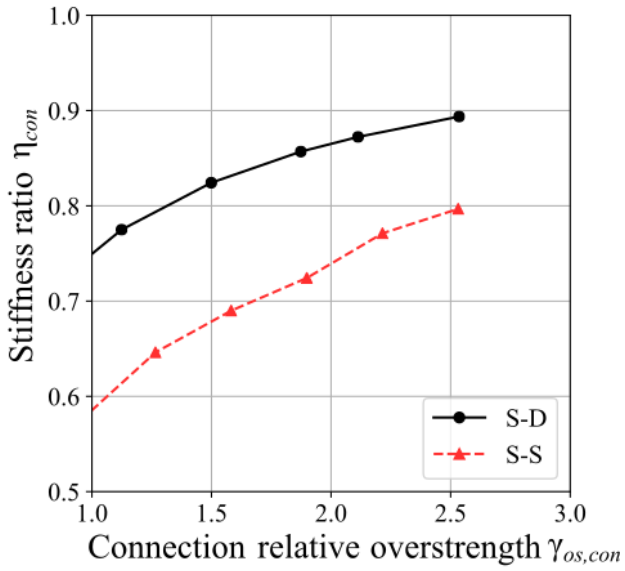

Figure 4.16 The relationship between stiffness ratio and connection relative overstrength

Figure 4.17 shows the pushover curves of S-D with different $\gamma_{os,con}$. It was illustrated that when the capacity design was not used ($\gamma_{os,con}$=1.0<$\gamma_{os,BRB}$), which meant that the connections were designed to be weaker than the expected maximum strength of BRBs considering their overstrength at the 2% drift ratio, the system stiffness was much lower than that when the capacity design would be achieved ($\gamma_{os,con}$=1.5 and $\gamma_{os,con}$=2.5>$\gamma_{os,BRB}$). This was because the inelastic deformation in the connections could occur. Therefore, it is important to keep $\gamma_{os,con}$ equal to or exceed the BRB overstrength factor $\gamma_{os,BRB}$ to maximize the efficiency of BRBs and avoid significant inelastic response or damage to the connections. When $\gamma_{os,con}$ was over $\gamma_{os,BRB}$ (i.e. $\gamma_{os,con}$=1.5 and $\gamma_{os,con}$=2.5), the stiffness differences were relatively small. For a cost-

effective connection design, $\gamma_{os,con}$ =$\gamma_{os,BRB}$=1.5 is recommended for both connections because this is the minimum value (i.e. $\gamma_{os,con}$=$\gamma_{os,BRB}$) to ensure the capacity design. The connections also had enough stiffness to effectively engage BRBs at this relative overstrength level.

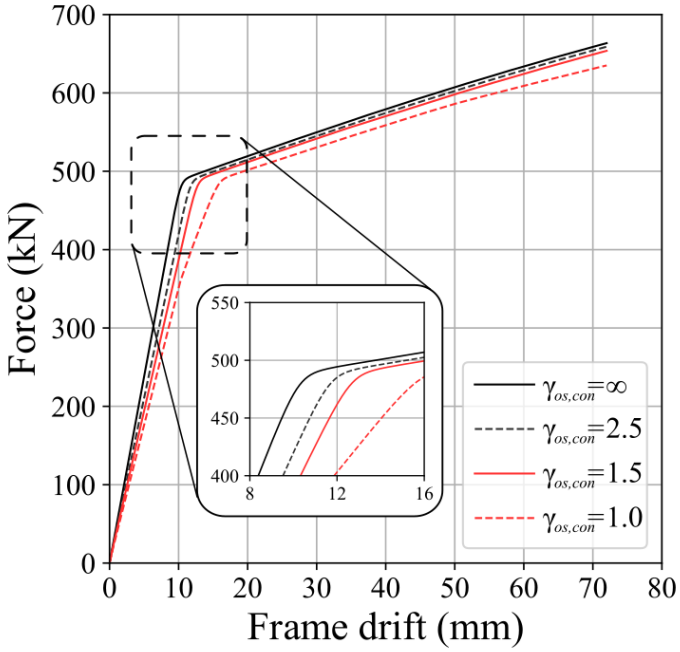

Figure 4.17 Pushover curves of S-D with different connection relative overstrength

Figure 4.17 also shows that the ultimate strength at the 2.0% drift ratio was 654 kN for $\gamma_{os,con}$ =1.5 and 659 kN for $\gamma_{os,con}$ =2.5 with less than 1% increase. The post-yield stiffness was similar among different $\gamma_{os,con}$ as it was controlled by the stiffness of BRBs. As a result, when $\gamma_{os,con}$ exceeded $\gamma_{os,BRB}$, the connection stiffness had a small impact on the initial stiffness and a negligible effect on the ultimate strength and post-yield stiffness. It should also be noticed that low initial stiffness could increase the yield drift of BRBGFs, so SLS might become the governing case for the system design.

4.4.2 Influence of manufacturing tolerances

The pin-end connections of BRBs to the gusset plates and the dowelled connections in S-D require tolerances for installation. The slack caused by the tolerances may reduce the system energy dissipation under cyclic loading (Wijanto and Clifton, 2014). Therefore, BRBGFs with different initial slips were modelled and the influence of manufacturing tolerances on the cyclic performance of the BRBGFs was investigated.

All connections were designed by the same connection relative overstrength factor $\gamma_{os,con}$ (=1.5). The benchmark BRBGF model contained two BRBs and three connections as shown in Figure 4.10. Each BRB allowed 1 mm tolerance in total from the pin holes on both ends according to NZS 3404 (1997), which could cause ±0.5 mm initial slip in the system. Similarly, each dowelled connection had 1 mm to 2 mm tolerances according to Eurocode 5 (2004), which might cause ±0.5 mm to ±1.0 mm initial slips. Therefore, the upper limits of initial slips for S-

D were assumed as ±4.0 mm (there were two BRBs in the S-D models and the initial slip was ±0.5 mm from each BRB, i.e. ±0.5×2; while there were one top connection and two bottom connections in the S-D models and the initial slip was ±1.0 mm from each connection as the maximum, i.e. ±1.0 mm×3. The upper limit of the initial slips was ±0.5 mm ×2 plus ±1.0 mm×3) and the lower limit was assumed as ±2.5 mm (±0.5 mm×2 from BRBs and ±0.5 mm×3 from the dowelled connections). The screwed connections were tight fit while a maximum 1 mm tolerance was considered conservatively to engage all STS completely. For S-S, the upper and lower limits were assumed as ±2.5 mm (±0.5 mm×2 from BRBs and ±0.5 mm×3 from the screwed connections) and ±1.0 mm (±0.5 mm×2 from BRBs and ±0.0 mm×3 from the screwed connections), respectively.

Figure 4.18 shows the hysteresis loops of S-D following the loading protocol in the frame tests in Chapter 3 as an example. It shows that S-D with ±2.5 mm initial slips started to carry the load 1.5 mm earlier than S-D with ±4.0 mm initial slips before yielding and when the load direction changed. However, they tended to be consistent at the post-yield stage. Figure 4.19 shows the energy dissipation in each cycle of S-D and S-S. The results showed that hysteresis loops with different initial slips were similar. The maximum difference of energy dissipations in one cycle was within 5% (117 kJ for "S-D ±2.5 mm" versus 112 kJ for "S-D ±4.0 mm" and 115kJ for "S-S ±1.0 mm" versus 110 kJ for "S-S ±2.5 mm" in cycle No. 17). Therefore, the initial slips from manufacturing tolerances increased the yield drift. A larger drift before yielding should be expected with larger manufacturing tolerances and SLS design may govern the system design. The manufacturing tolerances had a negligible impact on the ultimate strength and energy dissipation of the BRBGFs under cyclic loading as long as the manufacturing tolerances were defined within the reasonable range mentioned above.

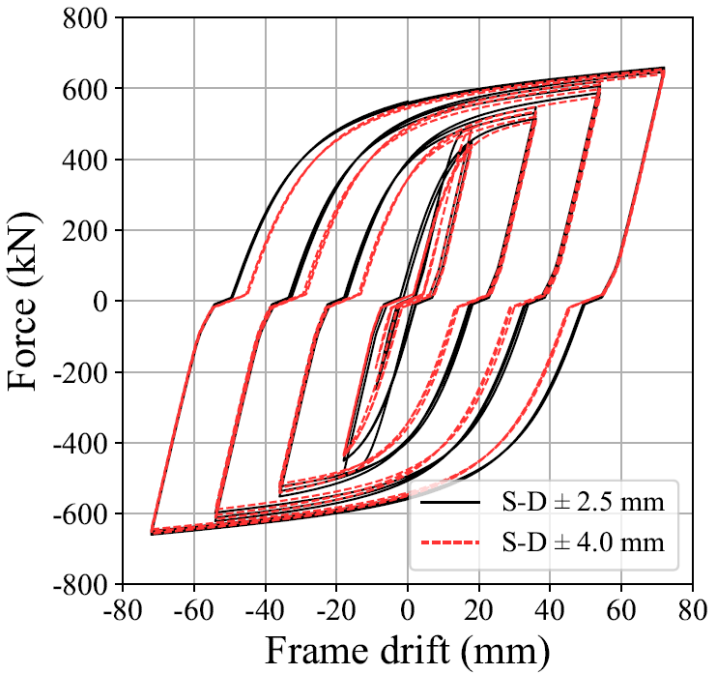

Figure 4.18 Hysteresis curves with different initial slips

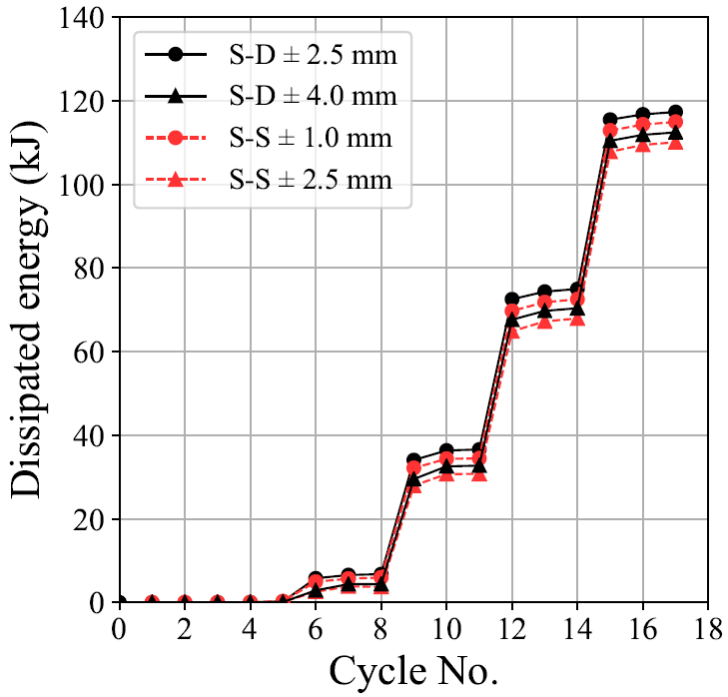

Figure 4.19 Energy dissipation per cycle of BRBGFs

4.5 Summary

This chapter presented component-based numerical models in OpenSees to simulate the cyclic behaviour of BRBGFs. Parametric studies were conducted by changing the stiffness of BRB-timber interface connections and the manufacturing tolerances. Their influence on the BRBGF cyclic performance was investigated. A summary is listed as follows:

1) The beam-on-foundation (BOF) model provided more accurate stiffness predictions of the dowelled connections when compared with the stiffness equations in Eurocode 5.
2) The combined analytical model based on timber-to-timber connections and timber-to-concrete connections from literature could predict the stiffness of the screwed connections with reasonable accuracy.
3) The BRBGF model predictions agreed well with the experimental results of two full-scale BRBGFs in force-drift responses, accumulated energy dissipation and BRB deformations.
4) The dowelled connections and the screwed connections as the BRB-timber interface connections effectively engaged the BRBs. The parametric studies showed that when connection relative overstrength factor $\gamma_{os,con}$ was equal to the BRB overstrength factor $\gamma_{os,BRB}$ (=1.5), the lateral stiffness of BRBGF with the dowelled connections achieved 82% of the lateral stiffness of the BRBGF with translationally rigid connections. For BRBGF with the screwed connections, its stiffness was 68% of the lateral stiffness of the BRBGF with translationally rigid connections. Further increasing the connection strength did not increase the system lateral stiffness significantly.

5) The manufacturing tolerances can cause initial slips of BRBGFs. The parametric studies showed that the practical manufacturing tolerances did not affect the energy dissipation and ultimate strength of the BRBGFs significantly under cyclic loading. However, excessive initial slips could cause higher slips before the yielding of BRBs and might affect the serviceability performance.

5 DIRECT DISPLACEMENT-BASED DESIGN

The experimental testing and numerical modelling in Chapter 3 and Chapter 4 have proved the great potential of BRBGFs used as a feasible LFRS for multi-storey heavy timber buildings. However, no seismic design methodology is readily available for such a new hybrid system, which may restrict its practical applications. This chapter presents a direct displacement-based design (DDBD) approach with which engineers can design this system efficiently by hand calculations. The critical design parameters of the DDBD approach will be derived to facilitate the extension of the DDBD approach for the BRBGF system. This chapter is based on a journal paper (Dong et al., 2021b) submitted to *Engineering Structures*.

5.1 Fundamentals of the DDBD approach

The primary process of the DDBD approach (Priestley et al., 2007a) is shown in Figure 5.1. The first step is to substitute the multi-degree-of-freedom (MDOF) structure with an equivalent SDOF system (Figure 5.1a). A displacement profile of the MDOF structure under seismic loads is assumed based on the prior knowledge of its LFRS type (e.g. via shake table tests), so the equivalent SDOF system characterised by its design displacement Δ_d, effective mass M_e, and effective height H_e can be calculated by Eq. 5.1-Eq. 5.3.

$$\Delta_d = \frac{\sum_{i=1}^{n} m_i \Delta_i^2}{\sum_{i=1}^{n} m_i \Delta_i} \quad \text{Eq. 5.1}$$

$$M_e = \frac{\sum_{i=1}^{n} m_i \Delta_i}{\Delta_d} \quad \text{Eq. 5.2}$$

$$H_e = \frac{\sum_{i=1}^{n} m_i \Delta_i H_i}{\sum_{i=1}^{n} m_i \Delta_i} \quad \text{Eq. 5.3}$$

where Δ_i is the design storey drift at the *i*-th storey;

m_i is the seismic mass at the *i*-th storey;

H_i is the height of the *i*-th storey from the ground; and

n is the total number of storeys.

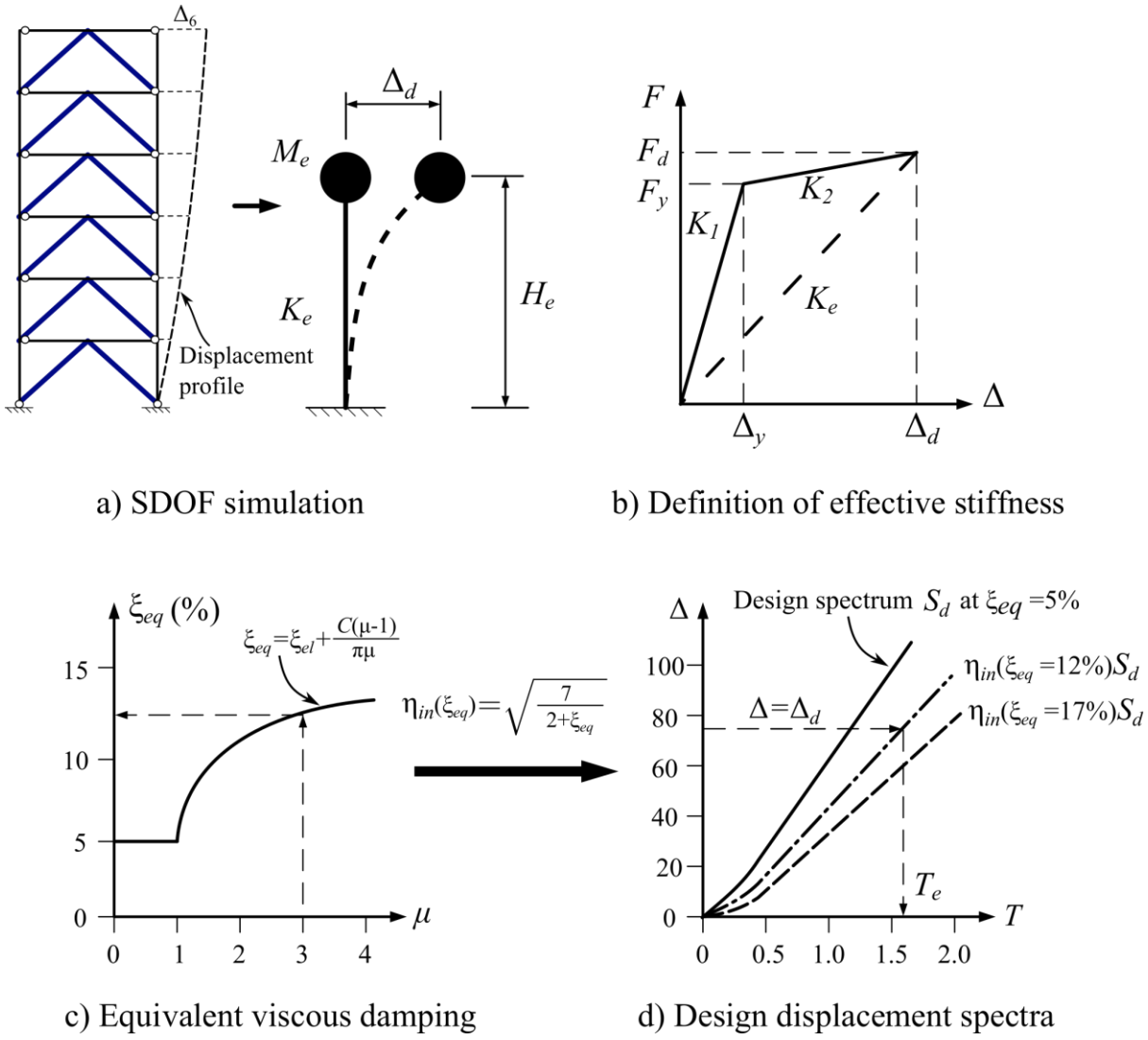

Figure 5.1 DDBD design approach (Priestley et al., 2007a)

The second step is to calculate the equivalent SDOF system ductility demand μ at the design displacement Δ_d according to Eq. 5.4 with the design and yield displacement points shown in Figure 5.1b. To quantify the effects of non-linear behaviour on the displacement demands, Priestley et al. (2007a) recommended characterising the equivalent SDOF system with an equivalent viscous damping ξ_{eq} that is a function of μ as shown in Figure 5.1c. The ξ_{eq} is obtained according to the ξ_{eq}-μ relationship. The design displacement spectrum of a SDOF system $S_d(T)$ is scaled to the ξ_{eq} as shown in Figure 5.1d by using spectral displacement reduction factor η_{in} that is a function of ξ_{eq}, so the required T_e for the equivalent SDOF system can be obtained according to Δ_d. After T_e is known, K_e and the design base shear force V_d will be determined using Eq. 5.5 and Eq. 5.6, respectively, when P-Δ effects are not significant.

$$\mu = \frac{\Delta_d}{\Delta_y} \qquad \text{Eq. 5.4}$$

$$K_e = (\frac{2\pi}{T_e})^2 M_e \quad \text{Eq. 5.5}$$

$$V_d = K_e \Delta_d \quad \text{Eq. 5.6}$$

The design base shear force V_d for the equivalent SDOF system is also the design base shear force for the MDOF structure, so the third step is to distribute V_d along with the height of the structure as storey forces F_i using Eq. 5.7. These forces are used to design the structural members in the MDOF structures, with possible adjustments to the force profile for taller buildings to mitigate higher mode effects.

$$F_i = \frac{m_i \Delta_i}{\sum_{i=1}^{n} m_i \Delta_i} V_d \quad \text{Eq. 5.7}$$

5.2 Extending the DDBD approach to the BRBGF system

To apply the DDBD approach to design the BRBGF system, the following knowledge is required 1) the determination of the displacement profile and design displacement at the performance limit state for the BRBGF system when substituting the BRBGF to an equivalent SDOF system (Figure 5.1a). 2) the determination of ductility factor μ for the BRBGF system (Figure 5.1c), which requires the estimation of the yield displacement. 3) the determination of the relationship between ξ_{eq} and μ to obtain T_e (Figure 5.1c and Figure 5.1d). This section discusses how these parameters are determined.

5.2.1 Displacement profile and limit state displacement

The design displacement Δ_d of the equivalent SDOF system depends on an assumed displacement profile and the limit state displacement of the MDOF structure as shown in Eq. 5.1a. Therefore, an appropriate design displacement profile is important for the DDBD approach. Some research (Medhekar and Kennedy, 2000c; Moghaddam and Hajirasouliha, 2006) has shown that the linear displacement profile (denoted as Profile L) as shown in Figure 5.2a provides an approximate match for the displacement response of steel CBF structures based on the analyses of 2 to 15 storeys X-braced CBF structures. Other research (Pettinga and Priestley, 2005; Wijesundara and Rajeev, 2012) has also shown that the parabolic displacement profile (denoted as Profile P) as shown in Figure 5.2b for moment-resisting frame structures proposed by Priestley et al. (2007a) is suitable for steel CBF structures. Additionally, Rajeev et al. (2017) verified the feasibility of Profile P based on numerous NLTHA of steel CBF structures. Al-Mashaykhi et al. (2019) highlighted the effects of the higher modes on the displacement profile of steel CBF structures and provided a cubic displacement profile (denoted as Profile C) as shown in Figure 5.2c for steel CBF structures based on the curve fitting of the NLTHA results of 12 different steel CBF structures. Because no shake table testing data or field monitoring data of any multi-storey BRBGF systems are available, these three displacement profiles will be checked in Chapter 6 by case studies to identify the most

suitable displacement profile for the BRBGF system. Figure 5.2 also shows that the first storey has the largest inter-storey drift ratio, so the performance limit state displacement is the first storey drift ratio θ_d. In terms of that, the three design displacement profiles of BRBGFs were expressed as a function of θ_d as shown in Eq. 5.8 (Sullivan et al., 2012). If more accurate displacement profiles of multi-storey BRBGF systems are available in the future, the displacement profile assumption can be improved but the whole process of the DDBD approach presented in this study will remain the same.

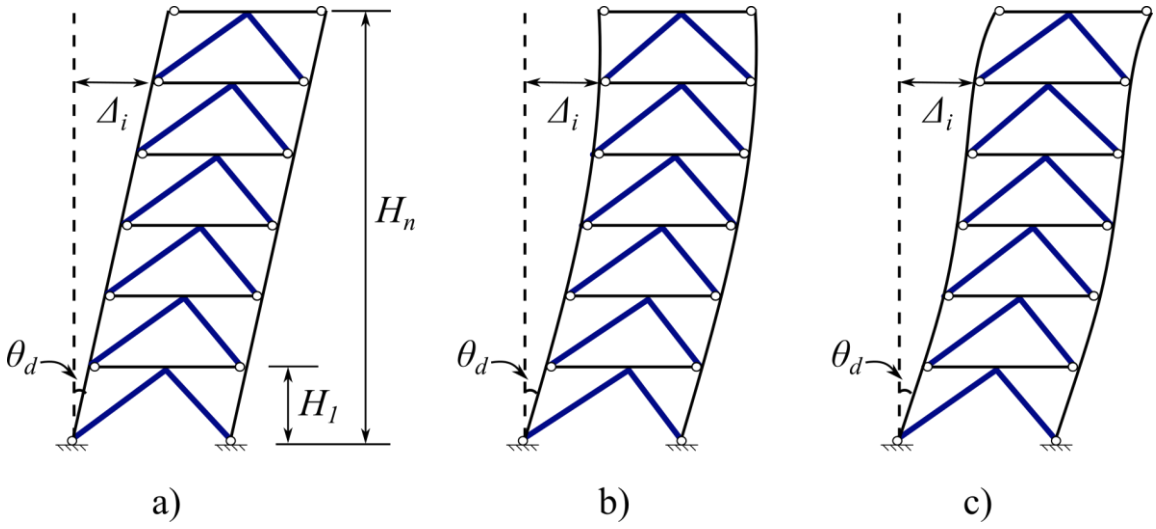

Figure 5.2 The assumed displacement profile a) Profile L; b) Profile P; c) Profile C

Past research illustrated that the higher mode actions might increase the total storey drift demands over the height (Gardiner et al., 2013) and Sullivan (2013) suggested reducing the first mode design displacement profile to account for the additional displacements caused by higher mode effects. Therefore, a design drift reduction factor ω_θ (Eq. 5.8d) adapted by Sullivan et al. (2012) was included in the displacement profile to account for higher mode effects for the BRBGF system.

For the linear displacement profile (profile L):

$$\Delta_i = \omega_\theta \theta_d H_i \qquad \text{Eq. 5.8a}$$

For the parabolic displacement profile (profile P):

$$\Delta_i = \omega_\theta \theta_d H_i \frac{(4H_n - H_i)}{(4H_n - H_1)} \qquad \text{Eq. 5.8b}$$

For the cubic displacement profile (profile C):

$$\Delta_i = \begin{cases} \theta_d H_i \dfrac{(5H_n - 2H_i)}{(5H_n - 2H_1)} & n \le 4 \\ \omega_\theta \theta_d H_i \dfrac{(7H_n^2 - 8H_i H_n + 5H_i^2)}{(7H_n^2 - 8H_1 H_n + 5H_1^2)} & n \ge 4 \end{cases} \qquad \text{Eq. 5.8c}$$

$$\omega_\theta = \begin{cases} 1.0 & n \leq 6 \\ 1 - 0.015(n-6) & 6 < n \leq 16 \end{cases} \quad \text{Eq. 5.8d}$$

The design inter-storey drift ratio limit θ_d depends on the performance requirements of both structural and non-structural elements. Recent research on low-damage non-structural elements showed that the improved design of non-structural elements could sustain a 2%-2.5% drift ratio with minor damage (Dhakal et al., 2016), so the performance limit was assumed to be governed by structural elements in this study. The serviceability performance limit of θ_d was set to be 0.33% based on New Zealand engineering practice (Hashemi et al., 2020). The repairable damage limit state of θ_d was set to be 1.0% because the BRBGF tests in Chapter 3 showed that at this drift ratio, the residual drift ratio could be over 0.5%, which was suggested as the permissible residual drift ratio for safety by McCormick et al. (2008). The ultimate limit state (ULS) drift ratio was set to be 2.0% conservatively because the BRBGF tests in Section 3.3 proved that the BRBGF system could achieve this drift limit without significant damages in timber and connections. Higher θ_d can be assumed if it can be verified by further testing.

5.2.2 Ductility factor

The ductility factor μ of the equivalent SDOF system is used to estimate the equivalent viscous damping ξ_{eq} as shown in Figure 5.1c before obtaining the effective period T_e. The yield displacement Δ_y is required to determine μ as shown in Eq. 5.4. This sub-section discusses the determination of Δ_y and links the ductility factor of each storey of the BRBGF system with its equivalent SDOF system.

5.2.2.1 Yield drift of one-storey BRBGFs

Numerical models of one-bay one-storey BRBGFs with 8 m span and 3.6 m height were built as shown in Figure 5.3. The experimental tests showed that the timber-steel interface connections had negligible moment-resisting capacity, so their rotational stiffness was set to be zero. The translational stiffness was modelled by *Pinching4* models and the initial slips were simulated by *ElasticMultiLinear* model as described in Chapter 4. There are several methods to define the yield drift (Priestley et al., 2007a), and the definition from Park (1989) was used because it can include the influence of the initial slips that may exist in the BRBGF system and the two well-defined linear parts of the backbone curves of the BRBGF specimens fit the definition well. The yield drift of one-storey BRBGFs $\Delta_{y,s}$ is defined as the lateral displacement corresponding to the yield strength $F_{k,BRB}$ which is calculated as Eq. 5.9 and is equal to the lateral force when both BRBs yield. Pushover analyses were conducted for the one-storey BRBGFs with and without the initial slips and Figure 5.4 shows the load-drift curves. The curves illustrated that the yield drift with initial slips $\Delta_{y,s}$ was the yield drift without initial slips $\Delta_{y,0}$ plus the initial slips Δ_s as shown in Eq. 5.10.

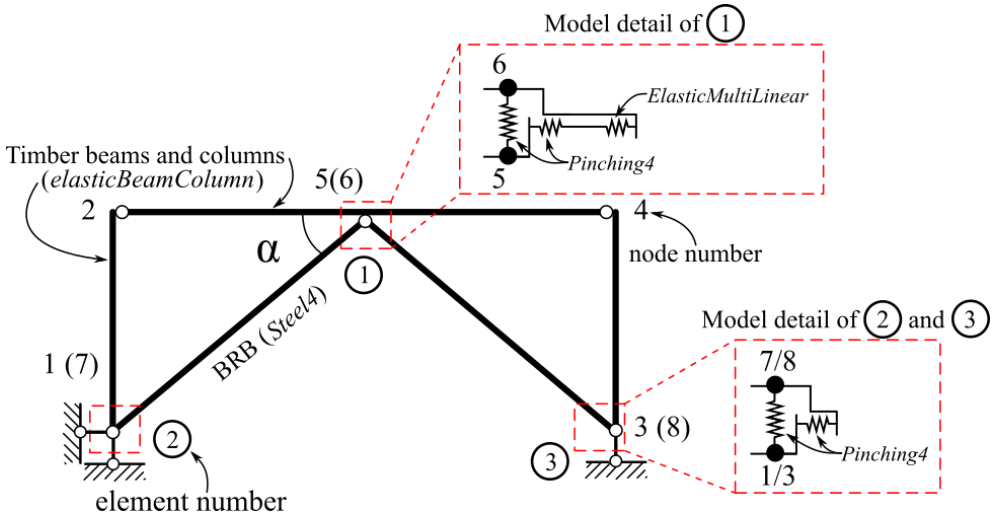

Figure 5.3 Numerical model of the one-storey BRBGF

$$F_{k,BRB} = 2\phi_m f_{ys,BRB} A_c cos\alpha \quad \text{Eq. 5.9}$$

$$\Delta_{y,s} = \Delta_{y,0} + \Delta_s \quad \text{Eq. 5.10}$$

where ϕ_m is the material overstrength factor for the steel core of BRB;

$f_{ys,BRB}$ is the steel yield strength;

A_c is the area of the yield zone of steel core of BRB, and

α is the inclined angle of the BRBs as shown in Figure 5.3.

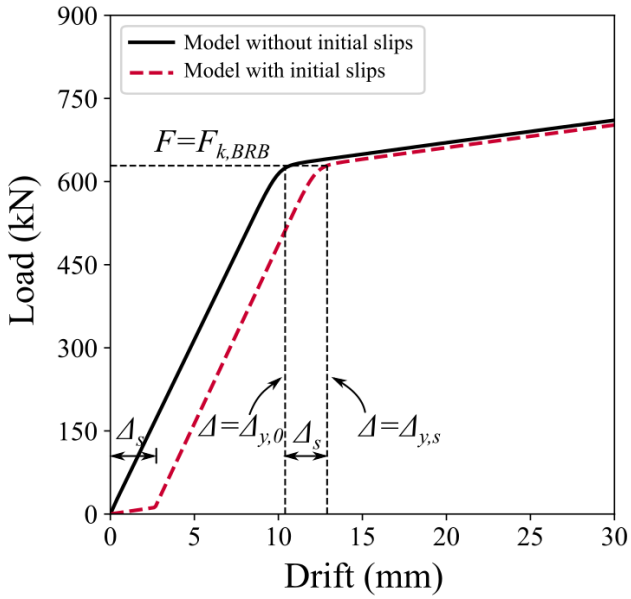

Figure 5.4 Yield drift definition

5.2.2.2 Yield drift of multi-storey BRBGFs

Past research (Della Corte, 2006; Maley et al., 2010; Sullivan et al., 2012; Wijesundara and Rajeev, 2012) has illustrated that the yield drift at the i-th storey $\Delta_{y,i}$ in a multi-storey building may need to consider not only the drift caused by the BRB deformation $\Delta_{y,i,BRB}$, but

also the drift caused by the column axial deformation $\Delta_{y,i,col}$, as shown in Figure 5.5. Similar to the one-storey BRBGF, the drift contribution of the initial slips $\Delta_{s,i}$ need to be included, so $\Delta_{y,i}$ was calculated by Eq. 5.11.

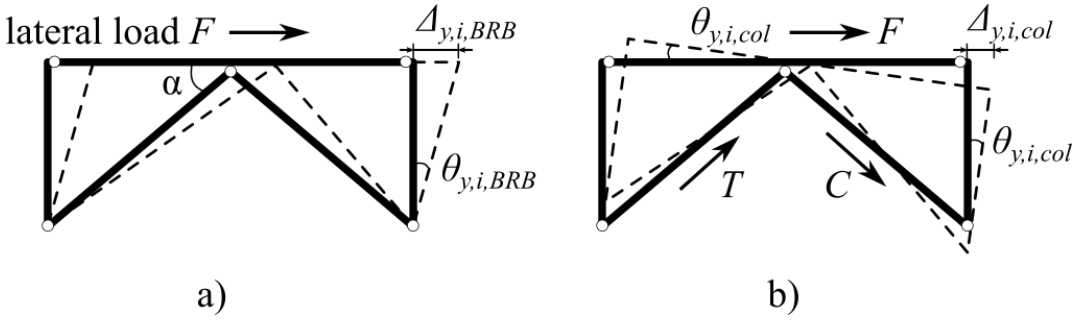

Figure 5.5 Yield drift components a) the drift contribution of the BRB deformation $\Delta_{y,i,BRB}$; b) the drift contribution of the column axial deformation $\Delta_{y,i,col}$

$$\Delta_{y,i} = \Delta_{y,i,BRB} + \Delta_{y,i,col} + \Delta_{s,i} \qquad \text{Eq. 5.11}$$

The component $\Delta_{y,i,BRB}$ was estimated by Eq. 5.12a based on the research by Sullivan et al. (2012). In steel BRB frames, the connections between BRBs and steel frames are usually considered to be translationally rigid and the frame lateral stiffness is governed by the stiffness of BRBs. However, in the BRBGF system, the connection stiffness should be taken into account. The connection stiffness is considered by introducing a stiffness adjustment factor λ as shown in Eq. 5.12b which defines the lateral stiffness ratio of BRBGF with the translationally semi-rigid BRB-timber connections and the BRBGF with translationally rigid connections (i.e. the horizontal and vertical stiffness of the *Pinching*4 model in Figure 5.3 is infinitely large), so λ is between 0 and 1.

$$\Delta_{y,i,BRB} = h_i \theta_{y,i,BRB} = h_i \frac{2\varepsilon_y}{\lambda sin2\alpha} \qquad \text{Eq. 5.12a}$$

with

$$\lambda = \frac{k_{BRBGF}}{k_{BRBGF,rigid}} \qquad \text{Eq. 5.12b}$$

$$\varepsilon_y = \frac{\phi_m f_{ys,BRB}}{f_{sm} E_{s,BRB}} \qquad \text{Eq. 5.12c}$$

where h_i is the storey height of the i-th storey;

$\theta_{y,i,BRB}$ is the drift ratio of the i-th storey caused by BRB deformations; and

ε_y is the BRB yield strain that depends on the material properties of the steel core (i.e. $f_{ys,BRB}$, ϕ_m, and $E_{s,BRB}$) and BRB geometry (i.e. f_{sm}).

Figure 5.6 shows a spring analogy model for a BRBGF. Because the top connection approximately carried the load twice as much as the bottom connections in the BRBGFs, the fastener number in the bottom connections was assumed to be half of the top connections. In

this regard, the translational stiffness of each bottom connection $k_{con,b}$ was approximately half of the translational stiffness of the top connection $k_{con.t}$ in the model (i.e. $k_{con.t}$=2$k_{con.b}$). To further simplify the spring analogy model, a stiffness ratio ν between $k_{con,b}$ and BRB lateral stiffness $k_{BRBGF,rigid}$ was defined as Eq. 5.13a. $k_{BRBGF,rigid}$ represents the BRBGF stiffness with the assumption of translationally rigid connections, i.e. the lateral stiffness governed by two BRBs only. Moreover, k_{BRBGF} can be calculated by Eq. 5.13b considering additional contributions from the translationally semi-rigid top and bottom connections. By comparing Eq. 5.12b and Eq. 5.13b, it is noticed that λ is a function of ν as shown in Eq. 5.13c.

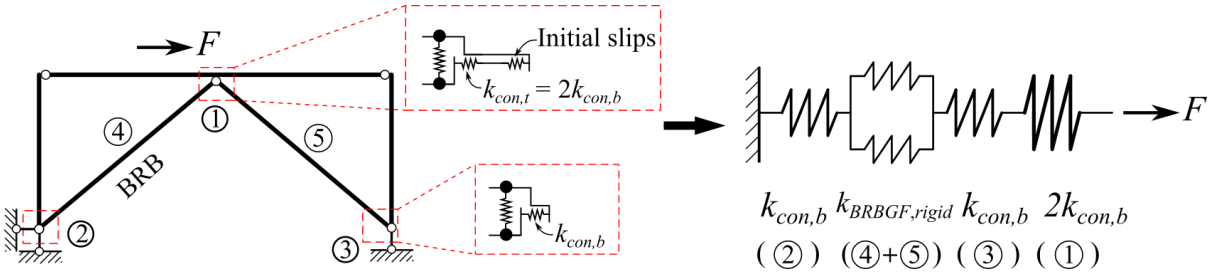

(a) (b)

Figure 5.6 BRBGF spring analogy

$$\nu = \frac{k_{con,b}}{k_{BRBGF,rigid}} \quad \text{Eq. 5.13a}$$

$$\frac{1}{k_{BRBGF}} = \frac{2}{k_{con,b}} + \frac{1}{2k_{con,b}} + \frac{1}{k_{BRBGF,rigid}} = \left(\frac{2\nu+5}{2\nu}\right)\frac{1}{k_{BRBGF,rigid}} \quad \text{Eq. 5.13b}$$

$$\lambda = \frac{2\nu}{2\nu+5} \quad \text{Eq. 5.13c}$$

The component $\Delta_{y,i,col}$ was calculated by Eq. 5.14a, assuming the columns have similar deformations in tension and compression (Wijesundara and Rajeev, 2012). Because it is difficult to determine the glulam column strain before choosing the member sizes for BRBs, glulam beams and columns, a strain adjustment factor ρ_j was used to convert the axial strain of glulam column at the j-th (j<i) storey $\varepsilon_{col,j}$ to the yield strain of yield core of BRB ε_y as shown in Eq. 5.14a. An average strain adjustment factor ρ_{avg} along with the whole height was empirically assumed as 0.4 to simplify the preliminary design. This value would be verified by NLTHA in Chapter 6.

$$\Delta_{y,i,col} = h_i\theta_{y,i,col} = h_i\frac{2\sum_{j=1}^{i-1}\varepsilon_{col,j}h_j}{L} = 2h_i\varepsilon_y\frac{\sum_{j=1}^{i-1}\rho_j h_j}{L} = 2h_i\varepsilon_y\rho_{avg}\frac{\sum_{j=1}^{i-1}h_j}{L} \quad \text{Eq. 5.14a}$$

$$\rho_j = f_{sm}E_{s,BRB}\frac{\sum_{k=j+1}^{k=n}A_{c,k}sin\alpha}{A_{col,j}E_{GL}} \quad \text{Eq. 5.14b}$$

where ρ_j is the strain adjustment factor between the glulam columns and BRB at the j-th storey (j<i);

L (=8 m) is the span of BRBGF;

$A_{c,k}$ is the BRB yield zone cross-section area at the k-th storey ($j<k\leq n$);

E_{GL} is the glulam column elastic modulus; and

$A_{col,j}$ is the glulam column cross-section area at the j-th storey ($j<i$).

5.2.2.3 Ductility factor of the equivalent SDOF system μ_{sys}

The ductility factor of the equivalent SDOF system μ_{sys} is defined as Eq. 5.15a according to Maley et al. (2010). Similar to Eq. 5.4, the ductility factor for the i-th storey μ_i is defined as Eq. 5.15b. Although the base shear force V_{base} was initially unknown, Eq. 5.15a contains the shear force in both the numerator and denominator. For the initial design, μ_{sys} can be obtained by assuming the total base shear V_{base} =1.0 and recognising that the strength proportions are a design choice. The shear force at i-th storey V_i was calculated by Eq. 5.15c. Different from Eq. 5.7, Sullivan et al. (2012) recommended Eq. 5.15d to distribute the base shear force along with the height of frame systems, where an additional 10% of the base shear force was allocated at the roof level to consider the higher mode effects.

$$\mu_{sys} = \frac{\sum_{i=1}^{n} V_i \Delta_i \mu_i}{\sum_{i=1}^{n} V_i \Delta_i} \qquad \text{Eq. 5.15a}$$

$$\mu_i = \frac{(\Delta_i - \Delta_{i-1})}{\Delta_{y,i}} \qquad \text{Eq. 5.15b}$$

$$V_i = \sum_{j=i}^{n} F_j \qquad \text{Eq. 5.15c}$$

where F_j is the distributed load at the j-th storey ($j\leq i$):

$$F_j = \begin{cases} 0.9\dfrac{m_j \Delta_j}{\sum_{i=1}^{n} m_i \Delta_i} V_{base} & j < n \\ \left(0.1 + 0.9\dfrac{m_n \Delta_n}{\sum_{i=1}^{n} m_i \Delta_i}\right) V_{base} & j = n \end{cases} \qquad \text{Eq. 5.15d}$$

5.2.3 Equivalent viscous damping ξ_{eq} and displacement reduction factor η_{in}

The relationship between ξ_{eq} and μ of the equivalent SDOF system is required for the DDBD approach as shown in Figure 5.1c. The ξ_{eq} is usually calculated by Eq. 5.16 as the sums of the elastic viscous damping ξ_{el} and hysteretic damping ξ_{hyst}. Traditionally, ξ_{hyst} is calculated by Eq. 5.17a based on the area-based approach proposed by Jacobsen (1960). However, past studies indicated that the area-based approach could be inaccurate, especially for those systems with high energy dissipation capacity (Dwairi et al., 2007; Grant et al., 2005). In this regard, ξ_{hyst} has been calibrated with Eq. 5.17b for different types of hysteretic models (Blandon and Priestley, 2005; Dwairi et al., 2007; Liu et al., 2015) and structures (Ghaffarzadeh et al., 2014;

E. Khan et al., 2016; Landi et al., 2007; Loss et al., 2012; Mazza and Vulcano, 2014; Sullivan, 2013; Sullivan and O'Reilly, 2014; Wijesundara et al., 2011; Yahyai and Rezayibana, 2015; Yan et al., 2018) including timber-steel hybrid structures (Bezabeh et al., 2016a; Z. Li et al., 2019) and steel BRB frames (Sullivan et al., 2012). However, the hysteretic behaviour of BRBGFs is different from other timber-steel hybrid structures. In addition, ξ_{hyst} for steel BRB frames was derived by using bi-linear hysteretic shape for BRBs and neglecting the influence of the connection stiffness (Sullivan et al., 2012). The bi-linear model may not represent the performance of BRBs accurately because the isotropic and kinematic hardening in tension and compression could be significant (Vigh et al., 2017). Additionally, the initial slips in BRBGFs may also reduce the ξ_{hyst}.

$$\xi_{eq} = \xi_{el} + \xi_{hyst} \quad \text{Eq. 5.16}$$

$$\xi_{hyst} = \frac{1}{2\pi}\frac{A_{hyst}}{F_m \Delta_m} \quad \text{Eq. 5.17a}$$

$$\xi_{hyst} = \frac{C(\mu - 1)}{\pi\mu} \quad \text{Eq. 5.17b}$$

where A_{hyst} is the dissipated energy in a full hysteretic loop as shown in Figure 5.7;

F_m and Δ_m are the maximum force and displacement for the hysteretic loop; and

C is a constant.

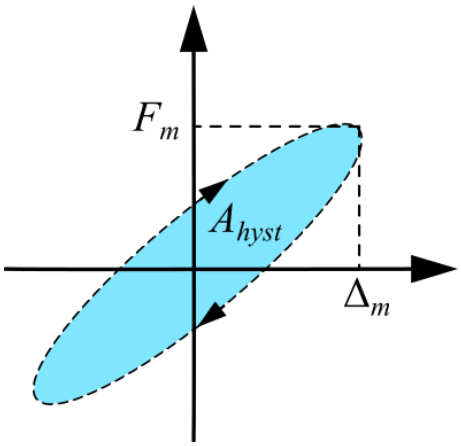

Figure 5.7 Dissipated energy in a full hysteretic loop

Eq. 5.18a and Eq. 5.18b are the equations for the displacement reduction factor η_{in} in previous Eurocode 8 (1998) and current Eurocode 8 (2005b) as a function of ξ_{eq}. This factor is usually used to scale the displacement spectrum and then to obtain the required effective period T_e as shown in Figure 5.1d. However, past research (Grant et al., 2005; Pennucci et al., 2011) has shown that Eq. 5.17b and Eq. 5.18 are dependent on the site seismicity. For example, research by Pennucci et al. (2011) showed that ξ_{eq}-μ relationship (Eq. 5.17b) calibrated by artificial earthquake records was quite different from that calibrated by real earthquake records. Some research (Sullivan and O'Reilly, 2014) also illustrated that Eq. 5.18a and Eq. 5.18b might

be suitable to use with ξ_{eq}-μ relationship calibrated with artificial and real earthquake records, respectively. The proposed ξ_{eq} in Eq. 5.17b was only a function of μ, so the dependence on the site seismicity was not explicitly considered. Using ξ_{eq}-μ relationship calibrated by specific earthquake records with different η_{in}-ξ_{eq} relationship may result in inconsistent design as shown in Figure 5.8a (Pennucci et al., 2011). To obtain a consistent design, ξ_{eq}-μ and η_{in}-ξ_{eq} relationships should both be calibrated under the same site seismicity as shown in Figure 5.8b. Many different ξ_{eq}-μ and η_{in}-ξ_{eq} relationships are required to be derived using different earthquake records, which is more complicated and has not been well considered in most of the previous research. The research by Pennucci et al. (2011) illustrated that there was no obvious dependency on site seismicity between η_{in} and μ, so for simplifying the design approach and improving the design accuracy, it was suggested to combine the two steps (Figure 5.1c and Figure 5.1d) into a single step and derive the η_{in} -μ relationship directly. In this study, an attempt was made to establish a direct η_{in} -μ relationship for the BRBGF system.

$$\eta_{in,1} = \sqrt{\frac{7}{2+\xi_{eq}}} \qquad \text{Eq. 5.18a}$$

$$\eta_{in,2} = \sqrt{\frac{10}{5+\xi_{eq}}} \qquad \text{Eq. 5.18b}$$

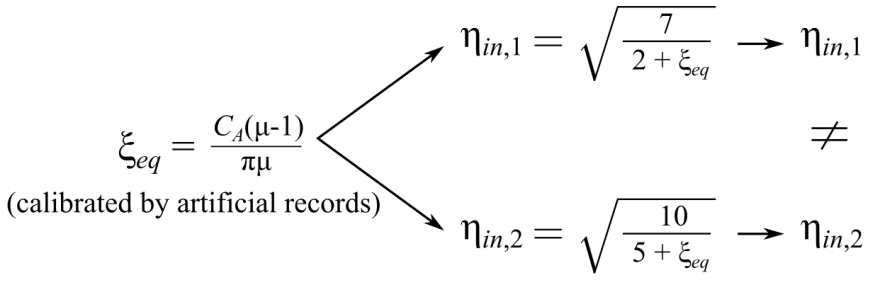

a) Inconsistent η_{in} due to the site seismicity

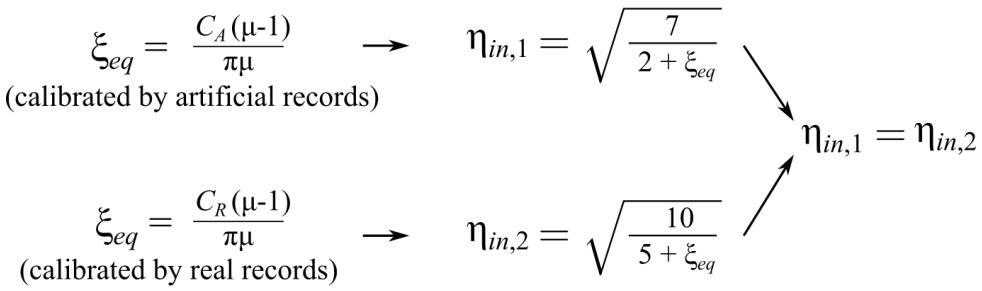

b) Consistent η_{in} by considering site seismicity

Figure 5.8 The effects of spectral damping sensitivity on design (Pennucci et al., 2011)

Figure 5.9 shows the comparison between the numerical modelling results of the BRBGF with the dowelled connections in Figure 4.11a with the Takeda fat hysteresis model in Figure 5.10 (r_t=0.05, β_t=0.3 and D=0.0). Although the Takeda fat model is usually used to represent the hysteresis loops of RC frames (Priestley et al., 2007a), the comparison showed that it was also able to provide an approximate fit to the hysteresis loops of the BRBGF and the maximum difference of the total energy dissipation was about 10% (291 kJ versus 261 kJ). Because the Takeda fat model dissipated slightly less energy than the BRBGF model and had similar hysteretic behaviour, and the η_{in}-μ relationship for the Takeda fat model given in Eq. 5.19 has been calibrated by Pennucci et al. (2011) with numerous NLTHA, it was decided to check if Eq. 5.19 could also be applied for the BRBGF system in this system. The verification process will be provided in Section 5.3.

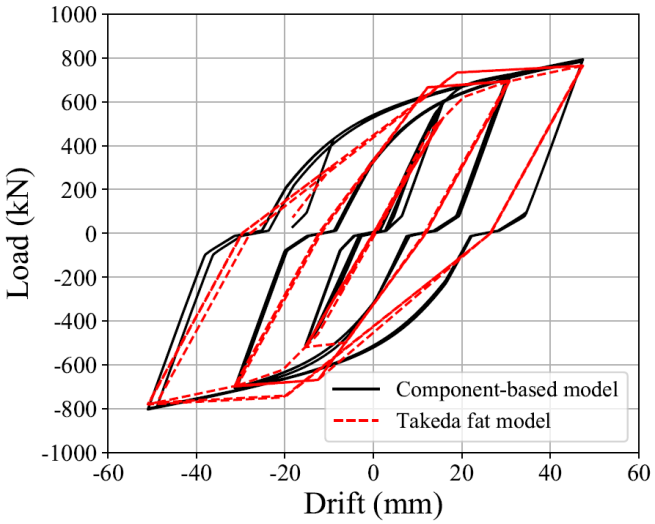

a) Hysteresis loops

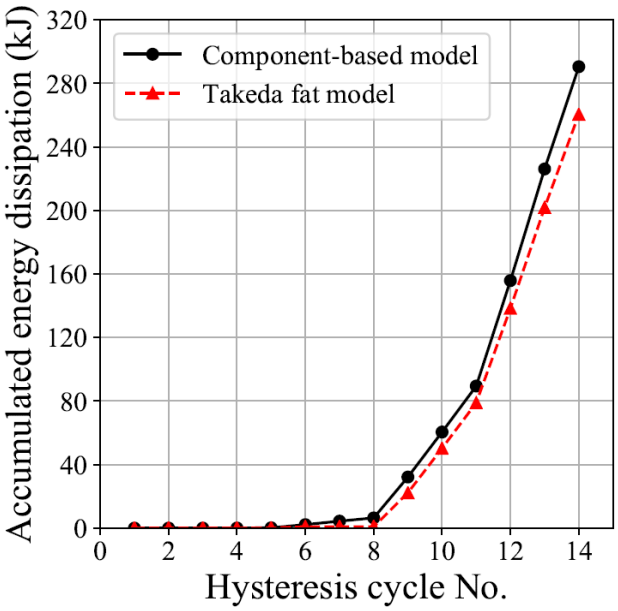

b) Accumulated energy dissipation

Figure 5.9 Comparison between the component-based model and Takeda fat model

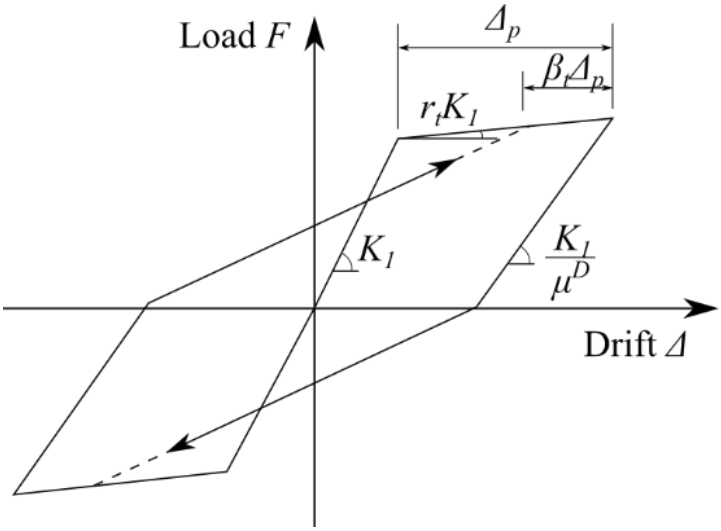

Figure 5.10 Takeda fat model (Priestley et al., 2007a)

$$\eta_{in,3} = \sqrt{\frac{\pi\mu}{11.04\mu - 7.9}} \qquad \text{Eq. 5.19}$$

5.3 Calibration of design parameters

The stiffness adjustment factor λ (Eq. 5.12b) needed to be determined and the feasibility of the η_{in}-μ relationship of the Takeda fat model (Eq. 5.19) for the BRBGF system needed to be assessed. Pushover analyses and NLTHA would be conducted by using the numerical models of the one-storey BRBGF as shown in Figure 5.3 to determine λ and assess Eq. 5.19, respectively.

5.3.1 Variables of the numerical models

A series of one-storey BRBGF models were built in OpenSees. The models had an 8 m span and 3.6 m height with BRB installed at an inclined angle α=42°. All BRBs are made of S235 steel according to Eurocode 3 (2005a) with a material overstrength ϕ_m=1.2 (Sullivan et al., 2012), elastic modulus $E_{s,BRB}$ =210 GPa and a BRB overstrength factor $\gamma_{os,BRB}$=1.5. Three design variables are considered based on the parametric studies in Section 4.4: 1) cross-section of the yield zone in BRBs A_c; 2) stiffness modification factor f_{sm} defined by Eq. 4.1; and 3) initial slips due to manufacturing tolerances. Table 5.1 lists the configurations of the BRBGFs under consideration. Three different cross-sections of BRBs were considered for implementation in the lower, middle and upper storey of a multi-storey BRBGF structure, which corresponded to a lateral design load $F_{k,BRB}$ (Eq. 4.7) of 226 kN, 436 kN and 629 kN, respectively. All connections were designed with a connection relative overstrength factor $\gamma_{os,con}$=$\gamma_{os,BRB}$ to achieve an economical connection design according to the parametric studies in Section 4.4, i.e. the design strength of connections was 1.5 times the load transferred to the connections when BRBs yielded. Although f_{sm} depends on the BRB geometry (Aguaguina et

al., 2019), it usually varies within ±10% if the same grade of steel is used. In this regard, three different values of f_{sm} were included to consider the influence of BRB stiffness. Besides, three different levels of initial slips caused by the manufacturing tolerances were considered for ideally tight, medium and maximum allowable manufacturing tolerances in practice as discussed in Chapter 4. Based on the combination in Table 5.1, 27 configurations of BRBGFs for the dowelled connections (S-D) and 27 configurations of BRBGFs for the screwed connections (S-S) were considered in the simulations and each of them was denoted according to the combination of design variables. For example, "S-D 75×20-1.22-2.5" represents a BRBGF with the dowelled connections, 75×20 mm yield zone of BRBs, f_{sm} =1.22, and ±2.5 mm initial slips.

Table 5.1 Parameters of one-storey BRBGF models

Variables	Values
Cross-section of yield zone (mm×mm)	45×12, 65×16, 75×20
f_{sm}	1.10, 1.22, 1.34
Initial slips (± mm)	±0.0, ±2.5, ±4.0 for BRBGFs with the dowelled connections (S-D); and ±0.0, ±1.0, ±2.5 for BRBGFs with the screwed connections (S-S)

5.3.2 Analysis of one-storey BRBGF models

The 54 configurations of numerical models were analysed following the procedure in Figure 5.11. The process will be described below.

5.3.2.1 Pushover analyses for λ

The pushover analyses were conducted for each of the 54 BRBGF models and the lateral stiffness k_{BRBGF} was recorded to calculate the λ. Table 5.2 and Table 5.3 list the results of λ for S-D and S-S, respectively. λ for S-D ranged from 0.70 to 0.74, while λ for S-S ranged from 0.50 to 0.56. The average of λ was used in Eq. 5.12a for the estimation of yield drift, i.e. λ=0.72 for S-D and λ=0.53 for S-S.

Table 5.2 The results of the stiffness adjustment factor λ for S-D

BRB cross-section	45×12			65×16			75×20		
f_{sm}	1.10	1.22	1.34	1.10	1.22	1.34	1.10	1.22	1.34
λ	0.74	0.72	0.70	0.74	0.71	0.70	0.74	0.72	0.70

Table 5.3 The results of the stiffness adjustment factor λ for S-S

BRB cross-section	45×12			65×16			75×20		
f_{sm}	1.10	1.22	1.34	1.10	1.22	1.34	1.10	1.22	1.34
λ	0.56	0.53	0.51	0.55	0.52	0.50	0.55	0.52	0.50

It is noted that although $\gamma_{os,BRB}$ can be different for BRB products from different manufacturers, the calibration process of λ should be the same and the approximate value of λ

can be calibrated for other BRB products with several pushover analyses. Therefore, the proprietary properties of BRBs will not restrain the application of the DDBD approach.

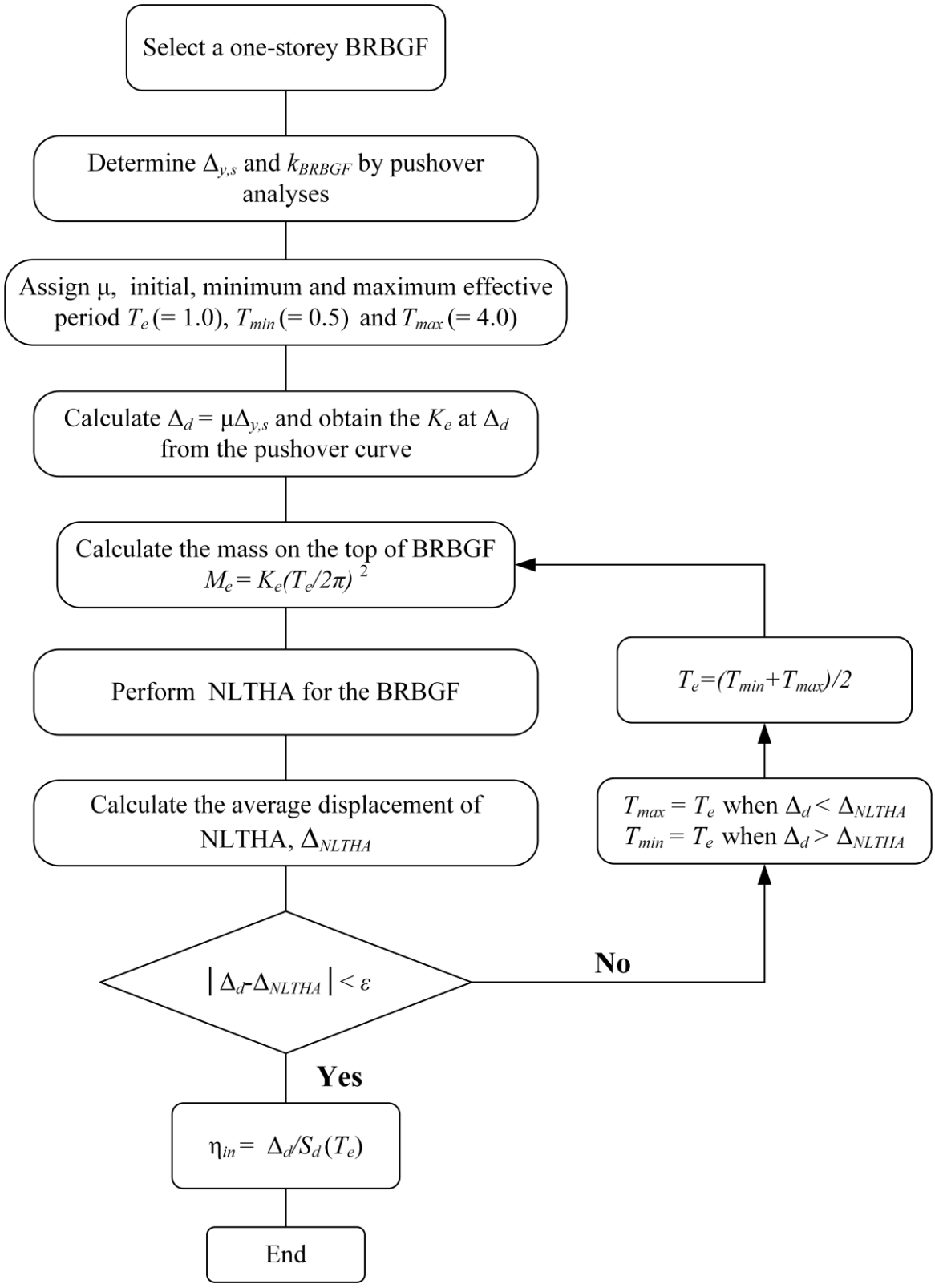

Figure 5.11 Procedure of parameter verification

5.3.2.2 Nonlinear time-history analyses (NLTHA) for η_{in}

NLTHA were conducted for each of the 54 BRBGF models to verify the η_{in}-μ relationship with the following steps.

Step 1: obtain the $F_{k,BRB}$ and $\Delta_{y,s}$ for each BRBGF model

The load-drift curves from the pushover analyses were obtained, and the $F_{k,BRB}$ *and* $\Delta_{y,s}$ of BRBGF models were recorded. For example, Figure 5.12 shows that the yield drifts for "S-D 75×20-1.22-0.0" and "S-D 75×20-1.22-0.0" were 10.4 mm ($\Delta_{y,0}$) and 12.9 mm ($\Delta_{y,s}$), respectively, and the $F_{k,BRB}$ was 629 kN according to Eq. 5.9.

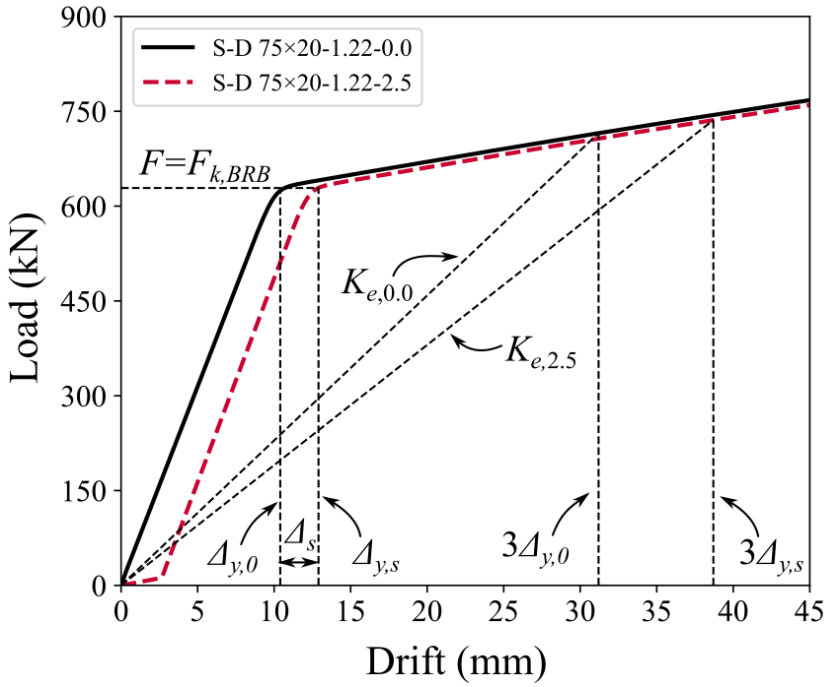

Figure 5.12 Pushover analysis of one-storey BRBGF

Step 2: assign μ and initial effective period T_e for BRBGF models

The ductility factor μ for the one-storey BRBGF models is defined as Eq. 5.20a. The maximum ductility factor μ_{max} was set as 6.0 and the maximum lateral design drift $\Delta_{d,max}$ of BRBGFs was set to be $\mu_{max}\Delta_{y,s}$. Although the experimental tests in Chapter 3 had a yield drift around 15 mm and only achieved a maximum ductility factor μ_{max} of 3.3, the pushover analyses for the numerical models showed that the yield drift $\Delta_{y,s}$ was approximately 12.0 mm if $\gamma_{os,con}$=$\gamma_{os,BRB}$ was achieved by using good-quality BRBs. The $\Delta_{y,s}$ from the BRBGF tests was larger than the numerical results from the pushover analyses because higher strength and stiffness of BRBs in the tests reduced $\gamma_{os,con}$. The experimental tests in Chapter 3 proved that the glulam frames were able to reach a 2% drift ratio (72 mm) without significant damages to the glulam members and connections, so μ_{max}=6.0 was a reasonable value for the BRBGF system. Higher μ_{max} (i.e. μ_{max}>6.0) may be assigned if test data at a higher drift are available. It is also noticed from Eq. 5.20 that at the same μ, BRBGFs with higher initial slips require higher deformation capacity.

The initial effective period T_e was set as 1.0 s for iterations.

$$\mu = \frac{\Delta_d}{\Delta_{y,s}} = \frac{\Delta_d}{\Delta_{y,0} + \Delta_s} \quad \text{Eq. 5.20a}$$

$$\Delta_d = \mu \Delta_{y,s} \quad \text{Eq. 5.20b}$$

Step 3: calculate K_e and M_e

The effective stiffness K_e was obtained from the pushover curves. For example, Figure 5.12 shows that the K_e for "S-D 75×20-1.22-0.0" and "S-D 75×20-1.22-0.0" were 22.9 kN/mm ($K_{e,0.0}$) and 19.0 kN/mm ($K_{e,2.5}$), respectively. The corresponding effective masses were calculated as 580 tons and 481 tons for "S-D 75×20-1.22-0.0" and "S-D 75×20-1.22-0.0", respectively according to Eq. 5.21.

$$M_e = K_e \left(\frac{T_e}{2\pi}\right)^2 \quad \text{Eq. 5.21}$$

Step 4: ground motion selection for NLTHA

Table 5.4 Ground motion records and scale factors for NLTHA

No.	Event	Station	RSN	Component	Magnitude	V_{s30} (m/s)	SF1	SF2
1	Chi-Chi	TAP042	1430	E	7.62	273	0.71	2.92
2	Landers	Desert Hot Springs	850	090	7.28	345	0.86	3.00
3	Hector	USGS 5295 North Palm Springs Fire Sta #36	1816	270	7.13	345	1.35	5.51
4	Darfield	Westerfield (WSFC)	-*	N00E	7.10	-	1.90	7.23
5	Loma Prieta	CDMG 47179 Salinas-John & Work	800	160	6.93	271	1.08	4.72
6	Kobe	OSAJ	1113	090	6.90	256	0.77	3.43
7	Superstition Hills-02	USGS 5210 Wildlife	729	090	6.54	208	0.41	1.89
8	Imperial Valley-06	Delta	169	352	6.53	275	0.40	1.47
9	Chi-Chi Taiwan-03	CHY055	2477	W	6.20	226	1.54	6.65
10	Chalfant Valley-02	CDMG 54171 Bishop-LADWP South St	549	180	6.19	271	0.83	3.02

*Note: from GeoNet database (https://www.geonet.org.nz/)

Ten ground motion records selected by Maley et al. (2013) from the Pacific Earthquake Engineering Research Centre database (PEER, 2005) and GeoNet (Houtte et al., 2017) were used as listed in Table 5.4. The near-fault effect was not considered in the records. Their average acceleration spectra were scaled to match the design acceleration spectra of soil type D in NZS 1170.5 (2004). The average acceleration spectra were scaled to the intensity levels

0.23g with a return period of 25 years as shown in Figure 5.13, so that T_e of the equivalent SDOF system mostly fell into the T_e >1.0 s region. The research by Dwairi et al. (2007) and Grant et al. (2005) has shown that η_{in} is lower when T_e <1.0 s than that when T_e >1.0 s. It is also found that T_e for most structures should fall into the T_e >1.0 s region for multi-storey buildings (Priestley et al., 2007a), so scaling into T_e >1.0 s region will result in a reasonable and conservative prediction. The scale factors are denoted as SF1 in Table 5.4 and the design acceleration spectrum $S_a(T)$ in Figure 5.13 was transferred to the design displacement spectrum $S_d(T)$ by Eq. 5.22 to calculate η_{in}.

$$S_d(T) = \left(\frac{T}{2\pi}\right)^2 S_a(T) \qquad \text{Eq. 5.22a}$$

$$S_a(T) = NZRC_h(T) \qquad \text{Eq. 5.22b}$$

$$C_h(T) = \begin{cases} 1.12 + 1.88\left(\dfrac{T}{0.1}\right) & 0.0s < T < 0.1s \\ 3.0 & 0.1s \le T < 0.56s \\ 2.4\left(\dfrac{0.75}{T}\right)^{0.75} & 0.56s \le T \le 1.5s \\ \dfrac{2.14}{T} & T > 1.5s \end{cases} \qquad \text{Eq. 5.22c}$$

where N (=1.0) is the near-fault factor;

Z (=0.3) is the hazard factor for Christchurch according to NZS 1170.5;

R (=0.25) is the return period factor; and

$C_h(T)$ is the spectrum shape factor.

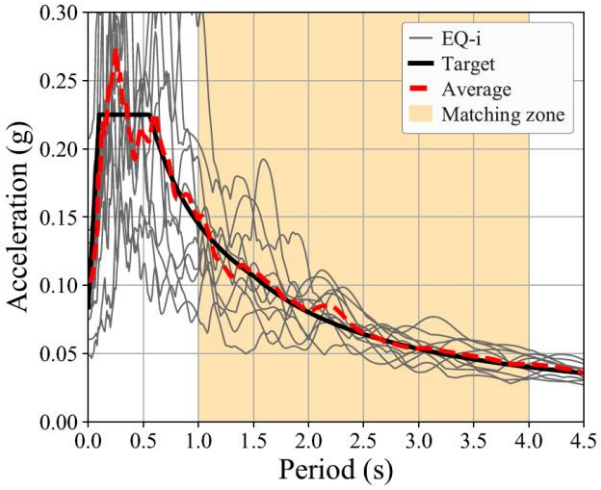

Figure 5.13 Acceleration spectra scaling process

Step 5: run NLTHA for the BRBGF models

The effective mass M_e in Step 3 was added at the top of the BRBGF models (i.e. node 2 and 4 in Figure 5.3). NLTHA were conducted for each model and the average drift Δ_{NLTHA} from the ten ground motions was obtained and compared with the target drift Δ_d calculated by Eq. 5.20b. If the difference between Δ_{NLTHA} and Δ_d was within the error tolerance ε (set as 5%), the effective period T_e would be recorded. Otherwise, the T_e would be replaced as shown in Figure 5.11 by the half-interval search. The initial upper and lower boundary of the effective periods T_{min} and T_{max} was set as 0.5 s and 4.0 s, respectively, because this range should cover all possible periods for the BRBGF models. The M_e was updated by Eq. 5.21 and the NLTHA were performed again with the updated M_e to obtain updated Δ_{NLTHA}. The iterations were repeated until the difference between Δ_{NLTHA} and Δ_d was within ε. For example, the initial Δ_{NLTHA} for "S-D 75×20-1.22-2.5" at μ=3.0 was 28.5 mm and Δ_d was 38.7 mm. The difference was over 5%, so T_e was replaced by 2.5 s according to the half-interval search for the next iteration. After six times of iterations (i.e. the T_e was assigned as 1.0 s, 2.5 s, 1.8 s, 1.4 s, 1.6 s and 1.7 s sequentially), Δ_{NLTHA} was 37.5 mm with a difference of less than 5%. The corresponding effective period T_e and effective mass M_e was 1.7 s and 1359 tons, respectively.

Step 6: calculate displacement reduction factor η_{in}

The displacement reduction factor η_{in} was calculated by Eq. 5.23. For example, Δ_d was 38.7 mm at μ=3.0 and the displacement spectrum $S_d(T_e)$ was 67.7 mm at T_e=1.7 s for "S-D 75×20-1.22-2.5". These resulted in η_{in}=0.57. The NLTHA were conducted for each one-storey BRBGF model from μ=1.5 to 6.0 with an increment of 0.5, resulting in 270 equivalent SDOF systems for S-D and 270 equivalent SDOF systems for S-S. Among the 270 equivalent SDOF systems for S-D, T_e of 27 equivalent SDOF systems fell outside the matching zone in Figure 5.13 and were removed. Similarly, 37 equivalent SDOF systems for S-S were removed. The rest of the systems were used to calculate η_{in} and the results of η_{in} are shown in Figure 5.14. It was found that the three variables in Table 5.1 had a minor impact on the η_{in}-μ relationship. For example, the η_{in} results from equivalent SDOF systems with different initial slips were plotted with different symbols in Figure 5.14 and no significant difference was observed among them. The reason might be that these variables primarily impacted the magnitude of the yield drift $\Delta_{y,s}$, while μ defined by Eq. 5.15b had included the influence of $\Delta_{y,s}$. Figure 5.14 also shows that the best-fitted curve (denoted as $\eta_{in,4}$) was close to $\eta_{in,3}$ for the Takeda fat model and slightly smaller than $\eta_{in,3}$, i.e. on the conservative side. It is worth mentioning that the data points in Figure 5.14 shifted slightly from convex to concave at higher ductility levels (μ≥5.0). This could be caused by the increasingly higher energy dissipation capacity of the BRB component-based models than Takeda fat model as shown in Figure 5.15. Therefore, $\eta_{in,3}$ (Eq. 5.19) based on numerous NLTHA can be used to represent the displacement reduction factor of the BRBGF system conservatively. The similarity between these two models was verified under cyclic loads (Figure 5.9a) and under transient loads (Figure 5.14).

$$\eta_{in} = \frac{\Delta_d}{S_d(T_e)} \qquad \text{Eq. 5.23}$$

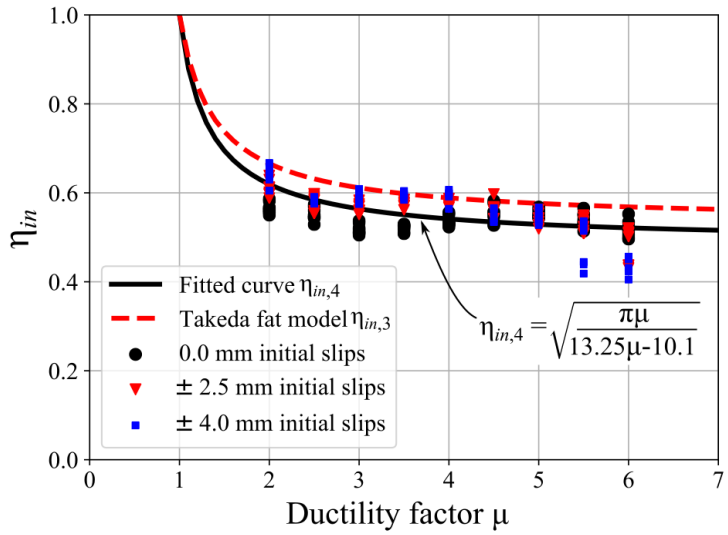

a) S-D model

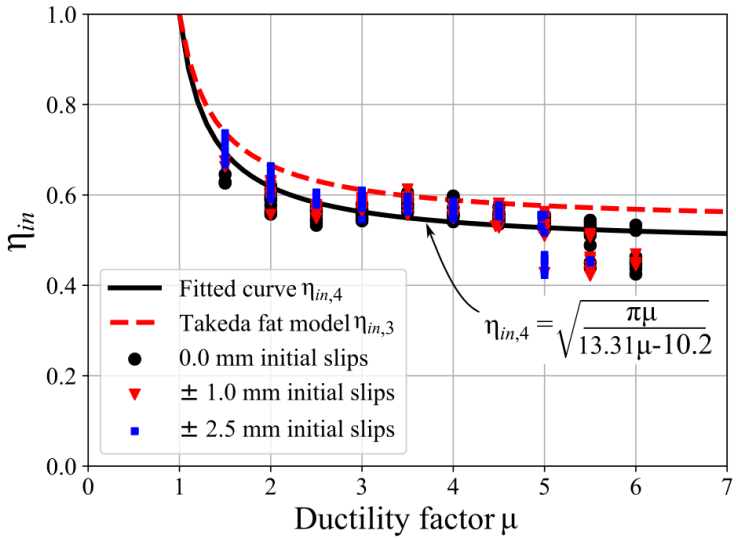

b) S-S model

Figure 5.14 η_{in}-μ relationship verification

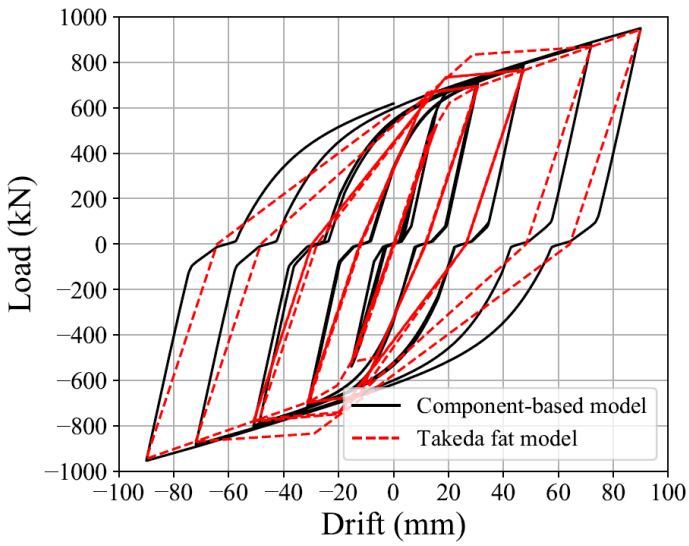

a) Hysteresis loop

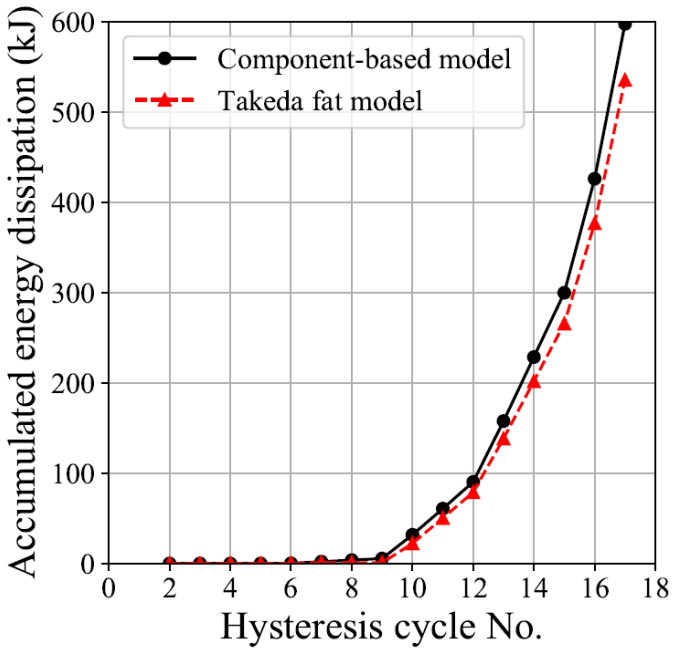

b) Energy dissipation

Figure 5.15 Comparison between component-based model and Takeda fat model at large displacement

5.4 Summary

This chapter extended the DDBD approach to the BRBGF system and the critical design parameters were discussed. In addition, the stiffness adjustment factor λ and displacement reduction factor η_{in} were verified by pushover analyses and NLTHA, respectively. A summary is listed as follows:

1) The stiffness of BRB-timber connections in BRBGFs needs to be considered. The stiffness adjustment factor λ=0.72 and λ=0.53 was introduced for the yield drift prediction of the BRBGF system with the dowelled connections and screwed connections, respectively, based on pushover analyses.
2) The relationship between η_{in} and ductility factor μ for the Takeda fat model was proved to be suitable for the BRBGF system and provided conservative prediction based on the NLTHA of one-storey BRBGF models. The strength and stiffness of BRBs and initial slips caused by manufacturing tolerances had negligible influence on the η_{in}-μ relationship.

6 VERIFICATION OF THE DDBD APPROACH

This chapter uses the DDBD approach to design case study BRBGF systems. The λ and η_{in}-μ relationship presented in Chapter 5 will be implemented to design a set of BRBGFs with three, six, and nine storeys at ULS. Then, numerical models of the multi-storey BRBGFs will be built based on the numerical method developed in Chapter 4. After that, NLTHA will be conducted for the BRBGF buildings to verify the assumed displacement profile and the feasibility of the DDBD approach. This chapter is based on a journal paper (Dong et al., 2021b) submitted to *Engineering Structures*.

6.1 Case study buildings

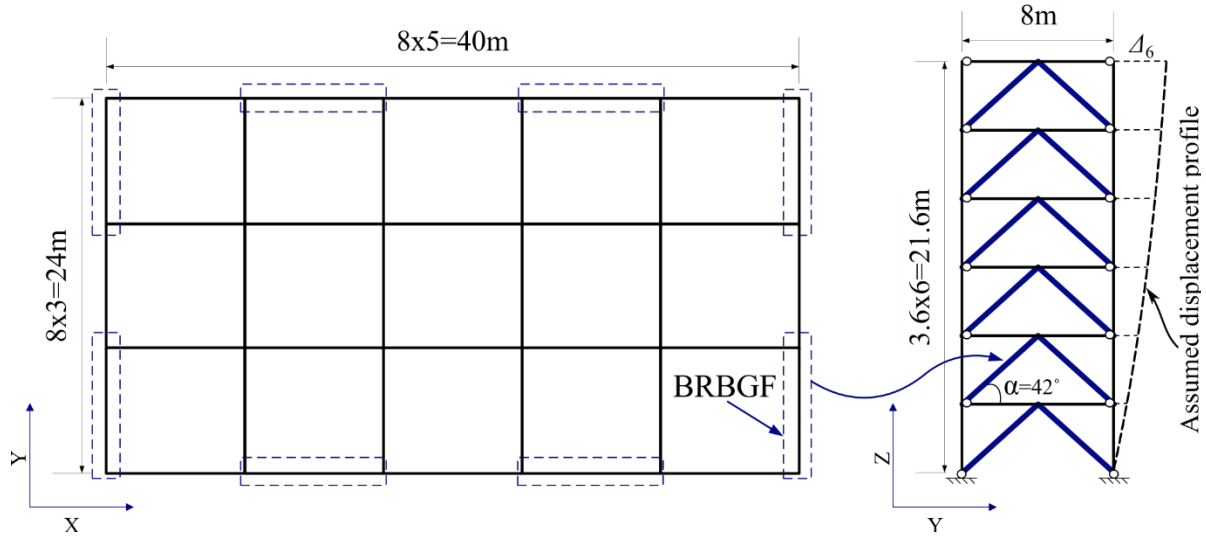

a) Plan view b) Side view

Figure 6.1 BRBGF-6 design example

A set of BRBGFs with three, six and nine storeys were assumed as case study buildings and they were denoted as BRBGF-3, BRBGF-6, BRBGF-9, respectively. For simplicity, these buildings shared the same floor plan. As an example, the floor plan and the elevation view of BRBGF-6 are shown in Figure 6.1. The buildings were located in Christchurch, New Zealand. The glulam columns were used and their cross-sections only changed every three storeys to facilitate transportation and minimize the number of splice joints. The column splice joints were pinned connections that only transfer the axial forces and shear forces because it is challenging and costly to achieve a moment column splice joint. The weights of the floors and roofs were obtained from the CLT manufacturer (XLam NZ Limited, 2016) and all loading information is listed in Table 6.1 according to NZS 1170.5 (2004). The materials used for the BRBGF buildings are listed in Table 6.2. The elastic viscous damping ratio ξ_{el} of the BRBGF system was assumed to be 2% according to the research by Hashemi et al. (2020).

Table 6.1 Loading information of case study buildings

Item	Value	Item	Value
Importance level	2	Return period factor *R*	1.0
Design working life	50 years	Near-fault factor *N*	1.0
Annual probability of exceedance	1/500	Dead load on floor	1.8 kPa
Site subsoil class	D	Dead load on roof	1.6 kPa
Hazard factor *Z*	0.3	Live load on floor	3 kPa

Table 6.2 Material properties of BRBGFs

Members	Materials	Properties
BRBs	S235 flat plate	Nominal yield strength $f_{ys,BRB}$ =235 MPa; Elastic modulus $E_{s,BRB}$ =210 GPa; Material overstrength factor ϕ_m =1.2.
Beams and columns	GL10 New Zealand *Radiata Pine*	Bending strength f_b =22 MPa; Compression strength parallel to grain f_c =26 MPa; Tension strength parallel to grain f_t =11 MPa; Shear strength f_s =3.7 MPa; Elastic modulus E_{GL} =10 GPa.
BRB-timber connections	Dowelled connections	The properties are the same as those listed in Table 3.2

6.2 Process of DDBD approach

The ULS design was conducted for the three buildings to verify the DDBD approach. The design inter-storey drift ratio limit θ_d was set to be 2.0% for the BRBGFs at ULS as explained in Subsection 5.2.1. The three displacement profiles described in Subsection 5.2.1 were used for the design, which resulted in nine building design scenarios as listed in Table 6.3. For example, the design information based on the three displacement profiles for BRBGF-6 is listed in Table 6.4-Table 6.6. For the other six building design scenarios, the detailed design parameters can be found in Appendix A.

Table 6.3 Case study building design

Case study building	Displacement profile
BRBGF-3	Profile L/ Profile P/ Profile C
BRBGF-6	Profile L/ Profile P/ Profile C
BRBGF-9	Profile L/ Profile P/ Profile C

The MDOF BRBGF system was transferred to its equivalent SDOF with the design displacement Δ_d, equivalent mass M_e and equivalent height H_e according to Eq. 5.1-Eq. 5.3.

The calculation results for BRBGF-6 are listed in Table 6.4-Table 6.6. Table 6.4-Table 6.6 show that the different displacement profiles resulted in different design displacement Δ_d.

Table 6.4 Design parameters for BRBGF-6 with Profile L (linear profile)

Storey	h_i	H_i	m_i (ton)	Δ_i (mm)	$\Delta_{y,i,BRB}$ (mm)	$\Delta_{y,i,col}$ (mm)	Δ_s *(mm)*	$\Delta_{y,i}$ (mm)	μ	V_i	F_i (kN)
1	3.6	3.6	65.6	72.0	11.1	0.0	2.5	13.6	5.3	1.00	21
2	3.6	7.2	65.6	144.0	11.1	1.7	2.5	15.3	4.7	0.95	43
3	3.6	10.8	65.6	216.0	11.1	3.5	2.5	17.0	4.2	0.85	64
4	3.6	14.4	65.6	288.0	11.1	5.2	2.5	18.8	3.8	0.71	85
5	3.6	18	65.6	360.0	11.1	7.0	2.5	20.5	3.5	0.51	107
6	3.6	21.6	38.0	432.0	11.1	8.7	2.5	22.3	3.2	0.27	118
Δ_d=295.3 mm, M_e=295 tons, H_e=14.8 m, μ_{sys}=4.4, T_e=3.01 s, V_{base}=438 kN											

Table 6.5 Design parameters for BRBGF-6 with Profile P (parabolic profile)

Storey	h_i	H_i	m_i (ton)	Δ_i (mm)	$\Delta_{y,i,BRB}$ (mm)	$\Delta_{y,i,col}$ (mm)	Δ_s *(mm)*	$\Delta_{y,i}$ (mm)	μ	V_i	F_i (kN)
1	3.6	3.6	65.6	72.0	11.1	0.0	2.5	13.6	5.3	1.00	31
2	3.6	7.2	65.6	137.7	11.1	1.7	2.5	15.3	4.3	0.94	59
3	3.6	10.8	65.6	197.2	11.1	3.5	2.5	17.0	3.5	0.84	84
4	3.6	14.4	65.6	250.4	11.1	5.2	2.5	18.8	2.8	0.68	107
5	3.6	18	65.6	297.4	11.1	7.0	2.5	20.5	2.3	0.49	127
6	3.6	21.6	38.0	338.1	11.1	8.7	2.5	22.3	1.8	0.25	138
Δ_d=243.7 mm, M_e=310 tons, H_e=14.4 m, μ_{sys}=3.9, T_e=2.46 s, V_{base}=544 kN											

Table 6.6 Design parameters for BRBGF-6 with Profile C (cubic profile)

Storey	h_i	H_i	m_i (ton)	Δ_i (mm)	$\Delta_{y,i,BRB}$ (mm)	$\Delta_{y,i,col}$ (mm)	Δ_s *(mm)*	$\Delta_{y,i}$ (mm)	μ	V_i	F_i (kN)
1	3.6	3.6	65.6	72.0	11.1	0.0	2.5	13.6	5.3	1.00	51
2	3.6	7.2	65.6	121.3	11.1	1.7	2.5	15.3	3.2	0.93	87
3	3.6	10.8	65.6	158.1	11.1	3.5	2.5	17.0	2.2	0.82	113
4	3.6	14.4	65.6	192.9	11.1	5.2	2.5	18.8	1.9	0.67	138
5	3.6	18	65.6	236.0	11.1	7.0	2.5	20.5	2.1	0.49	168
6	3.6	21.6	38.0	297.6	11.1	8.7	2.5	22.3	2.8	0.26	199
Δ_d = 198.5 mm, M_e = 315 tons, H_e=14.3 m, μ_{sys}=3.5, T_e = 1.86 s, V_{base}= 756 kN											

The yield drift at each storey was calculated by Eq. 5.11-Eq. 5.14 and each component is listed in Table 6.4-Table 6.6. Then the system ductility factor μ_{sys} was calculated by Eq. 5.15 where V_{base} was assumed to be 1.0. Table 6.4-Table 6.6 show that different displacement profiles led to different system ductilities μ_{sys} and base shear forces V_{base}. Profile L resulted in the largest μ_{sys} and lowest base shear forces among the three displacement profiles, while Profile C resulted in the lowest μ_{sys} and highest base shear forces. Therefore, Profile C provided the most conservative design among the three displacement profiles.

The system ductility μ_{sys} was used to calculate η_{in} according to Eq. 5.19. However, the η_{in}-μ relationship in Eq. 5.19 was for the equivalent SDOF system with ξ_{el}=5%. An elastic damping ratio adjustment factor γ_{el} derived by Pennucci et al. (2011) was used to adjust the η_{in}-

μ relationship at ξ_{el}=5% to that at ξ_{el}=2% (the corresponding η_{in} was denoted as $\eta_{in,\xi=2\%}$) as shown in Eq. 6.1 and Eq. 6.2. Similarly, the displacement spectrum S_d (T) in Eq. 5.22 was also based on ξ_{el}=5% and needed to be adjusted to that at ξ_{el}=2% (denoted as $S_{d,2\%}$ (T)) as well. $S_{d,2\%}(T)$ was obtained by using $\eta_{in,2}$ (Eq. 5.18b) according to Eurocode 8 (2005b) as shown in Eq. 6.3. For example, S_d(T), $S_{d,2\%}$ (T), $\eta_{in,\xi=2\%}$ $S_{d,2\%}$ (T) were calculated as shown in Figure 6.2 for BRBGF-6 with Profile P. The effective period T_e =2.46 s was obtained from the reduced displacement spectrum (i.e. $\eta_{in,\xi=2\%}\cdot S_{d,2\%}$ (T)) by using Δ_d =243.7 mm as shown in Figure 6.2. It is worth mentioning that the effective period T_e =2.46 s was based on the secant stiffness K_e according to Priestley et al. (Priestley et al., 2007a) and would be much longer than the fundamental period T_1 based on K_1 as shown in Figure 5.1b.

$$\eta_{in,\xi=2\%} = \frac{\Delta_d}{S_{d,2\%}(T)} = \gamma_{el}\eta_{in,\xi=5\%} = \gamma_{el}\eta_{in,3} \qquad \text{Eq. 6.1}$$

$$\gamma_{el} = \left(1 - 0.25\frac{5\% - \xi_{el}}{5\%}\right)^{1.5\frac{\mu-1}{\mu}} \qquad \text{Eq. 6.2}$$

$$S_{d,2\%}(T) = \eta_{in,2}(\xi_{el} = 2\%)S_d(T) = \sqrt{\frac{10}{5+\xi_{el}}}S_d(T) = \sqrt{\frac{10}{5+2}}S_d(T) \qquad \text{Eq. 6.3}$$

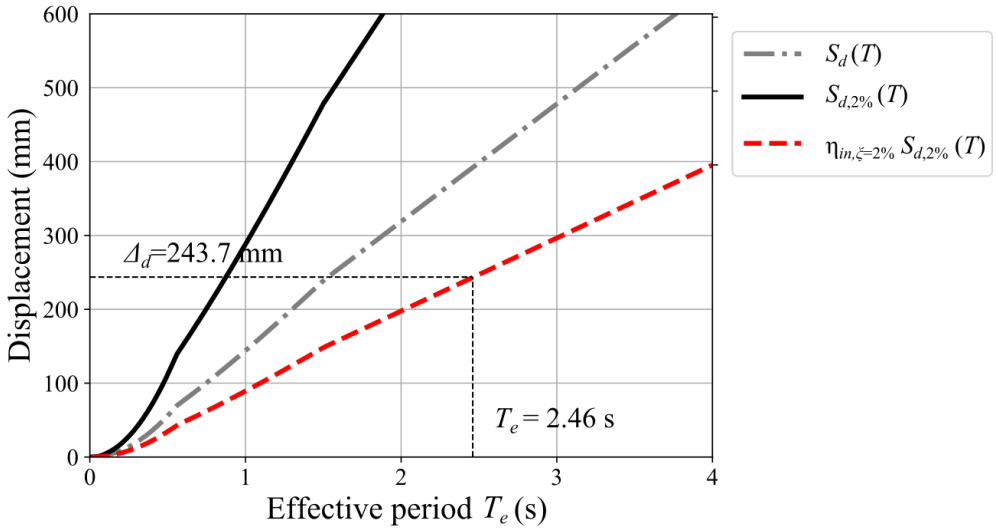

Figure 6.2 Adjusted displacement spectrum

The effective stiffness K_e and base shear force V_{base} included the P-Δ effects were obtained by Eq. 6.4 and Eq. 6.5, respectively according to Sullivan et al. (2012).

$$K_e = (\frac{2\pi}{T_e})^2 M_e \qquad \text{Eq. 6.4}$$

$$V_{base} = V_d + V_{P-\Delta} \qquad \text{Eq. 6.5a}$$

$$V_d = K_e\Delta_d \qquad \text{Eq. 6.5b}$$

$$V_{P-\Delta} = C_{P-\Delta} \frac{\sum_{i=1}^{n} m_i \, g \Delta_i}{H_e} \quad \text{Eq. 6.5c}$$

$$C_{P-\Delta} = \begin{cases} 0.0 & \frac{M_e g}{K_e H_e} < 0.05 \\ 1.0 & \frac{M_e g}{K_e H_e} \geq 0.05 \end{cases} \quad \text{Eq. 6.5d}$$

where, $V_{P\text{-}\Delta}$ is the addition base shear force in terms of the P-Δ effects;

$C_{P\text{-}\Delta}$ is the force adjustment factor for the P-Δ effects; and

g=(9.8m/s^2) is the gravitational acceleration.

The same process was conducted on all the nine BRBGF buildings. The design parameters of the three BRBGF buildings with Profile P are listed in Table 6.7 as an example. The detailed design information of the other six BRBGFs can be found in Appendix A.

Table 6.7 DDBD information of case study buildings with Profile P

Parameters	BRBGF-3	BRBGF-6	BRBGF-9
Δ_d (mm)	132.4	243.7	341.1
M_e (ton)	151	310	466
H_e (m)	7.6	14.4	21.4
μ_{sys}	4.5	3.9	3.4
$\eta_{in,2\%}$	0.48	0.49	0.50
T_e (s)	1.38	2.46	3.38
V_{base} (kN)	441	544	622

6.3 BRB and glulam member design

The base shear force V_{base} was distributed along with the height of BRBGFs according to Eq. 5.15d. The shear force at i-th storey V_i was resisted by two BRBs which were designed by Eq. 6.6. Glulam beams and columns were protected by the capacity design approach considering the BRB overstrength factor $\gamma_{os,BRB}$ (=1.5). The glulam columns were designed by the maximum axial load. The glulam beams were designed by the combination of the maximum axial load and the corresponding moment caused by the uneven force of two BRBs at the middle span (López and Sabelli, 2004). The member sizes for BRBGF-6 with three displacement profiles are listed in Table 6.8-Table 6.10 as an example. The member sizes for the other six BRBGFs can be found in Appendix A.

$$A_{c,i} = \frac{N_{i,BRB}}{\phi_m f_{ys,BRB}} \quad \text{Eq. 6.6a}$$

$$N_{i,BRB} = \frac{V_i}{2cos\alpha} \quad \text{Eq. 6.6b}$$

where, $A_{c,i}$ is the yield zone area of BRB at *i*-th storey; and

$N_{i,BRB}$ is the BRB axial load caused by V_i at *i*-th storey.

Table 6.8 Member size information of BRBGF-6 with Profile L

Storey	V_i (kN)	BRB cross-section (mm)	Middle span connection ($n_r \times n_c$)	Beam (mm)	Column (mm)
1	438	12×84	5×5	405×270	360×360
2	417	12×80	4×6	405×270	
3	374	12×72	3×7	360×270	
4	310	12×60	3×6	360×270	225×225
5	225	8×65	3×4	315×225	
6	118	8×35	2×4	315×225	

Table 6.9 Member size information of BRBGF-6 with Profile P

Storey	V_i (kN)	BRB cross-section (mm)	Middle span connection ($n_r \times n_c$)	Beam (mm)	Column (mm)
1	544	16×82	4×8	405×315	360×360
2	513	16×77	5×6	405×315	
3	455	16×68	4×7	405×270	
4	371	12×74	3×8	405×270	270×270
5	264	12×53	3×5	315×270	
6	138	8×42	3×3	315×270	

Table 6.10 Member size information of BRBGF-6 with Profile C

Storey	V_i (kN)	BRB cross-section (mm)	Middle span connection ($n_r \times n_c$)	Beam (mm)	Column (mm)
1	756	20×87	6×8	495×315	495×495
2	705	20×81	6×7	495×315	
3	618	20×71	5×8	450×315	
4	505	16×73	5×6	450×315	315×315
5	367	12×71	3×7	360×270	
6	199	8×57	3×4	360×270	

6.4 Verification by NLTHA

The DDBD approach was verified by NLTHA using the numerical models developed in OpenSees. The rigid diaphragm assumption was applied to the case study buildings, so the seismic load was assumed to be equally distributed into four BRBGFs in each direction of Figure 6.1. For simplification, only one bay BRBGF was modelled and the gravity frames were simulated as a leaning column as shown in Figure 6.3 with the BRBGF-6 model as an example. One-fourth of the seismic mass of the whole building was lumped onto the selected nodes of the BRBGF and the leaning members. These seismic mass m_{total} was allocated into the BRBGF

and the gravity frames according to their tributary areas. The seismic mass of floors and roofs in BRBGFs was calculated by Eq. 6.7 according to NZS 1170.5 (2004) and the load information in Table 6.1. The tributary area $A_{tributary}$ for BRBGFs in the X direction was 32 m^2 which came up with the seismic mass on floor $m_{f,f}$ (=8.7 tons) and roof $m_{r,f}$ (=5.1 tons). The rest of m_{total} were added on gravity frames modelled as the leaning column. The seismic mass on floor nodes and roof node were $m_{f,l}$ (=48.1 tons) and $m_{r,l}$ (=27.8 tons), respectively. The glulam columns were simulated by continuous elastic beam elements across three storeys and pin connections were assumed every three storeys to connect the lower-storey columns and upper-storey columns.

$$S_{d,earthquake} = (G + \varphi_E Q)A_{tributary} \quad \text{Eq. 6.7}$$

where $S_{d,earthquake}$ is the seismic load demand;

G and Q are the dead load and live load, respectively; and

$A_{tributary}$ is the corresponding tributary area.

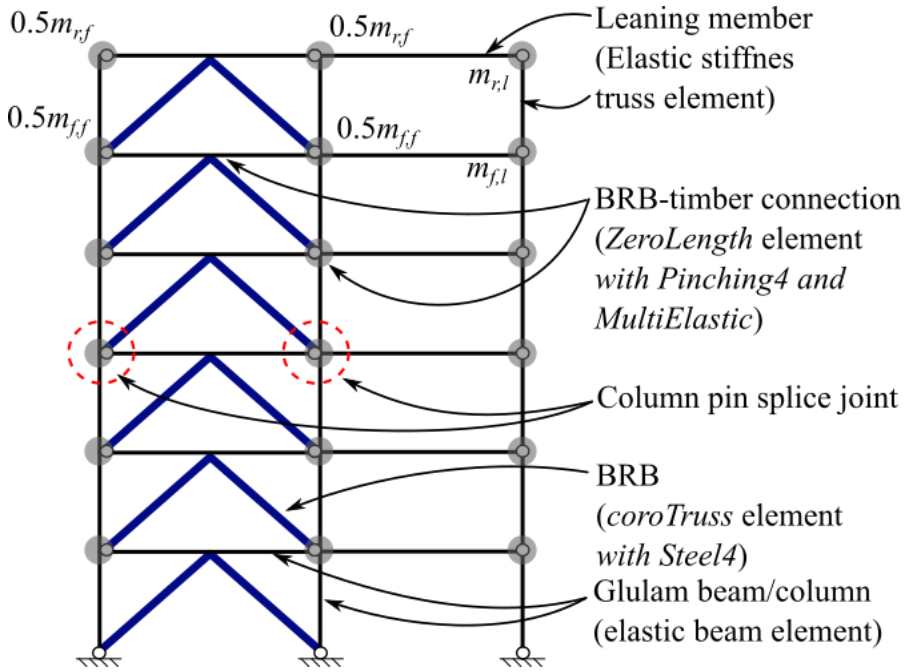

Figure 6.3 BRBGF-6 OpenSees model

The damping model from Lee (2020a, 2020b) was used for NLTHA. In the current implementation of Lee damping model in OpenSees, the damping coefficient matrix C_d is assumed to be proportional to the structural tangent stiffness matrix (Lee, 2021). Lee damping model targets a constant elastic damping ratio ξ_{el} over an assigned frequency range as shown in Figure 6.4, which complies with the basic assumption in earthquake dynamics of structures better than Rayleigh damping model (Chopra and McKenna, 2016). The general drawbacks of Rayleigh damping have been discussed in detail (Charney, 2008; Chopra and McKenna, 2016). Figure 6.4 shows ξ_{el} at the first natural frequency ($\omega_{f,s,1}$) and second natural frequency ($\omega_{f,s,2}$) of a BRBGF structure with 2.5 mm initial slips as well as ξ_{el} at the first natural frequency ($\omega_{f,ws,1}$)

of a BRBGF structure without initial slips. The BRBGF structure with initial slips had lower initial stiffness than that without initial slips and thus had lower first natural frequency $\omega_{f,s,1}$ when compared with $\omega_{f,ws,1}$. It is found from Figure 6.4 that the Rayleigh damping model may slightly underestimate ξ_{el} when the slips of BRBGF structures are overcome and significantly overestimate ξ_{el} at higher modes when compared with Lee damping model. Therefore, Lee damping model can avoid unrealistically high damping ratio prediction at higher modes. It also avoids spurious damping forces during inelastic responses.

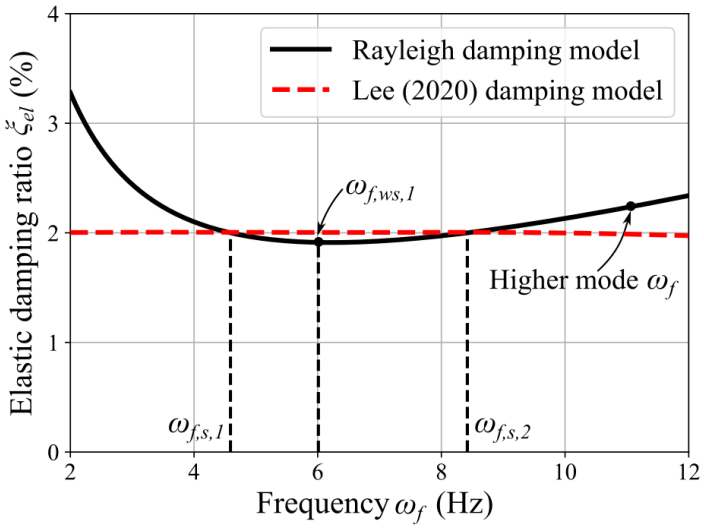

Figure 6.4 Damping ratio in different damping models

6.4.1 Ground motion selection

The same ten ground motions in Table 5.4 were scaled to match the design acceleration and displacement spectrum at ULS with a return period of 500 years. The matching period is from 0.3 s-3.5 s as shown in Figure 6.5, which is enough to cover most of T_1 and T_e for the case study buildings. The scale factors are listed in Table 5.4 as SF2.

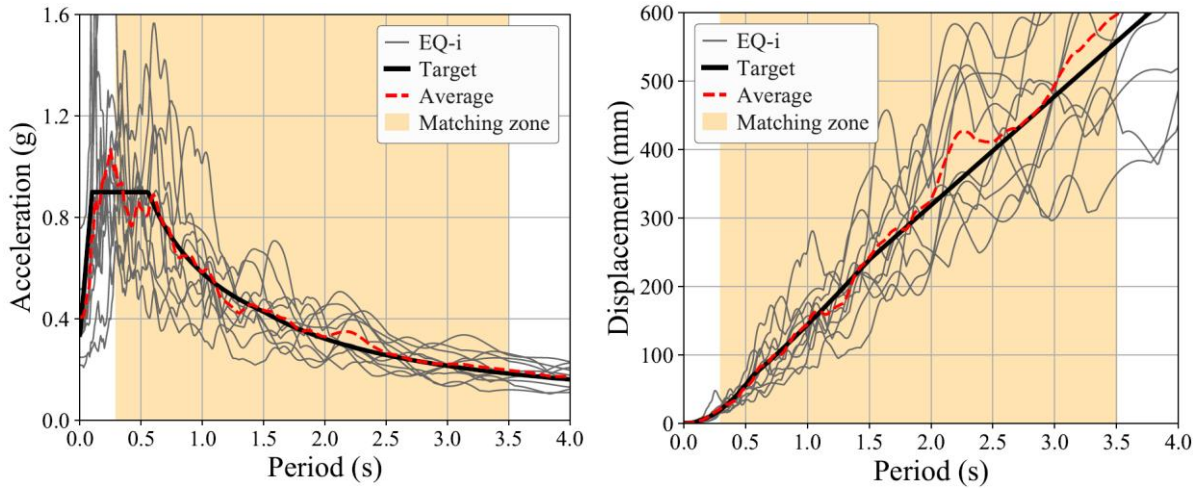

a) Acceleration spectra b) Displacement spectra

Figure 6.5 Acceleration spectrum and displacement spectrum matching

6.4.2 Displacement and inter-storey drift ratio responses

Figure 6.6-Figure 6.8 show the maximum displacement and inter-storey drift ratio (IDR) responses from the NLTHA of the nine BRBGFs. The design target values and the mean responses were also plotted. It can be seen from Figure 6.6 that the results of NLTHA of BRBGF-6 and BRBGF-9 designed with Profile L exceeded their design targets, which meant that the design with Profile L was unconservative for multi-storey BRBGF buildings. The reason could be that the column shortening was significant and comparable with the BRB deformations as shown in Table 6.4. The profile L only considered the drift contribution of BRB deformations but not the drift contribution of the column shortening. On the other hand, although the results of NLTHA of BRBGF buildings designed with Profile C provided a conservative design compared with the design targets as shown in Figure 6.8, the design with Profile C underestimated the system ductility factor μ_{sys} significantly. Larger cross-sections of members were used as listed in Table 6.10 when compared with those designed with Profile L and Profile P as listed in Table 6.8-Table 6.9. This meant that the design with Profile C might be uneconomical. It can be seen from Figure 6.7 that for the design with Profile P, the mean values of maximum IDR for BRBGF-6 and BRBGF-9 were 2.0% and 1.7% respectively. The maximum IDR responses were close to the design drift ratio limit θ_d (=2.0%) and the rest of IDR results were smaller than θ_d. Therefore, Profile P might be more suitable for the BRBGFs when compared with Profile L and Profile C. Overall, the DDBD approach using Profile P provided conservative and relatively accurate predictions for the maximum displacement and IDR responses.

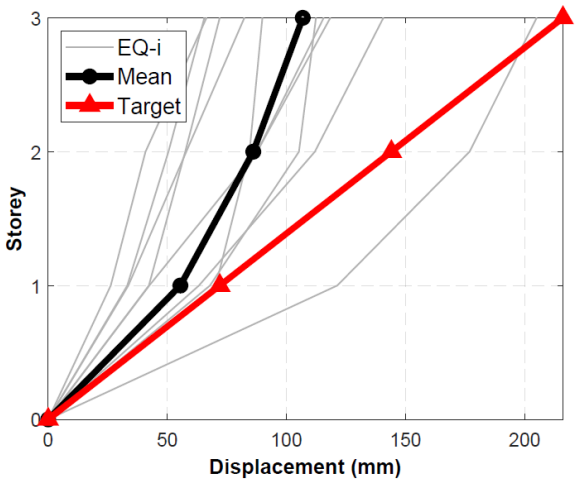

a) Displacement for BRBGF-3

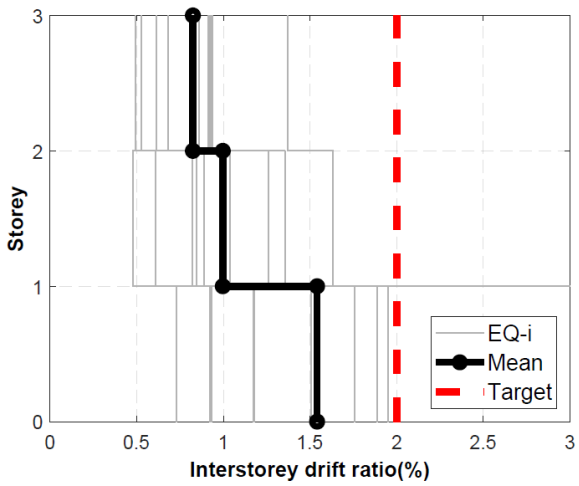

b) IDR for BRBGF-3

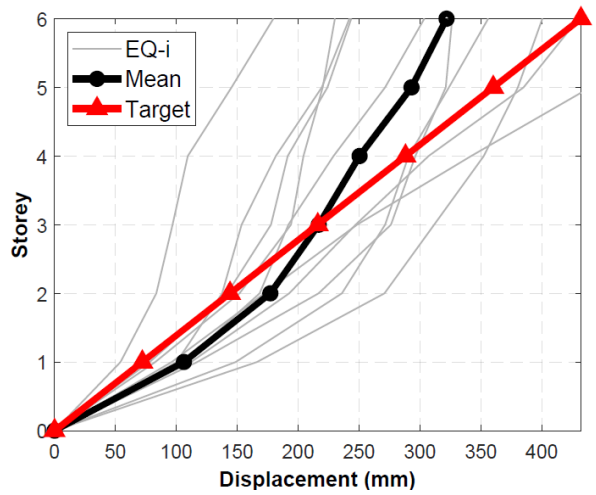

c) Displacement for BRBGF-6

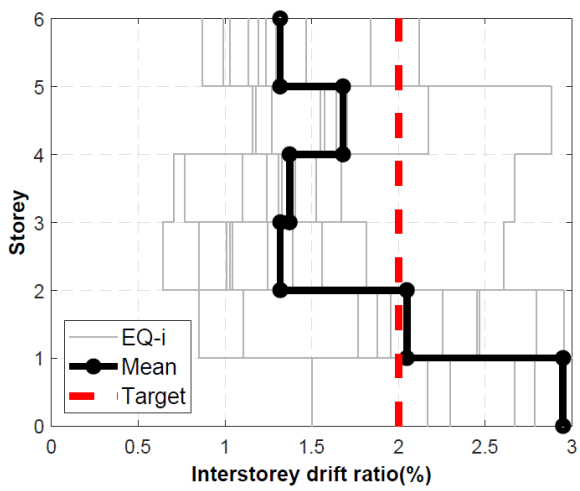

d) IDR for BRBGF-6

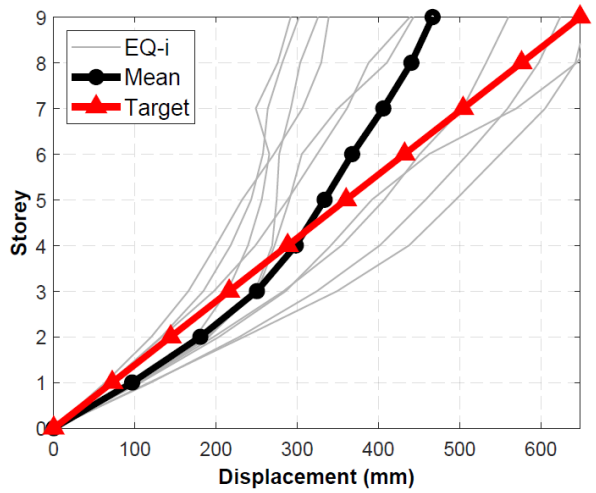

e) Displacement for BRBGF-9

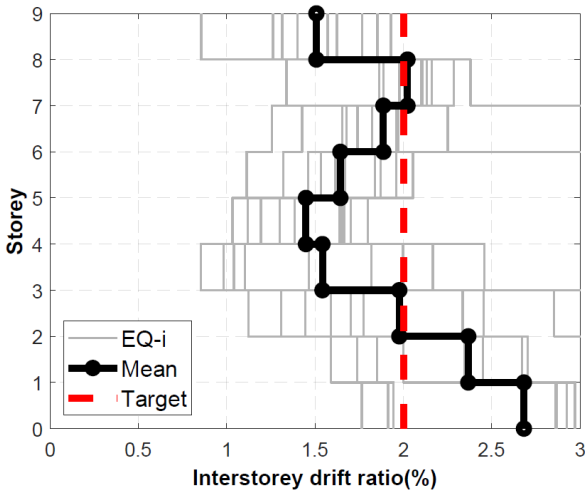

f) IDR for BRBGF-9

Figure 6.6 Maximum displacement (left) and inter-storey drift ratio (right) response with Profile L

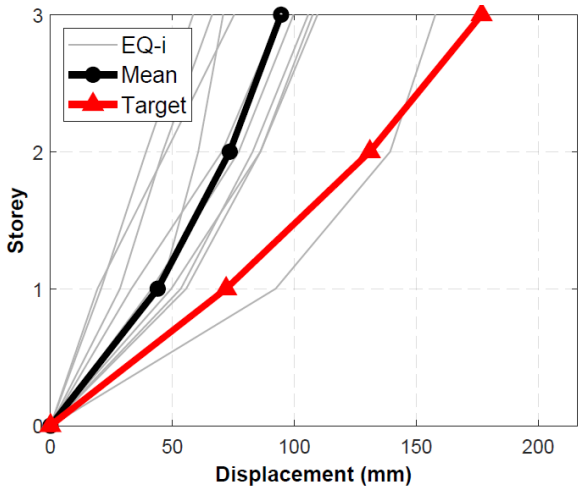

a) Displacement for BRBGF-3

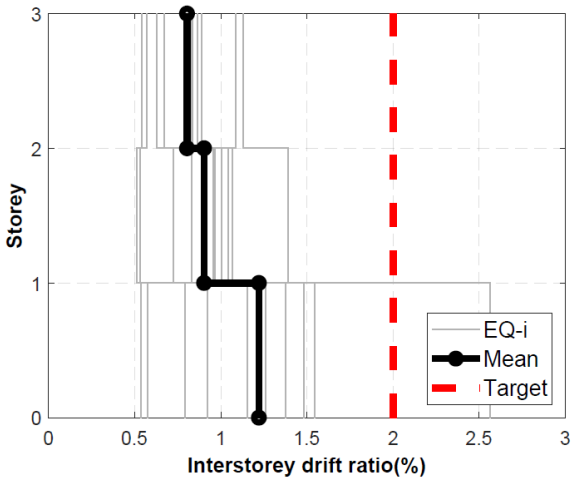

b) IDR for BRBGF-3

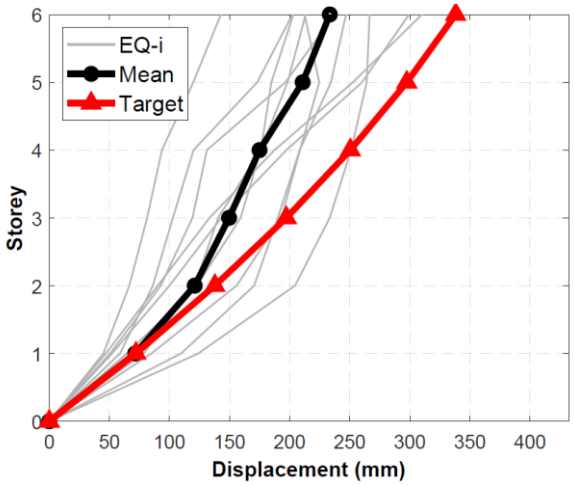

c) Displacement for BRBGF-6

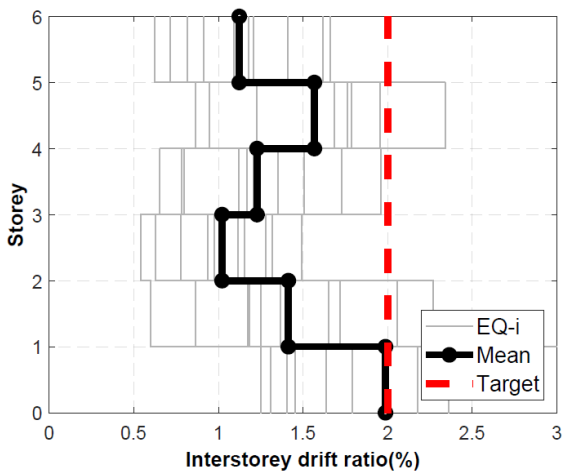

d) IDR for BRBGF-6

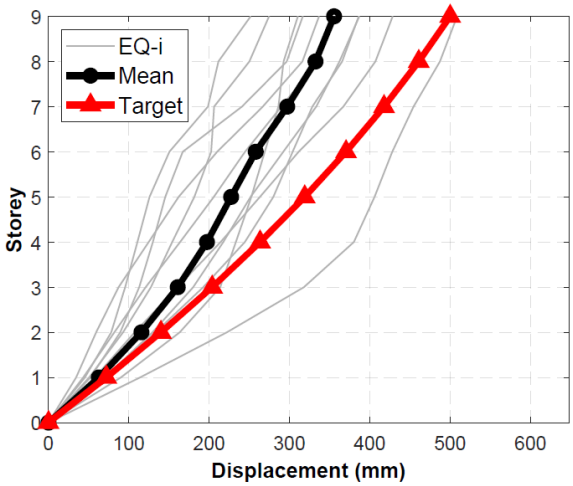

e) Displacement for BRBGF-9

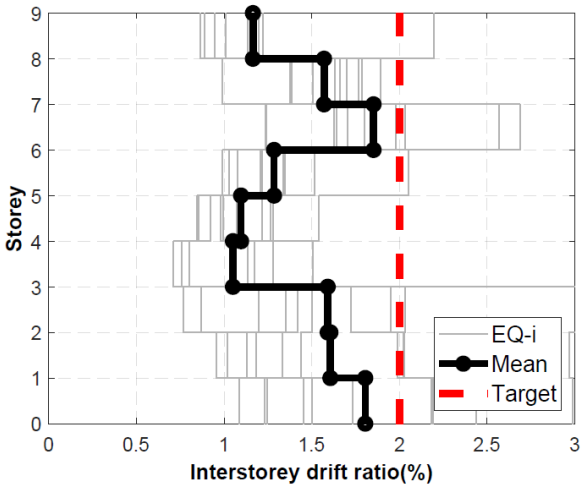

f) IDR for BRBGF-9

Figure 6.7 Maximum displacement (left) and inter-storey drift ratio (right) response with Profile P

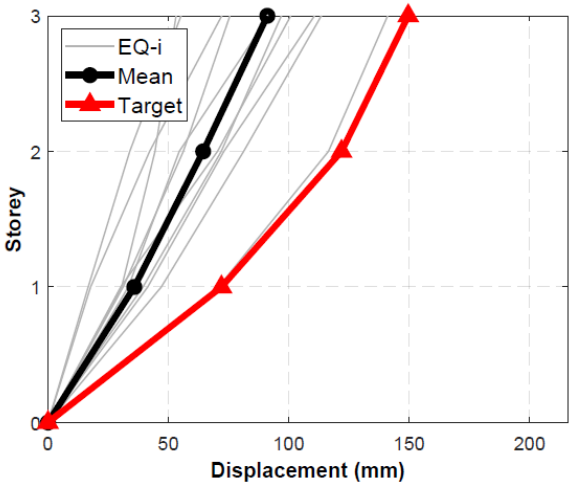

a) Displacement for BRBGF-3

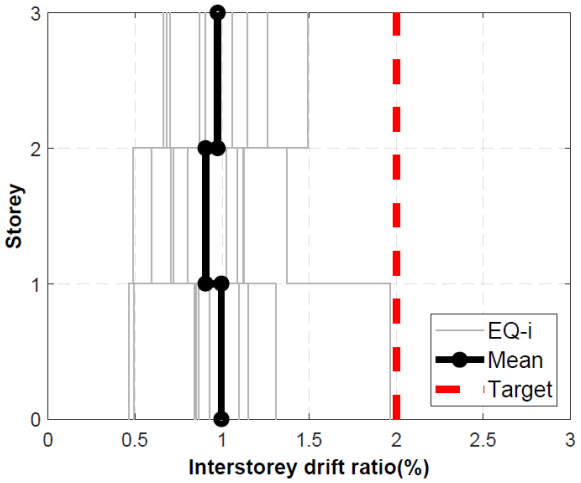

b) IDR for BRBGF-3

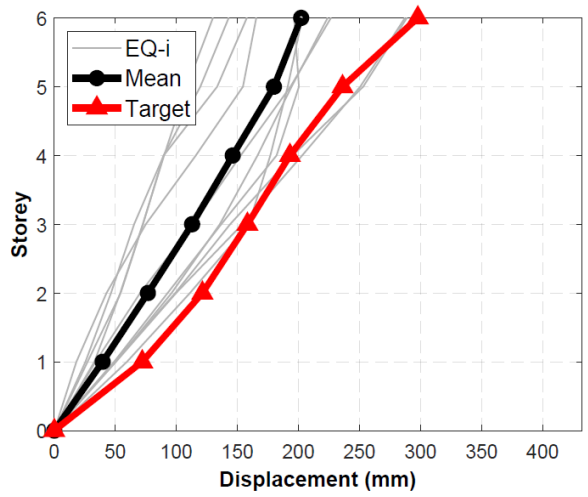

c) Displacement for BRBGF-6

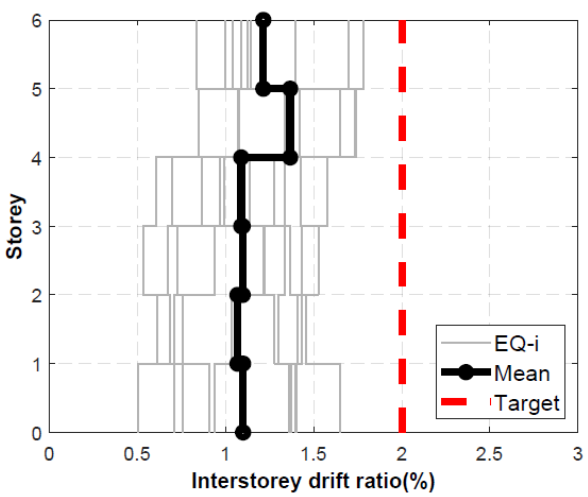

d) IDR for BRBGF-6

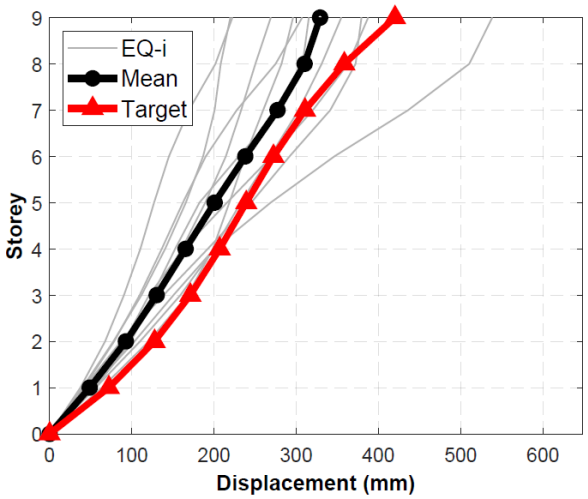

e) Displacement for BRBGF-9

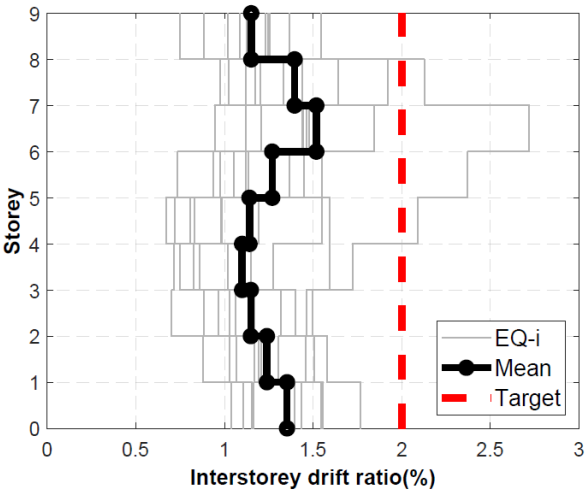

f) IDR for BRBGF-9

Figure 6.8 Maximum displacement (left) and inter-storey drift ratio (right) response with Profile C

It is also noted from Figure 6.7 that for all three BRBGFs, the DDBD approach predicted the IDR responses better for the first storey than the upper storeys. One reason might be the actual shear force distribution along with the height could be different from Eq. 5.15d because BRB frames are more sensitive to the formation of a soft storey (Erochko et al., 2011). The first floor was designed with higher ductility μ_1 as listed in Table 6.4-Table 6.6, so it was expected to enter the post-yield stage earlier. Once the first storey yielded, the stiffness of the storey significantly decreased. More deformations were likely to be concentrated on the first-yielded storey due to their lower stiffness. Although the soft storey is a potential issue for BRB frames in general, the design examples illustrated that the DDBD approach with a proper assumption of the displacement profile avoided concentration of excess deformations in one storey and the displacements of the entire building were well controlled. Another reason for the conservative predictions was that the BRB cross-section design (Eq. 6.6) neglected the strain hardening effect after yielding.

It can be seen from Figure 6.7 that the DDBD approach was more conservative for BRBGF-3 than BRBGF-6 and BRBGF-9. The reason was that the average strain adjustment factor $\rho_{s,avg}$ were 0.2, 0.42 and 0.44 for BRBGF-3, BRBGF-6 and BRBGF-9, respectively. Assuming $\rho_{s,avg}$ =0.4 for BRBGF-3 overestimated the $\Delta_{y,i,col}$ and underestimate the system ductility μ_{sys}. Because the BRBGF system is more likely to be used as LFRS for buildings with more than three storeys, it is suggested to use $\rho_{s,avg}$ =0.4 for the preliminary design.

6.4.3 Glulam member strength check

The glulam members were all designed considering the BRB overstrength factor $\gamma_{os,BRB}$ =1.5 to ensure that they remained elastic while BRBs start to yield. The maximum moments and axial forces in the columns and beams from the NLTHA of BRBGFs with Profile P were extracted from OpenSees to check the strength of glulam members because Profile P provided the most suitable design for the displacement and IDR responses. Eq. 6.8 according to NZS 3603 (1993) were used to calculate the combined strength factors (CSFs) and check the beam and column strength. Table 6.11 lists the glulam member sizes of BRBGFs and the mean value of maximum CSFs under the ten ground motions. The highest mean value of maximum CSFs in Table 6.11 were 0.87 for columns and 0.69 for beams, so all glulam members satisfied the strength requirement.

$$CSF_1 = \frac{M_{t,mean}}{\phi_{GL} M_n} + \frac{N_{t,mean}}{\phi_{GL} N_{nt}} \leq 1.0 \qquad \text{Eq. 6.8a}$$

$$CSF_2 = \frac{M_{c,mean}}{\phi_{GL} M_n} + \frac{N_{c,mean}}{\phi_{GL} N_{nc}} \leq 1.0 \qquad \text{Eq. 6.8b}$$

where $N_{t,mean}$ and $N_{c,mean}$ are the tension and compression loads, respectively;

$M_{t,mean}$ and $M_{c,mean}$ are the corresponding moment at $N_{t,mean}$ and $N_{c,mean}$, respectively;

N_{nt} and N_{nc} are the nominal strength in tension and nominal strength for buckling, respectively;

M_n is the nominal bending strength; and

ϕ_{GL} (=0.8) is the strength reduction factor for glulam.

It is also noticed that the CSFs were mostly smaller than 0.7 and CSFs for beams were generally smaller than those for columns at the same storey. This was because the IDR responses for most storeys were lower than 2.0%, the actual axial deformations of BRBs were smaller than the ultimate deformation. The force levels that BRBs achieved in the NLTHA were smaller than the design loads of BRB considering the BRB overstrength factor $\gamma_{os,BRB}$ (=1.5), so the loads transferred to the glulam members were smaller than the design loads. The beams had a large span (L=8 m) and the moment action in the beam was proportional to L^2, which caused the glulam beams more sensitive to the design load levels when compared with the glulam columns. The member sizes could be optimized by using different $\gamma_{os,BRB}$ along with the height based on μ_i as suggested by Lopez and Sabelli (2004), but the optimization is out of

the scope of this study. Based on the glulam member strength check and displacement responses of BRBGFs, the feasibility of the DDBD approach for the BRBGF hybrid system was verified.

Table 6.11 Combine strength factor of glulam members in BRBGFs with Profile P

	BRBGF-3				BRBGF-6				BRBGF-9			
Storey	Beam	*CSF**	*Col***	*CSF*	Beam	*CSF*	*Col*	*CSF*	Beam	*CSF*	*Col*	*CSF*
1	360×315	0.55	315***	0.52	405×315	0.69	360	0.87	450×315	0.64	540	0.61
2	360×270	0.43	315	0.33	405×315	0.52	360	0.61	450×315	0.58	540	0.56
3	360×270	0.30	315	0.03	405×270	0.44	360	0.34	405×315	0.53	540	0.40
4					405×270	0.42	270	0.54	405×315	0.45	405	0.54
5					315×270	0.49	270	0.43	405×270	0.46	405	0.46
6					315×270	0.26	270	0.05	405×270	0.45	405	0.30
7									405×270	0.42	270	0.54
8									315×225	0.52	270	0.45
9									315×225	0.30	270	0.05

Note: **CSF* is the maximum of CSF_1 and CSF_2 in Eq. 6.8; ***Col*= column; ***all columns are square columns, so only the width of column is listed.

6.4.4 Residual drift ratio response

The cyclic tests showed evident permanent displacement for the BRBGFs in Section 3.3.1. the residual drift ratio may be an issue for the repair and replacement of multi-storey buildings. Therefore, the NLTHA of the three BRBGFs with Profile P were conducted for an additional 50 s after they went through the ground motions. The maximum drift ratio at the last three seconds was decided as the residual drift ratio for a BRBGF building. Past research suggested limiting the residual drift ratio to 0.5% because the buildings with more than 0.5% residual drift ratio could cause high repair costs for non-structural elements (McCormick et al., 2008).

Figure 6.9 shows the mean values of the maximum residual drift ratio responses of the three BRBGF buildings designed with Profile P. The residual drift ratio responses of BRBGF-9 had higher variability than those of BRBGF-3 and BRBGF-6. The mean values of maximum residual drift ratios on the first storey of BRBGF-6 and BRBGF-9 were 0.6% and 0.7%, respectively, 12% and 34% higher than the design limit (0.5%). The DDBD design was not able to control the residual drift ratio because this is not a design target of the DDBD approach. The residual drift ratio is considered as a common issue for BRB frames (Kiggins and Uang, 2006). The residual drift ratio control for the BRBGFs requires further investigation, such as replacing common BRBs with self-centring BRBs made of shape memory alloy (Eatherton et al., 2014).

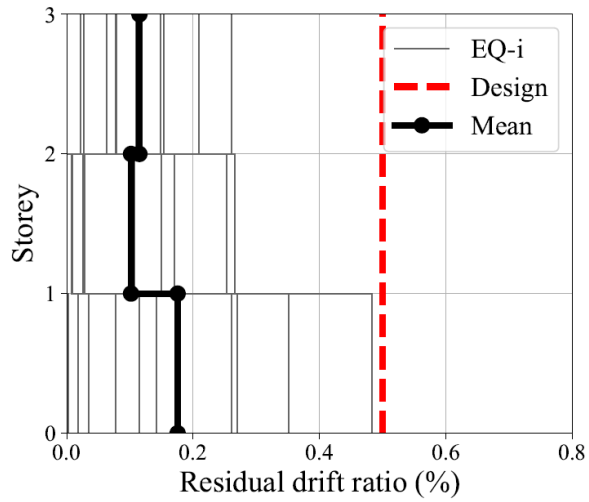

a) BRBGF-3

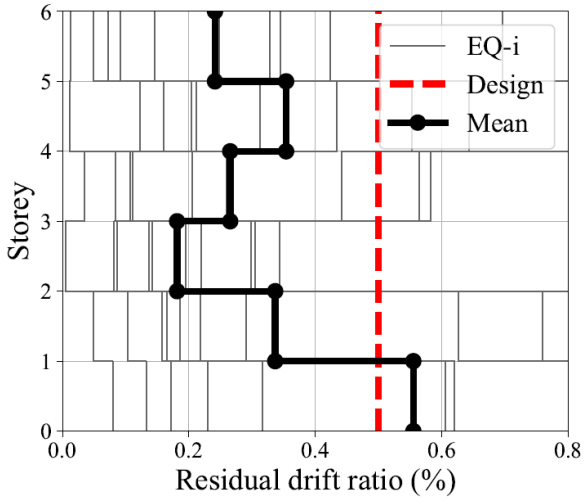

b) BRBGF-6

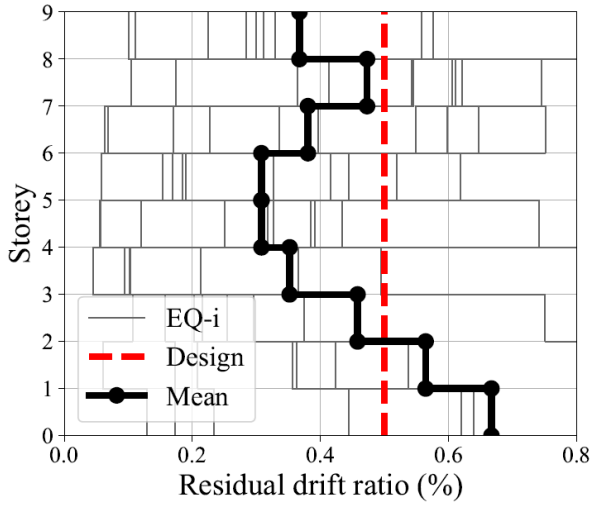

c) BRBGF-9

Figure 6.9 Maximum residual drift ratio responses for BRBGFs with Profile P

6.5 Summary

In this chapter, a set of BRBGF buildings with three, six, and nine storeys were designed following the DDBD approach. The verified η_{in}-μ relationship for Takeda fat model and λ for the BRBGFs with the dowelled connections in Chapter 5 were used in the DDBD approach. NLTHA were conducted for the BRBGF buildings to identify the suitable displacement profile for the DDBD approach and verify the DDBD approach. A summary is listed as follows:

1) The parabolic displacement profile for moment-resisting frames is more suitable for the DDBD approach of the BRBGF system when compared with the linear displacement profile and cubic displacement profile.
2) The NLTHA of the BRBGF buildings showed that the DDBD approach predicted the maximum displacement and inter-storey drift ratio responses conservatively.

3) Using the DDBD approach, the inter-storey drift ratios of BRBGF buildings were well controlled so that the formation of a soft storey was avoided.
4) DDBD approach could not provide control of the residual drift ratio responses because the residual drift ratio was not part of the design targets. The residual drift ratio control requires further investigation.

7 CONCLUSIONS AND FUTURE RESEARCH

7.1 Conclusions

This thesis presents a new timber-steel hybrid system that integrates BRBs into glulam frames. Two 8 m wide and 3.6 m high full-scale glulam frames with BRBs were built and tested in the laboratory under cyclic loading. Two different connection types (dowelled connections and screwed connections) were used to connect the BRBs with the glulam frames, respectively. The test data were then used to calibrate component-based numerical models for the BRBGF system. The influence of connection stiffness and initial slips on the system cyclic performance was investigated by parametric studies using the numerical models. Furthermore, a DDBD approach proposed by Priestley et al. (2007a) was extended to design the BRBGF system and the critical design parameters for the DDBD approach were discussed for the BRBGF system. Finally, a set of BRBGFs with three, six, and nine storeys were designed by the DDBD approach and the design assumptions were verified by NLTHA. The DDBD approach proved to be an effective design approach for the BRBGF hybrid system.

The main objectives of this thesis, as presented in Section 0, is to design and test the BRBGF hybrid system, develop reliable numerical tools for the system and introduce a suitable design approach for practical applications. Based on the research findings, the main conclusions are summarized as follows:

7.1.1 Experimental tests

1) The BRBGFs had higher load-carrying capacity when compared with the traditional timber-braced frames in literature. The BRBs provided enhanced ductility and energy dissipation for the glulam frames. The system ductility was more than double when compared with that of traditional timber-braced frames.
2) The capacity design approach worked well for the BRBGFs. The BRBs performed as ductile elements to dissipate energy while the glulam members and connections worked as non-ductile elements with minor damages.
3) The dowelled connections and screwed connections proved to have high strength and stiffness with negligible moment resisting capacity. They were efficient in engaging the BRBs to resist lateral loads.
4) If the load was below the SLS load, the BRBGF with the screwed connections had smaller initial slips than the BRBGF with the dowelled connections. However, both BRBGFs had comparable performance when the load exceeded the SLS load because the BRBs governed the system behaviour after BRBs' yielding.
5) Eurocode 5 provided a good strength prediction for the dowelled connections but a conservative strength prediction for the screwed connections because the friction contribution of the screwed connections was not considered.

6) The stiffness predictions based on Eurocode 5 and the ETAs significantly overestimated the actual stiffness for both the dowelled and screwed connections.

7.1.2 Numerical modelling

1) For the dowelled connections, the beam-on-foundation (BOF) model that was based on embedment tests provided more accurate stiffness predictions when compared with the stiffness equation in Eurocode 5.
2) For the screwed connections, the combined analytical model based on timber-to-timber connections and timber-to-concrete connections from literature was able to predict the stiffness conservatively with reasonable accuracy.
3) The predictions of the component-based BRBGF models agreed well with the experimental results of two full-scale BRBGFs in terms of force-drift responses, accumulated energy dissipation and BRB deformations.
4) The parametric studies showed that when connection relative overstrength factor $\gamma_{os,con}$ was equal to or slightly exceeded the BRB overstrength factor $\gamma_{os,BRB}$, the connections should be strong and stiff enough to engage BRBs. Further increasing the connection strength did not increase the system lateral stiffness significantly.
5) The parametric studies showed that the practical manufacturing tolerances did not significantly affect the energy dissipation and ultimate strength of the BRBGFs under cyclic loading. However, excessive initial slips could cause a larger inter-storey drift before the yielding of BRBs and might affect the serviceability performance.

7.1.3 Design approach

1) The connection stiffness between BRBs and glulam frames should be considered when estimating the yield drift of BRBGFs. The semi-rigid connections between BRBs and glulam frames caused higher yield drift and reduced the system ductility. The stiffness adjustment factor λ=0.72 for the BRBGF with the dowelled connections (S-D) and λ=0.53 for the BRBGF with the screwed connections (S-S) verified by the pushover analyses were recommended to estimate the yield drift of BRBGFs in the DDBD approach.
2) The η_{in}-μ relationship for the Takeda fat model was proven to be suitable for the BRBGF system and provided slightly conservative predictions when compared to the NLTHA results.
3) Based on the NLTHA, it was found that the strength and stiffness of BRBs and initial slips caused by manufacturing tolerances had a negligible impact on the η_{in}-μ relationship.
4) The displacement profile for moment-resisting frames was suitable for the DDBD approach of BRBGFs and provided conservative predictions.

5) The DDBD helped to avoid the formation of a soft storey by controlling the inter-storey drift ratio responses.
6) The NLTHA results showed that the DDBD approach predicted the maximum displacement and inter-storey drift ratio responses conservatively. The DDBD approach was verified to be an effective approach for the BRBGF system.

7.2 Intellectual contributions

The intellectual contributions to the academic advances and engineering practice are list below:

1) The experimental tests proved the feasibility of BRBGF system and provided two practical connection options for the BRB-timber interface connections.
2) The numerical modelling provided practical prediction methods of stiffness for the dowelled connections and screwed connections, which overcomes the limitation of the stiffness prediction in current standards and ETAs.
3) The practical DDBD design approach simplified the design of BRBGFs so engineers can design this hybrid system by hand calculations.

7.3 Recommendations for future research

Although the BRBGFs showed enhanced lateral performance compared with traditional timber-braced frames, more research is still needed to improve the structural performance, cost-effectiveness and construction speed of BRBGF buildings. Some suggestions are listed as follows:

7.3.1 Experimental design and tests

1) Tests of BRBGFs to a higher drift ratio is recommended so the fragility analysis and robustness analysis can be conducted to achieve a more comprehensive understanding of this hybrid system.
2) The dynamic influence of the manufacturing tolerances on the BRBGFs and connections requires further experimental verification, such as shake table tests.
3) The research on dowelled connections (Brown and Li, 2021) showed that increasing the dowel spacing and end distance could increase the stiffness of connections. On the other hand, increasing the spacing will increase the moment-resisting capacity. Therefore, it is recommended to conduct a stiffness optimization study on the spacing and the slenderness of dowels.
4) The assembly of the dowelled connections required higher manufacturing accuracy than the screwed connections. It is recommended to improve the detailing at the BRB-

timber interface, such as adding adjustable slotted holes at the end of BRBs to reduce the slips of connections and facilitate the installation of the dowelled connections.

5) The screwed connections at the bottom had larger slips perpendicular to timber grain due to the rotation of beam-column connections and the inclined loading to the timber grain under cyclic loading. It is recommended to conduct more experimental tests to quantify the influence of cyclic loading.
6) The screwed connections using counter-sunk steel holes (Krenn and Schickhofer, 2009) showed much higher stiffness when compared with the screwed connections using commercial washers. It is recommended to conduct more research to quantify the influence of different details. In addition, to minimize the slips of STS in the washers, 90° STS are recommended to be installed to resist the perpendicular-to-grain load or the washers should be fixed on the steel plates by welding. The improvements of the details are suggested to be compared by conducting experimental tests.
7) The reasons for significantly higher BRB overstrength factor $\gamma_{os,BRB}$ in the BRB component tests require further investigation and more test samples are probably needed to quantify the effects of design parameters. BRBs from different manufacturers are also suggested to implement in BRBGFs and an upper boundary value of $\gamma_{os,BRB}$ among BRB manufacturers will be beneficial to the application of the BRBGF hybrid system.

7.3.2 Numerical modelling

1) It is recommended to develop a more detailed model on the dowelled connections and the screwed connections to consider the influence of grain direction when test data are available.
2) Different core steel and different geometry of BRBs will impact the behaviour of BRBs. The core-binding, snagging and unbonding material viscoelastic effect need to be taken into account for broader applications of BRBGF structures with BRBs from different manufacturers. It is recommended to build more detailed BRB models to predict the BRB component performance accurately when BRB test data are available, such as the models from Stiler and Takeuchi (2021) and Jones (2020).
3) The BOF model for the dowelled connections still requires embedment tests. Although the embedment tests are relatively simple, the time-consuming tests possibly restrict the broader applications of the BOF model. It is recommended to develop a model for predicting the embedment load-displacement curves when more embedment test data are available.
4) The analytical model for the screwed connections was only verified for one type of STS product. More STS products should be verified to allow practical engineers to use the analytical model more confidently.

7.3.3 Design approach

1) The DDBD approach was applied to design up to nine-storey BRBGFs. For taller BRBGFs, improvements for the current DDBD approach are recommended such as using the factor modal combination rule to have a more accurate consideration on the higher mode effects (Abbasnia et al., 2014). Thus, the feasibility of the DDBD approach for taller BRBGFs requires further investigation and verification.
2) The residual drift ratio responses in some design scenarios exceeded the recommended drift ratio limit (0.5%), but the DDBD approach is not able to control the residual drift ratio. The elimination strategies of the residual drift ratio are suggested to be explored, such as using self-centring BRBs or BRB-related dual systems.
3) The torsional effects were not included in the DDBD approach. The influence of irregularity is suggested to be considered in the DDBD approach.
4) The near-fault effect was not considered in the selected ground motions due to the limited ground motion data, so the feasibility of the DDBD approach for the near-fault earthquakes is still unknown. It is suggested to conduct more research under the near-fault earthquakes with the DDBD approach.
5) The duration of ground motions has an influence on the deformation capacity of structures according to the research by Bhanu et al. (2020). The feasibility of DDBD for long-duration earthquakes needs further investigation.
6) The FBD approach is suggested to be developed for engineers who are more familiar with the traditional FBD approach. It is also suggested to compare the DDBD approach with the traditional FBD approach.

REFERENCES

Abbasnia, R., Tajik Davoudi, A., & Maddah, M. M. (2014). An improved displacement-based adaptive pushover procedure for the analysis of frame buildings. *Journal of Earthquake Engineering*, *18*(7), 987–1008.

Abrahamsen, R. B., & Malo, K. A. (2014). Structural design and assembly of "treet" - A 14-storey timber residential building in Norway. *WCTE 2014 - World Conference on Timber Engineering, Proceedings*, *April 2014*, 3–10.

Aguaguina, M., Zhou, Y., & Zhou, Y. (2019). Loading protocols for qualification testing of BRBs considering global performance requirements. *Engineering Structures*, *189*(November 2018), 440–457.

Aiken, I. D., Mahin, S. A., & Uriz, P. (2002). Large-scale testing of buckling-restrained braced frames. *Proceedings of the Japan Passive Control Symposium*, 35–44.

Al-mashaykhi, M., Rajeev, P., Wijesundara, K. K., & Hashemi, M. J. (2019). Displacement profile for displacement based seismic design of concentric braced frames. *Journal of Constructional Steel Research*, *155*, 233–248.

Ali, K. A., Ahmad, M. I., & Yusup, Y. (2020). Issues, impacts, and mitigations of carbon dioxide emissions in the building sector. *Sustainability (Switzerland)*, *12*(18).

American Institute of Steel Construction (AISC). (2016a). ANSI / AISC 360-16, Specification for Structural Steel Buildings. In *American Institute of Steel Construction*.

American Institute of Steel Construction (AISC). (2016b). Seismic provisions for structural steel buildings. ANSI/AISC 341-16. In *Seismic provisions for structural steel buildings*.

American Society for Testing and Materials. (2011). Standard Test Methods for Cyclic (Reversed) Load Test for Shear Resistance of Vertical Elements of the Lateral Force Resisting Systems for Buildings. *E2126*, *11*(Reapproved 2018), 1–15.

ASCE/SEI(ASCE/Structural Engineering Institute). (2016). *ASCE 7-16: Minimum design loads for buildings and other structures*.

ASTM standard. (2002). ASTM D5764: Standard Test Method for Evaluating Dowel-Bearing Strength of Wood and Wood-. In *American Society of Mechanical Engineers* (Vol. 03, Issue Reapproved).

Atlayan, O., & Charney, F. A. (2014). Hybrid buckling-restrained braced frames. *Journal of Constructional Steel Research*, *96*, 95–105.

Aurecon. (n.d.). *Aurecon's Brisbane office to move to 25 King Street*. https://www.aurecongroup.com/about/latest-news/2017/february/aurecon-brisbane-office-move

Australia and New Zealand Standards. (2004). NZS1170.5: Structural design actions - Part 5: Earthquake actions-New Zealand. In *Wellington, New Zealand*.

Avci-Karatas, C., Celik, O. C., & Yalcin, C. (2018). Experimental Investigation of Aluminum Alloy and Steel Core Buckling Restrained Braces (BRBs). *International Journal of Steel Structures*, *18*(2), 650–673.

Bejtka, I., & Blass, H. J. (2002). Joints with Inclined Screws. *Proceedings of CIB-W18 Timber Structures, Meeting 35, September*, 35-7–3.

Belleri, A. (2017). Displacement based design for precast concrete frames with not-emulative connections. *Engineering Structures*, *141*, 228–240.

Berman, J. W., & Bruneau, M. (2009). Cyclic testing of a buckling restrained braced frame with unconstrained gusset connections. *Journal of Structural Engineering*, *135*(12), 1499–1510.

Bezabeh, M. A., Tesfamariam, S., & Stiemer, S. F. (2016a). Equivalent Viscous Damping for Steel Moment-Resisting Frames with Cross-Laminated Timber Infill Walls. *Journal of Structural Engineering (United States)*, *142*(1).

Bezabeh, M. A., Tesfamariam, S., Stiemer, S. F., Popovski, M., & Karacabeyli, E. (2016b). Direct displacement-based design of a novel hybrid structure: Steel moment-resisting frames with cross-laminated timber infill walls. *Earthquake Spectra*, *32*(3), 1565–1585.

Bhanu, V., Chandramohan, R., & Sullivan, T. J. (2020). Influence of ground motion duration on the dynamic deformation capacity of steel frame buildings. *17th World Conference on Earthquake Engineering*, *002751*(Abstract ID).

Black, C. J., & Aiken, I. (2002). *Component Testing , Stability Analysis and Characterization of Buckling-Restrained Unbonded Braces TM University of California , Berkeley* (Issue January 2016).

Black, C. J., Makris, N., & Aiken, I. D. (2004). Component testing, seismic evaluation and characterization of buckling-restrained braces. *Journal of Structural Engineering*, *130*(6), 880–894.

Blandon, C. A., & Priestley, M. J. N. (2005). Equivalent viscous damping equations for direct displacement based design. *Journal of Earthquake Engineering*, *9*(SPEC. ISS. 2), 257–278.

Blass, H. J., Bejtka, I., & Uibel, T. (2006). *Tragfähigkeit von Verbindungen mit selbstbohrenden Holzschrauben mit Vollgewinde*. KIT Scientific Publishing.

Blass, H. J., & Kruger, O. (2010). *Schubverstärkung von Holz mit Holzschrauben und Gewindestangen. Band 15 der Reihe Karlsruher Berichte zum Ingenieurholzbau*. KIT Scientific Publishing, Karlsruhe.

Blomgren, H.-E., Koppitz, J.-P., Valdés, A. D., & Ko, E. (2016). The heavy timber buckling-restrained braced frame as a solution for commercial buildings in regions of high seismicity. *World Conference on Timber Engineering*.

Bocquet, J.-F., Epinal, F., Lemaître, R., & Bader, T. K. (2018). Design recommendations and example calculations for dowel-type connections with multiple shear planes. *Design of Connections in Timber Structures*, 241.

Bourahla, N. (2013). *Equivalent Static Analysis of Structures Subjected to Seismic Actions BT - Encyclopedia of Earthquake Engineering* (M. Beer, I. A. Kougioumtzoglou, E. Patelli, & I. S.-K. Au (eds.); pp. 1–13). Springer Berlin Heidelberg.

British Standard Institution (BSI). (1998). *Eurocode 8: Design of structures for earthquake resistance*.

British Standard Institution (BSI). (2002). *BS EN 12512:2001: Timber structures. Test methods. Cyclic testing of joints made with mechanical fasteners*.

British Standard Institution (BSI). (2004). *Eurocode 5: design of timber structures—Part 1-1: General—Common rules and rules for buildings*.

British Standard Institution (BSI). (2005a). 3: Design of Steel Structures: Part 1-1: General Rules and Rules for Buildings, BS EN 1993-1-1. In *London: British Standards Institution*. BSI.

British Standard Institution (BSI). (2005b). *Eurocode 8: Design of structures for earthquake*

resistance (Vol. 1, pp. 1991–1998).

British Standard Institution (BSI). (2016a). *EN 1382: Timber structures - test methods - withdrawal capacity of timber fasteners*.

British Standard Institution (BSI). (2016b). *EN 14358: 2016, Timber structures–Calculation and verification of characteristic values*. British Standard Institution.

Brown, J. R., & Li, M. (2021). Structural performance of dowelled cross-laminated timber hold-down connections with increased row spacing and end distance. *Construction and Building Materials*, *271*, 121595.

Brown, J. R., Li, M., Nokes, R., Palermo, A., Pampanin, S., & Sarti, F. (2020). Investigating the compressive toe of post-tensioned CLT core-walls using Particle Tracking Technology. *17th World Conference on Earthquake Engineering*.

Brown, J. R., Li, M., Palermo, A., Pampanin, S., & Sarti, F. (2021). Experimental Testing of a Low-Damage Post-Tensioned C-Shaped CLT Core-Wall. *Journal of Structural Engineering*, *147*(3).

Bruneau, M., Eng, P., Uang, C.-M., & Rafael Sabelli, S. E. (2011). *Ductile design of steel structures*. McGraw-Hill Education.

Buchanan, A., Deam, B., Fragiacomo, M., Pampanin, S., & Palermo, A. (2008). Multi-storey prestressed timber buildings in New Zealand. *Structural Engineering International: Journal of the International Association for Bridge and Structural Engineering (IABSE)*, *18*(2), 166–173.

Carreno, R., Lotfizadeh, K. H., Conte, J. P., & Restrepo, J. I. (2020). Material Model Parameters for the Giuffre-Menegotto-Pinto Uniaxial Steel Stress-Strain Model. *Journal of Structural Engineering*, *146*(2), 4019205.

Charney, F. A. (2008). Unintended consequences of modeling damping in structures. *Journal of Structural Engineering*, *134*(4), 581–592.

Chen, Z., & Popovski, M. (2020). Connection and System Ductility Relationship for Braced Timber Frames. *Journal of Structural Engineering*, *146*(12), 04020257.

Chinese Global Standards. (2010). *GB50010-2010: Code for design of concrete structures*. China Architecture & Building Press Beijing, China.

Chinese Global Standards. (2017). *GB50017-2017: Code for Design of Steel Structures*. China Architecture & Building Press Beijing, China.

Chopra, A. K., & McKenna, F. (2016). Modeling viscous damping in nonlinear response history analysis of buildings for earthquake excitation. *Earthquake Engineering & Structural Dynamics*, *45*(2), 193–211.

Chou, C., Liu, J., & Pham, D. (2012). Steel buckling-restrained braced frames with single and dual corner gusset connections: seismic tests and analyses. *Earthquake Engineering & Structural Dynamics*, *41*(7), 1137–1156.

Closen, M. (2012). *Self-Tapping Screw Assemblies Under Monotonic Loading*. The University of British Columbia.

Corebrace. (2019). *Corebrace design guide*. https://corebrace.com/resources/

Cui, J. (2021). *Seismic Performance of Buckling Restrained Braced Frames Subjected to Combined In-Plane and Out-of-plane Loading*. University of Canterbury.

Cui, J., Lee, C. L., & MacRae, G. A. (2018). Finite Element Modelling of Buckling Restrained Braces under Combined In-Plane and Out-of-Plane Loading. *Key Engineering Materials*, *763*, 908–915.

Della Corte, G. (2006). Vibration mode vs. collapse mechanism control for steel frames. *Proceedings of the 5th International Conference on Behaviour of Steel Structures in Seismic Areas - Stessa 2006*, 423–428.

Della Corte, G., D'Aniello, M., Landolfo, R., & Mazzolani, F. M. (2011). Review of steel buckling-restrained braces. *Steel Construction*, *4*(2), 85–93.

Della Corte, G., & Mazzolani, F. M. (2008). Displacement-Based Design Procedure for Steel Braced Structures. *Proceedings of the 14th World Conference on Earthquake Engineering*, 12–17.

Department of Economic and Social Affairs Population Division United Nations. (2019). *2019 Revision of World Population Prospects*. https://population.un.org/wpp/

Dhakal, R. P., Pourali, A., Tasligedik, A. S., Yeow, T., Baird, A., MacRae, G., Pampanin, S., & Palermo, A. (2016). Seismic performance of non-structural components and contents in buildings: an overview of NZ research. *Earthquake Engineering and Engineering Vibration*, *15*(1), 1–17.

Di Cesare, A., Ponzo, F. C., Lamarucciola, N., & Nigro, D. (2020). Experimental seismic response of a resilient 3-storey post-tensioned timber framed building with dissipative braces. *Bulletin of Earthquake Engineering*, *18*(15), 6825–6848.

Di Sarno, L., & Manfredi, G. (2012). Experimental tests on full-scale RC unretrofitted frame and retrofitted with buckling-restrained braces. *Earthquake Engineering & Structural Dynamics*, *41*(2), 315–333.

Dickof, C., Stiemer, S. F., Bezabeh, M. A., & Tesfamariam, S. (2014). CLT–Steel Hybrid System: Ductility and Overstrength Values Based on Static Pushover Analysis. *Journal of Performance of Constructed Facilities*, *28*(6).

Dietsch, P., & Brandner, R. (2015). Self-tapping screws and threaded rods as reinforcement for structural timber elements-A state-of-the-art report. *Construction and Building Materials*, *97*, 78–89.

Dong, W., & Li, M. (2019). A preliminary study on cyclic behaviour of SFS dowelled connections in glulam frames. *2019 Pacific Conference on Earthquake Engineering*, 1–11. https://ir.canterbury.ac.nz/handle/10092/16742

Dong, W., Li, M., He, M., & Li, Z. (2021). Experimental testing and analytical modelling of glulam moment connections with self-drilling dowels. *Journal of Structural Engineering*, *147*(5), 04021047.

Dong, W., Li, M., Lee, C., & Macrae, G. (2021a). Numerical modelling of glulam frames with buckling restrained braces. *Engineering Structures*, *239*, 112338.

Dong, W., Li, M., Lee, C., Macrae, G., & Abu, A. (2020). Experimental testing of full-scale glulam frames with buckling restrained braces. *Engineering Structures*, *222*(March), 111081.

Dong, W., Li, M., Sullivan, T., Lee, C.-L., MacRa, G., & Chang, T. (2021b). Direct displacement-based design of glulam frames with buckling restrained braces (under review). *Engineering Structures*.

Dorn, M. (2012). *Investigations on the Serviceability Limit State of Dowel-Type Timber Connections*. Vienna University of Technology.

Dwairi, H. M., Kowalsky, M. J., & Nau, J. M. (2007). Equivalent damping in support of direct displacement-based design. *Journal of Earthquake Engineering*, *11*(4), 512–530.

Eatherton, M. R., Fahnestock, L. A., & Miller, D. J. (2014). Computational study of self-

centering buckling-restrained braced frame seismic performance. *Earthquake Engineering & Structural Dynamics*, *43*(13), 1897–1914.

Ehlbeck, J., & Larsen, H. J. (1993). Eurocode 5 - Design of timber structures: Joints. *International Workshop on Wood Connector*, 9–23.

Elbashir, D., Branco, J. M., & Rodrigues, L. G. (2020). Reinforcement of dowel-type timber joints with self-tapping screws. *Proceedings of the Institution of Civil Engineers: Structures and Buildings*, *173*(12), 969–988.

English, R., MacRae, G., & Dhakal, R. (2012). Hysteretic Influence on Earthquake Induced Sliding Damage of Contents. *2012 NZSEE Conference*, *056*, 056. http://www.nzsee.org.nz/db/2012/Paper056.pdf

Erduran, E., & Yakut, A. (2004). Drift based damage functions for reinforced concrete columns. *Computers and Structures*, *82*(2–3), 121–130.

Erochko, J., Christopoulos, C., Tremblay, R., & Choi, H. (2011). Residual Drift Response of SMRFs and BRB Frames in Steel Buildings Designed according to ASCE 7-05. *Journal of Structural Engineering*, *137*(5), 589–599.

ETA(European Technical Assessment). (2019). *RothoBlaas Self-tapping screws and threaded rods ETA-11 / 0030 of 2019-10-08*.

European Technical Approval. (2016). *European Technical Approval ETA-11 / 0190*.

Fahnestock, L. A., Ricles, J. M., & Sause, R. (2007). Experimental evaluation of a large-scale buckling-restrained braced frame. *Journal of Structural Engineering*, *133*(9), 1205–1214.

Fan, X., Zhang, S., & Qu, W. (2011). Load-carrying behaviour of dowel-type timber connections with multiple slotted-in steel plates. *Applied Mechanics and Materials*, *94–96*, 43–47.

Fang, C., Yam, M. C. H., Zhou, X., & Zhang, Y. (2015). Post-buckling resistance of gusset plate connections: Behaviour, strength, and design considerations. *Engineering Structures*, *99*, 9–27.

Filiatrault, A., & Folz, B. (2002). Performance-Based Seismic Design of Wood Framed Buildings. *Journal of Structural Engineering*, *128*(1), 39–47.

FPInnovations. (2021). *Technical guide for the design and construction of tall wood buildings in Canada 2nd edition* (E. Karacabeyli & C. Lum (eds.); Issue May).

Galambos, T. V, & Ellingwood, B. (1986). Serviceability limit states: deflection. *Journal of Structural Engineering*, *112*(1), 67–84.

Gardiner, S., Clifton, G. C., & MacRae, G. A. (2013). Performance, damage assessment and repair of a multistorey eccentrically braced framed building following the Christchurch earthquake series. *Steel Innovations Conference 2013*.

Gattesco, N., & Toffolo, I. (2004). Experimental study on multiple-bolt steel-to-timber tension joints. *Materials and Structures/Materiaux et Constructions*, *37*(266), 129–138.

Ghaffarzadeh, H., Jafari, A., & Talebian, N. (2014). Equivalent viscous damping in direct displacement-based design of steel braced reinforced concrete frames. *The Structural Design of Tall and Special Buildings*, *23*(8), 604–618.

Ghobarah, A., Abou-Elfath, H., & Biddah, A. (1999). Response-based damage assessment of structures. *Earthquake Engineering and Structural Dynamics*, *28*(1), 79–104.

Gilbert, C. F. (2016). *Development of an innovative method for the adaptation of advanced structural bracing systems into heavy timber structures for seismic applications*. Carleton University.

Gilbert, C. F., & Erochko, J. (2019). Development and testing of hybrid timber-steel braced frames. *Engineering Structures*, *198*(1), 109495.

Girhammar, U. A., Jacquier, N., & Källsner, B. (2017). Stiffness model for inclined screws in shear-tension mode in timber-to-timber joints. *Engineering Structures*, *136*, 580–595.

Gohlich, R., Erochko, J., & Woods, J. E. (2018). Experimental testing and numerical modelling of a heavy timber moment-resisting frame with ductile steel links. *Earthquake Engineering and Structural Dynamics*, *47*(6), 1460–1477.

Gohlich, R. J. (2015). *Development of an Innovative Hybrid Timber-Steel Moment-Resisting Frame for Seismic-Resistant Heavy Timber Structures* [Carleton University].

Grant, D. N., Blandon, C. A., & Priestley, M. J. N. (2005). *Modelling inelastic response in direct displacement-based design*.

Griffis, L. G. (1993). Serviceability limit states under wind load. *Engineering Journal*, *30*(1), 1–16.

Guerrero, H., Ji, T., Teran-Gilmore, A., & Escobar, J. A. (2016). A method for preliminary seismic design and assessment of low-rise structures protected with buckling-restrained braces. *Engineering Structures*, *123*, 141–154.

Guo, Y. L., Zhu, J. S., Zhou, P., & Zhu, B. L. (2017). A new shuttle-shaped buckling-restrained brace. Theoretical study on buckling behavior and load resistance. *Engineering Structures*, *147*, 223–241.

Hashemi, A., Yousef-Beik, S. M. M., Zarnani, P., & Quenneville, P. (2021). Seismic strengthening of conventional timber structures using resilient braces. *Structures*, *32*(March), 1619–1633.

Hashemi, A., Zarnani, P., & Quenneville, P. (2020). Seismic assessment of rocking timber walls with energy dissipation devices. *Engineering Structures*, *221*(April).

He, M. J., & Liu, H. F. (2015). Comparison of glulam post-to-beam connections reinforced by two different dowel-type fasteners. *Construction and Building Materials*, *99*, 99–108.

He, M., Li, Z., Lam, F., Ma, R., & Ma, Z. (2014). Experimental Investigation on Lateral Performance of Timber-Steel Hybrid Shear Wall Systems. *Journal of Structural Engineering*, *140*(6), 04014029.

He, M., Luo, J., Tao, D., Li, Z., Sun, Y., & He, G. (2020). Rotational behavior of bolted glulam beam-to-column connections with knee brace. *Engineering Structures*, *207*(December 2019), 110251.

Hosford, W. F. (2005). *Mechanical behavior of materials* (Vol. 9780521846).

Houtte, C. Van, Bannister, S., Holden, C., Bourguignon, S., & Mcverry, G. (2017). The New Zealand strong ground motion database. *Bulletin of the New Zealand Society for Earthquake Engineering*, *50*(1), 1–20.

International Organization for Standardization (ISO). (2003). *Timber structures—Joints made with mechanical fasteners—Quasi-static reversed-cyclic test method, ISO16670* (First). ISO.

Ishida, S., & Takewaki, I. (2021). Optimal Seismic Design of Stiffness and Gap of Hysteretic-Viscous Hybrid Damper System in Nonlinear Building Frames for Simultaneous Reduction of Interstory Drift and Acceleration. *Frontiers in Built Environment*, *7*(March), 1–16.

Izzi, M., Flatscher, G., Fragiacomo, M., & Schickhofer, G. (2016). Experimental investigations and design provisions of steel-to-timber joints with annular-ringed shank nails for Cross-

Laminated Timber structures. *Construction and Building Materials*, *122*, 446–457.

Jacobsen, L. S. (1960). Damping in composite structures. *II WCEE, Tokyo, 1960*.

Jia, M., Lu, D., Guo, L., & Sun, L. (2014). Experimental research and cyclic behavior of buckling-restrained braced composite frame. *Journal of Constructional Steel Research*, *95*, 90–105.

Jockwer, R., & Jorissen, A. (2018). Stiffness and deformation of connections with dowel-type fasteners. *Design of Connections in Timber Structures*, 95.

Johansen, K. W. (1949). Theory of timber connections. *Int Assoc Bridge Struct Eng*, *9*, 249–262.

Jones, A. S. (2020). *Design and sensitivity of buckling restrained braces*. University of Canterbury.

Jones, A. S., Lee, C. C.-H., & MacRae, G. A. (2014). Review of buckling restrained brace design and behaviour. *2014 NZSEE Conference Proceedings*, 1–8.

Jorissen, A. J. M. (1998). *Double shear timber connections with dowel type fasteners*. Delft University Press Delft, The Netherlands.

Kasai, K., & Nishizawa, K. (2010). Experiments and dynamic analysis method for BRBs(in Japanese). *Academic Lecture Synopsis Collection. C-1, Structure III, Wood Structure, Steel Structure, Steel Reinforced Concrete Structure*, 807–808.

Kersting, R. A., Fahnestock, L. A., & López, W. A. (2015). Seismic design of steel buckling-restrained braced frames. *NIST GCR*, 15–917.

Khan, E., Kowalsky, M. J., & Nau, J. M. (2016). Equivalent Viscous Damping Model for Short-Period Reinforced Concrete Bridges. *Journal of Bridge Engineering*, *21*(2), 1–12.

Khan, R., Niederwestberg, J., & Hei, Y. (2021). Influence of insertion angle, diameter and thread on embedment properties of self-tapping screws. *European Journal of Wood and Wood Products*, *0123456789*.

Khoo, H., Tsai, K., Tsai, C., Tsai, C., & Wang, K. (2016). Bidirectional substructure pseudo-dynamic tests and analysis of a full-scale two-story buckling-restrained braced frame. *Earthquake Engineering & Structural Dynamics*, *45*(7), 1085–1107.

Khorasani, Y. (2011). *Feasibility study of hybrid wood steel structures*. University of British Columbia.

Kiggins, S., & Uang, C. M. (2006). Reducing residual drift of buckling-restrained braced frames as a dual system. *Engineering Structures*, *28*(11), 1525–1532.

Kim, H. S., & Chun, Y. S. (2004). Structural damage assessment of building structures using dynamic experimental data. *Structural Design of Tall and Special Buildings*, *13*(1), 1–8.

Kirstein, A., Siracusa, J., & Smith, T. (2018). The new timber von Haast replacement building in Christchurch. *2018 NZSEE Conference*, 1–9.

Kowalsky, M. J., Priestley, M. J. N., & MacRae, G. A. (1994). Displacement Based Design of RC Bridge Structures. *Proceedings of the Second International Workshop*.

Krawinkler, H., Medina, R., & Alavi, B. (2003). Seismic drift and ductility demands and their dependence on ground motions. *Engineering Structures*, *25*(5), 637–653.

Krenn, H., & Schickhofer, G. (2009). Joints with inclined Screws and Steel Plates as outer Members. *Proceedings of the International Council for Research and Innovation in Building and Construction, Working Commission W18 – Timber Structures, Meeting 42*.

Lam, F., Schulte-Wrede, M., Yao, C. C., & Gu, J. J. (2008). Moment resistance of bolted timber

connections with perpendicular to grain reinforcements. *10th World Conference on Timber Engineering 2008*, *2*, 978–985.

Landi, L., Diotallevi, P., & Tardini, A. (2007). Equivalent Viscous Damping for the Displacement-Based Seismic Assessment of Infilled RC Frames. *15th World Conference on Earthquake Engineering*.

Lee, C. L. (2021). Type 4 Bell-Shaped Proportional Damping Model and Energy Dissipation for Structures with Inelastic and Softening Response (under review). *Computers & Structures*.

Lee, C. L. (2020a). Proportional viscous damping model for matching damping ratios. *Engineering Structures*, *207*(August 2019), 110178.

Lee, C. L. (2020b). Sparse proportional viscous damping model for structures with large number of degrees of freedom. *Journal of Sound and Vibration*, *478*.

Lemaitre, R., Bocquet, J.-F., Schweigler, M., & Bader, T. K. (2019). Beam-on-Foundation Modelling as an Alternative Design Method for Timber Joints with Dowel-Type Fasteners–Part 2: Modelling Techniques for Multiple Fastener Connections. *6th INTER Proceedings, 2019: International Network on Timber Engineering Research 2019, Tacoma, USA, Karlsruher Institut Für Technologie, 2019*.

Lemaitre, R., Epinal, F., Bocquet, J.-F., Schweigler, M., & Bader, T. K. (2018). Beam-on-foundation modelling as an alternative design method for single fastener connections. *Design of Connections in Timber Structures*, 207.

Li, G. Q., Sun, Y. Z., Jiang, J., Sun, F. F., & Ji, C. (2019). Experimental study on two-level yielding buckling-restrained braces. *Journal of Constructional Steel Research*, *159*, 260–269.

Li, Z., Dong, H., Wang, X., & He, M. (2017). Experimental and numerical investigations into seismic performance of timber-steel hybrid structure with supplemental dampers. *Engineering Structures*, *151*, 33–43.

Li, Z., He, M., Lam, F., & Li, M. (2015). Load-sharing mechanism in timber-steel hybrid shear wall systems. *Frontiers of Structural and Civil Engineering*, *9*(2), 203–214.

Li, Z., He, M., Lam, F., Li, M., Ma, R., & Ma, Z. (2014). Finite element modeling and parametric analysis of timber–steel hybrid structures. *The Structural Design of Tall and Special Buildings*, *23*(14), 1045–1063.

Li, Z., Wang, X., He, M., & Dong, H. (2019). Seismic Performance of Timber-Steel Hybrid Structures. II: Calibration of Performance Objectives and Design Method. *Journal of Structural Engineering (United States)*, *145*(10).

Lin, P.-C., Tsai, K.-C., Wu, A., & Chuang, M.-C. (2020). *User Guide for BOD:buckling-restrained brace and connection design procedures*. http://bod.ncree.org.tw/Download.aspx

Lin, S. L., MacRae, G. A., Dhakal, R. P., & Yeow, T. Z. (2015). Building contents sliding demands in elastically responding structures. *Engineering Structures*, *86*, 182–191.

Lin, S. L., MacRae, G. a., Wu, a. C., Lin, P. C., & Tsai, K. C. (2012). Development and implementation of buckling restrained braces in Taiwan. *2012 New Zealand Society for Earthquake Engineering (NZSEE) Annual Technical Conference*, *094*.

Liu, T., Zordan, T., Zhang, Q., & Briseghella, B. (2015). Equivalent viscous damping of bilinear hysteretic oscillators. *Journal of Structural Engineering (United States)*, *141*(11), 1–12.

Lopez, W., & Sabelli, R. (2004). Seismic Design of Buckling-Restrained Braced Frames. In *Structural steel educational council steel tips*.

Loss, C., Zonta, D., & Piazza, M. (2012). Analytical model to evaluate the equivalent viscous damping of timber structures with dowel-type fastener connections. *World Conference on Timber Engineering 2012, WCTE 2012*, *2*(July), 516–525.

Macrae, G. A., & Clifton, G. C. (2015). Research on Seismic Performance of Steel Structures. *Steel Innovations 2015 Conference, September*, 3–4.

MacRae, G. A., Lee, C. L., Vazquez-Colunga, S. Y., Cui, J., Alizadeh, S., & Jia, L. J. (2021). BRB system stability considering frame out-of-plane loading and deformation zone. *Bulletin of the New Zealand Society for Earthquake Engineering*, *54*(1), 31–39.

Mahrenholtz, C., Lin, P., Wu, A., Tsai, K., Hwang, S., Lin, R., & Bhayusukma, M. Y. (2015). Retrofit of reinforced concrete frames with buckling-restrained braces. *Earthquake Engineering & Structural Dynamics*, *44*(1), 59–78.

Maley, T. J., Sullivan, T. J., & Corte, G. Della. (2010). Development of a displacement-based design method for steel dual systems with buckling-restrained braces and moment-resisting frames. *Journal of Earthquake Engineering*, *14*(SUPPL. 1), 106–140.

Maley, T., Sullivan, T. J., Lago, A., Roldan, R., & Calvi, G. M. (2013). *Characterising the seismic behaviour of steel MRF structures*. IUSS press.

Mazza, F., & Vulcano, A. (2014). Equivalent viscous damping for displacement-based seismic design of hysteretic damped braces for retrofitting framed buildings. *Bulletin of Earthquake Engineering*, *12*(6), 2797–2819.

Mazzoni, S., McKenna, F., Scott, M. H., & Fenves, G. L. (2006). OpenSees command language manual. *Pacific Earthquake Engineering Research (PEER) Center*, *264*.

McCormick, J., Aburano, H., Ikenaga, M., & Nakashima, M. (2008). Permissible Residual Deformation Levels for Building Structures Considering both Safety and Human Elements. *The 14th World Conference on Earthquake Engineering*, 8.

Medhekar, M. S., & Kennedy, D. J. L. (2000a). Displacement-based seismic design of buildings - application. *Engineering Structures*, *22*(3), 210–221.

Medhekar, M. S., & Kennedy, D. J. L. (2000b). Displacement-based seismic design of buildings - theory. *Engineering Structures*, *22*(3), 201–209.

Medhekar, M. S., & Kennedy, D. J. L. (2000c). *Displacement-based seismic design of buildings — application*. *22*, 210–221.

Medina, R. A., & Krawinkler, H. (2005). Evaluation of Drift Demands for the Seismic Performance Assessment of Frames. *Journal of Structural Engineering*, *131*(7), 1003–1013.

Menegotto, M. (1973). Method of analysis for cyclically loaded RC plane frames including changes in geometry and non-elastic behavior of elements under combined normal force and bending. *Proc. of IABSE Symposium on Resistance and Ultimate Deformability of Structures Acted on by Well Defined Repeated Loads*, 15–22.

Millen, M. (2015). *Misconceptions about equivalent viscous damping in earthquake engineering*. https://www.linkedin.com/pulse/misconceptions-equivalent-viscous-damping-earthquake-maxim-millen/

Mirdad, M. A. H., & Chui, Y. H. (2019). Load-slip performance of Mass Timber Panel-Concrete (MTPC) composite connection with Self-tapping screws and insulation layer. *Construction and Building Materials*, *213*, 696–708.

Mirdad, M. A. H., & Chui, Y. H. (2020). Stiffness prediction of Mass Timber Panel-Concrete (MTPC) composite connection with inclined screws and a gap. *Engineering Structures, 207*(November 2019), 110215.

Moghaddam, H., & Hajirasouliha, I. (2006). An investigation on the accuracy of pushover analysis for estimating the seismic deformation of braced steel frames. *Journal OfConstructional Steel Research, 62*, 343–351.

Moroder, D. (2016). *Floor diaphragms in multi-storey timber buildings*. University of Canterbury.

Munoz, W., Salenikovich, A., Mohammad, M., & Quenneville, P. (2008). Determination of yield point and ductility of timber assemblies: In search for a harmonised approach. *10th World Conference on Timber Engineering 2008, 2*, 1064–1071.

Murphy, C., Blomgren, H., & Rammer, D. (2019). Development of timber buckling- restrained braces for mass timber braced frames. *International Network on Timber Engineering Research (INTER) - Meeting Fifty-Two, Tacoma (US)*, 1–14.

Muszynski, L., Larasatie, P., Guerrero, J. E., & Albee, R. (2020). *Global CLT industry in 2020 : Growth beyond the Alpine Region*. *July*.

Naghavi, M., Rahnavard, R., Thomas, R. J., & Malekinejad, M. (2019). Numerical evaluation of the hysteretic behavior of concentrically braced frames and buckling restrained brace frame systems. *Journal of Building Engineering, 22* (December 2018), 415–428.

Nakamura, N., Suzuki, T., & Nakamura, S. (2012). Three-dimensional simulation analysis of a full-scale 5-story building with steel dampers. *Blucher Mech Eng Proc, 1*(1), 636–650.

New Zealand Standards. (1993). *NZS3603:1993 Timber structures standard* (Issue 1). Standards New Zealand.

New Zealand Standards. (1997). NZS 3404: Part 1:1997 - Steel Structure Standard. In *New Zealand Standards*. New Zealand Standards.

Nievas, C. I., & Sullivan, T. J. (2015). Applicability of the direct displacement-based design method to steel moment resisting frames with setbacks. *Bulletin of Earthquake Engineering, 13*(12), 3841–3870.

Nokes, R. (2017). *Streams: System Theory and Design*.

Ottenhaus, L. M. (2019). *Seismic Performance of Dowel-Type Connections in Tall Timber Buildings*. University of Canterbury.

Ottenhaus, L. M., Li, M., Nokes, R., Cammock, P., & McInnes, B. (2019). Use of particle tracking velocimetry in timber material and connection testing. *European Journal of Wood and Wood Products, 77*(2), 195–209.

Ottenhaus, L. M., Li, M., & Smith, T. (2018). Structural performance of large-scale dowelled CLT connections under monotonic and cyclic loading. *Engineering Structures, 176* (September), 41–48.

Ottenhaus, L. M., Li, M., Smith, T., & Quenneville, P. (2018a). Mode Cross-Over and Ductility of Dowelled LVL and CLT Connections under Monotonic and Cyclic Loading. *Journal of Structural Engineering (United States), 144*(7), 1–10.

Ottenhaus, L. M., Li, M., Smith, T., & Quenneville, P. (2018b). Overstrength of dowelled clt connections under monotonic and cyclic loading. *Bulletin of Earthquake Engineering, 16*(2), 753–773.

Ozaki, H., Konishi, Y., Matsui, R., & Takeuchi, T. (2014). Out-Of-plane stability factors for diagonally installed buckling restrained braces. *Journal of Structural and Construction*

Engineering, *79*(706), 1919–1929.

Ozcelik, R., & Erdil, E. F. (2019). Pseudodynamic test of a deficient RC frame strengthened with buckling restrained braces. *Earthquake Spectra*, *35*(3), 1163–1187.

Palmer, K. D., Christopulos, A. S., Lehman, D. E., & Roeder, C. W. (2014). Experimental evaluation of cyclically loaded, large-scale, planar and 3-d buckling-restrained braced frames. *Journal of Constructional Steel Research*, *101*, 415–425.

Pan, W. H., Tong, J. Z., Guo, Y. L., & Wang, C. M. (2020). Optimal design of steel buckling-restrained braces considering stiffness and strength requirements. *Engineering Structures*, *211*(February), 110437.

Pang, W., & Rosowsky, D. V. (2009). Direct displacement procedure for performance-based seismic design of mid-rise wood-framed structures. *Earthquake Spectra*, *25*(3), 583–605.

Park, R. (1989). Evaluation of ductility of structures and structural assemblages from laboratory testing. In *Bulletin of the New Zealand Society for Earthquake Engineering* (Vol. 22, Issue 3, pp. 155–166).

Park, R., & Paulay, T. (1975). *Reinforced concrete structures*. John Wiley & Sons.

PEER. (2005). *PEER NGA database*. Pacific Earthquake Engineering Research (PEER) Center University of California, Berkeley, CA. http://peer.berkeley.edu/nga/index.html

Pennucci, D., Calvi, G. M., & Sullivan, T. J. (2009). Displacement-based design of precast walls with additional dampers. *Journal of Earthquake Engineering*, *13*(1 SUPPL. 1), 40–65.

Pennucci, D., Sullivan, T. J., & Calvi, G. M. (2011). Displacement reduction factors for the design of medium and long period structures. *Journal of Earthquake Engineering*, *15*(SUPPL. 1), 1–29.

Pettinga, J. D., & Priestley, M. J. N. (2005). Designed With Direct Displacement-Based Design. *Journal of Earthquake Engineering*, *9*(2), 309–330.

Piazza, M., Polastri, A., & Tomasi, R. (2011). Ductility of timber joints under static and cyclic loads. *Proceedings of the Institution of Civil Engineers: Structures and Buildings*, *164*(2), 79–90.

Popovski, M. (2000). *Seismic performance of braced timber frames*. University of British Columbia.

Popovski, M. (2004). *Structural systems with riveted connections for non-residential buildings*. Rep.

Popovski, M., Prion, H. G. L., & Karacabeyli, E. (2003). Shake table tests on single-storey braced timber frames. *Canadian Journal of Civil Engineering*, *30*(6), 1089–1100.

Priestley, M. J. N. (1995). Myths and Fallacies in Earthquake Engineering--Conflicts Between Design and Reality. *Special Publication*, *157*, 231–254.

Priestley, M. J. N. (2003). *Myths and Fallacies in Earthquake Engineering, Revisited The Ninth Mallet Milne Lecture, 2003*. *May*, 98.

Priestley, M. J. N., Calvi, G. M., & Kowalsky, M. J. (2007a). *Displacement-based Seismic Design of Structures*. IUSS Press.

Priestley, M. J. N., Calvi, M. C., & Kowalsky, M. J. (2007b). *Displacement-based Design of Structures*. IUSS Press.

Priestley, M. J. N., & Kowalsky, M. J. (2000). Direct displacement-based seismic design of concrete buildings. *Bulletin of the New Zealand Society for Earthquake Engineering*, *33*(4), 421–444.

Qu, Z., Kishiki, S., Maida, Y., Sakata, H., & Wada, A. (2015). Seismic responses of reinforced concrete frames with buckling restrained braces in zigzag configuration. *Engineering Structures*, *105*, 12–21.

Qu, Z., Kishiki, S., Sakata, H., Wada, A., & Maida, Y. (2013). Subassemblage cyclic loading test of RC frame with buckling restrained braces in zigzag configuration. *Earthquake Engineering & Structural Dynamics*, *42*(7), 1087–1102.

Qu, Z., Xie, J., Wang, T., & Kishiki, S. (2017). Cyclic loading test of double K-braced reinforced concrete frame subassemblies with buckling restrained braces. *Engineering Structures*, *139*, 1–14.

Quintana Gallo, P., Carradine, D. M., & Bazaez, R. (2020). State of the art and practice of seismic-resistant hybrid timber structures. *European Journal of Wood and Wood Products*, *0123456789*.

Rahim, N. L. (2019). *Stiffness of bolted timber connection*. ResearchSpace@ Auckland.

Rahnavard, R., Naghavi, M., Aboudi, M., & Suleiman, M. (2018). Investigating modeling approaches of buckling-restrained braces under cyclic loads. *Case Studies in Construction Materials*, *8*(April), 476–488.

Rajeev, P., Wijesundara, K. K., Al-Mashaykhi, M., Hashemi, M. J., & Gad, E. (2017). Displacement profile for displacement based seismic design of concentric braced frames. *16th World Conference on Earthquake Engineering*.

Ringhofer, A. (2017). Axially Loaded Self-Tapping Screws in Solid Timber and Laminated Timber Products. In *Graz University of Technology*. Verlag der Technischren Universität Graz.

RNZ. (2020). *Climate emergency declaration by New Zealand government includes commitment to 2025 targets*. Radio New Zealand. https://www.rnz.co.nz/news/political/431942/climate-emergency-declaration-by-new-zealand-government-includes-commitment-to-2025-targets

Roldan, R., Sullivan, T. J., & Della Corte, G. (2016). Displacement-based design of steel moment resisting frames with partially-restrained beam-to-column joints. *Bulletin of Earthquake Engineering*, *14*(4), 1017–1046.

Rothoblaas. (2017). *VGU: 45° washer for VGS - Bright zinc plated carbon steel*. https://www.rothoblaas.com/products/fastening

Sabelli, R., Mahin, S., & Chang, C. (2003). Seismic demands on steel braced frame buildings with buckling-restrained braces. *Engineering Structures*, *25*(5), 655–666.

Sahoo, D. R., & Chao, S.-H. (2010). Performance-based plastic design method for buckling-restrained braced frames. *Engineering Structures*, *32*(9), 2950–2958.

Sahoo, D. R., & Prakash, A. (2019). Seismic behavior of concentrically braced frames designed using direct displacement-based method. *International Journal of Steel Structures*, *19*(1), 96–109.

Salawdeh, S., & Goggins, J. (2016). Direct displacement based seismic design for single storey steel concentrically braced frames. *Earthquake and Structures*, *10*(5), 1125–1141.

Sandhaas, C., & van de Kuilen, J. W. G. (2017). Strength and stiffness of timber joints with very high strength steel dowels. *Engineering Structures*, *131*, 394–404.

Sawata, K., Sasaki, T., & Kanetaka, S. (2006). Estimation of shear strength of dowel-type timber connections with multiple slotted-in steel plates by European yield theory. *Journal of Wood Science*, *52*(6), 496–502.

Sawata, K., & Yasumura, M. (2003). Estimation of yield and ultimate strengths of bolted timber joints by nonlinear analysis and yield theory. *Journal of Wood Science, 49*(5), 383–391.

Saxey, B., & Daniels, M. (2014). Characterization of Overstrength Factors for Buckling Restrained Braces. *Proceedings of the Australasian Structural Engineering Conference*.

Sheng, N., Yam, C. H., & Iu, V. P. (2002). Analytical investigation and the design of the compressive strength of steel gusset plate connections. *Journal of Constructional Steel Research*, *58*(11), 1473–1493.

Sitler, B., & Takeuchi, T. (2021). Higher-mode buckling and friction in long and large-scale buckling-restrained braces. *The Structural Design of Tall and Special Buildings*, *30*(1), e1812.

Stepinac, M., Rajcic, V., Tomasi, R., Hunger, F., Van de Kuilen, J.-W. G., & Serrano, E. (2013). Comparison of design rules for glued-in rods and design rule proposal for implementation in European standards. *Proceedings of CIB-W18 Meeting, Vol.46*.

StructureCraft. (2016). *T3 Minneapolis Office Building*. StructureCraft. https://structurecraft.com/projects/t3-minneapolis

Sullivan, T. J. (2013). Direct displacement-based seismic design of steel eccentrically braced frame structures. *Bulletin of Earthquake Engineering*, *11*(6), 2197–2231.

Sullivan, T. J., & O'Reilly, G. (2014). *Characterising the Seismic Behaviour of Steel Beam-Column Joints for Seismic Design*.

Sullivan, T. J., Priestley, M. J. N., & Calvi, G. M. (2006). Direct displacement-based design of frame-wall structures. *Journal of Earthquake Engineering*, *10*(1), 91–124.

Sullivan, T. J., Priestley, M. J. N., & Calvi, G. M. (2012). A Model Code for the Displacement-Based Seismic Design of Structures DBD12. *IUSS Press, PaviaTsakanika-Theohari E, Mouzakis H (2010) A Post-Byzantine Mansion in Athens. The Restoration Project of the Timber Structural Elements. In: Proceedings of the World Conference on Timber Engineering. Trento, ItalyVamvatsikos D, Cornell C (2*, *31*, 491514.

Sun, H., Jia, M., Zhang, S., & Wang, Y. (2019). Study of buckling-restrained braces with concrete infilled GFRP tubes. *Thin-Walled Structures*, *136*(December 2018), 16–33.

Takeuchi, T., Hajjar, J. F., Matsui, R., Nishimoto, K., & Aiken, I. D. (2012). Effect of local buckling core plate restraint in buckling restrained braces. *Engineering Structures*, *44*, 304–311.

Takeuchi, T., Matsui, R., & Mihara, S. (2016). Out-of-plane stability assessment of buckling-restrained braces including connections with chevron configuration. *Earthquake Engineering & Structural Dynamics*, *45*(12), 1895–1917.

Takeuchi, T., Ozaki, H., Matsui, R., & Sutcu, F. (2014). Out-of-plane stability of buckling-restrained braces including moment transfer capacity. *Earthquake Engineering & Structural Dynamics*, *43*(6), 851–869.

Teran-gilmore, A., & Coeto, G. (2011). *Displacement-Based Preliminary Design of Tall Buildings Stiffened with a System of Buckling-Restrained Braces*. *27*(1), 153–182.

Terán-Gilmore, A., & Ruiz-García, J. (2011). Comparative seismic performance of steel frames retrofitted with buckling-restrained braces through the application of Force-Based and Displacement-Based approaches. *Soil Dynamics and Earthquake Engineering*, *31*(3), 478–490.

Teran-gilmore, A., & Virto-cambray, N. (2009). *Preliminary Design of Low-Rise Buildings*

Stiffened with Buckling-Restrained Braces by a Displacement-Based Approach. *25*(1), 185–211.

ThinkWood. (n.d.). *Light frame + prefab: Preferred and prefabulous*. https://www.thinkwood.com/light-frame-and-prefab

Thornton, W. A. (1984). Bracing connections for heavy construction. *Engineering Journal*, *21*(3), 139–148.

Timmers, M., & Tsay Jacobs, A. (2018). Concrete apartment tower in Los Angeles reimagined in mass timber. *Engineering Structures*, *167*(March 2017), 716–724.

Tomasi, R., Crosatti, A., & Piazza, M. (2010). Theoretical and experimental analysis of timber-to-timber joints connected with inclined screws. *Construction and Building Materials*, *24*(9), 1560–1571.

Tremblay, R., Lacerte, M., & Christopoulos, C. (2008). Seismic response of multistory buildings with self-centering energy dissipative steel braces. *Journal of Structural Engineering*, *134*(1), 108–120.

Tsai, C. Y., Tsai, K. C., Chen, L. W., & Wu, A. C. (2018). Seismic performance analysis of BRBs and gussets in a full-scale 2-story BRB-RCF specimen. *Earthquake Engineering and Structural Dynamics*, *47*(12), 2366–2389.

Tsai, K.-C., Lai, J.-W., Hwang, Y.-C., Lin, S.-L., & Weng, C.-H. (2004). Research and application of double-core buckling restrained braces in Taiwan. *13th World Conference on Earthquake Engineering*, *200*.

Tsai, K. C., & Hsiao, P. C. (2008). Pseudo-dynamic test of a full-scale CFT/BRB frame - Part II: Seismic performance of buckling-restrained braces and connections. *Earthquake Engineering and Structural Dynamics*, *37*(7), 1099–1115.

Tsai, K., Hsiao, P., Wang, K., Weng, Y., Lin, M., Lin, K., Chen, C., Lai, J., & Lin, S. (2008). Pseudo-dynamic tests of a full-scale CFT/BRB frame—Part I: Specimen design, experiment and analysis. *Earthquake Engineering & Structural Dynamics*, *37*(7), 1081–1098.

Tsai, K., Wu, A., Pan, K., & Yang, H. (2017). *Buckling Restrained Braces for Existing and New Reinforced Concrete Frames*.

Uang, C., Nakashima, M., & Tsai, K. (2004). Research and application of buckling-restrained braced frames. *International Journal of Steel Structures*, *4*(4), 301–313.

Vazquez-Colunga, S. Y. (2021). *Analysis and design of gusset plates in buckling restrained braced frames*. University of Canterbury.

Vazquez-Colunga, S. Y., Lee, C. L., & MacRae, G. A. (2018). Effects of Out-of-Plane Displacements on Load Capacity of Gusset Plates in Buckling Restrained Braced Frames. *Key Engineering Materials*, *763*, 892–899.

Vazquez-Colunga, S. Y., Lee, C., & Macrae, G. A. (2019). Axial strength of gusset plates in buckling restrained braced frames under bidirectional monotonic loads. *2019 Pacific Conference on Earthquake Engineering*.

Vigh, L. G., Zsarnóczay, Á., & Balogh, T. (2017). Eurocode conforming design of BRBF – Part I: Proposal for codification. *Journal of Constructional Steel Research*, *135*(May 2016), 265–276.

Wang, C., Lyu, J., Zhao, J., & Yang, H. (2020). Experimental investigation of the shear characteristics of steel-to-timber composite joints with inclined self-tapping screws. *Engineering Structures*, *215*(April), 110683.

Wang, J., Li, B., Chou, C., & Chen, L. (2018). Cyclic experimental and analytical studies of buckling-restrained braces with various gusset connections. *Engineering Structures*, *163*(February), 38–50.

Watanabe, A., Hitomi, Y., Saeki, E., Wada, A., & Fujimoto, M. (1988). Properties of brace encased in buckling-restraining concrete and steel tube. In *Proceedings of Ninth World Conference on Earthquake Engineering (Vol.4)* (pp. 719–724).

Whitmore, R. E. (1952). *Experimental investigation of stresses in gusset plates*. Engineering Experiment Station, University of Tennessee, Knoxville.

Wijanto, S., & Clifton, G. C. (2014). Experimental testing and design of BRB with bolted and pinned connections. *Bulletin of the New Zealand Society for Earthquake Engineering*, *47*(4), 264–274.

Wijesundara, K. K. (2012). Seismic design of steel concentric braced frame structures using direct displacement based design approach. *The 2nd International Conference on Sustainable Built Environments (ICSBE2012)*.

Wijesundara, K. K., Nascimbene, R., & Sullivan, T. J. (2011). Equivalent viscous damping for steel concentrically braced frame structures. *Bulletin of Earthquake Engineering*, *9*(5), 1535–1558.

Wijesundara, K. K., & Rajeev, P. (2012). Direct displacement-based seismic design of steel concentric braced frame structures. *Australian Journal of Structural Engineering*, *13*(3), 243–257.

Will, P. (n.d.). *Innovation with CLT: the Earth Science Building*. Woodworks. https://www.woodworks.org/wp-content/uploads/CLT-FOIT.pdf

Woodard, A. C., & Milner, H. R. (2016). Sustainability of timber and wood in construction. In *Sustainability of Construction Materials* (Second Edi). Elsevier Ltd.

Woolman, J., & Mottram, R. A. (2013). *The Mechanical and Physical Properties of the British Standard EN Steels (BS 970-1955): EN 40 to EN 363*. Elsevier.

Wu, A. C., Tsai, K. C., Yang, H. H., Huang, J. L., Li, C. H., Wang, K. J., & Khoo, H. H. (2017). Hybrid experimental performance of a full-scale two-story buckling-restrained braced RC frame. *Earthquake Engineering and Structural Dynamics*, *46*(8), 1223–1244.

Xie, Q. (2005). State of the art of buckling-restrained braces in Asia. *Journal of Constructional Steel Research*, *61*(6), 727–748.

Xie, R. M., Rodgers, G. W., & Sullivan, T. J. (2019). *Influence of Damper Sub-System Stiffness on the Structural Performance of a System Equipped with a Viscous Damper*.

Xiong, H., & Liu, Y. (2016). Experimental Study of the Lateral Resistance of Bolted Glulam Timber Post and Beam Structural Systems. *Journal of Structural Engineering (United States)*, *142*(4), 1–11.

XLam NZ Limited. (2016). *Designing With Xlam cross laminated timber* (Issue September). https://www.xlam.co.nz/technical.html

Yahyai, M., & Rezayibana, B. (2015). A simplified methodology to determine damping for special concentrically-braced frames. *International Journal of Steel Structures*, *15*(3), 541–555.

Yan, L., Gong, J., & Zhang, Q. (2018). Investigation of global equivalent damping and statistical relationship of displacement between nonlinear static and dynamic analysis of reinforced concrete frame structures. *Earthquake Spectra*, *34*(3), 1311–1338.

Yang, B., & Lu, X. (2018). Displacement-Based Seismic Design Approach for Prestressed

Precast Concrete Shear Walls and its Application. *Journal of Earthquake Engineering*, *22*(10), 1836–1860.

Yousef-beik, S. M. M., Veismoradi, S., Zarnani, P., Hashemi, A., & Quenneville, P. (2020). Self-centring Bracing System: Avoidance of Elastic Buckling For Braces with One Intermediate Damper. *NZSEE Annual Conference*, 3–5.

Yu, Y. J., Tsai, K. C., Li, C. H., Weng, Y. T., & Tsai, C. Y. (2011). Analytical simulations for shaking table tests of a full scale buckling restrained braced frame. *Procedia Engineering*, *14*, 2941–2948.

Zhang, F., Chen, X., Chen, L., Leng, Y., Wang, M., & Xu, Q. (2018). Shaking table test study on a five-story post-and-beam glulam structure. *World Conference on Timber Engineering*.

Zhang, J., He, M. J., & Li, Z. (2018). Numerical analysis on tensile performance of bolted glulam joints with initial local cracks. *Journal of Wood Science*, *64*(4), 364–376.

Zhang, J., Liu, Z. F., Xu, Y., Zhang, M. L., & Mo, L. C. (2021). Cyclic Behavior and Modeling of Bolted Glulam Joint with Cracks Loaded Parallel to Grain. *Advances in Civil Engineering*, *2021*.

Zhang, Z., Zhang, S. N., Deng, E. F., Zhou, T. T., Yi, Y., He, H., & Li, N. N. (2020). Experimental study on seismic performance of double-level yielding buckling-restrained braced concrete frames. *Archives of Civil and Mechanical Engineering*, *20*(2), 1–16.

Zona, A., & Dall'Asta, A. (2012). Elastoplastic model for steel buckling-restrained braces. *Journal of Constructional Steel Research*, *68*(1), 118–125.

Zonta, D., Loss, C., Piazza, M., & Zanon, P. (2011). Direct displacement-based design of glulam timber frame buildings. *Journal of Earthquake Engineering*, *15*(3), 491–510.

Zsarnoczay, A. (2013). *Experimental and numerical investigation of buckling restrained braced frames for Eurocode conform design procedure development*. Budapest University of Technology and Economics.

Zsarnoczay, A., & Vigh, L. G. (2017). Eurocode conforming design of BRBF – Part II: Design procedure evaluation. *Journal of Constructional Steel Research*, *135*(May 2016), 253–264.

APPENDIX A DESIGN TABLES FOR BRBGF BUILDINGS

A.1 Design information for the equivalent SDOF systems

Table A1-A3 and Table A4-A6 list the design parameters of the equivalent SDOF systems for BRBGF-3 and BRBGF-9, respectively.

Table A1. Design parameters for BRBGF-3 with Profile L

Storey	h_i	H_i	m_i (ton)	Δ_i (mm)	$\Delta_{y,i,BRB}$ (mm)	$\Delta_{y,i,col}$ (mm)	Δ_s *(mm)*	$\Delta_{y,i}$ (mm)	μ	V_i	F_i (kN)
1	3.6	3.6	65.6	72.0	11.1	0.0	2.5	13.6	5.3	1.00	71
2	3.6	7.2	65.6	144.0	11.1	1.7	2.5	15.3	4.7	0.81	142
3	3.6	10.8	38.0	216.0	11.1	3.4	2.5	17.0	4.2	0.43	160
Δ_d=155.2 mm, M_e=144 tons, H_e=7.8 m, μ_{sys}=4.9, T_e=1.60 s, V_{base}=373 kN											

Table A2. Design parameters for BRBGF-3 with Profile P

Storey	h_i	H_i	m_i (ton)	Δ_i (mm)	$\Delta_{y,i,BRB}$ (mm)	$\Delta_{y,i,col}$ (mm)	Δ_s *(mm)*	$\Delta_{y,i}$ (mm)	μ	V_i	F_i (kN)
1	3.6	3.6	65.6	72.0	11.1	0.0	2.5	13.6	5.3	1.00	94
2	3.6	7.2	65.6	130.9	11.1	1.7	2.5	15.3	3.8	0.79	170
3	3.6	10.8	38.0	176.7	11.1	3.4	2.5	17.0	2.7	0.40	177
Δ_d=132.4 mm, M_e=151 tons, H_e=7.6 m, μ_{sys}=4.5, T_e=1.38 s, V_{base}=441 kN											

Table A3. Design parameters for BRBGF-3 with Profile C

Storey	h_i	H_i	m_i (ton)	Δ_i (mm)	$\Delta_{y,i,BRB}$ (mm)	$\Delta_{y,i,col}$ (mm)	Δ_s *(mm)*	$\Delta_{y,i}$ (mm)	μ	V_i	F_i (kN)
1	3.6	3.6	65.6	72.0	11.1	0.0	2.5	13.6	5.3	1.00	116
2	3.6	7.2	65.6	121.8	11.1	1.7	2.5	15.3	3.3	0.77	197
3	3.6	10.8	38.0	149.5	11.1	3.4	2.5	17.0	1.6	0.38	191
Δ_d=117.6 mm, M_e=156 tons, H_e=7.4 m, μ_{sys}=4.3, T_e=1.20 s, V_{base}=504 kN											

Table A4. Design parameters for BRBGF-9 with Profile L

Storey	h_i	H_i	m_i (ton)	Δ_i (mm)	$\Delta_{y,i,BRB}$ (mm)	$\Delta_{y,i,col}$ (mm)	Δ_s *(mm)*	$\Delta_{y,i}$ (mm)	μ	V_i	F_i (kN)
1	3.6	3.6	65.6	72.0	11.1	0.0	2.5	13.6	5.1	1.00	10
2	3.6	7.2	65.6	144.0	11.1	2.7	2.5	15.3	4.5	0.98	21
3	3.6	10.8	65.6	216.0	11.1	0.0	2.5	17.0	4.0	0.93	31
4	3.6	14.4	65.6	288.0	11.1	2.7	2.5	18.8	3.7	0.87	42
5	3.6	18.0	65.6	360.0	11.1	5.4	2.5	20.5	3.3	0.78	52
6	3.6	21.6	65.6	432.0	11.1	0.0	2.5	22.3	3.1	0.67	63
7	3.6	25.2	65.6	504.0	11.1	2.7	2.5	24.0	2.9	0.54	73
8	3.6	28.8	65.6	576.0	11.1	5.4	2.5	25.8	2.7	0.39	84
9	3.6	32.4	38.0	648.0	11.1	5.4	2.5	27.5	2.5	0.21	102
Δ_d=438.3 mm, M_e=444 tons, H_e=21.9 m, μ_{sys}=3.8, T_e=4.4 s, V_{base}=477 kN											

Table A5. Design parameters for BRBGF-9 with Profile P

Storey	h_i	H_i	m_i (ton)	Δ_i (mm)	$\Delta_{y,i,BRB}$ (mm)	$\Delta_{y,i,col}$ (mm)	Δ_s *(mm)*	$\Delta_{y,i}$ (mm)	μ	V_i	F_i (kN)
1	3.6	3.6	65.6	72.0	11.1	0.0	2.5	13.6	5.1	1.00	16
2	3.6	7.2	65.6	139.9	11.1	2.7	2.5	15.3	4.2	0.97	31
3	3.6	10.8	65.6	203.7	11.1	0.0	2.5	17.0	3.6	0.92	45
4	3.6	14.4	65.6	263.3	11.1	2.7	2.5	18.8	3.0	0.85	58
5	3.6	18.0	65.6	318.9	11.1	5.4	2.5	20.5	2.6	0.76	70
6	3.6	21.6	65.6	370.3	11.1	0.0	2.5	22.3	2.2	0.65	82
7	3.6	25.2	65.6	417.6	11.1	2.7	2.5	24.0	1.9	0.51	92
8	3.6	28.8	65.6	460.8	11.1	5.4	2.5	25.8	1.6	0.37	102
9	3.6	32.4	38.0	499.9	11.1	5.4	2.5	27.5	1.4	0.20	126
Δ_d=341.1 mm, M_e=466 tons, H_e=21.4 m, μ_{sys}=3.4, T_e=3.38 s, V_{base}=622 kN											

Table A6. Design parameters for BRBGF-9 with Profile C

Storey	h_i	H_i	m_i (ton)	Δ_i (mm)	$\Delta_{y,i,BRB}$ (mm)	$\Delta_{y,i,col}$ (mm)	Δ_s *(mm)*	$\Delta_{y,i}$ (mm)	μ	V_i	F_i (kN)
1	3.6	3.6	65.6	72.0	11.1	0.0	2.5	13.6	5.1	1.00	27
2	3.6	7.2	65.6	127.6	11.1	2.7	2.5	15.3	3.5	0.97	48
3	3.6	10.8	65.6	171.1	11.1	0.0	2.5	17.0	2.4	0.91	65
4	3.6	14.4	65.6	206.8	11.1	2.7	2.5	18.8	1.8	0.83	78
5	3.6	18.0	65.6	239.0	11.1	5.4	2.5	20.5	1.5	0.74	90
6	3.6	21.6	65.6	272.2	11.1	0.0	2.5	22.3	1.4	0.63	103
7	3.6	25.2	65.6	310.5	11.1	2.7	2.5	24.0	1.5	0.51	117
8	3.6	28.8	65.6	358.3	11.1	5.4	2.5	25.8	1.8	0.37	135
9	3.6	32.4	38.0	419.9	11.1	5.4	2.5	27.5	2.1	0.21	176
Δ_d=275.7 mm, M_e=476 tons, H_e=21.1 m, μ_{sys}=3.0, T_e=2.58 s, V_{base}=840 kN											

A.2 Member size information of the BRBGFs

The member size information of BRBGF-3 and BRBGF-9 is listed in Table A7-A12.

Table A7 Member size information of BRBGF-3 with Profile L

Storey	V_i (kN)	BRB cross-section (mm)	Middle span connection (n_r×n_c)	Beam (mm)	Column (mm)
1	373	12×75	3×8	360×270	270×270
2	302	12×61	3×6	360×270	
3	160	8×48	3×3	360×270	

Table A8 Member size information of BRBGF-3 with Profile P

Storey	V_i (kN)	BRB cross-section (mm)	Middle span connection ($n_r \times n_c$)	Beam (mm)	Column (mm)
1	441	12×79	3×8	360×315	315×315
2	347	12×64	4×5	360×270	
3	177	8×51	2×5	360×270	

Table A9 Member size information of BRBGF-3 with Profile C

Storey	V_i (kN)	BRB cross-section (mm)	Middle span connection ($n_r \times n_c$)	Beam (mm)	Column (mm)
1	504	16×73	6×8	405×270	315×315
2	388	12×75	6×7	360×270	
3	191	8×56	5×8	360×270	

Table A10 Member size information of BRBGF-9 with Profile L

Storey	V_i (kN)	BRB cross-section (mm)	Middle span connection ($n_r \times n_c$)	Beam (mm)	Column (mm)
1	477	16×71	4×7	405×270	495×495
2	468	16×71	4×7	405×270	
3	447	16×67	4×7	405×270	
4	416	16×63	4×6	405×270	360×360
5	374	12×75	3×7	360×270	
6	322	12×64	3×6	360×270	
7	259	12×53	3×5	315×225	225×225
8	186	12×37	3×4	315×225	
9	102	12×21	2×3	315×225	

Table A11 Member size information of BRBGF-9 with Profile P

Storey	V_i (kN)	BRB cross-section (mm)	Middle span connection ($n_r \times n_c$)	Beam (mm)	Column (mm)
1	622	20×74	6×6	450×315	540×540
2	606	20×72	5×7	450×315	
3	575	20×69	5×7	405×315	
4	530	20×63	4×8	405×315	405×405
5	472	16×70	4×7	405×270	
6	402	12×80	3×8	405×270	
7	320	12×64	3×6	405×270	270×270
8	228	8×69	3×5	315×225	
9	126	8×39	3×3	315×225	

Table A12 Member size information of BRBGF-9 with Profile C

Storey	V_i (kN)	BRB cross-section (mm)	Middle span connection ($n_r \times n_c$)	Beam (mm)	Column (mm)
1	840	20×97	7×7	540×315	630×630
2	812	20×94	6×8	540×315	
3	764	20×88	6×8	540×315	
4	699	20×80	6×7	495×315	495×495
5	621	16×89	6×6	495×315	
6	531	16×76	4×8	495×315	
7	428	12×82	5×5	405×270	315×315
8	311	12×60	3×6	405×270	
9	176	12×34	3×4	405×270	

APPENDIX B PUBLICATIONS

B.1 Journal publications

The following journal articles were published during the PhD study with their abstracts.

1) **Dong, W.**, Li, M., Lee, C.L. and MacRae, G., 2021. Numerical Modelling of Glulam Frames with Buckling Restrained Braces, Engineering Structures, 239, p.112338.

   Abstract: This paper presents component-based numerical models to simulate the seismic behaviour of a timber-steel hybrid structure consisting of glulam frames and buckling restrained braces (BRBs). The model is validated by existing experimental data of two full-scale BRB-braced glulam frames (BRBGFs) where dowelled connections and screwed connections were used as the critical BRB-timber interface connections, respectively. Parametric studies are also conducted by the validated model to investigate the influence of the interface connection stiffness and manufacturing tolerances on the performance of the BRBGFs. The studies showed that the interface connection relative overstrength factor γ=1.5 was a suitable value to engage BRBs, ensure ductile behaviour and achieve a cost-effective connection design. Manufacturing tolerances had a negligible impact on the ultimate strength and energy dissipation under cyclic loading but might affect the performance under serviceability limit state loads.

2) **Dong, W.**, Li, M., He, M. and Li, Z., 2021. Experimental Testing and Analytical Modeling of Glulam Moment Connections with Self-drilling Dowels, Journal of Structural Engineering, 147(5), p.04021047.

   Abstract: An experimental and analytical study on rotational behavior of glulam beam-column moment connections with self-drilling dowels (SDDs) is conducted. Connection properties including strength, stiffness, ductility, and energy dissipation were experimentally evaluated by testing seven full-scale connection specimens with and without self-tapping screw (STS) reinforcement along timber perpendicular to grain. All the connections showed high initial stiffness and high moment capacity when compared with the test results of bolted connections reported in the literature. The unreinforced connections had relatively low ductility due to timber splitting despite the increased fastener edge distance. The STS reinforcement effectively reduced the timber splitting tendency and encouraged the yielding of more SDDs, leading to slightly increased moment capacity, but significantly improved ductility. A modified analytical model (MAM) is then proposed to predict strength and rotation of the SDD moment connections based on force and moment equilibrium of the glulam members. Improved

prediction accuracy is achieved for the SDD moment connections when compared with the past analytical methods.

3) **Dong, W.**, Li, M., Lee, C.L., MacRae, G. and Abu, A., 2020. Experimental Testing of Full-scale Glulam Frames with Buckling Restrained Braces. Engineering Structures, 222, p.111081.

Abstract: This experimental study investigates cyclic performance of a timber-steel hybrid structural system consisting of glulam frames and buckling restrained braces (BRBs). The BRBs are designed as ductile elements in the hybrid system to dissipate energy under seismic loading. Following the capacity design approach, two full-scale 8 m wide and 3.6 m high BRB glulam frame (BRBGF) specimens were tested. The BRBs were connected to the glulam frames by pins and steel gusset plates. Dowelled connections with inserted steel plates were used in one specimen to connect the glulam members while screwed connections with steel side plates were used in the other specimen. The test results showed that the integration of BRBs into the glulam frames significantly improved the load carrying capacity and energy dissipation. Both BRBGF specimens achieved a minimum ductility factor of 3.0 based on CEN method. The connections and the glulam members were well protected without significant damage. Therefore, the dowelled connections and screwed connections provided solutions to engage BRBs efficiently to resist lateral loads in this hybrid system.

4) **Dong, W.**, Li, M., Ottenhaus, L.M. and Lim, H., 2020. Ductility and Overstrength of Nailed CLT Hold-down Connections. Engineering Structures, 215, p.110667.

Abstract: The structural performance of nailed hold-down connection systems used for cross-laminated timber (CLT) shear walls under monotonic and cyclic loading was experimentally evaluated. Critical connection performance parameters, including strength, stiffness, ductility, and overstrength, were derived from the testing of 68 hold-down connection specimens. The nailed CLT hold-down connections achieved moderate to high ductility when fracture failures of their metal brackets were avoided. The hold-down connection systems with 3 mm thick commercial brackets achieved ductility factors ranged from 2.7 to 4.3, while the hold-down connection systems composed of 10 mm thick steel plates and longer nails achieved larger ductility factors which ranged from 4.7 to 6.3. The overstrength factors of the hold-down systems ranged from 1.45 to 1.62 except the one composed of the 10 mm thick brackets and 100 mm long nails installed at wide spacing. It was also found that the yield strength of the nailed hold-down connections under monotonic loading was similar to that obtained by cyclic loading.

5) Li, M., **Dong, W.** and Lim, H., 2019. Influence of Lamination Aspect Ratios and Test Methods on Rolling Shear Strength Evaluation of Cross-Laminated Timber. Journal of Materials in Civil Engineering, 31(12), p.04019310.

Abstract: Rolling shear (RS) strength may govern load-carrying capacity of cross-laminated timber (CLT) subjected to high out-of-plane loading because high RS stresses may be induced in cross layers and wood typically has low RS strength. This study investigates RS strength properties of non-edge-glued CLT via experimental testing (short-span bending tests and modified planar shear tests) and numerical modeling. CLT specimens with different manufacturing parameters including two timber species (New Zealand–grown Douglas fir and Radiata pine), three lamination thicknesses (20, 35, and 45 mm), and various lamination aspect ratios (4.1–9.8) were studied. The lamination aspect ratio was found to have a substantial impact on RS strength of CLT. Higher aspect ratios led to a significant increase of RS strength, and an approximately linear relationship could be established. With similar lamination aspect ratios, the Radiata pine CLT had higher RS strength than the Douglas fir CLT. The two different test methods, however, yielded comparable RS strength assessments. Numerical models were further developed to study the influence of the test configurations and gaps in the cross layers on stress distributions in the cross layers. It was also found that the compressive stresses perpendicular to the grain in cross layers had negligible influence on the RS strength evaluations.

6) **Dong, W.**, Li, M., Kho, D., He, M. and Li, Z., 2019. Seismic Performance Evaluation of Steel Moment Frames Infilled with Plywood Shear Walls. New Zealand Timber Design Journal, 27(4), 21-28.

Abstract: This paper presents seismic performance evaluation and design of timber-steel hybrid shear walls consisting of steel moment frames infilled with plywood shear walls. This hybrid system can be easily incorporated into multi-storey light timber framed (LTF) buildings using construction materials that are readily available in the NZ construction market. A finite element (FE) model of the hybrid wall system was developed with its critical input parameters calibrated by connection test database of nailed plywood-timber connections as well as bolted and screwed timber-steel interface connections. The FE model was validated against existing hybrid wall testing data and then used to conduct a parametric study to establish shear wall response database of the hybrid walls with various configurations in terms of steel member sizes, nail sizes, and plywood thicknesses.

7) **Dong, W.**, Li, M., Sullivan J. T., Lee, C.L. and MacRae, G., Direct Displacement-based Design of Glulam Frames with Buckling Restrained Braces (under review), Engineering Structures.

Abstract: Buckling restrained braces (BRBs) can be integrated into glulam frames to form a new timber-steel hybrid system with enhanced energy dissipation capacity when compared with the conventional timber-braced glulam frame structures under seismic loading. This paper presents a direct displacement-based design (DDBD) approach for the BRB-braced glulam frame (BRBGF) buildings. Some critical design parameters of the DDBD approach were firstly derived for BRBGFs including the displacement profile, the yield displacement and the displacement reduction factor η_{in}. Then, using experimentally verified numerical models, pushover analyses and nonlinear time-history analyses (NLTHA) were conducted on a series of one-storey BRBGFs. The influence of the stiffness of the BRB-timber connections on the system yield drift was considered by a stiffness adjustment factor λ which was calibrated by the pushover analyses. The relationship between the displacement reduction factor η_{in} and the system ductility factor μ based on the Takeda fat model was proved to be applicable for the BRBGFs based on the results of NLTHA. At last, the DDBD approach was applied to the design of three case study BRBGF structures with three, six, and nine storeys and compared against the results of NLTHA. The comparison showed that the DDBD approach was a sound approach for the seismic design of multi-storey BRBGF buildings.

B.2 Conference publications

The following conference papers were published during the PhD study.

1) **Dong, W.**, Li, M., Lee, C.L., MacRae, G. and Abu, A., 2020. Critical Connection Behavior in BRB Glulam Frames under Lateral Loads. World Conference on Timber Engineering, Santiago.
2) **Dong, W.**, Li, M., Lee, C.L., MacRae, G. and Abu, A., 2020. Cyclic Tests of Glulam Frames with Buckling Restrained Braces (BRBs). 17th World Conference on Earthquake Engineering, Sendai.
3) **Dong, W.** and Li, M., 2019. A Preliminary Study on Cyclic Behaviour of SFS Dowelled Connections in Glulam Frames. Pacific Conference on Earthquake Engineering, Auckland.
4) Kho, D., **Dong, W.**, Li, M. and Lee, C.L., 2018. Cyclic Behavior of Timber-Steel Hybrid Shear Walls. New Zealand Society for Earthquake Engineering Conference, Auckland, 2018.